

Ph...  
13/15 ✓

FOE...  
13/15

12 NOV 1999

40 0685518 X



ProQuest Number: 10290294

All rights reserved

INFORMATION TO ALL USERS

The quality of this reproduction is dependent upon the quality of the copy submitted.

In the unlikely event that the author did not send a complete manuscript and there are missing pages, these will be noted. Also, if material had to be removed, a note will indicate the deletion.



ProQuest 10290294

Published by ProQuest LLC (2017). Copyright of the Dissertation is held by the Author.

All rights reserved.

This work is protected against unauthorized copying under Title 17, United States Code  
Microform Edition © ProQuest LLC.

ProQuest LLC.  
789 East Eisenhower Parkway  
P.O. Box 1346  
Ann Arbor, MI 48106 – 1346

**INVESTIGATION INTO THERMOGRAPHIC  
PHOSPHORS**

**ROBERT MARCUS RANSON**

A thesis submitted in partial fulfilment of the  
requirements of The Nottingham Trent University  
for the degree of Doctor of Philosophy

This research programme was carried out  
in collaboration with Rolls-Royce Plc.

**May 1999**

## ABSTRACT

Accurate temperature measurement of rotating components is problematic, particularly for parts within a hostile environment. Knowledge of the surface temperature of turbine blades within an engine would assist in the analysis and improvement of engine design and efficiency. This thesis presents work carried out during an EPSRC Case studentship, in collaboration with Rolls-Royce Plc., towards the development of phosphor thermography as a remote temperature sensing technique. The sensor is based upon the temperature dependence of the rise- and decay-times of the photoluminescent characteristics which are emitted by a phosphor when excited by pulsed laser radiation. By applying a phosphor coating to the component-under-test, the photoluminescent emission can be collected and analysed remotely resulting in the determination of the surface temperature of the component. Since no physical contact is required, this technique can be utilised for the temperature sensing of both static and rotating components.

This research has concentrated on the characterisation of two phosphors; namely, Europium doped Yttrium Oxide ( $Y_2O_3:Eu$ ) and Terbium doped Yttrium Aluminium/Gallium Oxide (YAGaG:Tb). Both phosphors have been optimised for their intensity emission levels and decay constant characteristics through the variation of the dopancy level. The discovery of a rise characteristic within the photoluminescent emission has led to a new, low temperature dependent characteristic. The modelling of the rise and decay characteristics has been performed, based upon the energy level transitions for these phosphors. This rise constant characterisation has extended the temperature sensing capabilities of  $Y_2O_3:Eu$  to a range of  $25^\circ C$  to  $+1100^\circ C$ . Previously, this phosphor was useful only between  $600^\circ C$  and  $+1100^\circ C$ .

Comparison, between the temperature dependence of the two phosphors, shows both are sensitive for the range of  $600^\circ C$  to  $+1100^\circ C$  and therefore are suitable for use within the field of turbine engines.  $Y_2O_3:Eu$  is more sensitive to temperature variation defined by the quenching rate i.e.  $Y_2O_3:Eu$  is  $15.4mC^{-1}$  and YAGaG:Tb is  $12.0mC^{-1}$ . Results presented show  $Y_2O_3:Eu$  to be a more efficient phosphor. Intensity emission levels of  $Y_2O_3:Eu$  are a factor of ten stronger than the emission levels of YAGaG:Tb.

The fabrication of thin film samples of  $Y_2O_3:Eu$  by RF Magnetron Sputtering, have provided intensity levels equal to those obtained from thermographic paints. Lifetime experimentation has shown thermographic paints to survive for only one hour at  $1200^\circ C$  compared with the thin film samples which lasted for up to ten hours. Thus, a robust thermographic coating has been demonstrated which exhibits the ability for long term use within the hostile environment of a turbine engine to aid in the temperature sensing of turbine blades.

## **Acknowledgements**

The success of this investigation has been largely due to the co-operation and assistance from a multitude of sources. I would like to begin by thanking my supervisors Prof. Clive Thomas, Dr. Wayne Cranton and Dr. Ian McClean for the opportunity of this research; their assistance in the preparation of papers, presentations and this thesis; and their technical discussions, all of which have been provided throughout this doctoral study.

Special thanks must go to Rolls-Royce Plc, the industrial collaborators of this CASE study, for financial assistance and the loan of valuable equipment. I would like to extend this thanks specifically towards Dr. John Mutton and Mr. Colin Bird for their technical contributions to the field of phosphor thermography.

I would also like to express gratitude to all my colleagues within the Optoelectronic Research Group for their assistance provided over the past three years - especially Dr. Robert Stevens for the technical, but enlightening, discussions and Mr. Marc Craven for assisting in the growth of the thin films.

Also, I wish to thank all my friends for their social support and encouragement over recent years, with special thanks towards Dr. Richard Petty, Mr. Richard Day and Mr. Robin Hotchkiss.

Finally, my gratitude goes to my family, whose continuous encouragement has maintained my spirit towards the completion of this study.

## List of Publications

### Conferences :-

- 1] I.P.McClean, R.M.Ranson, C.B.Thomas, J.E.Mutton, A.J.Simons "*High Temperature Thick and Thin Film Thermographic Sensor*" Measurement Technology, Sensor and Transducer Conference at MTEC'97, 22nd-23rd January 97, NEC Birmingham,
- 2] R.M.Ranson, "*Development of Phosphor Thermography*" PREP'99 (Postgraduate Research in Electronics, Photonics and Related Fields), paper no.A4.1, 5-7 January 99, UMIST.

### Papers :-

- 3] R.M.Ranson, E.Evangelou, C.B.Thomas, "*Modelling the fluorescent lifetime of  $Y_2O_3:Eu$* ", Jn. Applied Physics Letters, pp 2663-2664, Vol 72 (21), May 98
- 4] R.M.Ranson, C.B.Thomas, M.R.Craven, "*Thin Film Coating for Phosphor Thermography*" I.O.P. Jn. Measurement Science and Technology, pp1947-1950, Vol. 9, 98

### Patent Applications :-

- 5] R.M. Ranson, C.B. Thomas, I.P. McClean, "*Phosphor Thermography Sensing Using Rise Time Analysis*"  
UK Patent No. GB 9723018.9 (1 Nov 1997)  
European Patent No. EP 98308317.1 (13 Oct 98)  
US Patent No. US 09/175,451 (20 Oct 98)
- 6] R.M. Ranson, C.B. Thomas, "*Thin Film Coating for Phosphor Thermography*"  
UK Patent No. GB 9826281.9 (1 Dec 1998)

## Contents

<b>Abstract</b>	<b>ii</b>
<b>Acknowledgements</b>	<b>iii</b>
<b>List of Publications</b>	<b>iv</b>
<b>Contents</b>	<b>v</b>
<b>List of Figures</b>	<b>ix</b>
<b>List of Tables</b>	<b>xii</b>
<b>List of Abbreviations</b>	<b>xiii</b>
<b>List of Variables</b>	<b>xv</b>
<b>1. INTRODUCTION TO PHOSPHOR THERMOGRAPHY .....</b>	<b>1</b>
1.1 BACKGROUND .....	1
1.2 CURRENT TECHNIQUES.....	2
1.3 PHOSPHOR THERMOGRAPHY .....	5
<i>1.3.1 Introduction.....</i>	<i>5</i>
<i>1.3.2 Comparison With Previous Techniques.....</i>	<i>6</i>
<i>1.3.3 Previous Work.....</i>	<i>7</i>
1.4 SUMMARY OF THE THESIS.....	8
<b>2. REVIEW OF THERMOGRAPHIC PHOSPHORS.....</b>	<b>11</b>
2.1 DEFINITION OF A PHOSPHOR .....	11
<i>2.1.1 A Brief History of Phosphors.....</i>	<i>11</i>
<i>2.1.2 Luminescent Properties.....</i>	<i>12</i>
<i>2.1.3 The Mechanism of Luminescence.....</i>	<i>13</i>
2.1.3.1 Luminescent Centres .....	14
2.1.3.2 The Excitation and Relaxation Process .....	15
<i>2.1.4 Temperature Dependent Properties .....</i>	<i>15</i>
2.2 PHOSPHOR PREPARATION .....	21
2.3 PHOSPHORS UNDER INVESTIGATION.....	22

<b>3. EXPERIMENTAL DETAIL</b> .....	<b>27</b>
3.1 PHOSPHOR SPECIFICATION .....	27
3.2 PHOSPHOR PREPARATION .....	28
3.2.1 <i>Powder</i> .....	28
3.2.2 <i>Thick Film</i> .....	29
3.2.3 <i>Thin Film</i> .....	30
3.3 TEMPERATURE CONTROL .....	33
3.4 EMISSION SPECTRA.....	38
3.5 DECAY CONSTANT CHARACTERISATION.....	42
3.5.1 <i>Response Time of The Measurement System</i> .....	44
3.6 LABVIEW CONTROL SOFTWARE.....	50
3.6.1 <i>Communication Requirements</i> .....	51
3.6.2 <i>Emission Spectrum Programme</i> .....	52
3.6.3 <i>Decay Constant Programme</i> .....	55
3.7 SUMMARY .....	58
<b>4. EUROPIUM DOPED YTTRIUM OXIDE</b> .....	<b>59</b>
4.1 BACKGROUND .....	59
4.1.1 <i>Crystal Structure</i> .....	61
4.1.2 <i>Dopant Dependency</i> .....	63
4.2 EMISSION SPECTRA OF $Y_2O_3:Eu$ .....	64
4.2.1 <i>Dopant Dependency</i> .....	64
4.2.2 <i>Temperature Dependency</i> .....	67
4.3 DECAY AND RISE CONSTANT CHARACTERISATION .....	69
4.3.1 <i>Derivation of Formulae</i> .....	69
4.3.2 <i>Temperature Dependency</i> .....	72
4.3.3 <i>Dopant Dependency</i> .....	73



4.4 SUMMARY .....	78
<b>5. TERBIUM DOPED YTTRIUM ALUMINIUM/GALLIUM OXIDE .....</b>	<b>80</b>
5.1 BACKGROUND .....	80
5.1.1 <i>Crystal Structure</i> .....	81
5.2 EMISSION SPECTRA .....	82
5.2.1 <i>Dopant Intensity Dependency</i> .....	82
5.2.2 <i>Temperature Dependency</i> .....	84
5.3 TEMPERATURE DEPENDENCE CHARACTERISATION.....	85
5.3.1 <i>Single Exponential Method</i> .....	85
5.3.2 <i>Double Exponential Characteristics</i> .....	89
5.4 COMPARISON OF SINGLE AND DOUBLE EXPONENTIAL CHARACTERISATION .....	97
5.5 SUMMARY .....	99
<b>6. COMPARISON OF PHOSPHORS.....</b>	<b>101</b>
6.1 INTRODUCTION .....	101
6.2 INTENSITY COMPARISON.....	102
6.3 TEMPERATURE DEPENDENCY COMPARISON .....	110
6.4 LIFETIME COMPARISON (THICK FILM ONLY) .....	113
6.5 RECOMMENDED PHOSPHOR FOR FUTURE DEVELOPMENT .....	118
<b>7. THIN FILM PHOSPHOR THERMOGRAPHY .....</b>	<b>120</b>
7.1 INTRODUCTION .....	120
7.2 GROWTH OF $Y_2O_3:Eu$ THIN FILMS .....	122
7.3 POST GROWTH ANNEALING PROCESS .....	125
7.3.1 <i>Thermal Annealing Experimentation</i> .....	126
7.4 LIFETIME EXPERIMENTATION.....	131
7.5 ANGULAR MEASUREMENT .....	134
7.6 ROUGHNESS MEASUREMENT .....	140

7.7 SUMMARY .....	142
<b>8. CONCLUSIONS AND FUTURE WORK .....</b>	<b>144</b>
8.1 INTRODUCTION .....	144
8.2 ACHIEVEMENTS .....	145
8.3 RECOMMENDATIONS.....	149
8.4 FUTURE WORK. ....	149
<b>References</b>	<b>153</b>
<b>Appendix A</b>	<b>160</b>
LabVIEW Control Programme	

## List of Figures

Figure 1-1 A Simple Thermographic System.....	5
Figure 2-1 Emission and Excitation Spectra of $Y_2O_3:Eu$ .....	13
Figure 2-2 Energy Level schematic showing electron transitions .....	14
Figure 2-3. Diagram Showing The Principle of Two-Peak Intensity Method .....	16
Figure 2-4 Illustration of the Decay Constant Principle .....	18
Figure 2-5 Temperature Dependence Characteristic of the Decay Constant.....	19
Figure 2-6 Configurational Co-ordinate Diagram Of A Simple Two Energy Level System .....	20
Figure 3-1 Cross-Section Diagram of The Pellet Die.....	29
Figure 3-2 Illustration of the RF Magnetron Sputtering System .....	32
Figure 3-3 Interferometric Thin Film Thickness Monitor Graph .....	33
Figure 3-4 Illustration of the Pellet Holder .....	35
Figure 3-5 Top Cross-Sectional View of Excitation/Collection Set-up Within A High Temperature Controlled Environment .....	36
Figure 3-6 Optical Rod Assessment Layout .....	37
Figure 3-7 Illustration of the "Overhang" Characteristic of a Spectrometer .....	39
Figure 3-8 Illustration of Projecting Lens Requirements .....	40
Figure 3-9 Schematic of Emission Spectra Set-up .....	40
Figure 3-10 Schematic showing the Decay Constant Measurement Set-up.....	43
Figure 3-11 Photo of The Spectron Nd:YAG Pulse Laser System.....	44
Figure 3-12 Digital Storage Oscilloscope Output (a) complete pulse and (b) closer inspection of the laser spike interference .....	45
Figure 3-13 Gating Board (a) response over complete pulse width (b) initial gate Delay and switch-on time.....	49
Figure 3-14 Spectral Response of Type-9558QB and Type-9954B Photomultiplier Tubes, obtained from Electron Tubes Ltd Data Sheets.....	50
Figure 3-15 Communication Diagram of Measurement Equipment.....	51
Figure 3-16 Block Flow Diagram of the Emission Spectra Programme .....	53
Figure 3-17 Block Flow Diagram of Decay Constant Measurement Programme .....	56
Figure 3-18 Photo of The Decay Constant Measurement Programme in Operation .....	57
Figure 4-1 Excitation Spectrum of $Y_2O_3:Eu$ , provided by Phosphor Technology Ltd. ....	60
Figure 4-2 Sites of Symmetry of $Y_2O_3:Eu$ .....	61
Figure 4-3 Energy Level Diagram of $Y_2O_3:Eu$ .....	62
Figure 4-4 Concentration Dependence Curves of $Y_2O_3:Eu$ 611nm due to Cathodoluminescence Excitation .....	63
Figure 4-5 Emission Spectra of $Y_2O_3:Eu$ at Various Dopant Concentrations .....	65
Figure 4-6 Intensity Graphs of $Y_2O_3:Eu$ Over Full Dopant Concentrations.....	66
Figure 4-7 Emission Spectra of $Y_2O_3:Eu$ 3.4a/o .....	68

Figure 4-8 611nm Peak Intensity of Y <sub>2</sub> O <sub>3</sub> :Eu over the full temperature range .....	68
Figure 4-9 Schematic of electron detrapping within Y <sub>2</sub> O <sub>3</sub> :Eu.....	70
Figure 4-10 Observed Emission from Y <sub>2</sub> O <sub>3</sub> :Eu 3.4 a/o and the Resultant Curve Fits.....	71
Figure 4-11 Rise and Decay Characteristics of Y <sub>2</sub> O <sub>3</sub> :Eu 3.4 a/o.....	73
Figure 4-12 Decay Constant Characteristics of Y <sub>2</sub> O <sub>3</sub> :Eu .....	74
Figure 4-13 Rise Constant Characteristics of Y <sub>2</sub> O <sub>3</sub> :Eu .....	76
Figure 4-14 Energy Difference Calculations for the <sup>5</sup> D <sub>1</sub> (C <sub>3i</sub> ) to <sup>5</sup> D <sub>0</sub> (C <sub>2</sub> ) Transition .....	77
Figure 5-1 Excitation Spectrum of YAGaG:Tb .....	81
Figure 5-2 Room Temperature Emission Spectra of YAGaG:Tb .....	82
Figure 5-3 Schematic of Energy Levels of Tb Ion showing the Stark Splitting of <sup>5</sup> D <sub>4</sub> and <sup>7</sup> F <sub>5</sub> Energy Levels.....	83
Figure 5-4 Emission Spectra of YAGaG:Tb 20a/o At Various Temperatures .....	84
Figure 5-5 Decay Constant Characterisation of YAGaG:Tb Using a Single Exponential Curve Fit at (a) 355nm and (b) 266nm Excitation.....	86
Figure 5-6 Schematic of a Single Site Energy Level Diagram to Illustrate the Rise Time Mechanism of the Terbium Atom.....	88
Figure 5-7 Rise Constant Characteristics of YAGaG:Tb at 266nm Excitation .....	89
Figure 5-8 Illustration of a Single Exponential Fit of the Photoluminescent from YAGaG:Tb at a Temperature of 855°C .....	90
Figure 5-9 An Illustration of the 544nm Transitions of Isolated Terbium Atoms.....	91
Figure 5-10 Double Exponential Characterisation of YAGaG:Tb Using 355nm Excitation .....	92
Figure 5-11 Double Exponential Characteristics of YAGaG:Tb Using 266nm Excitation.....	93
Figure 5-12 Illustration of The Double Exponential Rise Characteristic of YAGaG:Tb 1a/o and The Resultant Curve Fits .....	95
Figure 5-13 Double Exponential Rise Constant Characterisation of YAGaG:Tb at 266nm Excitation.....	96
Figure 5-14 Comparison of Exponential Fits for YAGaG:Tb 5a/o .....	97
Figure 6-1 Blackbody Radiance Of The Visible Spectrum At Various Temperatures.....	103
Figure 6-2 Intensity Comparison of Y <sub>2</sub> O <sub>3</sub> :Eu and YAGaG:Tb at Room Temperature.....	104
Figure 6-3 Peak Intensity Comparison of Y <sub>2</sub> O <sub>3</sub> :Eu and YAGaG:Tb Over Full Temperature Range at 266nm Excitation .....	105
Figure 6-4 Labsphere Arrangement for the Measurement of Quantum Efficiency .....	107
Figure 6-5 Relative Coupling Efficiency Measurement of Y <sub>2</sub> O <sub>3</sub> :Eu .....	109
Figure 6-6 Comparison of Decay Constant Characterisation (a) at 355nm and (b) 266nm excitation.....	111
Figure 6-7 Intensity of Thermographic Paints.....	115
Figure 6-8 Lifetime Measurement of Thick Film Samples.....	117
Figure 7-1 Photographs of the Y <sub>2</sub> O <sub>3</sub> :Eu samples of various thickness grown by RF Magnetron Sputtering .....	124
Figure 7-2 Intensity Comparison of Non-Annealed Y <sub>2</sub> O <sub>3</sub> :Eu 35a/o Thin Films .....	125
Figure 7-3 Annealed Samples of Y <sub>2</sub> O <sub>3</sub> :Eu 35a/o for Various Temperatures and Periods of Time ....	127

Figure 7-4 Intensity Measurement of Annealed Thin Film Samples at 900°C .....	128
Figure 7-5 Intensity Measurement After Annealing at 1100°C .....	129
Figure 7-6 Intensity Measurement After Annealing at 1200°C .....	130
Figure 7-7 Comparison of the Annealing Conditions Investigated .....	131
Figure 7-8 Intensity Measurement of Thin and Thick Film Samples During Lifetime Experimentation	132
Figure 7-9 Photographs of Lifetime Experimentation.....	133
Figure 7-10 Photograph Of The Angular Distribution Measurement System .....	135
Figure 7-11 Comparison of Angular Distribution between Thick and Thin Films.....	136
Figure 7-12 Comparison of the Emission Angular Distribution of Thin and Thick Films .....	137
Figure 7-13 Angular Distribution of Emitted light with Laser fired at Various Angles .....	138
Figure 8-1 Absorption Spectrum Of $Y_2O_3:Eu$ .....	152

## List of Tables

Table 2-1 Temperature Characteristics of Previously Analysed Phosphors from Literature Survey ...	24
Table 3-1 Optical Rod Assessment Results.....	38
Table 3-2 Summary of Calibration Measurements of Spectrometer .....	42
Table 4-1 Calculated Parameters for the observed emission of $Y_2O_3:Eu$ 3.4 a/o.....	71
Table 5-1 Comparison Table of Calculated Decay Constants For YAGaG:Tb 5a/o.....	98
Table 5-2 Comparison Between The Single and Double Exponential Temperature Dependent Characteristics of YAGaG:Tb.....	98
Table 6-1 Calibration Data of the Photomultiplier Tube 9954B.....	108
Table 6-2 Comparison of Single Exponential Calibration Details .....	112
Table 7-1 Thickness Colour Chart for $Y_2O_3:Eu$ Thin Film Grown onto Silicon Substrate.....	123
Table 7-2 Roughness measurements of both thin and thick films of $Y_2O_3:Eu$ .....	141

## List of Abbreviations

Å	Angstroms ( $10^{-10}$ metres)
Al	Aluminium
a/o	Atomic percent
Ar	Argon
au	Arbitrary units
BeAl <sub>2</sub> O <sub>4</sub>	Beryllium Aluminium Oxide (Alexandrite)
c	Speed of light
C	Concentration
C <sub>2</sub>	Site of symmetry of Y <sub>2</sub> O <sub>3</sub>
C <sub>3i</sub>	Site of symmetry of Y <sub>2</sub> O <sub>3</sub>
CF	Central frequency
Cr	Chromium
CRT	Cathode Ray Tube
CW	Continuous wave
°C	Degree Celsius
DC	Direct current
DSO	Digital storage oscilloscope
DVM	Digital voltmeter
Dy	Dysprosium
EPSRC	Engineering and Physical Sciences Research Council
Eu	Europium
Eu <sub>2</sub> O <sub>3</sub>	Europium Oxide
eV	Electron volt
Ga	Gallium
Gd	Gadolinium
Gd <sub>2</sub> O <sub>3</sub>	Gadolinium Oxide
GEC	General Electric Company
<i>h</i>	Planck's Constant
HBW	Half-band width
HeCd	Helium Cadmium
H <sub>2</sub> S	Hydrogen Sulphide
InBO <sub>3</sub>	Indium Boroxide
<i>k</i>	Boltzmann's Constant
K	Kelvin
La <sub>2</sub> O <sub>2</sub> S	Lanthanum Oxysulphide
LaOBr	Lanthanum Oxybromide
LaPO <sub>4</sub>	Lanthanum Phosphate
LED	Light emitting diode

LET FEL	Lateral Emitting Thin Film Electroluminescent
LuPO <sub>4</sub>	Lutetium Phosphate
Mg <sub>4</sub> FGeO <sub>6</sub>	Magnesium Fluorogermanate
Mn	Manganese
mol%	Concentration as mole percent
N <sub>2</sub>	Nitrogen
Nd	Neodymium
O <sub>2</sub>	Oxygen
PL	Photoluminescent
PMT	Photomultiplier tube
Pr	Praseodymium
PT	Phosphor Thermography
$p_{\lambda}$	Reflectance of integrating sphere wall at wavelength, $\lambda$
Q.E.	Quantum efficiency
R.A.	Roughness Average
RF	Radio frequency
Rmax	Maximum peak-to-valley height as a measure of roughness
rpm	Revolutions per minute
S	Phonon frequency factor
Sc <sub>2</sub> O <sub>3</sub>	Scandium Oxide
ScPO <sub>4</sub>	Scandium Phosphate
T%	Throughput of an integrating sphere
Tb	Terbium
Ti	Titanium
UV	Ultra-violet
$\nu$	Wavelength
VI	Virtual Instrument
Vs	Versus
$W_{\lambda}$	Spectral radiant emittance at a specific wavelength
Y	Yttrium
Y <sub>3</sub> Al <sub>5</sub> O <sub>12</sub> (YAG)	Yttrium Aluminium Garnet
Y <sub>3</sub> (Al/Ga) <sub>5</sub> O <sub>12</sub> (YAGaG)	Yttrium Aluminium/Gallium Oxide
Y <sub>2</sub> O <sub>3</sub>	Yttrium Oxide
Y <sub>2</sub> O <sub>2</sub> S	Yttrium Oxysulphide
YPO <sub>4</sub>	Yttrium Phosphate
Y <sub>2</sub> SiO <sub>5</sub>	Yttrium Silicate
YVO <sub>4</sub>	Yttrium Vanadate
ZnS	Zinc Sulphide



## List of Variables

$d$	Thickness of deposited film
$\Delta E$	Thermal activation energy
$f_e$	Fraction of integrating sphere wall which is detected
$f_i$	Fraction of integrating sphere wall where no reflectance occurs
$F_{pl}$	Focal length of projecting lens
$F_{cm}$	Focal length of collimating mirror
$H_{pl}$	Height of projecting lens
$H_{cm}$	Height of collimating mirror
$I(t)$	Intensity at a given time
$I_o$	Initial intensity
$I_{tot}$	Total intensity
$I_a$	Intensity due to Site A of YAGaG:Tb
$I_b$	Intensity due to Site B of YAGaG:Tb
$I_{a1}$	Intensity due to 544nm transition of Site A of YAGaG:Tb
$I_{a2}$	Intensity due to two stage relaxation process of Site A of YAGaG:Tb
$I_{b1}$	Intensity due to 544nm transition of Site B of YAGaG:Tb
$I_{b2}$	Intensity due to two stage relaxation process of Site B of YAGaG:Tb
$m$	Number on intensity cycles during deposition
$n$	Refractive index of deposited film
$n_d$	Number of decaying electrons
$n_{c3i}$	Number of electrons at site $C_{3i}$ of $Y_2O_3:Eu$
$n_{c2}$	Number of electrons at site $C_2$ of $Y_2O_3:Eu$
$n_{tot}$	Total number of excited electrons
$n_a$	Number of excited electrons at State A of YAGaG:Tb
$n_b$	Number of excited electrons at State B of YAGaG:Tb
$N$	Noise level
$N_o$	Initial excited population
$N(t)$	Excited population at a given time
$P$	Probability of a transition
$Q$	Quenching rate
$t$	Time
$t_o$	Oscilloscope triggered delay
$T$	Temperature
$T_q$	Quenching temperature
$W_r$	Probability of a radiative transition
$W_{nr}$	Probability of a non-radiative transition
$\alpha$	Solid angle of the collimating mirror

$\tau$	Radiative decay
$\tau_d$	Decay Constant - phosphor and temperature variant
$\tau_r$	Rise Constant - phosphor and temperature variant
$\tau_o^r$	Initial Rise Constant
$\tau_a^d$	Decay Constant of Site A of YAGaG:Tb
$\tau_b^d$	Decay Constant of Site B of YAGaG:Tb
$\tau_a^r$	Rise Constant of Site A of YAGaG:Tb
$\tau_b^r$	Rise Constant of Site B of YAGaG:Tb
$\lambda$	Wavelength
$\lambda_{ex}$	Excitation wavelength
$\lambda_{em}$	Emission wavelength

# 1. Introduction To Phosphor Thermography

## 1.1 Background

Phosphor Thermography is a remote sensing technique being developed for the measurement of the temperature of rotating components within hostile environments<sup>[1,2,3]</sup>. Several technologies, such as turbine engines, combustion engines, motors and generators, are currently in great need of an accurate temperature sensing technique to facilitate modelling analysis and diagnostic instrumentation<sup>[4,5]</sup>. Of specific importance is the measurement of temperature within turbine engines<sup>[6,7]</sup> and particularly for the sensing of turbine blades. For example, recent tests carried out at Rolls-Royce Plc, have shown temperatures to reach in excess of 1200°C. These high temperatures cause strain and stress on components leading to structural damage and a reduction in engine efficiency. From a safety point of view, the failure of the turbine blades would lead to loss of power and eventual shutdown of the engine, with the potential of a mid-flight catastrophe. The cost of investigation into the cause is very expensive and time consuming, and results in the aircraft being taken out-of-service. However, present techniques for temperature measurement may have errors as high as  $\pm 50^\circ\text{C}$ . Reduction of this error is vital if engines are to operate with higher thrusts. Use of a temperature sensing technique as a diagnostic tool, increases the knowledge of the components capabilities with temperature; leading to better design, better efficiency, longer lifetime and greater engine thrust.

Measurement of temperature within turbine engines is problematic due to a number of factors. Firstly, there is the hostile environment that exists which causes erosion of the sensors currently utilised. Secondly, any sensor must have little if any effect on the aerodynamics of the system which are vital to the engine's efficiency. Finally, many components that require measurement of temperature within such a system are moving or

rotating, which causes difficulties in the transfer of information from the sensor to the analysing equipment.

In the world of sensing, many methods exist for individual applications, each having its own advantage. Discussed below are the current methods utilised within the turbine engine industry and the problems they encounter.

## **1.2 Current Techniques**

At present, there are three techniques utilised for temperature sensing within turbine engines; thermocouples, pyrometry and thermal paints<sup>[8]</sup>.

(i) Thermocouples are widely used as a temperature sensor, but have several weaknesses when utilised in engine environments. For a thermocouple to be used, the junction has to be in contact with the area which is being measured. Immediately, technical problems exist when moving/rotating components are involved. Conventional surface-mounted thermocouples would require the re-design of the components to allow for the detrimental effects on the aerodynamic flow due to the thermocouples presence. Development into embedding the junction within the component has taken place but problems still exist. Both the hostile environments and the large centrifugal/centripetal forces that exist within such a system cause erosion of the thermocouple's junction resulting in the loss of measurement. Also, the transfer of information from the sensor to the analysing equipment is problematic. Two methods currently utilised are slip rings and telemetry. The use of a slip-ring has shown that the high temperatures reached and the fast rotational speeds cause very rapid wear of the slip rings, resulting in this method having a very poor lifetime. Telemetry requires a transmitter to be associated with each thermocouple and a corresponding receiver external to the engine's environment, to translate the information to the data analysing equipment. This method is expensive and the transmitters have poor lifetimes again due to

the hostile environments. Also, electromagnetic interference exists within the engine; inducing a low signal-to-noise ratio, leading to a reduction in accuracy.

(ii) Radiation pyrometry is a remote sensing technique and so by-passes many of the problems associated with thermocouples, like bonding to components and electromagnetic interference. It relies on the intensity level of blackbody radiation emitted by the blades when high temperatures are reached. However, due to the surface emissivity of the blade material varying with the operation of the engine, knowledge of the blade's emissivity properties is required prior to installation to allow for the calibration of the sensing equipment. Also, existing within such a hostile environment, many other components of various temperatures exist; each emitting its own level of blackbody radiation. Many pyrometers have the inability to focus, resulting in the collection of blackbody levels from several sources within their field of view; so producing low signal-to-noise ratios leading to problems in signal analysis. The dirty environment can also lead to a reduction of the intensity level and so mis-calculation of actual temperatures.

(iii) The third method is the use of thermal paints. Like phosphor thermography, it too utilises the thermal properties of phosphors. A thermal paint will undergo a colour change as a result of the temperature it has reached. Unfortunately, although a thermal paint can have a wide temperature sensing range of 510 - 1110°C, accuracy is lost due to there being only 7-10 colour changes occurring over the complete range. Therefore, the measurement is only accurate to approximately  $\pm 50^{\circ}\text{C}^{[8]}$ . Also, the paints will only indicate the maximum temperature achieved during the test run, therefore requiring a multitude of test runs for the full analysis of a single system. The results are only obtained by visual inspection and comparison with calibrated colour charts after the test runs are complete. Therefore, the use of thermal paints is not a time resolved solution, and the high cost of disassembly of the

engine makes this a very expensive method. The main advantage is the ability to provide a temperature profile over the complete component's surface, and so remains a widely used method.

To overcome these problems, a new temperature sensing technique is required with :-

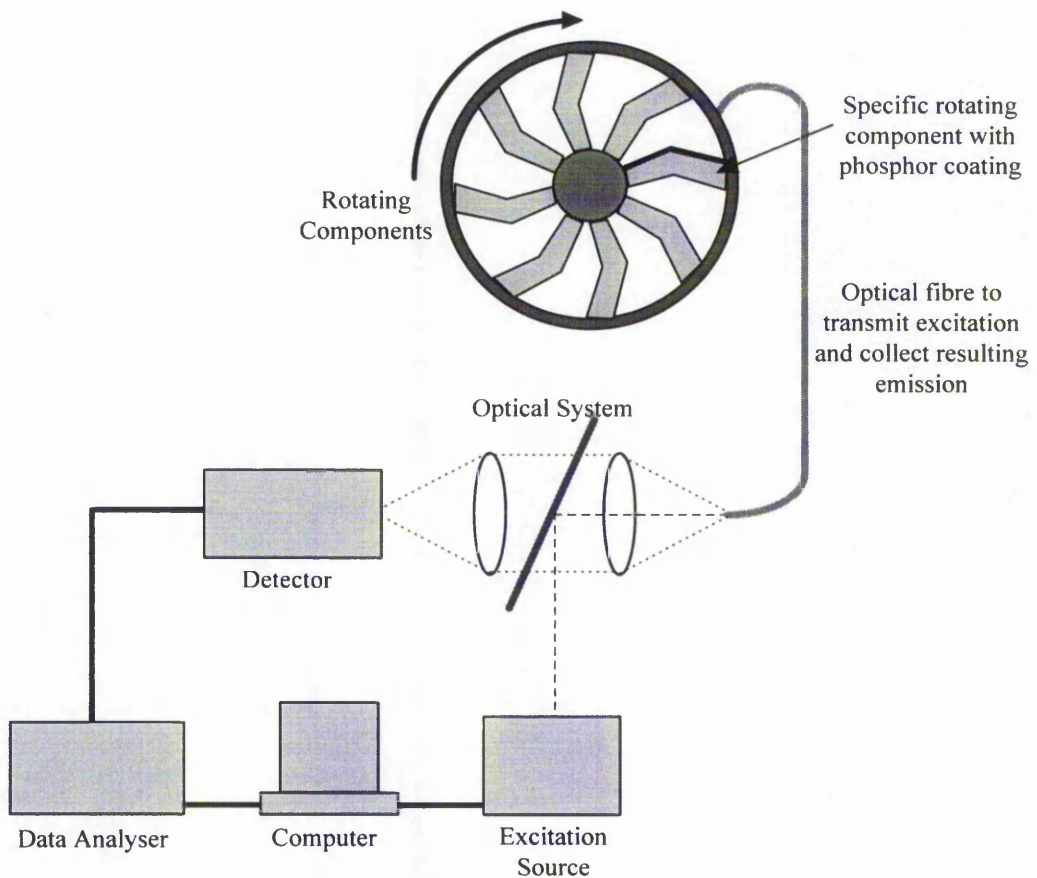
- a) The ability to sense temperature without physical contact to the component
- b) A high temperature sensing range of from at least 600°C to in excess of 1100°C
- c) A higher degree of accuracy  $\sim \pm 5^\circ\text{C}$
- d) Time resolved capability
- e) Properties are non-detrimental to the aerodynamics and efficiency of the engine
- f) The ability to withstand the corrosive environment, therefore extending the lifetime of the sensor
- g) Immunity to electromagnetic interference
- h) Focusability to facilitate the sensing of specific components

The proposed solution investigated here is phosphor thermography, a remote sensing laser-induced luminescence method that was first demonstrated by Cates<sup>[9]</sup> in the early 1980's. Utilised are the thermal properties of photoluminescence which are emitted by a phosphor when excited by an external source. Optical excitation and collection of the luminescence makes this a remote sensing method, without the associated problems mentioned above. The next section will describe the process in some detail.

### 1.3 Phosphor Thermography

#### 1.3.1 Introduction

Phosphor Thermography (PT) is a remote sensing method for the measurement of the temperature of rotating components within hostile environments<sup>[1,2,3]</sup>. The temperature dependent properties of laser-induced photoluminescence of phosphors are utilised for this sensing method. When a phosphor is excited by an pulsed ultra-violet laser, the intensity of the resultant photoluminescence with respect to time will decay usually in a single exponential manner. It is the rate of decay that is temperature dependent. Simple application of a phosphor coating to the components-under-test, allows the temperature of the component to be continuously monitored. A schematic diagram of such a system is shown below in Figure 1-1.



**Figure 1-1 A Simple Thermographic System**

First, the optical system couples the excitation source into the optical fibre, which transmits and focuses the source onto the component-under-test. This component has been coated with a pre-calibrated phosphor coating, which will emit luminescence of a specific wavelength due to its properties. The resultant emission is collected by the same optical fibre and focused onto the detector by a series of lenses. The detector converts the captured light into a voltage signal which in-turn is captured by the data analyser. The computer then allows for comparison with the pre-calibrated data and results in the determination of the temperature of the component.

### **1.3.2 Comparison With Previous Techniques**

In comparison with currently used methods, phosphor thermography has several advantages. Firstly, the information from the component is an optical signal, which will be unaffected by the electromagnetic interference, compared with the transmission of an electrical signal provided by thermocouples. Also the phosphor coating thickness, whether a thick paint or a thin film, is minimal in comparison with thermocouples and so is much less detrimental to the aerodynamics of the engine. The thickness of the coating also minimises the thermal gradient that exists between the surface of the component with that of the sensor, so is less prone to error. Because the collection optics are at a distance from the components, both static and rotating parts can be monitored.

Compared with pyrometry - also an optical based method - phosphor thermography does not have the problem of interference from other bodies. The excitation source is focused onto a specific component, and therefore only signals from that component are collected by the optics. Unlike pyrometry whose detection is limited to the intensity level of blackbody emission, phosphor thermography relies on the temperature dependent properties which are intensity independent, hence the technique has the capability of use within dirty environments; although, signal-to-noise ratio is still a limiting factor.



This technique has two strong advantages over thermal paints. Firstly, phosphor thermography is time resolved, allowing for real-time capture of data. As a result, full analysis of a turbine engine's environment, conditions and capabilities can be obtained during a single test run rather than the multitude required by thermal paints to achieve similar knowledge. This dramatically reduces the cost of system, as each test-run costs hundreds of thousands of pounds. Secondly, better accuracy is achieved with phosphor thermography;  $\pm 1^{\circ}\text{C}$ , compared with the  $\pm 50^{\circ}\text{C}$  of thermal paints.

### 1.3.3 Previous Work

Temperature dependence of phosphors was first noticed in the late 1930's after the introduction of the fluorescent lamp<sup>[1,10]</sup>. It was the loss of luminescence output from the lamp as temperature increased that was detrimental to its function, and so led to investigations into a more temperature stable phosphor. It was first suggested in 1937 by Neubert<sup>[11]</sup> that such properties could be utilised for the measurement of temperature. For example, Magnesium Fluorogermanate was developed as a lamp phosphor in 1950's<sup>[10]</sup>, but it was not until the work of Wickershiem et al in the late 70's and early 80's, cited by various references<sup>[1,3,12,13]</sup>, that the phosphor was used in early thermometry based measurement systems. This was followed by further investigations into the temperature dependence of phosphors leading to the first remote temperature sensing systems using thermographic phosphors in the 1980's developed by Cates<sup>[9,14]</sup>. The experiment involved measuring the temperature of the wall of a gas centrifuge. Since then, research into this field has expanded with experiments on the remote temperature measurement of magnets within an electric generators<sup>[15]</sup> and electric motors<sup>[16]</sup>; the surface temperature of an inductively heated rotating discs<sup>[17]</sup>; and the surface temperature of components within gas turbine engines<sup>[18]</sup>. The phosphor is attached to the surface under investigation with the use of a binder. The best binder in terms of adhesion properties, to-date, is a ceramic based refractory paint. In experiments carried out within the hot section of an engine by Noel et

al<sup>[18]</sup>, the temperature measured using phosphor thermography agreed with those determined by pyrometry. A problem exists though, with a significant amount of the phosphor coating being lost due to the high temperatures reached. Noel et al<sup>[18]</sup> fabricated thin film thermographic phosphors which are harder and smoother than phosphor/binder coatings and were found to be more durable. Unfortunately, the thin film layers had the disadvantage of a weaker emission intensity than the thick films. Also, the deposition equipment required for the application of the thin film is expensive, for example a sputtering or an electron beam deposition system.

#### **1.4 Summary Of The Thesis**

Research on phosphors for the development of a sensor has been carried out in collaboration with Rolls-Royce Commercial Aero Engines Plc, Derby, as an EPSRC CASE studentship. The aim is to use of phosphor thermography as a diagnostic tool, for the development of the turbine blades within commercial aero-engines. A necessary requirement is the need to identify a phosphor for optimum signal-to-noise ratio and of equal importance is the provision of strong bonding to the turbine blades. The programme for this thesis has been to investigate suitable phosphors and fully characterise these materials to identify an optimum phosphor. Also to produce a more robust, longer lasting film than currently used by any practitioners of phosphor thermography in aero-engine evaluation. Below is a summary of each chapter.

- **Chapter 2 Review of Thermographic Phosphors.**

This chapter describes the criteria required for the investigation of suitable phosphors, commencing with an explanation of the process involved in phosphor thermography, followed by a description of the fluorescent properties. The chapter concludes with a summary of previous investigations in the field of phosphor thermography, discussing the development of the sensor and the phosphors temperature dependent capabilities.

- **Chapter 3 Experimental Detail**

A full description of the instrumentation required to fully characterise the phosphors is given. Discussed are the problems and the limitation factors encountered along with the resolved solutions. Details of the LabVIEW software and data analysis process are given, allowing for an automated computer controlled photoluminescent system.

- **Chapter 4 Europium Doped Yttrium Oxide**

This is one of the most widely investigated phosphors due to its efficiency as a luminescent material. Here, will be detailed the variation of this phosphor with Europium doping along with its temperature dependent characterisation. Also included is the extension of previously unknown temperature sensing capabilities due to the discovery of a new novel temperature dependent characteristic, namely the “Rise-Constant” of the photoluminescent signal.

- **Chapter 5 Terbium Doped Yttrium Aluminium/Gallium Oxide**

Similar to Chapter 4, discussed here will be the photoluminescent properties of this phosphor. Full characterisation results will be given, along with the optimisation of the phosphor in terms of dopancy levels.

- **Chapter 6 Comparison of Phosphors**

The question to be answered is which of the two phosphor investigated is most suitable for use as a thermographic sensor within aero-engine designs. A comparison is made between the criteria of intensity emission levels, detectability at extreme temperatures, temperature dependent characteristics and lifetime measurements of thick films, produced by Rolls-Royce, will be discussed.

- **Chapter 7 Thin Film Phosphor Thermography**

Chapter 6 concludes that the lifetime measurements of thick films is problematic. Investigated was the production of the optimised phosphor grown as a thin film by RF magnetron sputtering. Both the growth of such films and the post-growth processes required are detailed and improvement in intensity levels are given. Finally, there are details of the lifetime tests carried out, providing a way forward for thin film phosphor thermography.

- **Chapter 8 Conclusion**

A summary of the work and achievements obtained during the programme, with discussion of the temperature sensing method's future in industry.

## 2. Review of Thermographic Phosphors

### 2.1 Definition Of A Phosphor

A phosphor<sup>[12,13]</sup> is a material which exhibits luminescent properties and usually takes the form of a ceramic host, such as an oxide or a garnet, with the dopant being a rare-earth ion. Luminescence is the term used to describe the emission of visible electromagnetic radiation from a material after the absorption of energy. There are many methods of excitation utilised for various applications like electroluminescence for display technology<sup>[19]</sup> and cathodoluminescence for televisions<sup>[20]</sup>. For phosphor thermography the excitation process is photoluminescence, utilising optical excitation. The remainder of the chapter will describe the properties exhibited by the phosphors, the processes taking place and how these materials are utilised for the measurement of temperature.

#### 2.1.1 A Brief History of Phosphors

A significant discovery was made in 1866 by Theodore Sidot<sup>[21]</sup> during an experiment into the growth of crystal structure. The investigation involved the growth of ZnS which exhibited light emitting properties in the dark, which later became known as phosphorescence. During the late 19th century, research into luminescent properties of phosphors made extensive progress due to the work of Philip EA Lenard and co-workers in Germany. They originated the principle that a phosphor consisted of a host material with luminescent centres, produced by firing metallic based impurities into the compound. These phosphors are alkaline earth chalcogenides and are now referred to as the Lenard phosphors<sup>[22]</sup>. The introduction of the fluorescent lamp in 1938 by GEC, Great Britain<sup>[23]</sup>, led to the increase in demand for better lighting for industrial applications. Together with the development of the Cathode Ray Tube (CRT), research into the properties and mechanisms of the luminescence of phosphors began to increase.

Humbolt Leverenz at Radio Corporation of America carried out detailed work on the ZnS type phosphors for the development of suitably characterised phosphors for the CRT. His work is published in a book entitled “An Introduction to Luminescence of Solids”<sup>[24]</sup> and is still valued today. After the Second World War, solid-state luminescence evolved into one of the most widely researched areas. This led to a much greater understanding of the mechanisms and properties of lattices and their impurities; especially due to the concept of the configurational co-ordinate model of luminescent centres which was introduced pre-war by P W Pohl and co-workers in Germany during their study of Ti<sup>+</sup> activated alkali halide phosphor<sup>[12]</sup>. Since then, advances in optical spectroscopy have clarified the energy levels and transitions based on crystal field theory.

Phosphors can be classified by a variety of ways, but the most widely used method is by the application within which they are utilised and is as follows: (1) light sources for lighting and fluorescent tubes, (2) display devices such as CRTs and electroluminescent displays, (3) detector systems like X-Ray screening, and (4) other applications, such as luminescent paint and phosphor thermography.

### **2.1.2 Luminescent Properties**

For photoluminescence<sup>[12,13,20,25]</sup>, when a phosphor is excited using a UV light source, the phosphor emits a spectrum of emissive light. The emission of light from a luminescent material is described as a combination of fluorescence - light emitted during the excitation period, and phosphorescence - light that is emitted after excitation has ceased. It is the temperature dependent properties of the phosphorescent emission that are utilised within phosphor thermography. Within an emission spectrum there are various spectral lines with varying intensities due to the multitude of atomic energy levels which exist. Furthermore, the intensity of each individual spectral line may vary according to the wavelength of the excitation. This may be characterised in terms of an excitation spectrum, where the

intensity level of the major peak is monitored while the excitation wavelength is varied, resulting in the excitation spectrum for that specific emitted wavelength of that particular phosphor.

Figure 2-1 shows the excitation and emission spectra of  $\text{Y}_2\text{O}_3:\text{Eu}^{[26]}$ ; one of the phosphors under investigation. The major spectral peak occurs at 611nm (in the red region of visible light). Furthermore, the excitation spectrum provides knowledge of the energy levels to which excitation can occur. This can be excitation into the host lattice or energy transfer directly into the europium ion. It also indicates the optimum excitation wavelength for the maximum intensity of the 611nm spectral line.

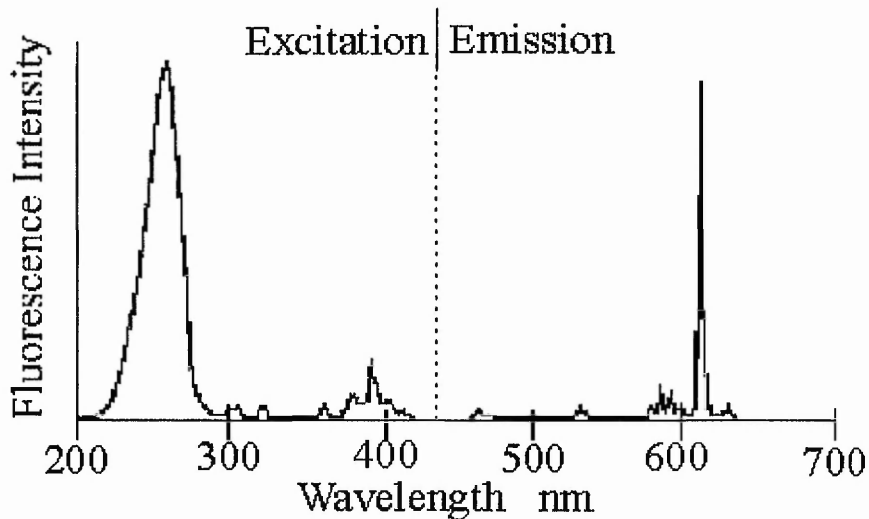


Figure 2-1 Emission and Excitation Spectra of  $\text{Y}_2\text{O}_3:\text{Eu}$

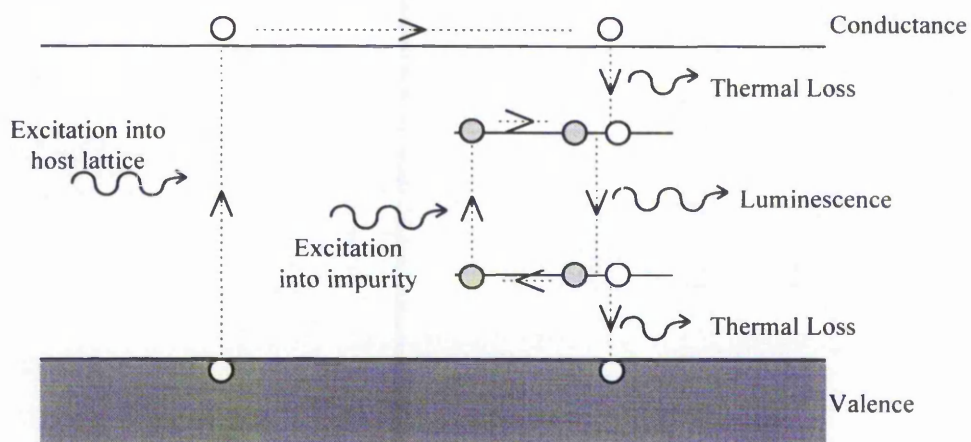
### 2.1.3 The Mechanism of Luminescence

Luminescence can be described as a two stage process, the excitation of electrons into higher energy levels and the relaxation of those electrons back to the stable energy states from which they originate. For excitation into the higher energy levels, electrons must

absorb the required energy to make the energy transition. For photoluminescence, this is achieved due to the absorption of light, thus producing the excitation spectrum as previously described. The electrons are now sited at an unstable energy level, and will release energy through radiative or non-radiative paths back to the zero-energy states. Consequently, energy is released thermally (non-radiative path) or by the emission of a photon (a radiative path). Therefore, photons of various wavelengths are emitted and thus produce the emission spectrum of the material.

### 2.1.3.1 Luminescent Centres

The introduction of an impurity (also referred to as the dopant ion or activator) within an host crystal structure provides the energy levels for the production of luminescence. Typically, the energy transition between the valence and the conduction band of the host lattice of an oxide material is of several electron volts (eV). When an impurity exists within the host lattice, the discrete energy levels of the impurity may be situated within the forbidden energy gap of the host. Figure 2-2 shows a simple energy level diagram of a host crystal and a luminescent centre. As shown, absorption of energy leads to a possible excitation / re-combination process of an electron resulting in the emission of light.



**Figure 2-2 Energy Level schematic showing electron transitions**



### ***2.1.3.2 The Excitation and Relaxation Process***

For photoluminescence, a phosphor can be excited by the radiation of light lying in the ultra-violet and visible regions of the spectrum. As explained previously in this chapter, the wavelength of the absorbed light can be given in terms of electron volts and therefore related to the energy levels. For the radiated wavelength to be absorbed, it must have sufficient energy to excite the electrons from the ground state to an upper level. Shown in Figure 2.2 are the possible routes an electron may or may not take when excited with sufficient energy provided by the radiated wavelength. If the energy is sufficient enough, an electron may be excited across the band-gap of the host lattice. This electron will then relax back to a lower stable energy level. The route undertaken will consist of a series of energy transitions, where the loss of energy by the excited electron is either thermally released or emitted as luminescence.

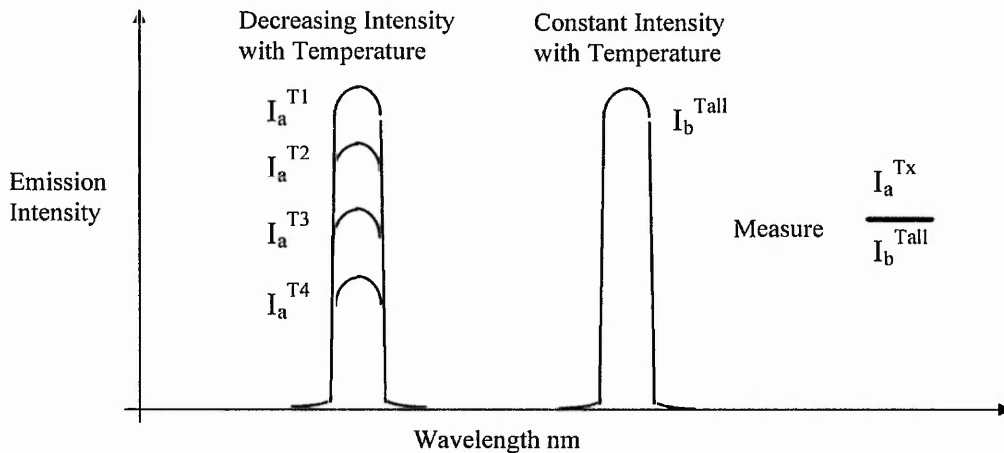
If the energy provided is lower than that required to excite into the conduction band, excitation can occur directly within the luminescent centre. Again, the excited electron will undergo a relaxation transition which is likely to result in the emission of luminescence. Within a luminescent centre, the existence of many energy states produces a multitude of both radiative and non-radiative transitions to the lower ground state. Each transition has a probability of occurrence, and so produces a variety of intensities for the radiative transitions. This is represented by the spectral lines of the phosphor's emission spectra. As a result, the excitation spectra consists of both broad and sharp absorption lines as shown in Figure 2-1, a combination of the absorption by the host lattice, yttrium oxide, and by the luminescent centre, europium.

### **2.1.4 Temperature Dependent Properties**

For a phosphor to be utilised in the field of temperature sensing, it must exhibit some form of temperature dependency. Two forms of temperature dependency are exhibited. The first

is the variation of spectral line peak intensity with temperature, and the second is the decay time or lifetime temperature dependence of the luminescent centre.

As previously stated, when excited all phosphors emit a spectrum of various wavelengths and intensities. Some phosphors will emit two wavelengths of strong intensity whose emission intensity levels vary independently with temperature. Ideally, the intensity of one peak is independent of temperature which then is chosen as a reference, and compared with the second peak whose level varies with temperature. The temperature of the phosphor can be determined by monitoring the ratio of the two peaks. Figure 2-3 shows the principle of this method.



**Figure 2-3. Diagram Showing The Principle of Two-Peak Intensity Method**

Within an aero-engine, the dirty environment that exists leads to surface fouling which reduces the intensity levels collected by the detector. Assuming the loss of intensity due to surface fouling is equivalent at each wavelength, the above figure shows that by utilising the ratio between the two peaks, the ratio's value will not reduce and so measurement of temperature is still feasible. As shown, most phosphors have spectral lines whose intensity decreases with temperature. This leads to a weakening signal-to-noise ratio at high temperatures which increases the error of the measurement. Conversely, work by Goss et

al<sup>[27]</sup> and Chyu<sup>[28]</sup> have illustrated the potential of this method using the phosphor Dysprosium doped Yttrium Aluminium Oxide, YAG:Dy, whose spectral line intensity increases with temperature.

The second, and potentially preferred method, is the use of the decay time of phosphorescence which is light emitted after excitation has ceased. After excitation, the number of electrons,  $N$ , that have been excited to a discrete energy level will return to a lower state. The rate of change of the decreasing excited population is dependent upon the probability of the transition<sup>[29]</sup>,  $P$ , to the lower state and is defined as :-

$$\frac{dN}{dt} = -PN \quad \text{Equation[1]}$$

Integrating the above equation and defining  $N_0$  as the initial population, the population  $N$  at any given time,  $t$ , is :-

$$N(t) = N_0 \exp(-Pt) \quad \text{Equation[2]}$$

With an exponential decrease in the number of electrons, the probability of de-excitation can be re-written as the decay constant,  $\tau_d$ , where :-

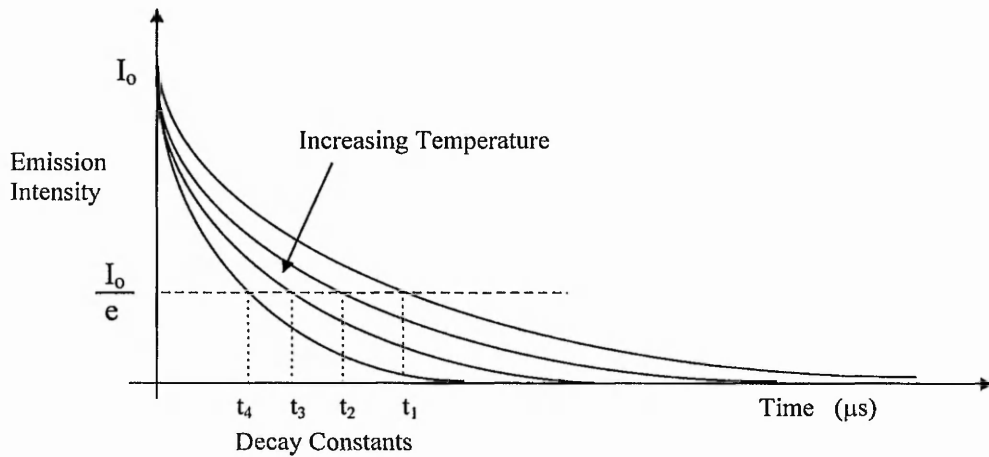
$$\tau_d = P^{-1} \quad \text{Equation[3]}$$

For a radiative transition, the energy released by the relaxing electron is emitted as a photon. As intensity,  $I(t)$ , is proportional to the number of generated photons,  $N(t)$ , Equation 2 can be re-written in terms of fluorescent intensity levels as :-

$$I(t) = I_0 \exp\left(\frac{-t}{\tau_d}\right) \quad \text{Equation[4]}$$

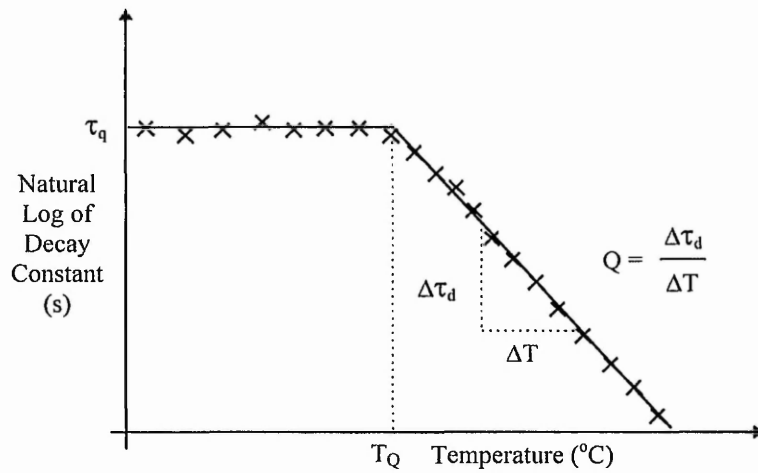
where  $I_0$  is the initial intensity level.

Figure 2-4 shows how the photoluminescent signal decays and illustrates the decay constant,  $\tau_d$ , is a function of temperature. This is a characteristic of each individual phosphor.



**Figure 2-4 Illustration of the Decay Constant Principle**

However, the temperature dependence of the decay constant only occurs above a specific temperature known as the quenching temperature,  $T_Q$ . As an example, Figure 2-5 shows the natural log of the decay constant plotted against temperature for a typical phosphor. Beyond  $T_Q$ , the decay constant decreases exponentially with temperature. The rate at which the decay constant varies with temperature is called the quenching rate,  $Q$ , and is a measure of the temperature sensitivity of the phosphor. Hence, the characteristic defines the range and accuracy of the phosphor as a temperature sensor.



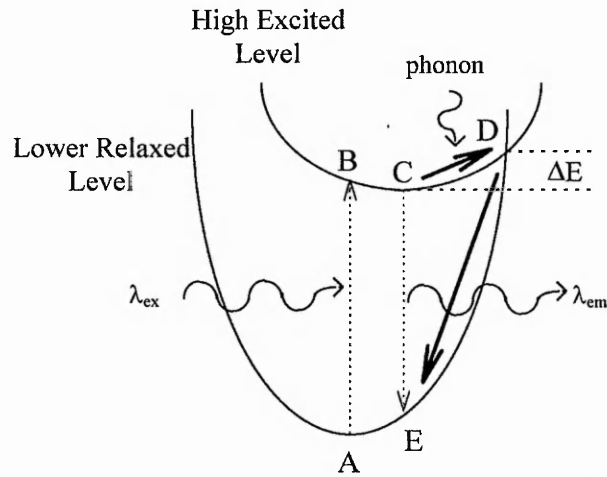
**Figure 2-5 Temperature Dependence Characteristic of the Decay Constant**

Within the exponentially decreasing region, the relationship between the decay constant and the temperature,  $T$ , of the phosphor can usually be represented by<sup>[30]</sup>:-

$$\tau_d = \tau_q \exp [-Q(T - T_Q)] \quad \text{Equation[5]}$$

where  $\tau_q$  is the decay constant at the quenching point. From equation 5, it can be determined that  $Q$  has the units of inverse temperature.

The mechanism that leads to this characteristic is explained with reference to Figure 2-6, which shows a configurational co-ordinate diagram<sup>[31]</sup> of a two energy level system. Path A-to-B represents the absorption process of an inner shell transition from the lower energy level to the higher level. This is the absorption of the exciting wavelength,  $\lambda_{ex}$ , for photoluminescence. The excited state relaxes to the lowest point, C, with the loss of energy being emitted as a phonon (thermal energy). At position C, the excited electron will either relax to the lower energy level at point E via emitting a photon,  $\lambda_{em}$ ; or will absorb thermal energy, a phonon, and be excited to point D. This leads to the electron relaxing to point A non-radiatively.



**Figure 2-6 Configurational Co-ordinate Diagram Of A Simple Two Energy Level System**

By denoting the probability of a radiative transition as  $W_r$  and a non-radiative transition as  $W_{nr}$ , the probability  $P$  from Equation 2 can be re-defined as the sum of the two possible transitions<sup>[32]</sup> :-

$$P = W_r + W_{nr} \quad \text{Equation[6]}$$

and Equation 3 is re-written as :

$$\tau_d = (W_r + W_{nr})^{-1} \quad \text{Equation[7]}$$

The radiative probability,  $W_r$ , is fixed for a specific transition between two energy levels and is independent of temperature. It is the non-radiative transition probability,  $W_{nr}$ , which is temperature dependent and is governed by thermal relaxation processes. For thermal relaxation to occur, the electron must first be thermally excited to the cross-over point of the two energy levels (point D in Figure 2-6). The energy required,  $\Delta E$ , is known as the

thermal activation energy. The probability,  $W_{nr}$ , of the electron making the transition C-to-D via thermal activation is defined as <sup>[32]</sup>:

$$W_{nr} = S \exp\left(\frac{-\Delta E}{kT}\right) \quad \text{Equation(8)}$$

where  $k$  is Boltzmann constant,  $T$  is the temperature and  $S$  is the phonon frequency factor. As shown, the non-radiative transition is strongly temperature dependent. This leads to thermal quenching, where the emission efficiency decreases and the decay constant of the luminescent centre shortens at high temperatures (see equation 7).

Of the two methods of monitoring temperature change, the decay time technique is preferable for use within turbine engines for a number of reasons. Firstly, there is a wide choice of phosphors available which show decay time variance with temperature. Compared with the two peak method, only a limited number of phosphors showing two peak temperature dependence exist, and hence limits the thermographic sensor capabilities. Secondly, the two peak intensity method requires the use of two detectors, one for each wavelength, compared with the decay time which requires only one. This reduces both the size and cost of the final instrumentation. Thirdly, and most important, is the sensitivity to temperature. Decay time has shown an accuracy of  $\pm 0.3^\circ\text{C}$ <sup>[16]</sup> compared with two-peak method quoted with an accuracy of  $\pm 9\text{-}50^\circ\text{C}$ <sup>[27]</sup>, but varies depending on the temperature range under investigation, especially where levels of blackbody radiation are high.

## **2.2 Phosphor Preparation**

The preparation of the phosphor material plays an important role for fluorescent properties<sup>[33,34]</sup>. The starting materials are mixed in crucibles and fired under controlled atmospheric conditions. It is the parameters within the controlled atmosphere which dictate the properties of the final material, like the particle size of the material, the stoichiometry of the host lattice, and the valence of the dopant (e.g. Europium,  $\text{Eu}^{2+}$  or  $\text{Eu}^{3+}$ )

Where the activator and host material are chemically compatible, as is the case with rare-earth activated phosphors, the method of coprecipitation is often used. For example,  $Y_2O_3:Eu^{3+}$  is produced by coprecipitating the oxalates from solution and firing the precipitate. The firing of the phosphor is of great importance for the fluorescent efficiency of the phosphor material. Once the material has been precipitated, the dopant may or may not be positioned correctly within the host lattice. It is the firing of the material which leads to the re-positioning of the dopant, making the phosphor much more efficient. This is shown later, in the annealing process of thin films to enhance the fluorescent emission intensity.

### **2.3 Phosphors Under Investigation**

In the field of phosphor thermography, a wide range of phosphors have been investigated for the suitable temperature dependent characteristics due to the numerous applications requiring such a temperature sensing technique, see section 1.3.3 . A literature survey was carried out in the initial phase of this study to summarise the characteristics of previously investigated phosphors. Table 2-1 gives details of the phosphors, their emitted wavelengths, the excitation source used and their temperature sensing capabilities.

One of the major contributions to the field of phosphor thermography<sup>[35-42,44,47]</sup>, has been the work carried out by the researchers Allison and Cates of Oak Ridge National Laboratory, USA; and Noel and Borella of Los Alamos Research Laboratory, USA. Collaborating bodies have included EG & G Energy Measurement Group (Turley and Lewis), Pratt & Whitney Aero-engine Manufacturers, University of Virginia (Dowell) and University of Tennessee (Bugos). In all cases, the decay time method was utilised with excitation at 337nm (Nitrogen laser) or 355nm (third harmonic of Nd:YAG laser). Both high and low temperature sensitive phosphors were investigated for many applications including walls of gas centrifuge<sup>[9]</sup>, combustion engines<sup>[41]</sup> and turbine blades<sup>[36,42]</sup> within both military and



commercial Pratt & Whitney engines. Many bonding methods for phosphors have been studied to test both adhesiveness within the hostile environments and for long-term survivability. As well as the use of epoxy resins for chemical bonding methods, the thin film techniques of electron beam deposition and RF sputtering have been investigated. Their results show good survivability for the films upto  $1000^{\circ}\text{C}$ <sup>[35,36,42]</sup>, but with weak emission compared to chemical bonding methods<sup>[35]</sup>.

Laboratory experimentation has shown temperature measurement capabilities of upto  $1400^{\circ}\text{C}$ <sup>[39]</sup> with  $\text{Y}_2\text{O}_3:\text{Eu}$ ,  $\text{YAG:Tb}$  and  $\text{YAG:Dy}$ . For tests on Pratt & Whitney engines, thermal barrier coatings are used to protect the turbine blades from the extreme temperatures. Also, a two fibre system was utilised, one to transmit the excitation wavelength and one to collect the fluorescence, in order to minimise laser interference with the collected signal. Minimisation of blackbody radiation observed by the detector was achieved using a mechanical shutter system<sup>[39]</sup> with promising results. Unfortunately, the speed of the shutters was slow, each with a maximum possible speed of 1ms.

Zhang, Grattan and Palmer<sup>[45,48,49]</sup> have utilised phosphor thermography for the production of fibre-optic sensors. Their method consists of coating the tip of a two fibre optic system with the phosphor, alexandrite<sup>[45,49]</sup> or  $\text{Nd:YAG}$ <sup>[48]</sup>. A quartz sheath surrounds the silica fibres producing a temperature probe, meeting requirements for temperature measurements within plasma deposition systems or microwave heating<sup>[48]</sup>.

Phosphor	Emitted Wavelength (nm)	Temperature Range (°C)	Decay Time (μs)	Excitation Wavelength (nm)	Reference
Y <sub>2</sub> O <sub>3</sub> : Eu	611	450 - 1180	1000 - 0.05	355 (Nd:YAG)	35
	611	600 - 1200	300 - 0.4	337 (N <sub>2</sub> )	36
	no data	500 - 1200	800 - 0.04	unknown	38
	611	540 - 1100	1000 - 0.15	337 (N <sub>2</sub> )	39
	611	650 - 1200	1000 - 0.02	337 (N <sub>2</sub> )	42
	514	70 - 170	45 - 1.5	337 (N <sub>2</sub> )	43
	612	550 - 900	800 - 2.0	337 (N <sub>2</sub> )	44
	611	500 - 1050	1000 - 0.1	266 (Nd:YAG)	46
	612	600 - 930	1200 - 20	337 (N <sub>2</sub> )	47
Y <sub>2</sub> O <sub>3</sub> : Dy	no data	425 - 540	250 - 5.5	355 (Nd:YAG)	35
Y <sub>2</sub> O <sub>3</sub> : Gd	blue	no data	no data	337 (N <sub>2</sub> )	36
Y <sub>2</sub> O <sub>2</sub> S : Eu	red	30 - 300	no data	337 (N <sub>2</sub> )	36
Y <sub>2</sub> O <sub>2</sub> S : Tb	544	260 - 540	450 - 2.0	337 (N <sub>2</sub> )	36
	545	200 - 550	700 - 1.0	337 (N <sub>2</sub> )	44
Y <sub>2</sub> O <sub>2</sub> S : Pr	white	no data	no data	337 (N <sub>2</sub> )	36
YAG : Dy	no data	1055 - 1470	11 - 6.5	355 (Nd:YAG)	35
	461	1150 - 1480	20 - 5.0	337 (N <sub>2</sub> )	39
YAG : Tb	543	925 - 1425	45 - 0.04	337 (N <sub>2</sub> )	39
Y <sub>2</sub> (Al/Ga) <sub>5</sub> O <sub>12</sub> :Tb	544	600 - 1100	2000 - 0.8	266 (Nd:YAG)	46
Nd : YAG	1064	700 - 900	257 - 235	810 (diode)	48
LuPO <sub>4</sub> : Dy	no data	975 - 1225	500 - 120	355 (Nd:YAG)	35
	no data	900 - 1175	500 - 40	unknown	38
LuPO <sub>4</sub> : Eu	no data	725 - 1100	2000 - 5.0	355 (Nd:YAG)	35
	no data	750 - 1100	2000 - 3.5	unknown	38
YPO <sub>4</sub> : Eu	no data	670 - 1100	2000 - 1.5	unknown	38
YVO <sub>4</sub> : Eu	no data	500 - 725	400 - 2.5	355 (Nd:YAG)	35
	617	350 - 500	290 - 4.0	337 (N <sub>2</sub> )	36
	618	450 - 750	400 - 2.0	337 (N <sub>2</sub> )	42
YVO <sub>4</sub> : Dy	no data	310 - 410	130 - 5.0	355 (Nd:YAG)	35
	574	280 - 370	140 - 20	337 (N <sub>2</sub> )	36
	575	300 - 400	129 - 5.8	337 (N <sub>2</sub> )	37
Mg <sub>4</sub> FGeO <sub>6</sub> :Mn	no data	70 - 700	4000 - 1.2	355 (Nd:YAG)	35
	664 + 637	435 - 730	3000 - 340	337 (N <sub>2</sub> )	36
La <sub>2</sub> O <sub>2</sub> S : Eu	no data	-23 - 155	120 - 1.0	355 (Nd:YAG)	35
	no data	140 - 240	130 - 4.5	355 (Nd:YAG)	35
	no data	240 - 330	250 - 4.8	355 (Nd:YAG)	35
	537	-200 - 200	120 - 20	337 (N <sub>2</sub> )	36
	537	95 - 290	250 - 0.8	337 (N <sub>2</sub> )	41
	514	0 - 100	25 - 0.8	337 (N <sub>2</sub> )	44
	537	100 - 210	200 - 10	337 (N <sub>2</sub> )	44
La <sub>2</sub> O <sub>2</sub> S : Tb	green	no data	no data	337 (N <sub>2</sub> )	36
LaPO <sub>4</sub> : Eu	no data	460 - 750	2000 - 2.5	unknown	38
Sc <sub>2</sub> O <sub>3</sub> : Eu	red	400 - 1200	no data	337 (N <sub>2</sub> )	36
ScPO <sub>4</sub> : Eu	597	650 - 1200	1336 - 1.0	395	36
BeAl <sub>2</sub> O <sub>4</sub> : Cr	690	0 - 400	2 - 100	669	45
		400 - 700	100 - 0.8	(diode laser)	
	no data	20 - 700	300 - 1.0	670 (diode)	49

Table 2-1 Temperature Characteristics of Previously Analysed Phosphors from Literature Survey

From the data shown in Table 2.1, the decision was made to investigate two phosphor systems, namely, Europium doped Yttrium Oxide ( $Y_2O_3:Eu$  - red emitter) and Terbium doped Yttrium Aluminium/Gallium Oxide ( $Y_2(Al/Ga)_5O_{12}:Tb$  - green emitter) A third phosphor, Gadolinium doped Yttrium Oxide ( $Y_2O_3:Gd$ - blue emitter) was also investigated but under excitation of the Nd:YAG laser showed very weak emission levels and so was omitted from further investigation. Each phosphor would be characterised as follows:-

- Dopancy Dependency - High levels of blackbody radiation leads to a reduction in signal-to-noise ratio at extreme temperatures. Past investigations have been carried out on phosphors of single dopant concentration. For this study, the intensity of the phosphorescence will be optimised by varying the concentration of the dopant. As well as the intensity of emission, the temperature dependent characteristics would also vary due to changes in dopancy levels.
- Excitation Wavelength - The laser system available through Rolls-Royce Plc, was a Nd:YAG laser (Spectron 130mW 14ns pulse) with output wavelengths of 355 and 266nm. Excitation wavelength can affect both the intensity levels and the temperature characteristics. Absorption spectra of both phosphors indicate 266nm would induce greater intensity emission. Unfortunately, tuning of the laser to the fourth harmonic (266nm) leads to a reduction in laser power, and so may not result in better efficiency.
- Temperature Dependence - All phosphors would have their temperature dependence characteristics investigated for both excitation wavelengths over the full temperature range of interest (25-<sup>+</sup>1100°C). Dopancy levels are known to affect the characteristics and so would be fully investigated.
- Coating Methods - Initial experimentation would be carried out on powder samples in the form of a pressed pellet. Two coating methods would be investigated. Firstly, production of a spray paint using epoxy resin as a chemical bonding method, and

secondly, growth of thin films of the optimum dopant concentration via RF Magnetron Sputtering. Past investigations have shown thin films to have a high survival rate, but with lower emission levels. Lifetime and intensity comparison would be made on samples. Further work into optimisation of thin films would be carried out to maximise intensity and minimise the thermal gradient. This would include full investigation into the thickness dependency and the post-growth process of annealing.

One of the major problems with all past experimentation is the collection of the emitted phosphorescence and the transmittance to the detector system. The optical system must maximise the signal received by the detector in order to fully investigate the temperature dependent capabilities of the phosphors. A full investigation into the optical system and arrangement of equipment was therefore required. This particularly includes the technique required to capture the signal from inside the furnace and also focusing of the captured signal onto the detector.

### 3. Experimental Detail

#### 3.1 Phosphor Specification

As discussed in Chapters 1 and 2, the temperature measurement of turbine blades can be achieved via phosphor thermography. The sensory component of this technique is the phosphor, the temperature dependent characteristics of which define the sensing capabilities of the complete system. To meet the requirements for turbine engine diagnostic equipment, the phosphor must have :-

- a) a single wavelength emission with strong intensity levels to overcome the background noise of blackbody radiation
- b) no wavelength shift due to high temperatures
- c) a temperature dependent decay constant
- d) the ability to be excited via use of Nd:YAG pulse laser 355 or 266nm
- e) a temperature sensing range from 600°C to over 1100°C
- f) a decay constant which varies within a specified time window due to rotational speed limitations
- g) long-term survivability at high temperatures within hostile environments

For the analysis of the phosphors capabilities, the first stage is the characterisation of their spectral emission. This is to determine which of their spectral lines is the strongest in terms of intensity and therefore can be utilised for the decay constant method. Varying the dopancy levels will vary the emission intensity and possibly cause spectral shifts due to changes in the crystal field. Once clarification of the major spectral line has been determined, intensity comparisons between all dopancy levels are made to achieve full

optimisation. Also, full decay constant characterisation of each phosphor is measured to determine its suitability for use in phosphor thermography.

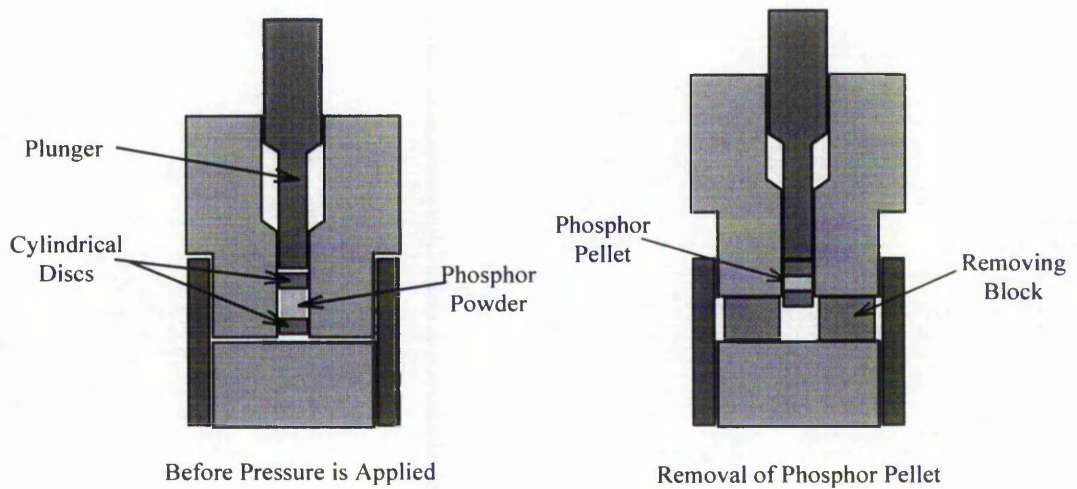
### **3.2 Phosphor Preparation**

The phosphors were supplied by two sources, Phosphor Technology Ltd and University of Greenwich. Several samples of each phosphor were purchased with various dopant concentrations. All samples are fully characterised in the form of a powder. Tests include emission spectra, intensity comparison and temperature dependence characterisation. A selection of optimum powders were sent to Rolls-Royce plc, to be processed into a thermographic paint and coated onto test coupons. Full details on the epoxy resin utilised and the process undertaken cannot be provided due to confidentiality. These coupons were tested for intensity comparison and temperature dependency, checking whether the epoxy resin binder had affected the properties of the phosphor. Lifetime tests were carried out on the coupons as a measure of their survivability within a hostile environment. Finally, an optimum phosphor was chosen for thin film growth by RF magnetron sputtering. Lifetime and intensity comparison with the thick film coupons were carried out to determine the optimum coating.

#### **3.2.1 Powder**

Before characterisation of the phosphor powders could begin, they had to be pressed to form a pellet which could be held within the furnace. Illustrated in Figure 3-1 is the die for the production of the pellets. A small quantity of the phosphor powder is placed between two cylindrical discs. These have been manufactured with precision clearance tolerance to allow for sliding movement within the die. Pressure of 3000lb/inch<sup>2</sup> is then applied using an oil hydraulic pump. Checks are made regularly to ensure the pressure remains at 3000lb/inch<sup>2</sup>. After a period of ten minutes, the pressure is released and a removing block is positioned between the two halves of the die. Low pressure is re-applied and the cylindrical

discs and resultant phosphor pellet are pushed through. The resultant pellets were 5mm in diameter and 2mm in thickness.



**Figure 3-1 Cross-Section Diagram of The Pellet Die**

### 3.2.2 Thick Film

To produce thick films of the phosphor, chemical bonding methods are utilised. This involves the use of an epoxy resin mixed with the phosphor and is a method currently used for the production of luminous thermal paints<sup>[1,8]</sup>. As well as investigating an epoxy's adhesion properties and so the lifetime of the film, consideration must be given to its effect on the properties of the phosphor. Firstly, they must be chemically compatible to ensure no change of the thermal characteristics of the phosphors. Secondly, the epoxy resin must reduce neither the coupling of UV to the phosphor nor the outcoupling of the emitted fluorescence. The thick film paint was coated onto test coupons. These were supplied by Rolls-Royce Plc and produced to simulate a turbine blade

Factors which can effect the properties of the paint are given below :

- Milling of the compounds. The milling of a powder reduces the particle size of the compound. Reduction in particle size produces a finer mixture of phosphor and epoxy resin. This increases the bonding ability of the mixture to the components.
- Epoxy resin ratio. The epoxy resin is a mixture of solvents the ratio of which effects the adhesion and lifetime of the resin.
- Epoxy resin to phosphor ratio. This will result is maximum emission intensity achievable, while maintaining the adhesion properties to withstand the harsh environment.
- Surface treatment. Once the paint has been applied to the components surface, heat treatment is undertaken to “bake” the test coupon so creating a strong bond of paint to metal.

### 3.2.3 Thin Film

A robust and longer lasting coating is required for phosphor thermography to be feasible within a turbine engine environment. Many methods have been investigated for a variety of applications including sputtering<sup>[50,51]</sup>, electron beam vapour deposition<sup>[36,51]</sup>, sol-gel processing<sup>[52,53]</sup> and laser ablation<sup>[54,55]</sup>, all producing a thin film with promising results. At NTU, the display research group currently utilise radio-frequency (RF) magnetron sputtering as the method for the production of thin films for LETFEL (laterally emitting thin film electroluminescent) devices<sup>[56,57,58]</sup>. Due to the availability of the equipment and the years of valuable experience of the group, this technique was utilised for the growth of thin films of thermographic phosphors.

Sputtering is a physical vapour deposition method where ions are accelerated by an electric field towards the target - the material to be deposited. The target acts as the cathode and the

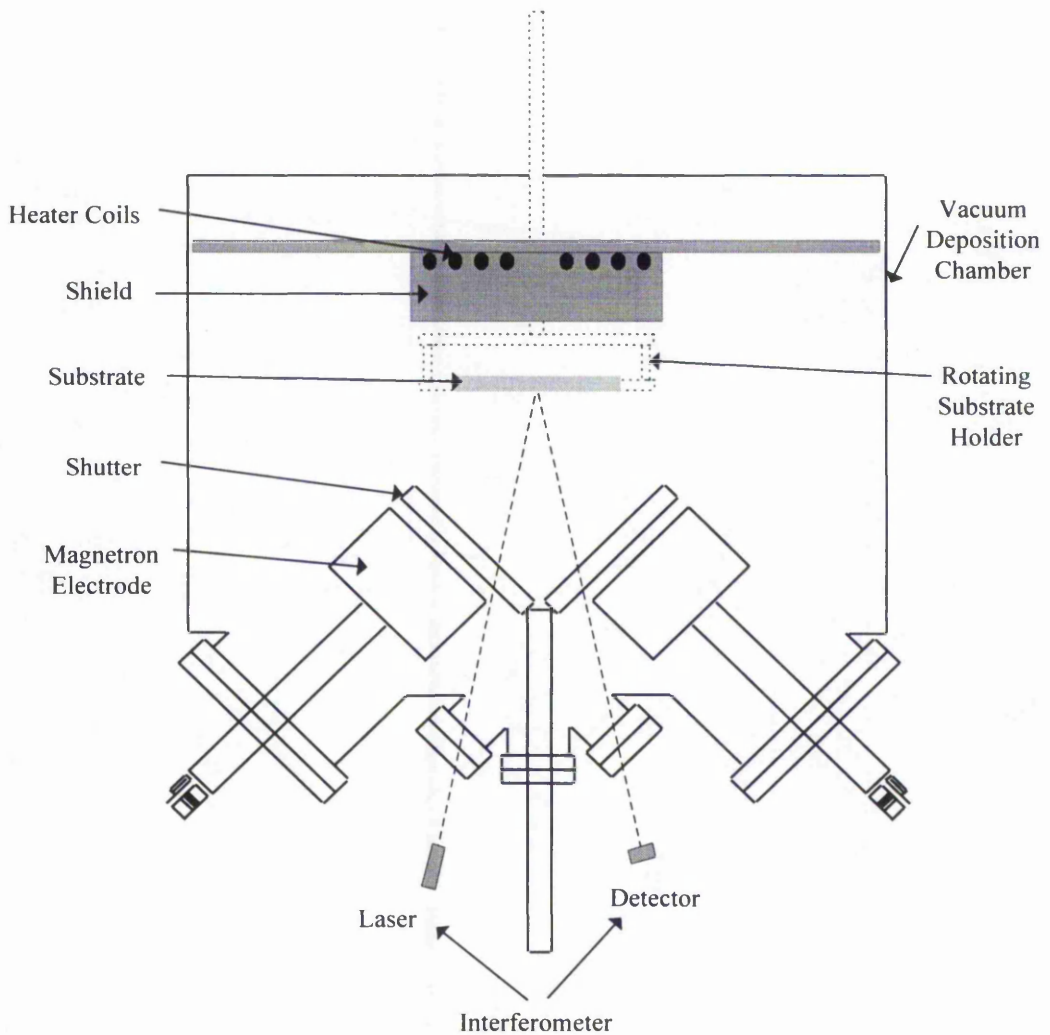


substrate can be grounded, biased or left floating. Initially, the system is vacuum pumped to a pressure of  $1 \times 10^{-7}$  bar. An inert gas of 3mTorr is then allowed into the chamber to act as the sputter gas. When RF power is applied, the resultant electron emission from the target excites the sputter gas creating a plasma, a self-sustaining glow discharge. Within the plasma, due to the electrons being more mobile than the positive ions, a greater number of electrons are attracted to the target during the positive half of the cycle compared with the positive ions during the negative half. Overall, during a complete cycle the target gains more negative charge and so is classified as the cathode which attracts the high energy positive ions. These ions provide sufficient incident energy to eject the atoms from the target. On impact with a surface, the kinetic energy of the ejected atoms is converted into heat, resulting in the fusion of the atom to the surface. The substrate requiring the deposition of a material is therefore positioned facing the target.

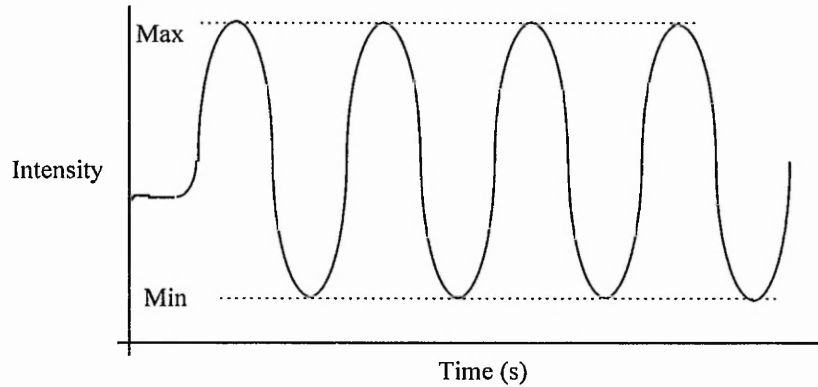
Damage to the thin film can occur due to the bombardment of the electrons from the plasma. The solution is to create a magnetic field which confines the plasma around the target and away from the substrate. This is achieved with a magnetron electrode, where a series of magnets are positioned behind the target. The use of magnets allows both magnetron or planar sputtering to occur within the system. As well as reducing the possibility of damage to the thin film, the confinement of the plasma increases its ionisation efficiency. This in turn, reduces the required pressure to maintain the plasma, thus increasing the mean path of ejected atoms to the substrate. Hence, the deposition rate of the target increases.

An illustration of the RF Magnetron Sputtering system used is shown in Figure 3-2. The substrate is positioned on a rotating holder situated in the centre of the system. This is powered by a small DC motor during deposition and leads to uniform growth of the thin film. Above the holder is a heater which is moved down prior to deposition. It provides temperature control of the substrate which affects the deposition rate. A shield is also

incorporated to prevent deposition occurring to the back of the substrate or onto the heating coils. The system contains three electrodes (two of which are shown in the illustration). This allows deposition of three targets without the requirement of opening up the chamber to atmospheric conditions. The shutters are installed to protect the electrodes when not in use.



**Figure 3-2 Illustration of the RF Magnetron Sputtering System**



**Figure 3-3 Interferometric Thin Film Thickness Monitor Graph**

Interferometry is the method used for monitoring the thickness of the thin film during deposition. A visible laser (625nm) continuous beam is fired at the substrate and is reflected from both the surface of the depositing thin film and that of the substrate. The phase shift of the reflected rays differ due to the distance travelled through the thin film. The combination of rays result in the intensity of the signal detected by the photodiode varying between a maximum and minimum as shown in Figure 3-3. By knowing the refractive index of the material, the thickness of the thin film can be determined.

$$\lambda = 2nmd \quad \text{Equation [9]}$$

where  $\lambda$  is the wavelength of the laser,  $n$  is the refractive index,  $m$  is the number of intensity cycles and  $d$  is the thickness. Unfortunately, the refractive index of a material can vary due to the temperature of the substrate. As a result, this method is used as a guide only during deposition and the thickness of the thin film is determined afterwards using a DEKTAK profilometer.

### **3.3 Temperature Control**

All experimentation requires the phosphor sample to be positioned within a temperature controlled environment. This was achieved through use of a Carbolite furnace (model no.

CWF 12/5) capable of reaching 1200°C. Several problems that required consideration were as follows :

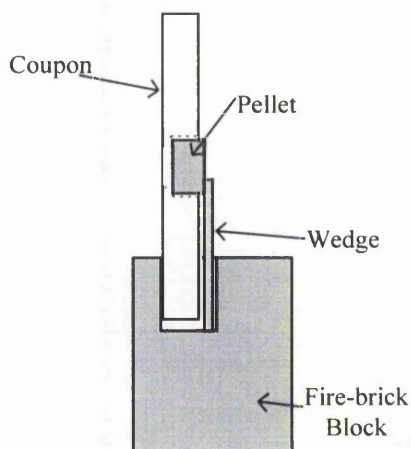
- a) The sample-under-test has to be held inside the furnace.
- b) The sample required both accurate measurement and control of its temperature.
- c) The excitation source had to be focused onto the sample inside the furnace.
- d) The resultant emission had to be collected from within the furnace.

Each of the above points are now discussed in subsequent paragraphs.

#### **a) Sample Holder**

A simple holder was designed to position the samples under test within the furnace. With the samples being tested in three forms, the holder was designed around a test coupon, which itself could be modified to hold a powder pellet. A fire-brick block was produced and the coupon sat within a slot cut in the middle of the block. The coupons could be positioned vertically within the furnace allowing for easy collection of the fluorescence. To accommodate the pellets, a blank test coupon had two holes drilled through its centre, a 4.5mm hole straight through followed by a 5mm hole drilled to a depth of three-quarters of the thickness of the coupon. This allowed the pellet to sit against the “resultant lip” within the coupon. A small wedge piece was positioned behind to hold the pellet in place.

Figure 3-4 illustrates the holder showing the accommodation of the pellet. The back of the pellet was not completely covered to allow the thermocouple to be in contact with the phosphor. For tests made on the thick and thin films, the samples were simply placed within the slot and wedges positioned behind to hold them vertically.



**Figure 3-4 Illustration of the Pellet Holder**

#### **b) Temperature Control**

The furnace was controlled by a Eurotherm temperature controller which sensed the temperature of the furnace via a internal K-type thermocouple. To control and monitor the temperature of the samples, the internal thermocouple was removed and replaced with an external K-type thermocouple which was attached to the sample. RS232 communication was available through the temperature controller allowing for remote control via a computer.

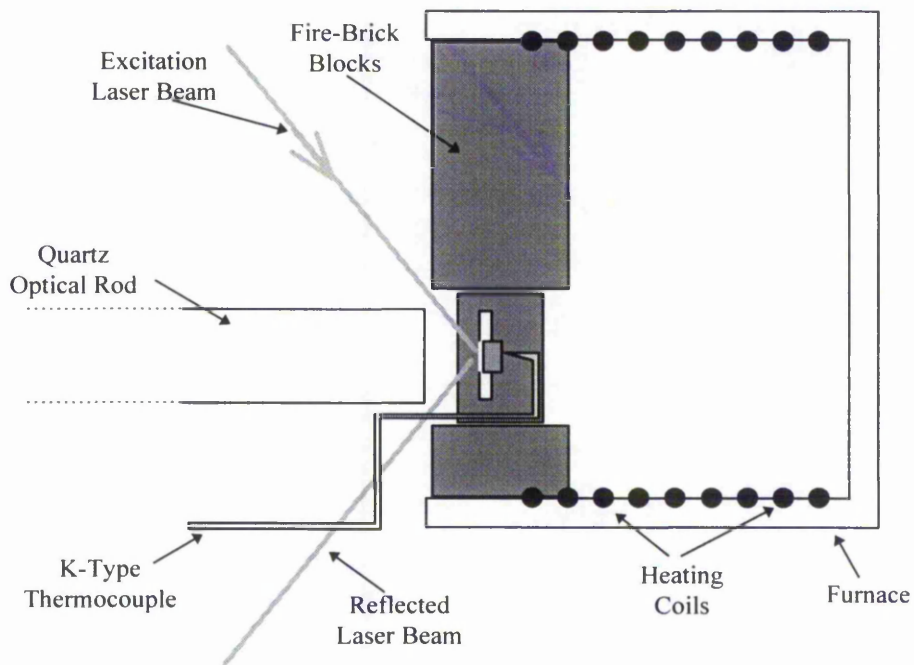
#### **c) Excitation**

To allow a direct path for the excitation beam to reach the sample, the door of the furnace was removed. A safety switch which cut-off the power to the heating elements when the door is open was therefore disconnected. To maintain the temperature within the furnace, blocks of fire-brick were positioned in the doorway. Enough room was left for access to move the sample and allow the positioning of the thermocouple to the back of the sample.

#### **d) Collection of the fluorescence**

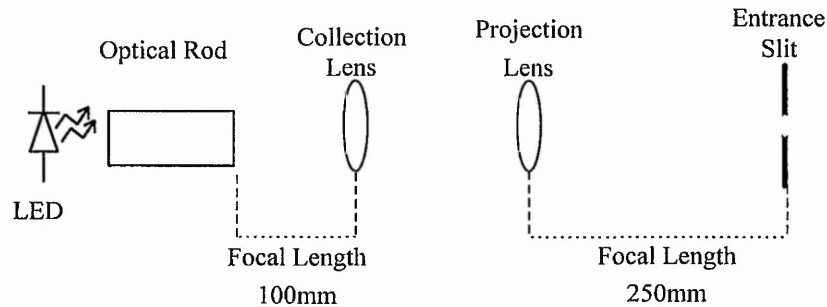
Collection of the fluorescence was problematic. In order to maximise the signal-to-noise ratio, the optics required positioning as near to the source as possible. This meant they had

to withstand the temperatures reached within the furnace. Initial ideas were based on the use of a quartz lens with a short focal length positioned as close to the sample as possible. Unfortunately, a holder for the lens required materials that also had the capabilities of experiencing the extreme temperatures. No satisfactory solution was found, hence this idea was abandoned. The solution was to transfer the emitted fluorescence further away from the furnace, where a holder could be positioned capable of operating at the temperatures reached. This was efficiently achieved by the use of an optical rod as a waveguide. The rod was a 200mm quartz rod which has a softening temperature of  $1665^{\circ}\text{C}^{[59]}$ . The complete arrangement within the furnace is illustrated in Figure 3-5.




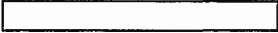

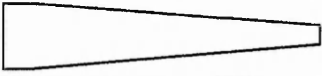
**Figure 3-5 Top Cross-Sectional View of Excitation/Collection Set-up Within A High Temperature Controlled Environment**

To maximise the transmission efficiency of the optical rod, several simple designs of rods were assessed. A two lens system was utilised to capture and project the light into the monochromator. For calibration, a light emitting diode (LED) replaced the phosphor sample as the light source. Figure 3-6 is an illustration of the optical rod assessment layout.



**Figure 3-6 Optical Rod Assessment Layout**

A photomultiplier tube is attached to the exit slit of the monochromator, which is tuned to the centre wavelength of the LED (590nm). The voltage reading from the detector represents the intensity of light transmitted by the optical arrangement. As a baseline test, the LED was positioned at the focal length of the collection lens. By positioning various optical rods between the LED and the collection lens, the transmission efficiency of each optical rod was assessed via direct comparison with the baseline test reading. This transmission efficiency is given as a percentage of the baseline test. Results obtained are tabulated below in Table 3-1.

Configuration	Voltage Reading	Transmission Efficiency
No Rod - baseline test (ideal)	(418mV)	-----
Short clear rod with tapered end 	100mV	-76%
1st clear rod- 200mm length 	170mV	-60%
2nd clear rod - 300mm length 	150mV	-64%
Long tapered rod - 250mm length 	65mV	-84%

**Table 3-1 Optical Rod Assessment Results**

Several tapered rods were assessed in order to maximise the collection of light and condense this captured light to a small point source. Unfortunately, a large percentage of captured light was lost through the side of the rod. The final solution was an optical quartz rod 200mm in length and 12.5mm diameter (the maximum allowed for positioning the rod without interference to the excitation beam).

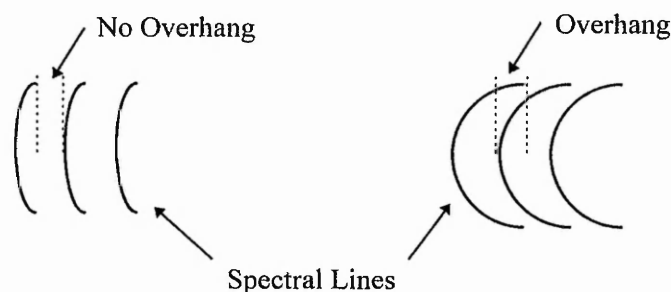
### **3.4 Emission Spectra**

For spectral measurements the excitation source utilised was a steady state Ohmnichrome HeCd, 325nm ultra-violet, 12mJ laser. The emission spectra of phosphors under investigation are characterised using a SPEX 1702 spectrometer with a 3/4m single grating, blazed at 500nm. The basic operation of a spectrometer<sup>[60,61]</sup> is as follows. The light source is coupled into the spectrometer through the entrance slit and is captured by the first Czerny-Turner mirror. This is a collimating mirror which focuses the collected light onto the diffraction grating. The diffraction grating separates the light source into individual wavelength components and, depending upon the angle of the grating, focuses a particular



wavelength onto the second Czerny-Turner mirror. This in turn, focuses the selected wavelength through the exit slit. The intensity of the particular wavelength is measured by the detector, a photomultiplier tube (PMT), attached to the exit slit.

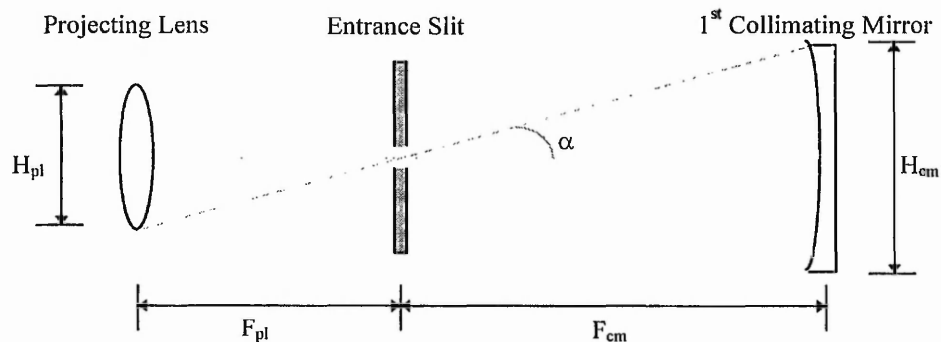
Several factors effect the resolution of the spectrometer and therefore need to be taken into consideration during the set-up of the optics. Firstly, in order to obtain efficient resolution, the diffraction grating must be fully irradiated with the light source. In turn, this indicates that the light passing into the spectrometer must fully illuminate the first collimating mirror. Secondly, the spectral bandpass of the system is a function of the reciprocal linear dispersion which depends upon the grating constant, the focal length, the spectral order of the grating, and the entrance's slit width. With the slit's width being the only variable of the four factors, it governs the bandpass of the system. For example, from a table of reciprocal linear dispersion values for the SPEX 1702 system, to obtain a bandpass of 0.1nm the slit's width would be set to 0.1mm. Thirdly, The slit's height is important as optical 'overhang' of spectral lines is known to exist at the exit slit. In simple terms, a multitude of spectral lines as viewed by the exit slit is illustrated in Figure 3-7. As the height of the entrance slit is increased, the 'overhang' of one spectral line to the next increases, therefore inducing an increase in error.



**Figure 3-7 Illustration of the "Overhang" Characteristic of a Spectrometer**

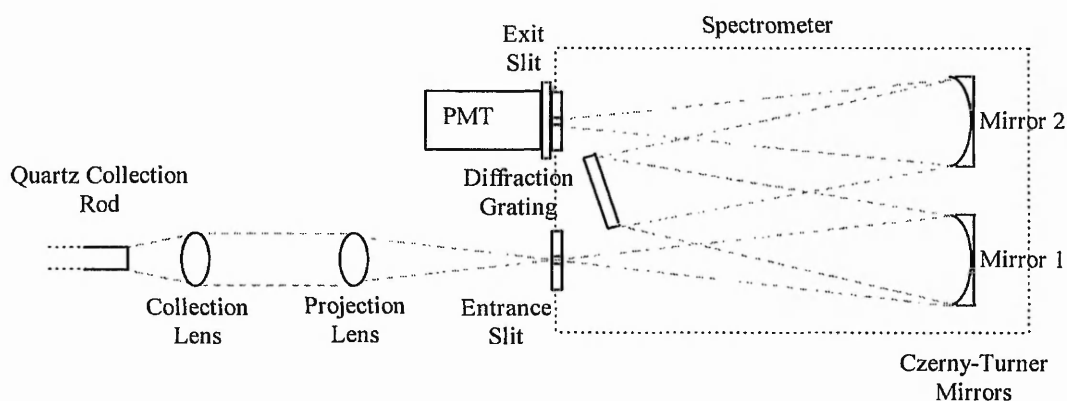
To fully illuminate the first collimating mirror, the solid angle of the projecting lens must match that of the mirror. Figure 3-8 illustrates the requirements of the projecting lens. With

the dimensions of the collimating mirror - height = 100mm and focal length = 750mm - the solid angle,  $\alpha$ , is calculated as  $3.81^\circ$ . The relationship between the focal length,  $F_{pl}$ , and the height,  $H_{pl}$ , for the projecting lens is therefore  $F_{pl} = 7.5 \times H_{pl}$ .



**Figure 3-8 Illustration of Projecting Lens Requirements**

If a single lens was to be used to collect and project the fluorescence into the spectrometer, the lens would require to be positioned at twice the focal length from both the source and the entrance slit. This would result in poor collection of fluorescence from the sample. To maximise the collected fluorescence, a separate collection lens with short focal length is used, therefore creating a two lens system for the transfer of light into the spectrometer. Figure 3-9 shows the collection and focusing of light through the spectrometer.



**Figure 3-9 Schematic of Emission Spectra Set-up**

The photomultiplier tube (Thorn EMI Electron Tube 9558QB) attached to the exit slit converts the light into a current output. This is read as a voltage across a load resistor by the Keithley digital voltmeter which is computer controlled. The diffraction grating is motorised and controlled by the Compudrive, the control system of the spectrometer. The compudrive sets the wavelength range over which measurement is to be made, and the step size to be taken. LabVIEW software was written to send the user information to the compudrive and take readings remotely from the digital voltmeter. As a result, no manual control of the system was required once fully set-up.

To calibrate the spectrometer two light sources of known emission spectra were utilised. The first was a mercury lamp, the emission spectra of which consists of two major peaks at 435.833 and 546.073 nm. This enabled the calibration of two peaks over a wide spectral range. The second light source was a sodium vapour lamp which has two peaks very close together at 588.995 and 589.592 nm, allowing for accurate calibration of resolution over a very short wavelength range.

The calibration results are summarised in Table 3-2. The table specifies the spectral line that was under investigation for each test and the step-size of the spectrometer. From these parameters, the expected peak could be determined and compared with the measured peak. The result was an error value and the diffraction grating was re-tuned accordingly. After a multitude of calibration tests, results showed an accuracy of  $\pm 0.4$  to  $0.7\text{\AA}$  was achievable.

Test No.	Spectral Line (nm)	Accuracy (Å)	Expected Peak (Å)	Measured Peak (Å)	Error (± Å)
Test_014	435.833	5	4360	4360	0
Test_015	546.073	5	5460	5480	+ 20
Test_021	435.833	1.5	4357.5	4363.5	+ 5.5
Test_022	546.073	1.5	5460.5	5468.0	+ 7.5
Test_033	435.833	1	4358	4359	+ 1
Test_034	546.073	1	5461	5466	+ 5
Test_049	435.833	0.1	4358.3	4359.0	+ 0.7
Test_050	546.073	0.1	5460.7	5461.2	+ 0.5
Test_051	588.995	0.1	5889.9	5890.4	+ 0.4
	589.592	0.1	5895.9	5896.4	+ 0.5

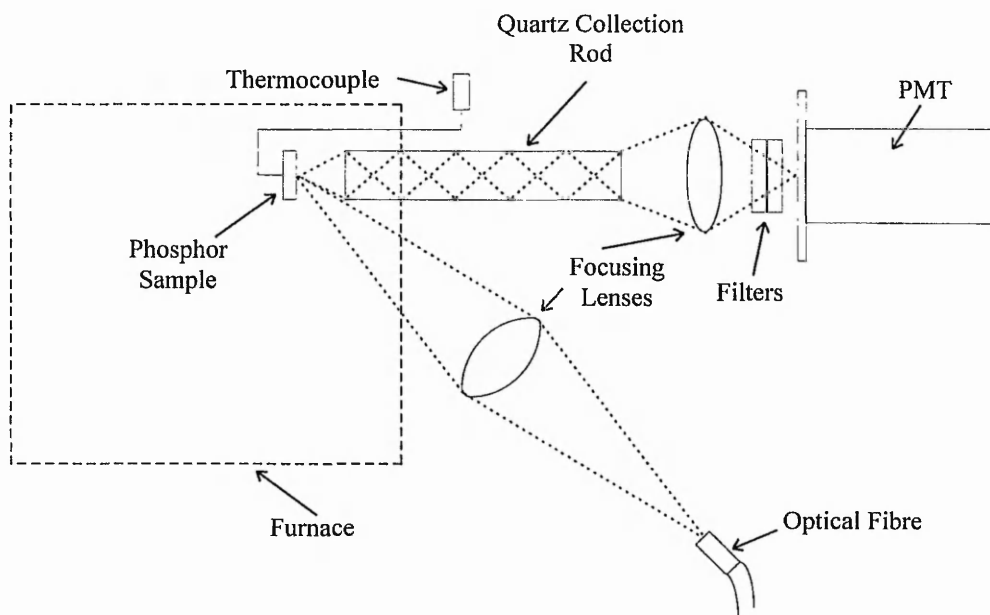
**Table 3-2 Summary of Calibration Measurements of Spectrometer**

### 3.5 Decay Constant Characterisation

Past investigations into the decay constant of phosphors have utilised a monochromator to detect the characteristics of a single peak. At high temperatures, due to the losses of the optical coupling system and the low signal emission levels from the phosphors, difficulties existed in detecting a signal above the noise level. To overcome this problem, by bypassing the losses of the monochromator and the optical coupling system, the detector is positioned closer to the emitting source, so a higher signal level would be detected. As illustrated in Figure 3-10, this was achieved by using a single lens collection and focusing system with

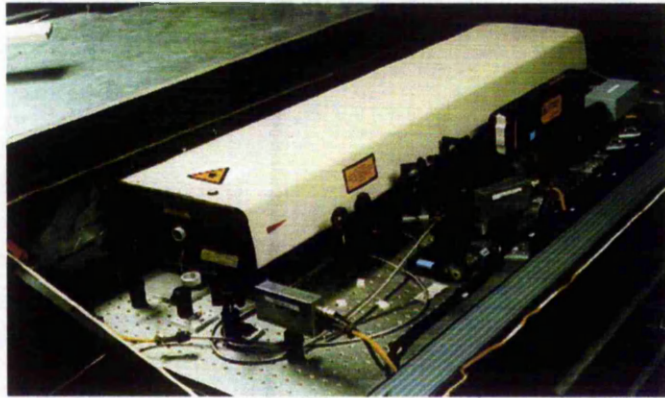
filters for wavelength range selection situated between the quartz rod and the photomultiplier tube (PMT).

Excitation of the phosphor is achieved using a Spectron 130mW Nd:YAG 10-14nS pulse laser (355nm or 266nm). The emitted luminescence is collected by a quartz rod and focused onto the collection window of a PMT (Electron Tubes Ltd type 9558QB) via a single quartz lens. Two filters are positioned between the rod and PMT specific to the emitted wavelength being captured, with a bandwidth sufficient to accommodate for any wavelength shift that occurs due to increasing temperature. For example, when measuring the characteristics of  $Y_2O_3:Eu$  a UV high pass filter (cut-on 520nm) and a narrow band filter (CF 610nm, HBW 10nm) are used. The signal output of the PMT is read by a Gould 4028 DSO (digital storage oscilloscope) which is computer controlled to allow for automated data capture. Once again, LabVIEW software has been written to control all equipment, see Section 3.6.



**Figure 3-10 Schematic showing the Decay Constant Measurement Set-up**

The Spectron Nd:YAG pulse laser was provided by Rolls-Royce Plc as part of the CASE Studentship. As shown in Figure 3-11, it is positioned on a test-bed with an optical layout to couple the laser into a fibre optic. This allows for the excitation of materials to occur at a distance away from Spectron laser, which is temperature sensitive.



**Figure 3-11 Photo of The Spectron Nd:YAG Pulse Laser System**

### **3.5.1 Response Time of The Measurement System**

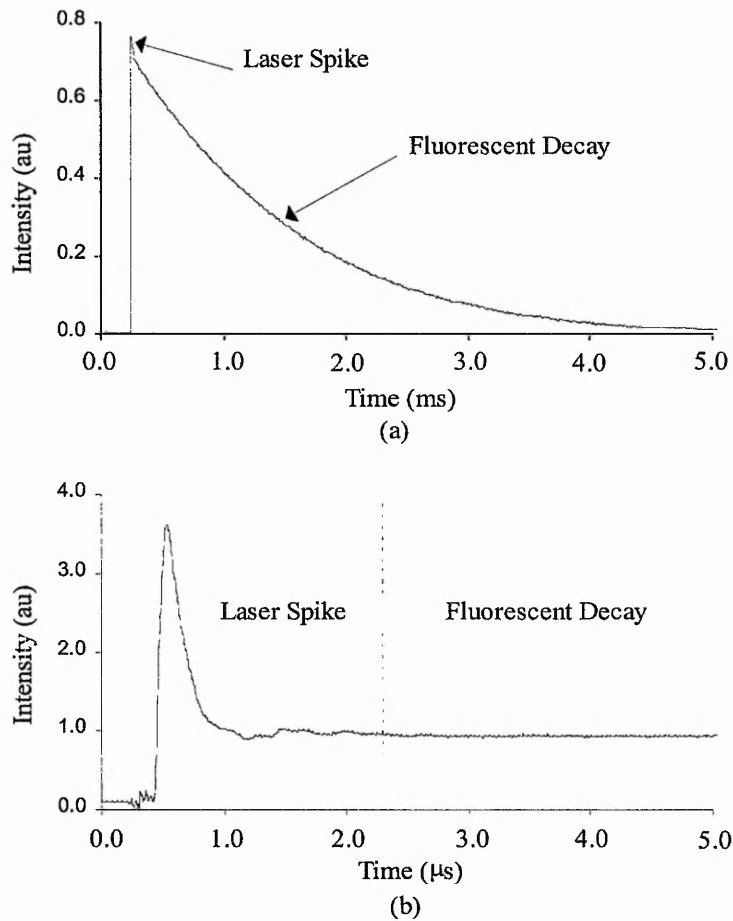
At high temperatures, the decay constant will be of the order of sub-micro seconds. As a result, the response time of the system must be minimised to achieve accurate measurements at these high temperatures. As will be shown, the limiting factor to the system response was the interference of the laser pulse.

#### **Laser Pulse Interference**

Initial tests were carried out with the Spectron Laser tuned to 355nm. As an example, Figure 3-12(a and b) show the typical signal received by the digital oscilloscope. The signal consisted of the fluorescent decay pulse and the laser spike interference

For the low temperatures, the interference of the laser spike would be negligible due to the strong and long fluorescent signal emitted by the phosphor. Clearly, 3.12b demonstrates that unwanted noise associated with the laser lasts for at least 1 microsecond. At higher

temperatures, when the lifetime of the fluorescent signal is of the same order, the laser spike becomes a dominating factor and so leads to a reduction in measurement accuracy. Also, when measuring the characteristics of low dopant concentrations of  $Y_2O_3:Eu$ , the detection of the laser spike results in the loss of signal from the rise period of fluorescence, hence reducing the effectiveness of this novel low temperature sensing characteristic.



**Figure 3-12 Digital Storage Oscilloscope Output (a) complete pulse and (b) closer inspection of the laser spike interference**

Three factors contribute to the laser interference. Firstly, there is the detection of the excitation wavelength within the photomultiplier tube. On reaching the phosphor sample, a small percentage of the laser pulse is reflected and captured by the optics. A high-pass filter

is positioned in front of the detector to reduce the strength of the laser pulse collected by the detector. This detection leads to saturation of the detector and therefore a slow response time. As a result, the laser pulse detected appears to last for at least  $1\mu\text{s}$ , even though it only has a  $14\text{ns}$  pulse width. Unfortunately, due to the strength of the laser in comparison to the emitted fluorescence, any additional filters required to further reduce the laser signal would also degraded the strength of the fluorescent signal. To compensate for this weaker fluorescent signal, the power of the photomultiplier tube would require an increase to provide more gain. In turn, this would make the detector more responsive to laser interference, and so decrease the response time of the system even further.

Secondly, fluorescence occurs within the fibre system utilised for transferring the pulse from the Spectron laser to the sample. This fibre was incorporated into the laser system by Rolls-Royce engineers, and utilised when exciting a phosphor coated on a turbine blade within an engine. This was determined by a series of tests involving a silicon wafer replacing the phosphor sample. The laser beam was directed onto the reverse side of the wafer which provided a rough surface for a uniformly scattered reflection. Therefore, only the laser reflection and fluorescence external to the phosphor would be detected. Observations were made of the detected signal after the removal of individual components from within the optical arrangement. It was not until the optical fibre and associated coupling optics were removed from the arrangement that the detected signal was reduced. Tests were then carried out with the signal being passed through the monochromator before reaching the detector. This was to determine the spectral response of the fluorescence from within the fibre. At first the signal appeared constant throughout the visible spectrum, apart from at  $710\text{nm}$  where the second harmonic of the  $355\text{nm}$  laser pulse was detected, and therefore it appeared that the fluorescence of the fibre had a flat spectral response. This was not the case, but was a result of electromagnetic interference contributing to the response of the system.



The electromagnetic interference was due to both the high voltage and the Q-switching mechanism for providing the pulsed output from the Spectron laser supply. The coaxial cable both to and from the detector would pick-up the interference on its earth shielding. Removal of this interference is achieved by wrapping the coaxial cable around electromagnetic compatible inductors which absorbed the floating voltages from the earthing. Also, the analysis equipment was moved as far as possible away from the Spectron power supply to minimise the effect.

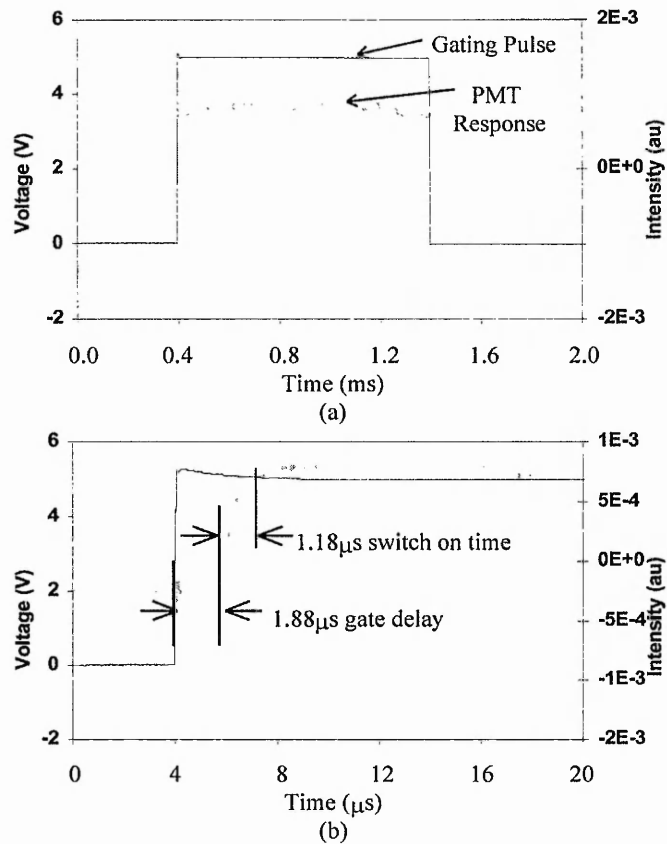
Further reduction of the response time was achieved when the laser was re-tuned to 266nm. This drastically reduced the laser's interference mainly from the detection of the laser pulse. A glass lens was utilised for focusing the detected signal onto the photomultiplier tube and acted as a filter for the laser pulse. Glass has a spectral response which cuts out the ultra-violet. Due to the position of the cut-off point, some of the 355nm would be allowed to pass compared with all of the 266nm being reflected. As a result, along with the electromagnetic consideration, when using 266nm as the excitation wavelength, the response of the system was reduced to  $0.3\mu\text{s}$  - a considerable improvement.

#### **Gating Of The Photomultiplier Tube**

Another method for improving the response of the detected signal, is to use a gating system where the photomultiplier tube will only detect within a specified time window. This would allow the detector to be turned on immediately after the laser pulse has occurred, and so would not be detected. Of the photomultiplier tubes available, the most suitable for the requirements was the type-9954B from Electron Tubes Ltd. The principles of operation for a photomultiplier tube are as follows. The incident light is focused onto the window of the tube - the photocathode. This light sensitive region absorbs the energy of the incident photons which provides enough energy for the ejection of photoelectrons from the surface of the material. This process is referred to as the photoelectric effect<sup>[62,63]</sup>. These

photoelectrons are accelerated towards the first dynode and on impact produce secondary electrons. In turn, these are accelerated towards the next dynode and the process is repeated. At the last dynode, the electrons are collected by the anode, thereby producing a current output relative to the intensity of the incident light. The gain of the tube is controlled by the voltage applied which is distributed between the series of dynodes by the voltage divider board.

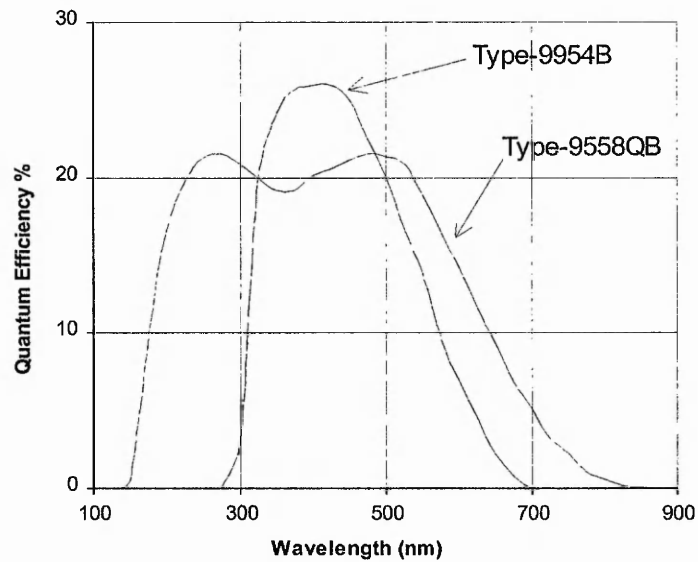
During normal operation, the first dynode is held at a potential of 150V relative to the photocathode. The gating board switches its potential to -20V, resulting in the electrons collecting around the outer ring of the first dynode rather than on the active region. These electrons are then conducted away through the voltage divider. The pulse applied to drive the gating board is provided by a pulse generator. The specifications of the gating board included a gate delay of  $2\mu\text{s}$  and a switch on time of  $0.2\mu\text{s}$ . With the laser being externally triggered by the pulse generator with the same delay as above, only the switch on time of the photomultiplier tube would result in lost of data. The response time of the system would be reduced to  $0.2\mu\text{s}$ . Unfortunately, as shown in Figure 3-13, the above specification could not be matched and the fastest switch on time achievable was  $1.18\mu\text{s}$ . Although, this was comparable to the current response time of the system, the non linear response of the detector when excited with a constant source resulted in the gating board being removed from the system.



**Figure 3-13 Gating Board (a) response over complete pulse width (b) initial gate Delay and switch-on time**

Also, the spectral response of the type-9954B was better suited to phosphor thermography than that of the type-9558QB and is illustrated in Figure 3-14. The 9558QB had been specifically purchased for spectral measurements and so had a wide spectral response, allowing for the detection of both the infra-red and the ultra-violet regions of the spectrum. Two advantages are gained due to the narrower spectral response of the 9954B. Firstly, at high temperatures, the limiting factor to the response of the detector is the level of blackbody radiation. This causes drainage of the current output from the photomultiplier, therefore reducing its sensitivity. With the 9954B having a lower quantum efficiency in the

infra-red region of the spectrum, the high levels of blackbody radiation reached within the high temperature environment will be less detrimental to its capabilities.



**Figure 3-14 Spectral Response of Type-9558QB and Type-9954B Photomultiplier Tubes, obtained from Electron Tubes Ltd Data Sheets**

Secondly, it has already been shown that the detection of the laser pulse reduces the response time of the system. Again, the spectral response of the 9954B only becomes effective just below 300nm compared with the 9558QB which is sensitive from 150nm. With the laser tuned to 266nm, its effect on the response of the detector would be drastically reduced when using the 9954B tube. No advantages occurred with the gating, hence this method was abandoned in favour of the steady-state method of measurement using the 9954B tube.

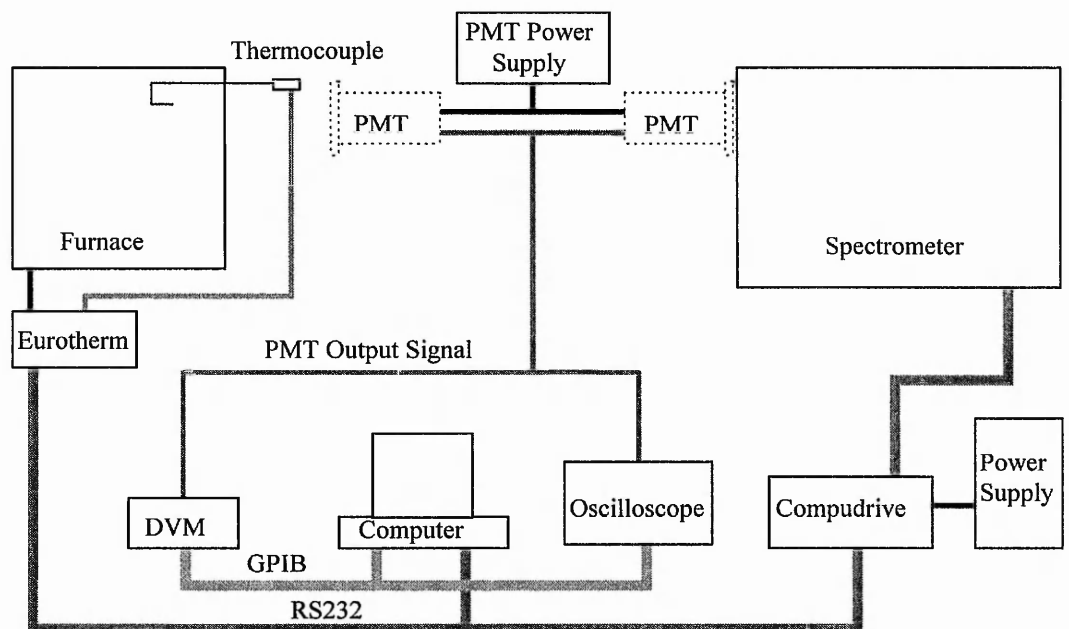
### **3.6 LabVIEW Control Software**

All the equipment used for this investigation is computer controlled to allow for ease of use and automated data collection. The software is written using National Instruments LabVIEW, a graphical based programming language. The program created is referred to as

a Virtual Instrument (VI) because it operates as an instrument through a user interface. Each VI consists of a graphical representation of control buttons and graphs, therefore simulating the front panel of a physical instrument; and a block diagram, pictorially showing the options and route taken for the solution. The VIs can be hierarchical and modular, so producing a top-level program followed by sub-programs, called subVIs. Full details of the control software can be found in Appendix A.

### 3.6.1 Communication Requirements

For the two measurement systems combined, Figure 3-15 shows the layout of the equipment and the communication links required.



**Figure 3-15 Communication Diagram of Measurement Equipment**

Both RS232, for the Compudrive and the Eurotherm, and GPIB, for the DVM and the oscilloscope, communications links are required. All settings are held within the LabVIEW software. The Spectrometer is powered by the compudrive, which in turn is powered by its own power supply. The RS232 communication line is shared between the Eurotherm and

the CompuDrive due to only one serial port being available within the system. This is taken into consideration within the software to stop communication conflicts. Also note, two PMTs are shown, but again only one is used at any one time.

### **3.6.2 Emission Spectrum Programme**

The emission spectrum programme allows the temperature of the phosphor to be set through the temperature controller, and would also control the wavelength being set by the CompuDrive. Before measurement could begin, the default parameters within the CompuDrive are altered to allow for two-way communication. Details of the default parameters and the options available can be found in Appendix A. Figure 3-16 shows a simplified flow chart of the programme. The main menu provides the user with three options :-

- i) Set the temperature of the phosphor
- ii) Collect the spectrum
- iii) Exit.

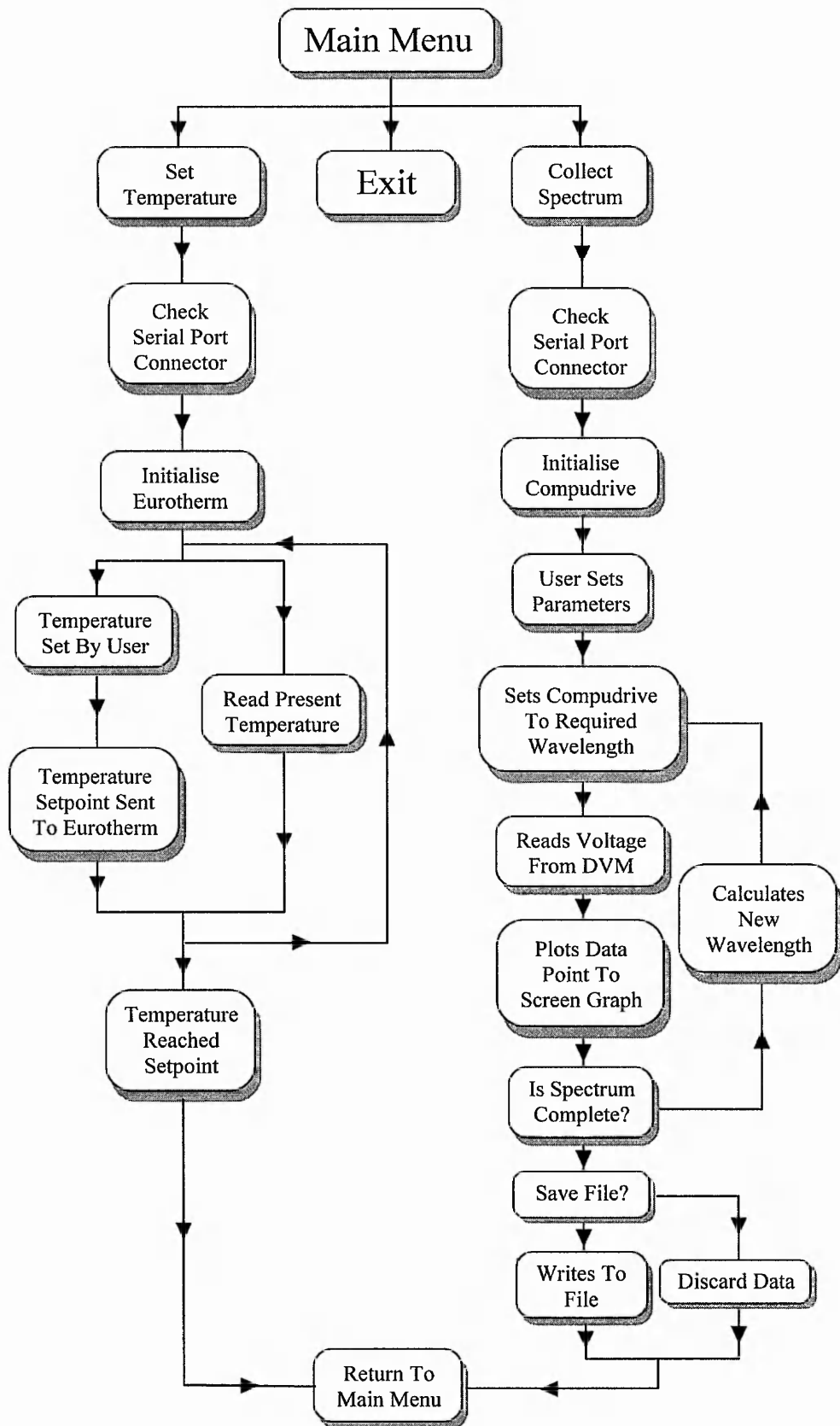


Figure 3-16 Block Flow Diagram of the Emission Spectra Programme

### **Setting the temperature**

Before the temperature of the phosphor can be set, the user is asked to check that the serial port connector is connected to the temperature controller. This was due to the serial port available being shared between the temperature controller and the compudrive. If the serial port was connected to the compudrive instead of the temperature controller, the programme would fail and the system would require re-booting. The temperature controller is then initialised and the user enters the temperature controller's virtual instrument to set the required temperature. In parallel, the present temperature is read from the eurotherm. Both of these options are within a one second time loop, during which time, the user could reset the temperature if required and monitor the present temperature. When the user is satisfied with the present temperature, one leaves the temperature controller interface and returns to the main menu.

### **Collect Spectrum**

Once again, the user has to check the serial port connector to stop a programme failure. The compudrive is initialised and the user is then asked to enter the parameters. These include the starting and finishing wavelengths, the number of data points, the measurement period for each data point, the name of the operator and the filename. After entering the parameters, the file is created and stores the parameters set by the user. The compudrive is then set to the starting wavelength. The voltage representing the intensity is read from the Keithley Digital Voltmeter. This reading is averaged over the measurement period set by the user. The data point is plotted to a screen graph and appended to the user defined file. The next wavelength to be measured is then calculated and sent to the compudrive. This process is repeated until the full spectrum is completed. Finally, the user can either save the file or discard the data and is returned to the main menu.



### 3.6.3 Decay Constant Programme

Within the decay constant programme, the four options available for the user are :

- i) Set the temperature
- ii) Collect and measure the decay constant
- iii) Transfer Curve
- iv) Exit

Figure 3-17 shows the block flow diagram of the programme.

#### **Setting The Temperature**

This subVI of the programme is the same as use within the emission spectrum programme.

#### **Collect and Measure Decay Constant**

Before capturing and measuring the decay constant, the detected signal is averaged on the digital storage oscilloscope to minimise noise. For example, by averaging over a 30 second period with the frequency of the laser at 20 Hz, the detected signal consists of the average of 600 pulses. First, the temperature controller is initialised and has its present temperature read and stored. The oscilloscope is then initialised and placed into store mode. This stores the averaged signal on the oscilloscope screen. The user enters the filenames for both the current decay curve and the overall decay constant versus temperature graph. The data is captured from the oscilloscope and written to the user defined file. The captured data undergoes a curve fitting routine resulting in the calculation of the decay constant. This routine is averaged over ten times. The calculated decay constant value is written to the screen and appended to the decay constant versus temperature file. The user is prompted to

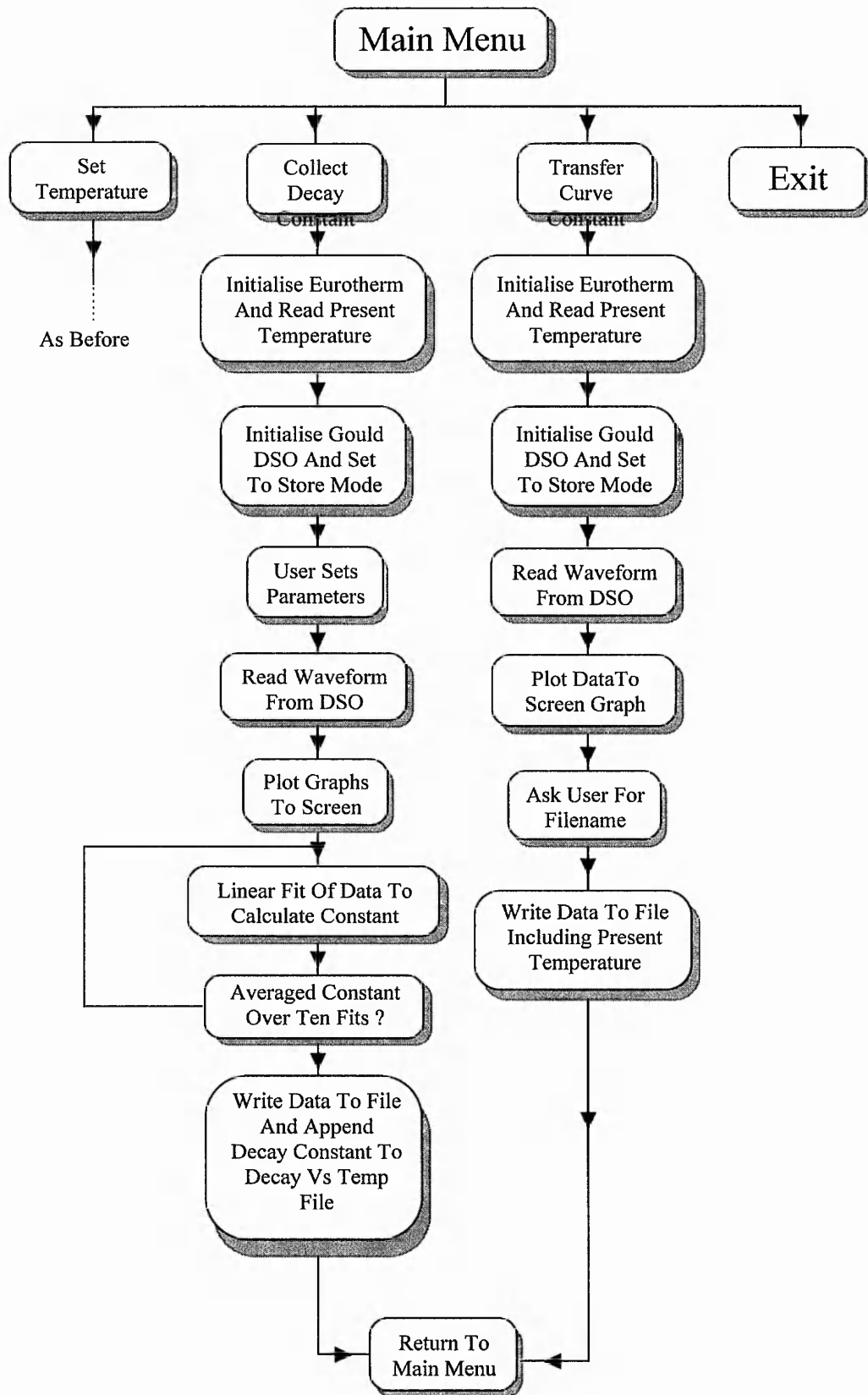
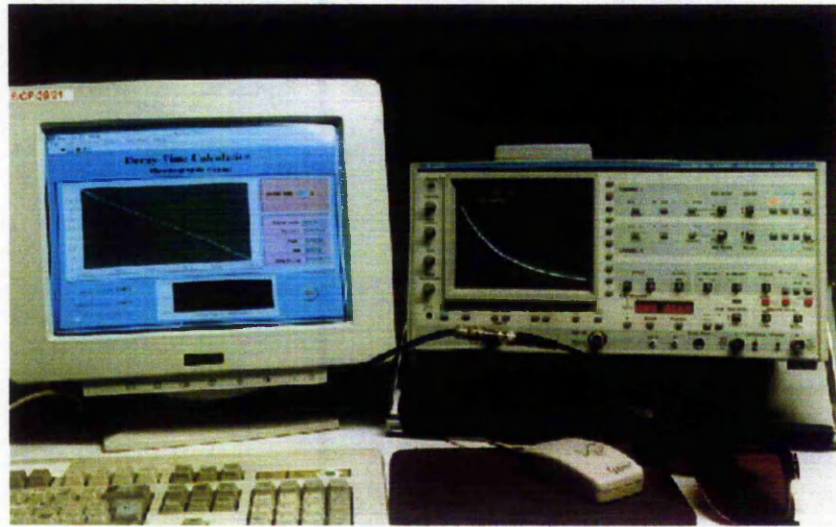


Figure 3-17 Block Flow Diagram of Decay Constant Measurement Programme

save the files and is returned to the main menu. Figure 3-18 shows the programme in operation.



**Figure 3-18 Photo of The Decay Constant Measurement Programme in Operation**

As shown above, the exponential decay captured on the oscilloscope is plotted as a straight line on the virtual instrument created by the software. Referring to equation 4 of Chapter 2, the natural log of the decay of phosphorescence is :-

$$\ln(I(t)) = \ln(I_0) - \frac{1}{\tau_d} t \quad \text{Equation [10]}$$

A simple linear curve fitting routine is implemented within the programme. The decay constant is determined by the gradient of the fitted curve.

### **Transfer Curve**

Similar to the collecting of the decay curve, the transfer curve routine was written to capture curves from the oscilloscope without any curve fitting routine. Referring to the block flow diagram, the procedure is the same as above, but with the user providing a filename after the curve has been captured. This routine was used for collecting the rise-time characteristics and the full curves which could be analysed later.

### **3.7 Summary**

Two measurement systems have been designed for the characterisation of thermographic phosphors. The first is the emission spectra system, which has been calibrated to an accuracy of  $\pm 0.4$  to  $0.7\text{\AA}$  across the full visible spectrum; and the second is the decay constant measurement system. Both systems involve the use of a furnace allowing for the characteristics to be measured with respect to temperature variation. An investigation was carried out to maximise the collection of photoluminescence from within the furnace. The solution was to use a quartz collection rod which provided a means of transferring the photoluminescence signal to outside the furnace. This allowed the detector to be positioned at a sufficient distance away from the furnace so as not to be affected by the temperature. Also, in order to maximise the signal-to-noise ratio detected, the optics have been optimised through use of collection and focusing lenses and a series of filters. Finally, both systems are automated through the use of LabVIEW software. These virtual instruments provide the user with computer controlled systems, allowing for ease of use and collection of data for further analysis.

With the measurement systems fully calibrated, the complete characterisation of the phosphors was undertaken. Each phosphor was characterised in two forms - as a powder pellet and as a thick film. This involved the optimisation of each phosphor and a comparison between their capabilities for use within the temperature sensing of turbine blades. The most suitable phosphor was chosen and grown as a thin film using the process of RF magnetron sputtering. The following chapters will discuss the results obtained.

## 4. Europium Doped Yttrium Oxide

### 4.1 Background

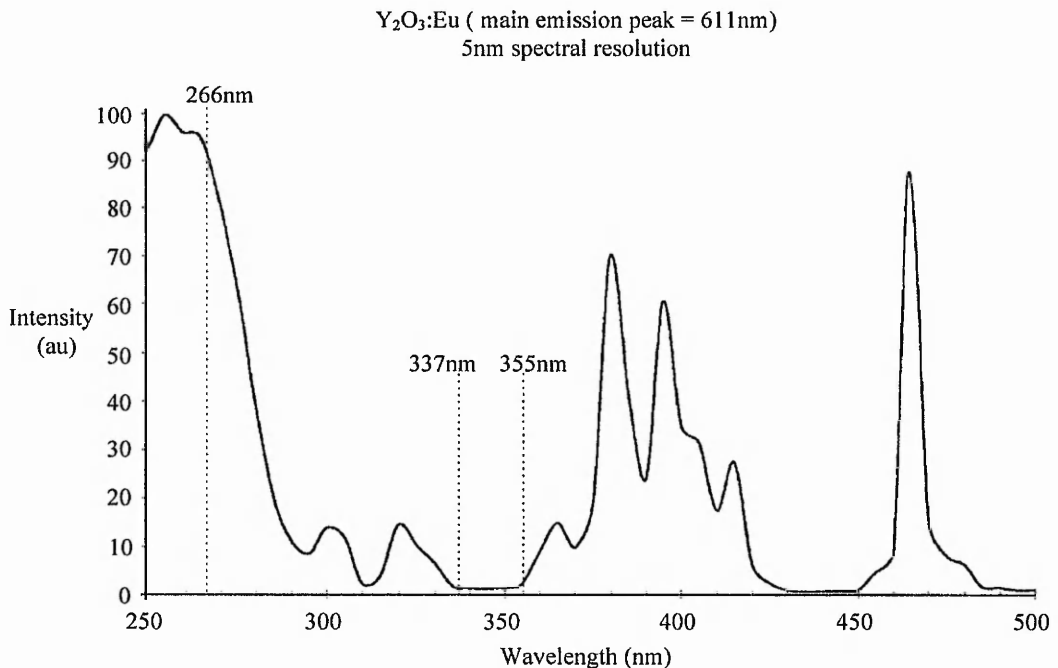
During the 1950's, with the television industry expanding, phosphors were required to produce each of the three primary colours required for full colour television. Early phosphors provided the necessary colours, but suffered a variety of problems including low brightness and instability in maintaining correct colour balance, especially in the red-emitting spectrum. In 1955<sup>[64]</sup>, it was proposed that the ideal red-emitting phosphor should have "a sharp spectral line at 610nm", for which the early phosphors failed due to their broad band emission in the deep-red spectra, an insensitive region of the human's eye response. Extensive research to discover this ideal phosphor began, with the discovery of Europium doped Yttrium Vanadate Oxide,  $YVO_4:Eu$  (618nm), in 1962<sup>[65]</sup>.

During the 1960's, the ever increasing demand for colour television, resulted in the expansion of the rare-earth phosphor industry to produce more efficient and stronger emissive phosphors on a larger scale at lower cost.  $YVO_4:Eu$  was replaced in 1967 with Europium doped Yttrium Oxysulphide<sup>[64]</sup>,  $Y_2O_2S:Eu$  (626nm), developed by the Radio Corporation of America (now the Sarnoff Centre, Princeton). At the same time, the alternative Europium doped Yttrium Oxide  $Y_2O_3:Eu$  (611nm) was produced, which had a slightly higher luminous efficiency than  $Y_2O_2S:Eu$ .

Since then,  $Y_2O_3:Eu$  has become one of the most widely investigated phosphors for both cathodoluminescence and photoluminescent thermographic applications. It is the decay constant characteristic of this phosphor which has been utilised specifically for the measurement of temperature. Previous work<sup>[36,38,39,42]</sup> has shown that as a thermographic phosphor,  $Y_2O_3:Eu$  has a temperature range of 600 to 1200°C, with a decay characteristic of 1.5ms to sub 1 $\mu$ s. These measurements were carried out using excitation wavelengths of

337nm and 355nm, i.e. a nitrogen pulse laser and the third harmonic of a Nd:YAG laser. These are the two most widely used wavelengths in the laser industry.

Figure 4-1 shows the excitation spectra of  $Y_2O_3:Eu$  for the 611nm emission peak, courtesy of Phosphor Technology Ltd. It can be seen that both 337nm and 355nm are not the most beneficial excitation wavelengths to utilise for the excitation process. A more significant excitation wavelength to utilise would be 266nm. The excitation source available for this investigation was a Nd:YAG Spectron 130mW 10-14nS pulsed laser (on loan from the collaborating body of Rolls-Royce Plc). The fourth harmonic of Nd:YAG is 266nm.



**Figure 4-1 Excitation Spectrum of  $Y_2O_3:Eu$  , provided by Phosphor Technology Ltd.**

Reference to Figure 4-1 indicates that a wavelength of 266nm corresponds to the charge transfer band of  $Y_2O_3:Eu$ . For  $Y_2O_3:Eu$ , this is the region where energy is absorbed by the oxygen atoms and transferred to the europium atoms<sup>[66]</sup>. This leads to a much more intense

emission of the 611nm peak. Consequently, for this investigation, both 355 and 266nm excitation is studied, in order to examine the increased efficiency that should be produced by 266nm excitation, and also to facilitate direct comparison with previously published results where 355nm was used as the excitation wavelength.

#### 4.1.1 Crystal Structure

Extensive research into the crystal structure and the optical properties of  $Y_2O_3:Eu$  has taken place over the past 40 years<sup>[67-74]</sup>. The crystal structure of  $Y_2O_3$  is of the rare-earth sesquioxide C-type with each  $Y^{3+}$  ion being surrounded by six oxygen atoms sited at six corners of the cube. Figure 4-2 shows the subsequent cuboidal structures and leaves two vacant corners, resulting in two  $Y^{3+}$  sites of symmetry  $C_2$  and  $C_{3i}$  (also referred to as the  $S_6$  symmetry site)<sup>[37]</sup>.

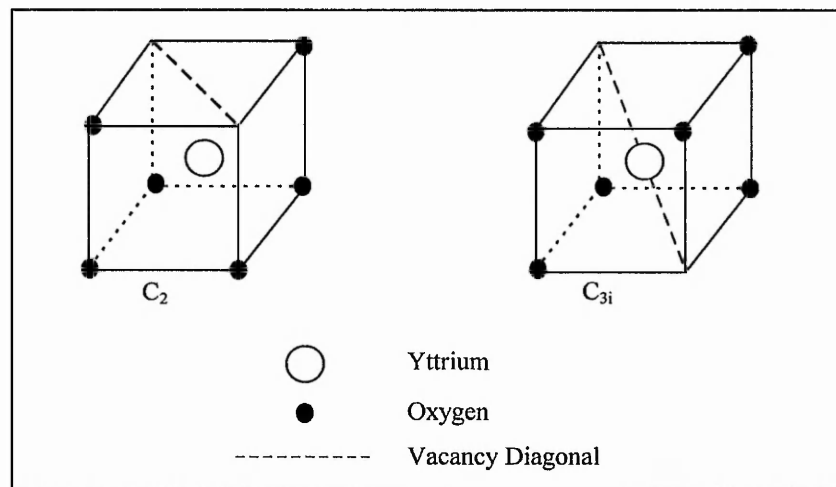
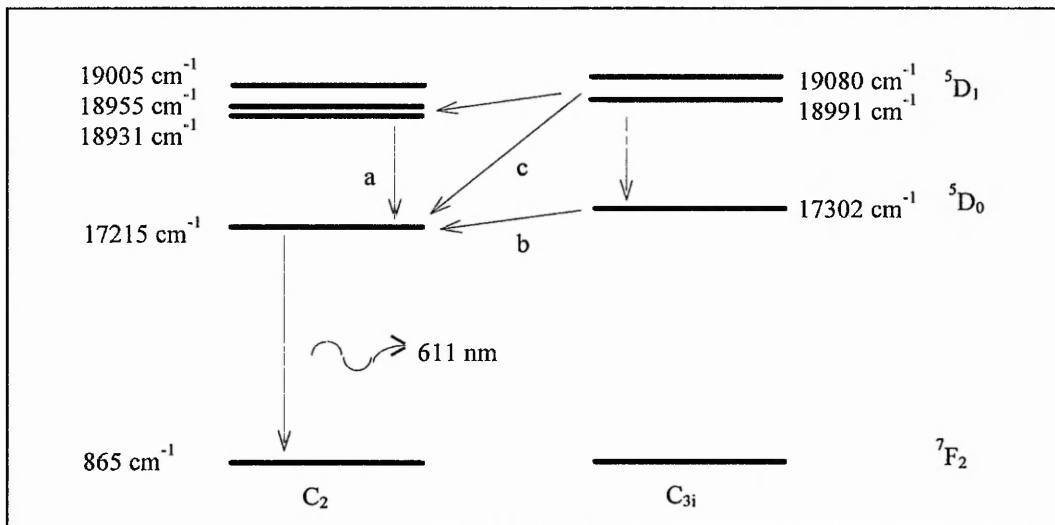


Figure 4-2 Sites of Symmetry of  $Y_2O_3:Eu$



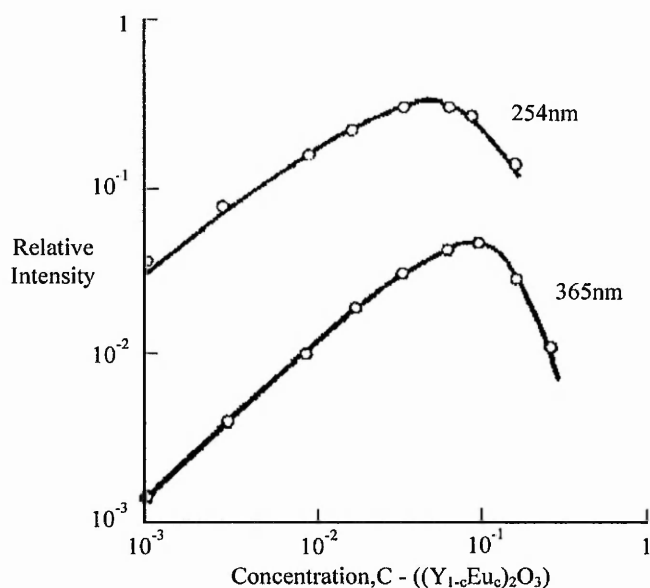
**Figure 4-3 Energy Level Diagram of  $\text{Y}_2\text{O}_3:\text{Eu}$**

With  $\text{Y}_2\text{O}_3:\text{Eu}$ , the  $\text{Eu}^{3+}$  ions can sit in these sites of symmetry, producing energy levels depicted in Figure 4-3. The resultant 611 nm peak is a transition from  $5D_0(C_2)$  to  $7F_2(C_2)$ . By exciting with a shorter wavelength, it is shown that the excited electrons absorb more energy and move into higher, more unstable energy levels. Before emitting at 611 nm, they must reach the  $5D_0(C_2)$  site. This occurs due to loss of energy through a series of transitions between energy levels. Also, electrons which have been excited within the  $C_{3i}$  site require transferring to the  $C_2$  site before the 611 nm transition can occur. Previous work by Heber et al.<sup>[70]</sup> gives evidence for three potential energy transfer paths between the  $5D_1$  and  $5D_0$  levels as shown on Figure 4-3. Emission at 611 nm is therefore clearly affected by the transition to the  $5D_0(C_2)$  level from the  $5D_1(C_2$  and  $C_{3i})$  sites. Energy transitions along paths a and b have been observed for  $\text{Y}_2\text{O}_3:\text{Eu}$  powder to be faster than  $5 \mu\text{s}$ <sup>[72,73]</sup>, however the transition along path c ( $5D_1(C_{3i})$  to  $5D_0(C_2)$ ) has been observed to be appreciably slower by Hunt and Pappalardo<sup>[72]</sup>. This slower transition results in the rise time component of the fluorescent lifetime, and the transition of  $5D_0$  to  $7F_2$  of  $C_2$  site produces the decay characteristic, as described later.



### 4.1.2 Dopant Dependency

Past investigations into the fluorescent properties of phosphors vary the dopancy, defined as the ratio of activator to host lattice concentration. Such an example is  $Y_2O_3:Eu$  where studies have been of cathodoluminescence, as shown in Figure 4-4. Here it can be seen that the 611nm emission intensity varies with the dopancy<sup>[75]</sup>. Also, two wavelengths of excitation were investigated, the shorter of which (254nm) showed an order of magnitude greater intensity and a dopancy shift to lower concentrations for maximum emission. For thermography, maximisation of emission is very important at extreme temperatures where the level of blackbody emission becomes a high noise factor. Hence for this study, the dopancy of  $Y_2O_3:Eu$  is characterised over the full range from 0-100 atomic percent(a/o) and at both excitation wavelengths, i.e. 355nm and 266nm of the Nd:YAG laser.



**Figure 4-4 Concentration Dependence Curves of  $Y_2O_3:Eu$  611nm due to Cathodoluminescence Excitation**

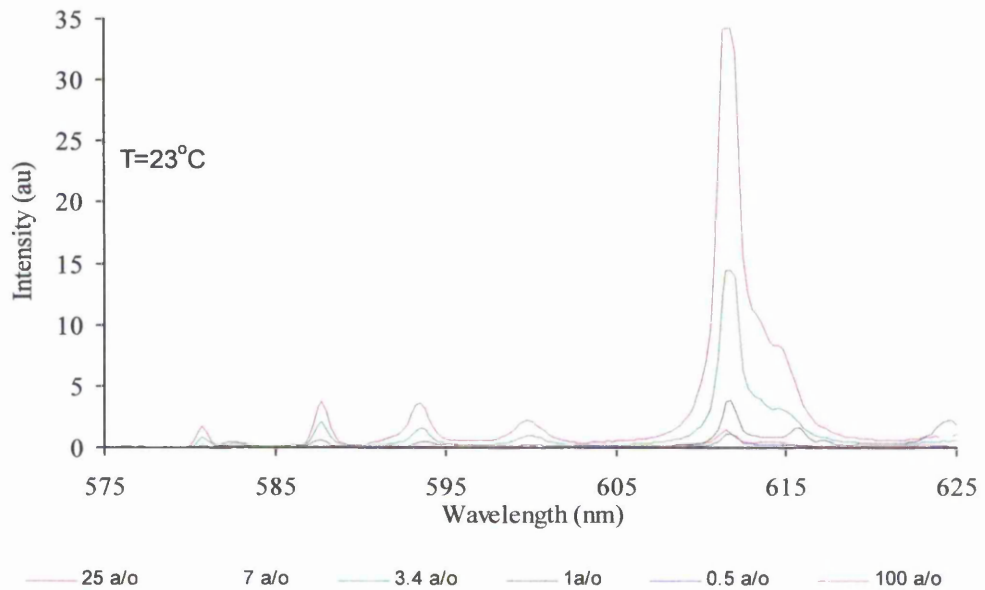
## **4.2 Emission Spectra of $Y_2O_3:Eu$**

In order to define the strongest spectral line for  $Y_2O_3:Eu$ , the emission spectra was examined. Hence, further investigation into the phosphor's temperature dependent properties would concentrate on this wavelength. To determine the spectra, a continuous power excitation source, namely a HeCd 325nm laser, was utilised. Two areas of importance required investigation. Firstly, what effect does varying the dopant concentration have on the emission spectra; i.e. does the wavelength shift and is there any broadening or narrowing of the spectral lines? And secondly, does the emission spectra differ at elevated temperatures?

### **4.2.1 Dopant Dependency**

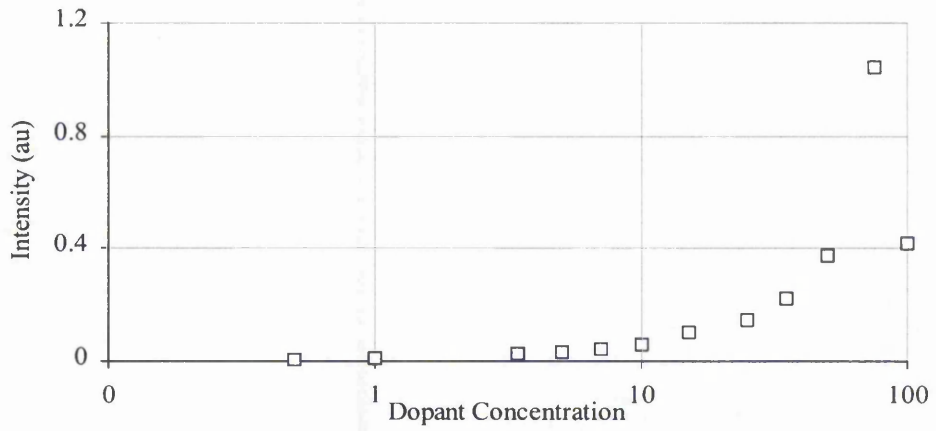
For this investigation, the emission spectra of  $Y_2O_3:Eu$  was characterised over a dopant concentration range from 0.5 a/o to 25 a/o of Europium. Figure 4-5 shows the spectra obtained using the 325nm excitation source. The spectra remains constant for all concentrations in terms of spectral line emission with no shifts occurring, but does show an increase in intensity of these lines with dopant concentration. The maximisation of intensity without emission wavelength shifts occurring is very important for thermography as explained earlier.

The spectra of  $Eu_2O_3$ , shown as 100 a/o in Figure 4.5, was also measured and showed no spectral shifts. Given that no spectral line shift occurs with the main emission at 611nm independent of dopant concentration, work concentrated on the variation of intensity level of the 611nm peak via the decay-constant measurements. Therefore, only a 10nm bandwidth centred at 610nm of light would be analysed and utilised for the temperature dependent characterisation of the phosphor. The maximisation of signal-to-noise ratio remains a high priority. Therefore, calibration of the intensity of the 611nm spectral line through the 10nm bandpass filter was investigated.

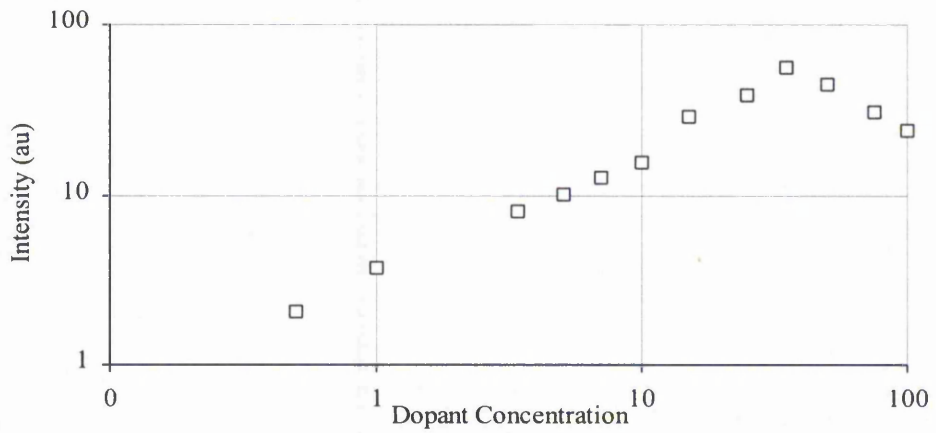


**Figure 4-5 Emission Spectra of Y<sub>2</sub>O<sub>3</sub>:Eu at Various Dopant Concentrations**

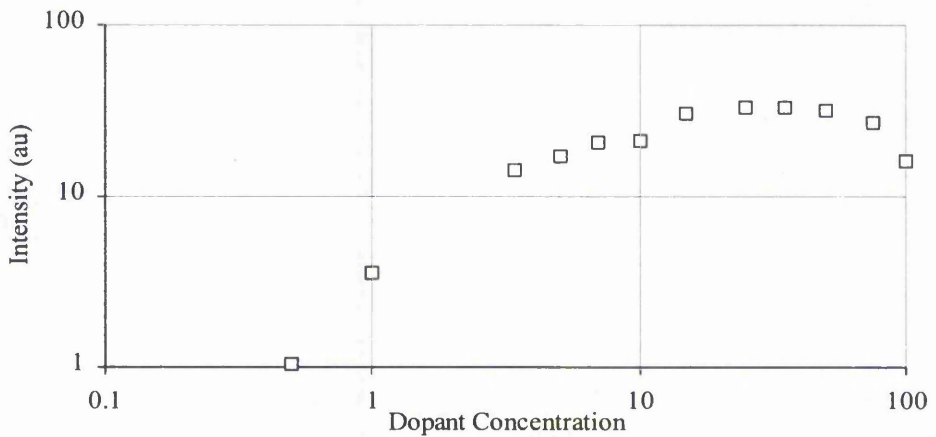
Results shown in Figure 4-6, indicate that the maximum intensity emission due to dopant variance occurs in a region between 25 to 35 a/o. Three methods of comparing the intensity were measured and are as follows a) the peak intensity during pulsed excitation with the 355nm of the Nd:YAG laser, b) the integrated area of the complete pulse emission during 355nm pulsed excitation, and c) the continuous intensity value using the 325 CW laser. Graphs b) and c) show maximum intensity to occur between 25 to 35a/o; whereas, graph a) shows maximum intensity at 75a/o.



a) Peak intensity using the 355nm Nd:YAG pulse laser



b) Steady-State (integrated pulse) intensity using the 355nm Nd:YAG pulse laser



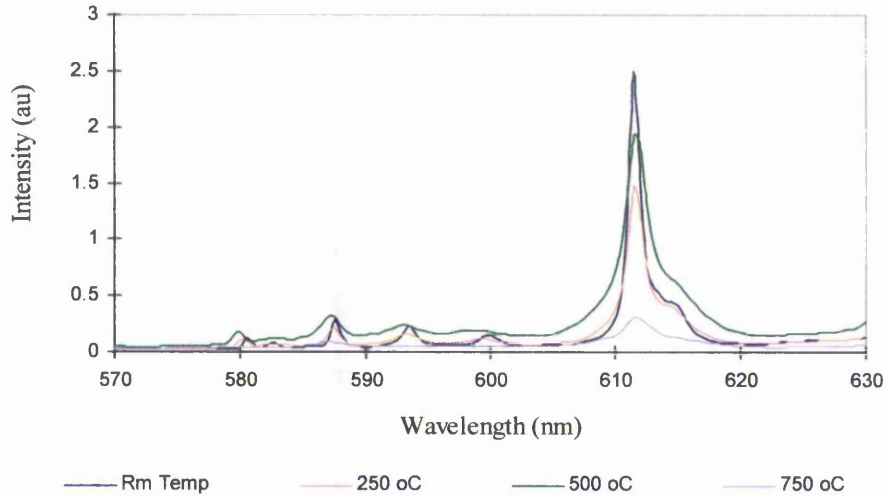
c) Steady-State intensity using the 325nm continuous HeCd laser

**Figure 4-6 Intensity Graphs of  $Y_2O_3:Eu$  Over Full Dopant Concentrations**

Relating this to decay constant measurements, intensity increases with dopant concentration as more photons are emitted due to the increase in dopant concentration. Overall intensity reaches a maximum when the phosphor has reached a quenching point; the point at which the higher energy levels are saturated with excited electrons. Beyond this point, the peak intensity increases due to the increase in the decay rate; the rate at which electrons return to the ground state. This leads to photons being released quicker, and so the intensity is stronger within a fixed time frame. Compared with the overall intensity, a decrease in intensity levels occurs after this quenching point due to an increase in the probability of non-radiative transitions. This results in the phosphor becoming less efficient in the photoluminescent process. These intensity measurements are taken at room temperature, but peak intensity emission is very important at higher temperatures when the signal-to-noise ratio becomes the dominating factor.

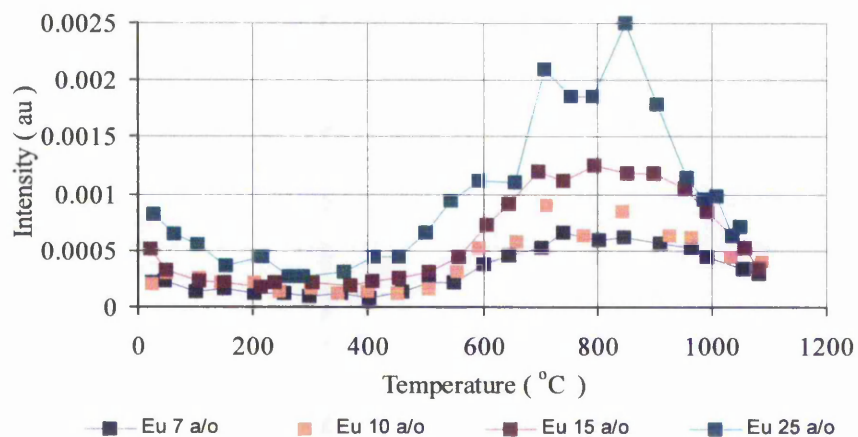
#### **4.2.2 Temperature Dependency**

The intensity emission at high temperatures is very important in order to have a high enough signal-to-noise ratio within the complete measurement system. Furthermore, it is vital to determine if any wavelength shift occurs. For a single dopant concentration, the spectra were measured at four temperatures. Figure 4-7 shows the  $Y_2O_3:Eu$  3.4a/o spectral variation against temperature and indicates once again, that no spectral shift occurs, whereas intensity changes. This is typical of other phosphors with different doping levels.



**Figure 4-7 Emission Spectra of  $Y_2O_3:Eu$  3.4a/o**

As a further measurement, the intensity of the 611 nm peak was collected and compared over the full temperature range. Figure 4-8 shows the peak intensity of four dopant concentrations up to a temperature of  $+1100^{\circ}C$ . Results show even though intensity does vary considerably, the relationship between dopancy and intensity remains constant over the full temperature range. Therefore, maximisation of intensity at room temperature by varying dopancy, will lead to maximisation at high temperature.



**Figure 4-8 611nm Peak Intensity of  $Y_2O_3:Eu$  over the full temperature range**

### **4.3 Decay and Rise Constant Characterisation**

As previously described in chapter 2, there are two temperature dependent characteristics within photoluminescence that can be utilised for the measurement of temperature. Previous investigations<sup>[36, 38, 39, 40]</sup> into  $Y_2O_3:Eu$  have shown a decay characteristic suitable for the temperature range 600 to 1200°C. The results presented here show two important new effects. Firstly, there is the demonstration by the author of a new temperature dependent rise constant characteristic which may be used for thermography. Specifically, for low dopant concentrations of  $Y_2O_3:Eu$ , the emission after pulsed excitation includes a rise period in intensity. Further investigation into this characteristic has shown low temperature dependency, therefore extending the temperature sensing range of the phosphor. And secondly, the temperature dependent characteristics of both decay and rise constants vary due to the dopant concentration.

#### **4.3.1 Derivation of Formulae**

As explained in section 2.1.4, when a phosphor is excited using a UV pulse, the photoluminescent emission intensity decays exponentially with time and the rate of decay can be defined by the following equation :-

$$I(t) = I_0 \text{Exp}\left(-\frac{t}{\tau}\right) \quad \text{Equation[11]}$$

where  $I(t)$  = Intensity at time= $t$ ,  $I_0$  = Intensity at time= $0$  and  $\tau$  = radiative decay-constant.

Relating this back to the energy diagram given in section 4.1.1, Equation 11 can be re-written in terms of the number of electrons excited to a specific energy level as:-

$$n_d(t) = n_o(t) \exp^{-\frac{(t - t_o)}{\tau_d}} \quad \text{Equation[12]}$$

where  $n_d(t)$  = the no. of electrons that have decayed to  ${}^7F_2$  ( $C_2$ );  $n_o(t)$  = the total no. of electrons at  ${}^5D_0$  ( $C_2$ );  $t_o$  = time delay due to triggering of oscilloscope and  $\tau_d$  = decay constant of electrons from  ${}^5D_0$  to  ${}^7F_2$  ( $C_2$ ).

However,  $n_o(t)$  is not fixed, but is the consequence of electrons excited directly into the  ${}^5D_0$  ( $C_2$ ) level together with those proceeding into this level from the slower transition from the  ${}^5D_1$  ( $C_{3i}$ ) site. Assuming a single exponential decay process,  $n_o(t)$  is then described as :

$$n_o(t) = n_{e2} + n_{c3i} \left[ 1 - \exp^{-\frac{(t - t_o)}{\tau_r}} \right] \quad \text{Equation[13]}$$

where  $n_{e2}$  = the no. of electrons directly excited to  ${}^5D_0$  ( $C_2$ );  $n_{c3i}$  = the no. electrons excited to  ${}^5D_1$  ( $C_{3i}$ ) and  $\tau_r$  = decay constant of electrons from  ${}^5D_1$  ( $C_{3i}$ ) to  ${}^5D_0$  ( $C_2$ ). Hence the equation describing the entire process is as follows :-

$$n_d(t) = n_{e2} \exp^{-\frac{(t - t_o)}{\tau_d}} + n_{c3i} \left[ 1 - \exp^{-\frac{(t - t_o)}{\tau_r}} \right] \exp^{-\frac{(t - t_o)}{\tau_d}} \quad \text{Equation[14]}$$

Shown schematically on Figure 4-9 are representations of the variation with time of both  $n_{e2}$  and  $n_{c3i}$  as described by this equation.

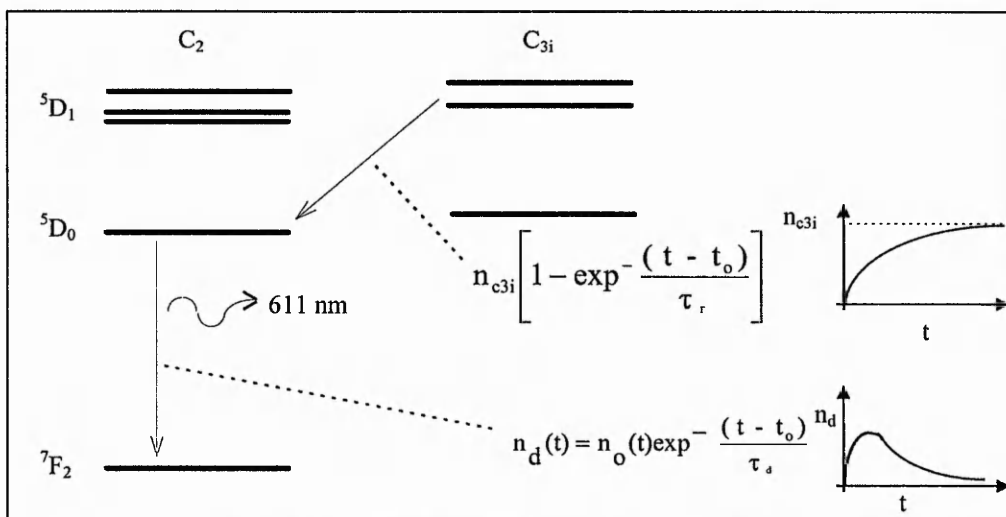
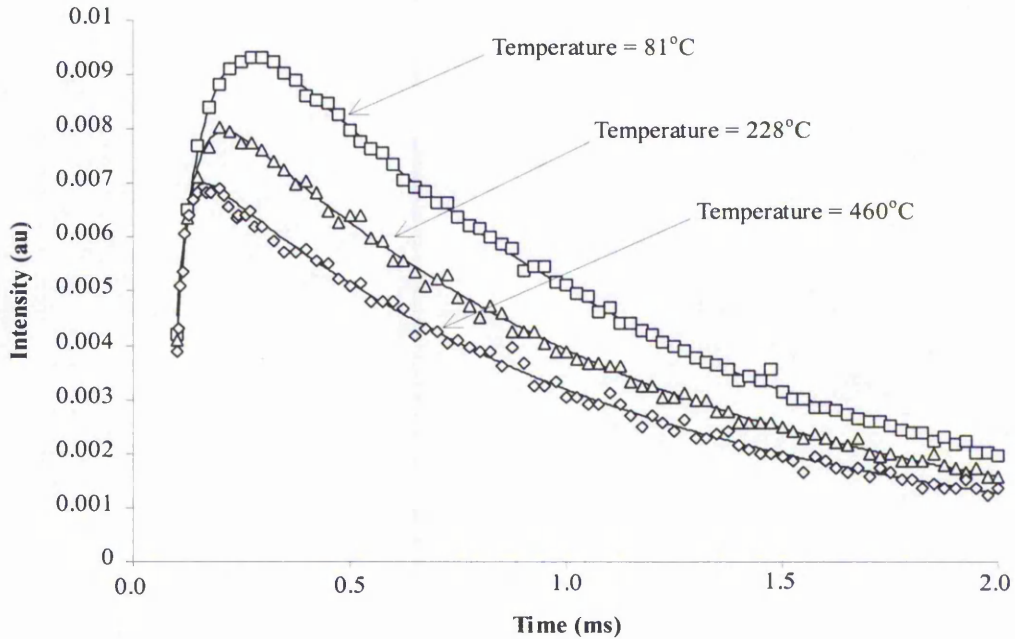


Figure 4-9 Schematic of electron detrapment within  $Y_2O_3:Eu$



Since luminescence is proportional to the number of electrons undergoing thermal detrapping, the above equation is used to calculate the observed rise- and decay- constants. Examples of such curve fits are shown in Figure 4-10, the emission observed from  $Y_2O_3:Eu$  3.4a/o at various temperatures.



**Figure 4-10 Observed Emission from  $Y_2O_3:Eu$  3.4 a/o and the Resultant Curve Fits**

For the examples in Figure 4-10, the curve fits obtained are shown as solid lines. The resultant parameters for each of the fits are summarised within Table 4-1.

Temperature (°C)	$n_{c2}$	$n_{c3i}$	Decay Constant $\tau_d$ (s)	Rise Constant $\tau_r$ (s)	Time Delay $t_0$ (s)
81	6.24E-03	8.80E-03	1.06E-03	1.55E-04	1.23E-04
228	4.74E-3	4.22E-03	1.03E-05	4.03E-05	1.09E-04
460	4.20E-03	3.22E-03	1.00E-03	2.02E-05	1.03E-04

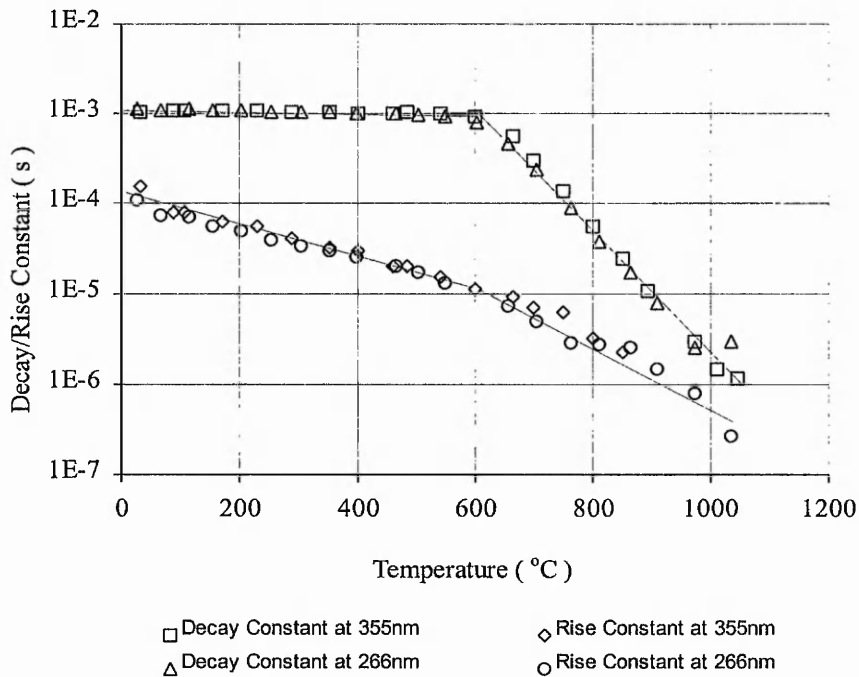
**Table 4-1 Calculated Parameters for the observed emission of  $Y_2O_3:Eu$  3.4 a/o**

It should be noted that the values provided for the number of electrons at each site is not an absolute value but is representative of the intensity which is proportional to the number of electrons undergoing the transitions. The rise and decay constants calculated from the observed emission show dependencies upon both temperature and dopancy.

### 4.3.2 Temperature Dependency

As previously mentioned, a phosphor has its temperature dependent range defined by the quenching temperature and quenching rate. Past results for  $Y_2O_3:Eu$  state the range extends from  $600^\circ C$  to  $1200^\circ C$ <sup>[35,36,38,39,42]</sup>. For this investigation, each sample was characterised at two available excitation wavelengths of 355nm and 266nm. Below Figure 4-11 shows the decay and rise constant characteristics of the low dopant concentration of  $Y_2O_3:Eu$  3.4 a/o. Results obtained indicate that a change in excitation wavelength does not vary the temperature dependent characteristics, with a quenching temperature of  $575^\circ C$  and a quenching rate of  $17mC^{-1}$  for the decay characteristics. (As will be shown later, the characteristics vary with dopant concentration).

More importantly, the rise constant characteristics show two differences from the decay constant. Firstly, there is the temperature range,  $25^\circ C$  to  $850^\circ C$ , over which the rise constant characteristics are variable. In contrast, the decay constant is invariable until the quenching temperature of  $575^\circ C$  is reached. Other thermographic phosphors with decay constant characteristics are currently utilised for lower temperature ranges. Secondly, the rise constant is an order of magnitude faster than that of the decay. This allows for much faster rotating systems to be analysed where the collection window is too small for the enough data to be collected for utilising the decay constant.



**Figure 4-11 Rise and Decay Characteristics of  $Y_2O_3:Eu$  3.4 a/o**

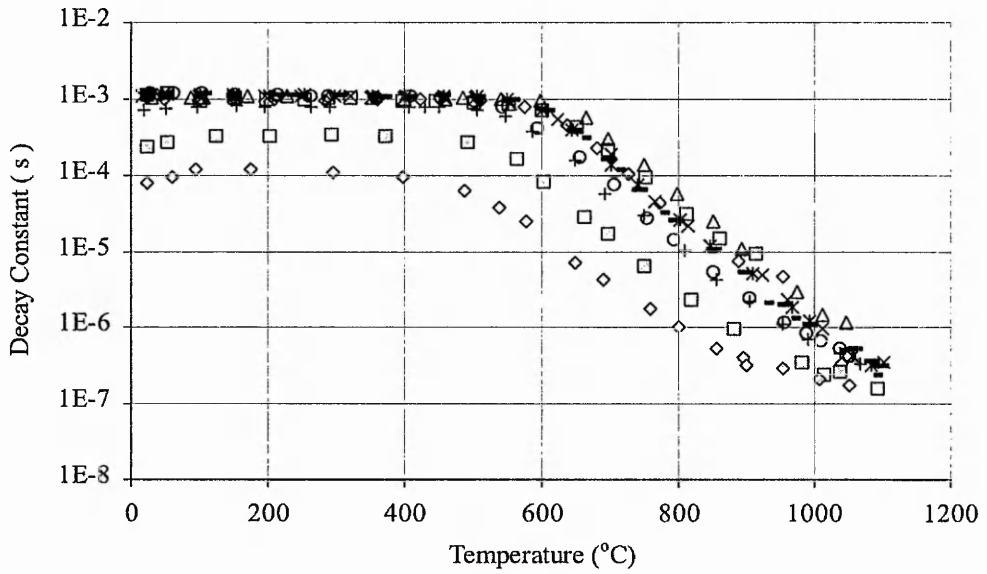
In some applications, both decay and rise constants can be utilised for the measurement of temperature, with rise-constant measurements used for 25°C to 800°C and decay constant for the range 600°C to 1200°C. This allows for a wider temperature sensing range to be investigated while utilising the properties of a single phosphor.

### 4.3.3 Dopant Dependency

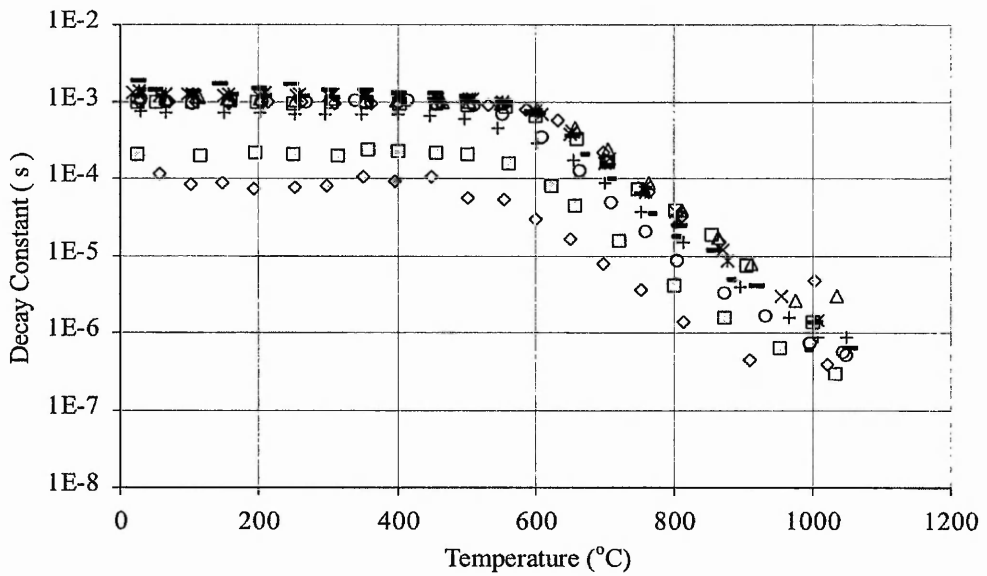
Earlier in this chapter, the importance of maximisation of intensity was discussed and it was shown that this can be achieved via the optimisation of dopancy. At the same time, temperature dependent characteristics must be maintained. Hence, full characterisation of  $Y_2O_3:Eu$  was carried out over the dopant concentration range of 0.5 - 75 a/o.

Firstly, for decay constant characterisation, Figure 4-12 show the decay-constant characteristics of  $Y_2O_3:Eu$  at both excitation wavelengths with varying dopancy. Results indicate that the consistency is maintained upto a dopancy of 25a/o, with a quenching

temperature at 575°C and the quenching rate of 17mC<sup>-1</sup>. Above this dopancy level, the quenching temperature decreases with an increasing dopancy.



(a)



(b)

- |           |          |           |          |          |          |
|-----------|----------|-----------|----------|----------|----------|
| □ 0.5 a/o | ◇ 1 a/o  | △ 3.4 a/o | × 5 a/o  | × 7 a/o  | ■ 10 a/o |
| — 15 a/o  | ○ 25 a/o | + 35 a/o  | □ 50 a/o | ◇ 75 a/o |          |

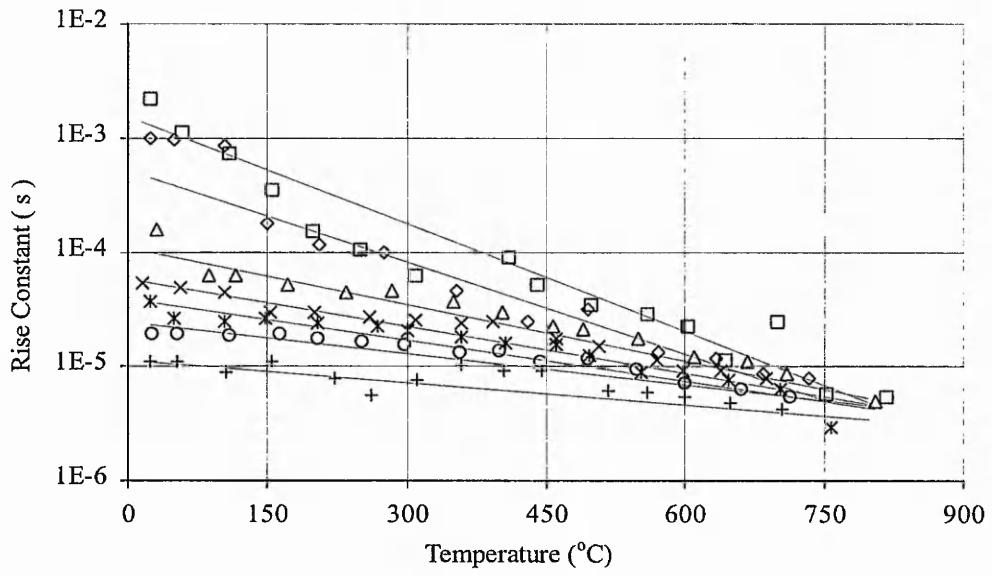
**Figure 4-12 Decay Constant Characteristics of Y<sub>2</sub>O<sub>3</sub>:Eu**

**a) 355nm excitation, and b) 266nm excitation**

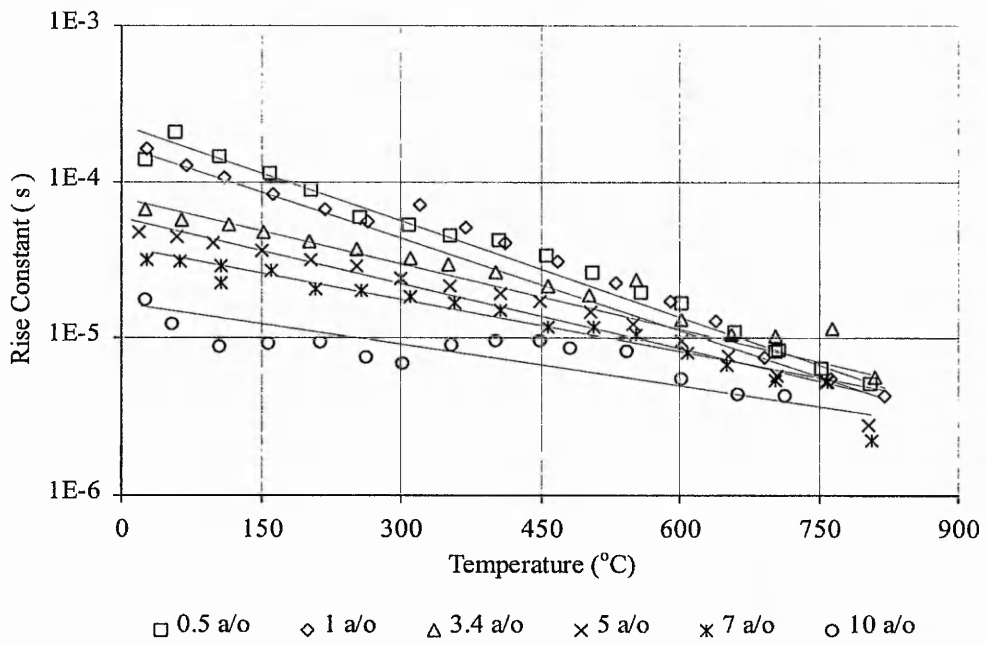
Due to an increasing dopancy, the crystal structure becomes more and more populated with pure  $\text{Eu}_2\text{O}_3$ , and less and less with  $C_2$  and  $C_{3i}$  sites. Therefore, the Eu atoms are becoming dominant over the yttrium atoms, and so become closer together. This causes changes in the energy levels, and the probability of non-radiative decay from those levels. The result is a decrease in the decay constant .

With rise constant characteristics the dependency on dopant concentration is immediate. The temperature range over which the rise characteristic exists is  $25^\circ\text{C}$  to  $800^\circ\text{C}$ . However, results show a decrease in the rise constant as dopancy increases. This continues upto a concentration  $15\text{a/o}$ , beyond which no detectable rise in emission is observed, even at room temperature.

As with the variance of the decay characteristics due to the increase in the dopancy of europium, the physical distance between the neighbouring sites of symmetry becomes shorter. Therefore, the probability of the  $C_{3i}$  to  $C_2$  transition increases, resulting in a reduction of the rise constant. Eventually, when the dopancy of europium reaches a high level, the distance has been reduced to such an extent that the transition between the sites of symmetry becomes undetectable. Hence, at dopancy levels of  $15\text{a/o}$ , no rise time characteristic were detected.



(a)



(b)

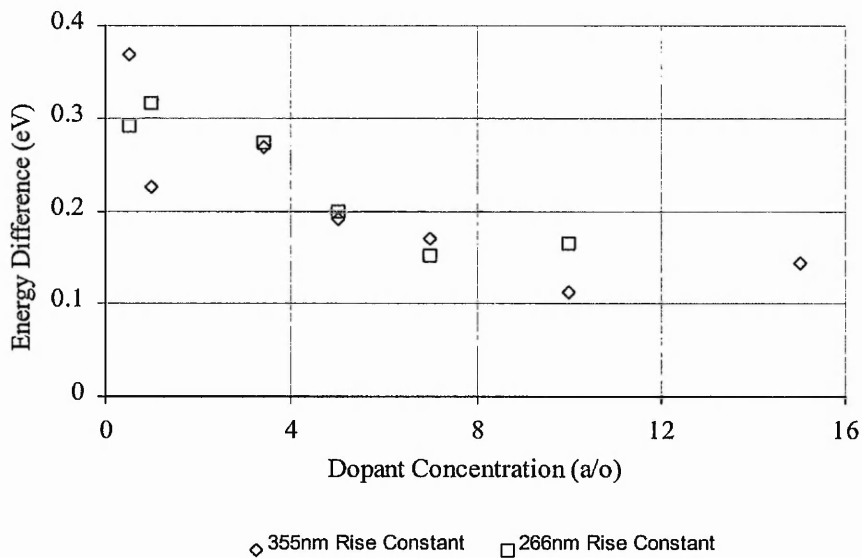
**Figure 4-13 Rise Constant Characteristics of  $Y_2O_3:Eu$**

**(a) 355nm excitation, and (b) 266nm excitation**

As shown, the rise constant,  $\tau_r$ , decreases with increasing temperature and can be described by a single exponential as follows:-

$$\tau_r(T) = \tau_0^r \exp\left(\frac{\Delta E}{kT}\right) \quad \text{Equation[15]}$$

where  $\tau_0^r$  = Initial Rise Constant at temp 0K,  $\Delta E$  = activation energy of the transition,  $k$  = Boltzmann's Constant and  $T$  = ambient temperature. By plotting the natural log of  $\tau_r(T)$  against  $1/T$ , the resultant straight line obtained has a gradient of  $\Delta E/k$ , and so we can calculate the energy difference of the transition which provides the rise constant characteristic. Figure 4-14 shows the calculated energy difference of the rise characteristic and its variance due to dopancy. Past work by Heber et al<sup>[70]</sup>, have indicated that the energy difference between the  $^5D_1$  ( $C_{3i}$  site) and the  $^5D_0$  ( $C_2$  site) is 0.228eV. These were results obtained from a single dopant concentration of 5.0 mol% Eu.



**Figure 4-14 Energy Difference Calculations for the  $^5D_1(C_{3i})$  to  $^5D_0(C_2)$  Transition**

The relationship between the calculated energy difference and the dopancy level of europium is a result of the physical distance between the neighbouring sites. Crystal field

effects on the energy levels of the atoms will vary depending on the proximity of the neighbouring atoms. The closer together two atoms become, the greater the effect each will have on the other's energy levels. It therefore follows, as shown within Figure 4-14, as the dopancy level of europium is increased, the energy difference between the  $C_{3i}$  and  $C_2$  sites of symmetry will decrease.

#### **4.4 Summary**

Complete characterisation of  $Y_2O_3:Eu$  has been examined. The findings of this investigation are summarised in terms of emission spectra characterisation, temperature dependent characterisation, discovery of a new temperature dependent characteristic and dopancy dependency of these characteristics.

The emission spectra of  $Y_2O_3:Eu$  has shown the peak emission wavelength of 611nm, is independent on both temperature and the dopancy of europium. Spectra at temperatures upto 750°C were measured, with results indicating a variance in emission intensity levels but without the occurrence of a shift in peak wavelength. This facilitates for the removal of the spectrometer from the detection system, which is replaced with the use of filters specific to the wavelength. The resultant advantage is that the detector is positioned closer to the source thereby reducing loss of the signal. Intensity comparison of the detected 611nm peak wavelength at both excitation wavelengths show maximum intensity to occur at a dopancy of 25 a/o for 355nm and 10 to 15a/o for 266nm.

The conventional temperature dependent characteristic of the decay constant was investigated, producing results which consolidated with previous work. The additional information provided by this investigation is the variation of the characteristic with respect to the dopancy of europium. The decay constant characteristics remain constant upto dopancy levels of 25a/o, from which point there is a decrease. These characteristics are independent of the excitation wavelengths investigated.



The discovery of the new rise constant temperature characteristic provided a innovative aspect within this investigation. The initial rise in intensity with respect to time has provided a low temperature variant, ranging from room temperature upto 800°C, and was found to be dependent upon dopancy levels upto 10 a/o. This characteristic is due to the transition from  $C_{3i}$  to  $C_2$  sites of symmetry and is confirmed by the calculation of the energy difference between the two sites.

It is concluded,  $Y_2O_3:Eu$  has the ability to be utilised as a thermographic phosphor whose temperature sensing capabilities range from 25°C to 1100°C via use of both rise and decay constant characteristics. The dopancy dependency of these characteristics allows for optimisation of emission intensity levels and sensitivity to temperature changes for specific field requirements. Importantly, the phosphor has shown the potential for use as a thermographic phosphor within the field of temperature sensing of turbine blades.

## 5. Terbium Doped Yttrium Aluminium/Gallium Oxide

### 5.1 Background

Due to the expansion of the television industry, the improvement in efficiency for green emitting phosphors has been continuously under investigation. For example, to produce the high illumination levels on the screen for projection CRTs, a much higher current density is required. This leads to high temperatures being reached on the screens which reduces the phosphor efficiency. Therefore, a number of green emitting phosphors of oxide based were investigated including  $Y_3Al_5O_{12}:Tb$  (YAG:Tb),  $InBO_3:Tb$ ,  $Y_2SiO_5:Tb$ ,  $LaOBr:Tb$  and  $Gd_2O_2S:Tb$ <sup>[76]</sup>. Of these phosphors, YAG:Tb remained the most efficient at high temperatures. Sulphide based phosphors have also been investigated, but show a much greater reduction in intensity compared to the oxide based phosphors as a result of the temperature increase.

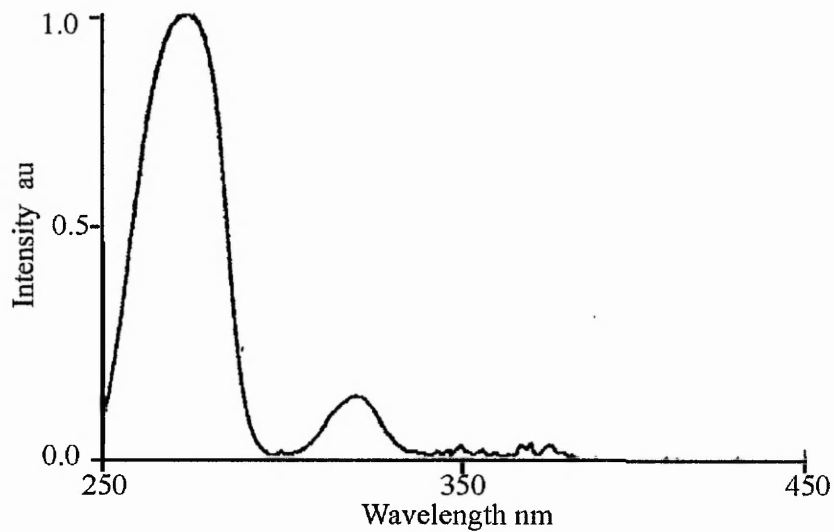
To improve the brightness and resolution of projection CRTs in order to meet customer requirements, the efficiency of the phosphor required improvement. Ohne and Abe<sup>[77]</sup> reported that Citchley and Lunt increased the brightness of YAG:Tb phosphor by replacing a proportion of the Aluminium with Gallium, thus producing the phosphor Yttrium Aluminium/Gallium Oxide ( $Y_3(Al/Ga)_5O_{12}$  -YAGaG). Ohne and Abe extended this study further by investigating the properties of this phosphor while varying the Al-to-Ga ratio<sup>[77]</sup>. Results showed that the brightness was highest between ratios of three-to-two and two-to-three at several Tb concentrations.

As discussed in section 2.3, YAG:Tb showed suitable characteristics for potential use as a thermographic phosphor within gas turbine engines. At extreme temperatures, a high signal-to-noise ratio is required; therefore, the intensity emission of the phosphor must be maximised. Due to the improvement of emission intensity reported by Ohne and Abe<sup>[77]</sup>, Terbium doped Yttrium Aluminium/Gallium Oxide (YAGaG:Tb) was investigated by the

author as a potential thermographic phosphor. These phosphor samples were provided by Greenwich University, who had investigated the cathodoluminescent properties of the phosphor with maximum intensity being achieved at a ratio of 1:1 (Aluminium : Gallium). As before, dopancy dependency was investigated with the terbium concentration varying from 1 to 50 atomic percent (a/o).

### 5.1.1 Crystal Structure

As with Yttrium Oxide, Yttrium Aluminium Garnet ( $Y_3Al_5O_{12}$  - YAG), is a cubic material which has the garnet structure<sup>[78,79]</sup>. In the host YAGaG, the gallium atom replaces a percentage of the aluminium atoms. To produce the green emitting phosphor, the host is doped with terbium, which replaces the yttrium atoms. Shown in Figure 5-1 is the excitation spectra of YAGaG:Tb<sup>[80]</sup>, provided by Rolls-Royce Plc, which exhibits two broad excitation regions centred at 325nm and 260nm. This would imply that a greater intensity emission is achievable by utilising the 266nm rather than the 355nm emission of the Nd:YAG pulse laser.



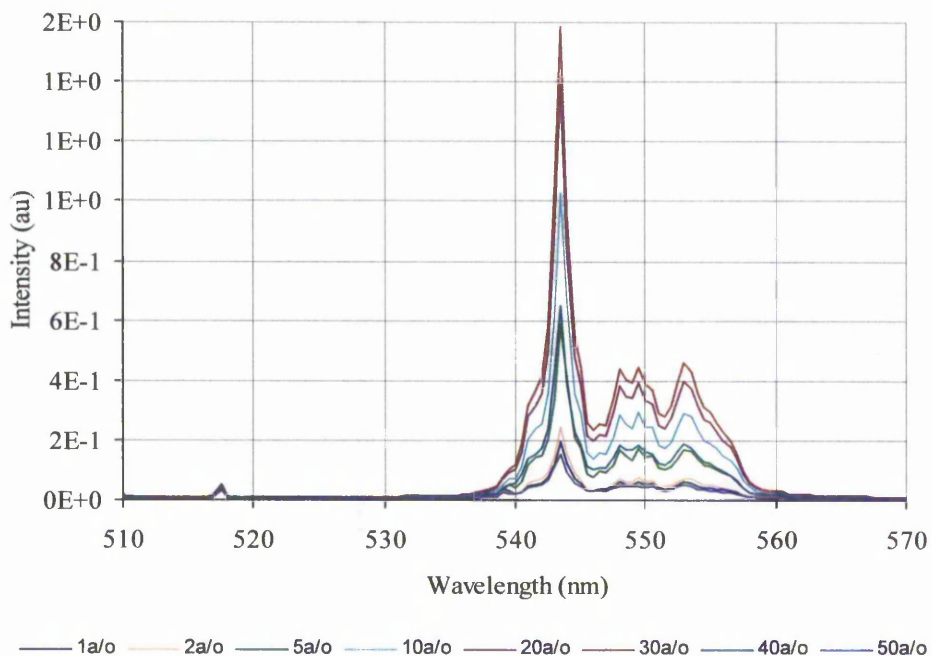
**Figure 5-1 Excitation Spectrum of YAGaG:Tb**

## 5.2 Emission Spectra

Before the full temperature dependence characteristics were investigated, the emission spectra was measured to determine the fluorescent spectral response of the phosphor. Previous investigations<sup>[46,77]</sup> have shown YAGaG:Tb to have a major spectral line at 544nm within the green region of the visible spectrum. Hence, the intensity of this spectral line was investigated for both dopant concentration and temperature dependency.

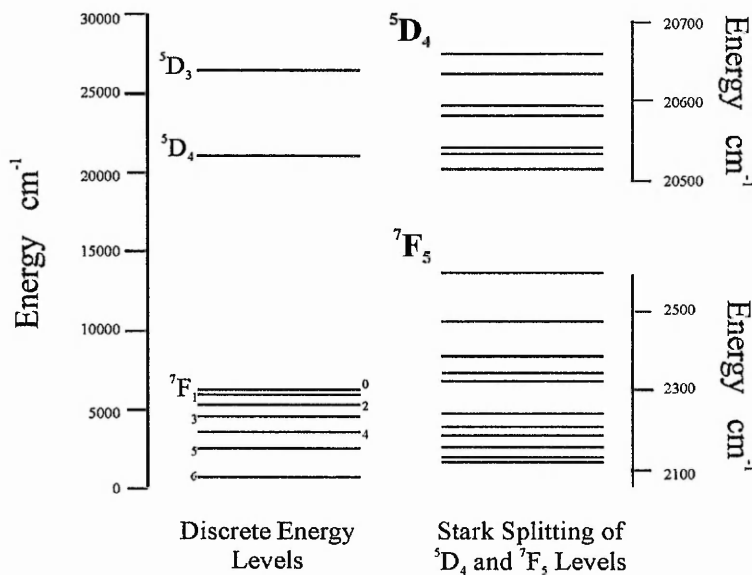
### 5.2.1 Dopant Intensity Dependency

Figure 5-2 shows the measured emission spectra of YAGaG:Tb for the full range of dopant concentrations investigated taken at room temperature. Results show that the major spectral line of 544nm does not shift with dopant concentration and remains dominant over the weaker lines. Maximisation of the intensity of the 544nm line is achieved with a dopancy level of 20 to 30a/o.



**Figure 5-2 Room Temperature Emission Spectra of YAGaG:Tb**

These spectra were obtained using the HeCd 325nm CW laser and a spectrometer. Results show a group of spectral lines exist between 540-560nm, which is referred to as a spectral group and is due to the Stark effect<sup>[81]</sup>. The Tb ion's discrete energy levels are split into groups of finely spaced energy levels due to the crystal field effect of the host lattice. The spectral group shown is a result of electron transitions occurring between the discrete levels of  $^5D_4$  and  $^7F_5$  levels of the Tb ion. Figure 5-3 shows the energy levels of an isolated Tb ion and the Stark Splitting effect of discrete energy levels  $^5D_4$  and  $^7F_5$ <sup>[81]</sup>.

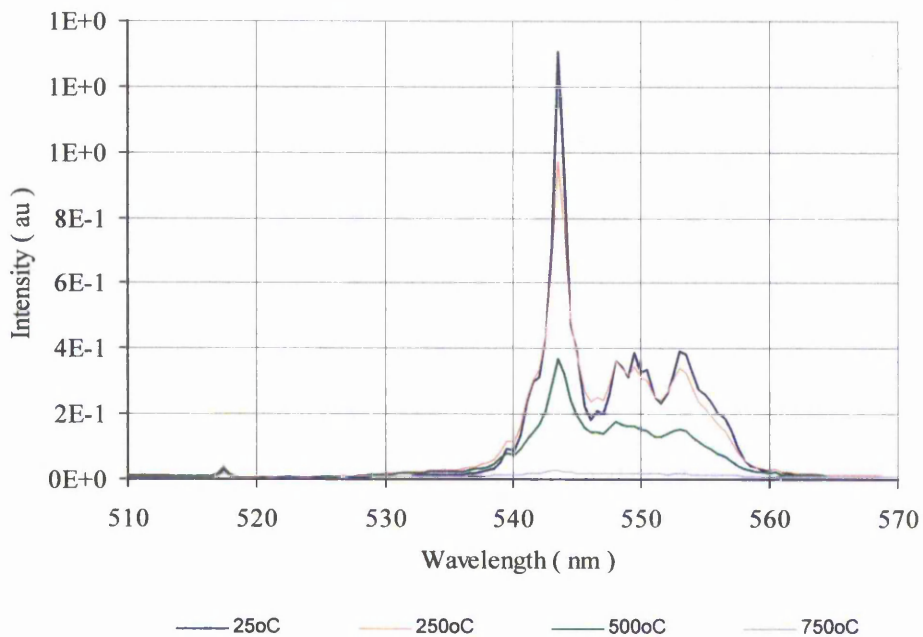


**Figure 5-3 Schematic of Energy Levels of Tb Ion showing the Stark Splitting of  $^5D_4$  and  $^7F_5$  Energy Levels**

As shown in the energy diagram, the maximum and minimum energy difference attainable is  $\sim 18600$  and  $17900 \text{ cm}^{-1}$  respectively. The  $^5D_4$  energy level splits into seven sub-levels, and the  $^7F_5$  consists of eleven. Therefore, there are seventy-seven possible transitions between these subsequent sub-levels. In terms of wavelength, this represents a spectrum spread from 538-557 nm. In the presented experiments, emission spectra was measured with a resolution of 1nm and so these individual spectral lines are indistinguishable.

### 5.2.2 Temperature Dependency

The emission spectra were measured at various temperatures. Results shown in Figure 5-4 indicate that no spectral shifts occur due to increasing temperature. More importantly, the intensity of the 544nm peak shows a steady decrease with rising temperature. This reduction of intensity will be problematic at high temperatures, leading to a lower signal-to-noise ratio and so a higher measurement error.



**Figure 5-4 Emission Spectra of YAGaG:Tb 20a/o At Various Temperatures**

As discussed in the previous chapter, maximisation of the intensity is vital for the phosphor to be successful at extreme temperatures. Further examination of intensity with respect to the excitation wavelength and the dopancy was required to achieve this maximisation. These tests were carried out along with the other phosphor samples under investigation, and so results are presented later in section 6.2. Here, both phosphors are compared for maximisation of intensity at both excitation wavelengths available from the Nd:YAG laser.

### **5.3 Temperature Dependence Characterisation**

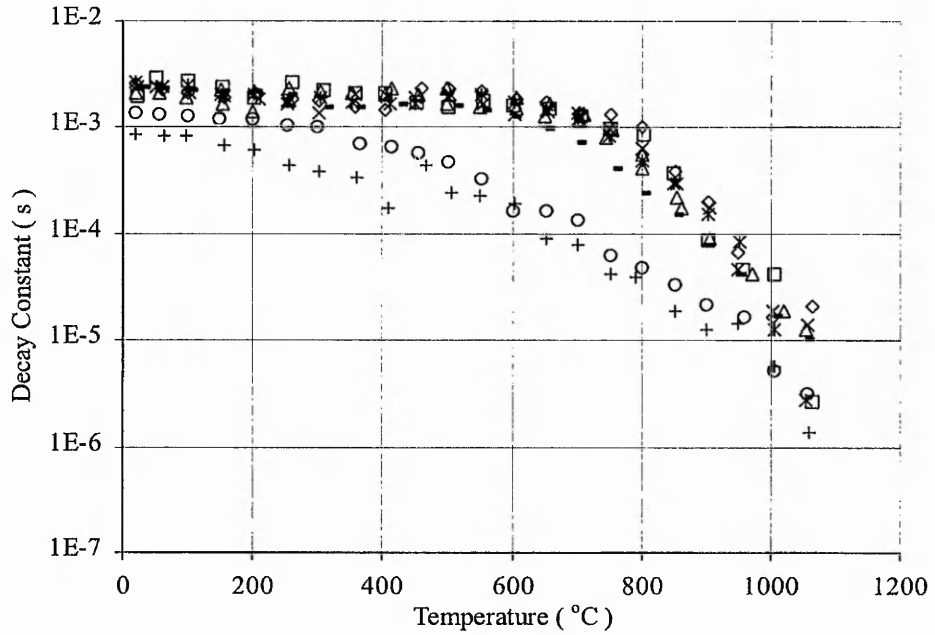
A previous investigation<sup>[46]</sup> into the temperature dependence of YAGaG:Tb presented data for the decay constant characteristics with a temperature range of 660°C to 1100°C using a single exponential fitting routine. Terbium emits a peak wavelength at 544nm as shown in section 5.2, and the decay constant characteristics were measured at this wavelength. The filters used within the measurement system were a cut-on filter at 520nm and a narrow bandpass filter centred at 545nm with a 10nm bandwidth. Both filters were purchased from Ealing Optics. As detailed in Chapter 3, all measurements were carried out on powder pellet samples. Calculation of the decay constant was initially made using the single exponential equation within the LabVIEW software.

And compared with  $Y_2O_3:Eu$ , two differences exist with the temperature dependent characteristics. Firstly, at high temperatures the single exponential curve fitting routine was no longer providing accurate fits (see section 5.4), leading to unstable decay characteristics. Further examination of the photoluminescence decay characteristics was necessary and the results indicated these characteristics were actually of a double exponential nature. And secondly, a rise characteristic only existed for low dopant concentrations at 266nm excitation. Therefore, both the rise and decay characterisation of YAGaG:Tb required all data to be investigated using both single and double exponential curve fitting routines. The software utilised for this characterisation of data was Jandel Scientific TableCurve.

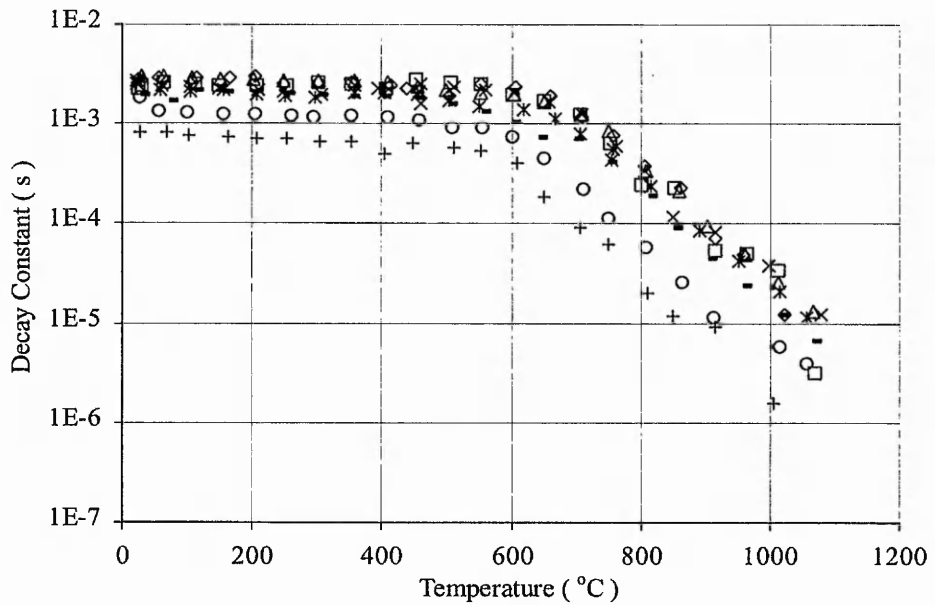
#### **5.3.1 Single Exponential Method**

##### **Decay Constant Characterisation**

Using the single exponential function as described in section 2.1.3.2, the temperature dependent decay constant characteristics at both excitation wavelengths, 355nm and 266nm, were measured and the results are presented in Figure 5-5.



(a)



(b)

□ 1a/o    ◇ 2a/o    △ 5a/o    × 10a/o    \* 20a/o    - 30a/o    ○ 40a/o    + 50a/o

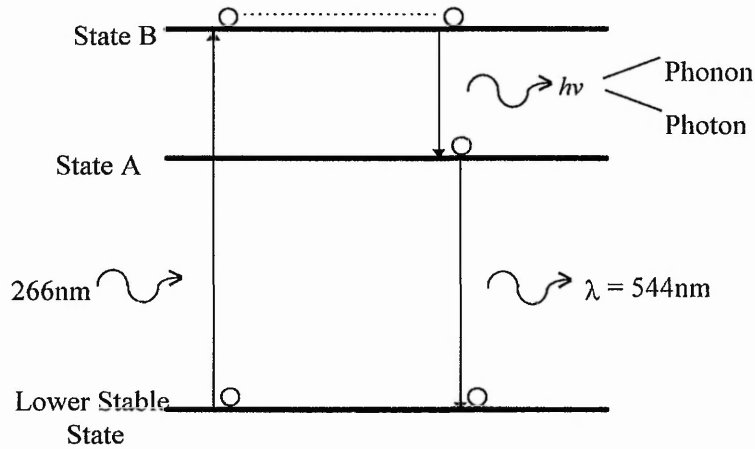
**Figure 5-5 Decay Constant Characterisation of YAGaG:Tb Using a Single Exponential Curve Fit at (a) 355nm and (b) 266nm Excitation**



For 355nm excitation, the decay constant characteristics show that low dopancy levels have a quenching temperature of 700°C with a decay constant of 1.33ms and a quenching rate of  $13.2\text{mC}^{-1}$ . This is consistent upto a dopancy level of 20-30 a/o. At dopancy levels of 40 and 50 a/o the decay constant varies from room temperature, but with a significant change occurring at 400°C. For 266nm excitation, at dopancy levels below 30a/o the quenching temperature is 650°C and has a quenching rate of  $12.1\text{mC}^{-1}$ , both of which are slightly lower than the characteristics obtained with 355nm excitation. Above a dopancy level of 30a/o, the quenching temperature starts to decrease. The decay constant remains independent to temperature upto this point followed by a steady exponential decrease with temperature. Comparison between the 355nm and 266nm characterisation shows that 266nm excitation produces a decay constant whose characteristics are more stable and consistent with dopancy.

#### **Rise Constant Characterisation**

The rise characteristic of YAGaG:Tb differed from that of  $\text{Y}_2\text{O}_3\text{:Eu}$ , in that it only occurred at an excitation wavelength of 266nm and for low dopancy levels. It is assumed that the characteristic is a result of a transition between two energy levels internally within a single atom rather than a transition between neighbouring sites of symmetry, as with  $\text{Y}_2\text{O}_3\text{:Eu}$ . Figure 5-6 shows the possible undergoing transitions and energy levels for such a mechanism. For this explanation, the higher energy level from which the resultant rise characteristic occurs is referred to as State B, and the 544nm emission is a result of the electron transition from State A to the lower stable energy level. When excited with 266nm, a percentage of the electrons are excited into the higher State B. These electrons will relax to State A exponentially, therefore increasing the number of electrons at this energy level. Electrons from State A are also undergoing the exponential relaxation process, resulting in the emission at 544nm.



**Figure 5-6 Schematic of a Single Site Energy Level Diagram to Illustrate the Rise Time Mechanism of the Terbium Atom**

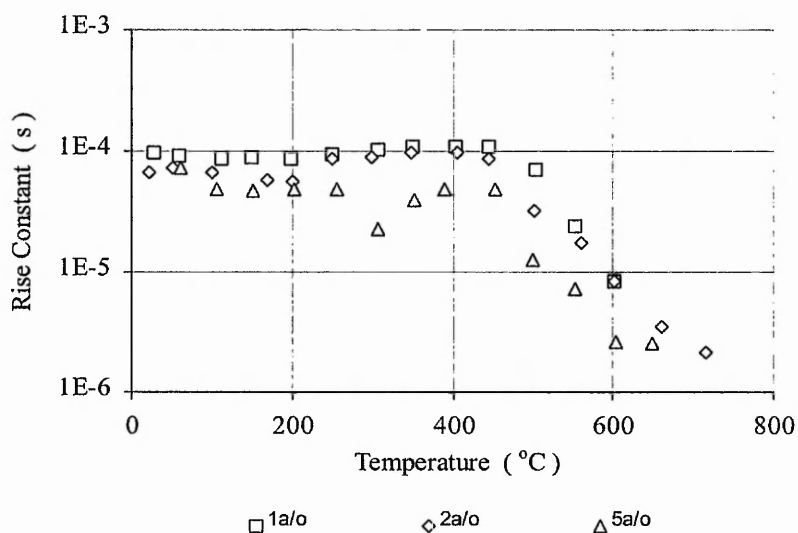
Assuming each of these transitions occur at a single exponential rate, the emission of 544nm is a combination of the two processes. It should be noted that the resultant equation is the same as that derived for the rise characteristic of  $Y_2O_3:Eu$ , but the difference is that the energy levels involved are both from the same terbium atom and not from neighbouring sites of symmetry. The resultant equation in terms of the number of electrons undergoing the process is :-

$$n_{tot}(t) = n_a \exp\left(\frac{t-t_0}{\tau_d}\right) + n_b \left(1 - \exp\left(\frac{t-t_0}{\tau_r}\right)\right) \exp\left(\frac{t-t_0}{\tau_d}\right) \quad \text{Equation[16]}$$

where  $n_{tot}(t)$  is the total number of electrons undergoing the 544nm transition as a function of time,  $n_a$  is the number directly excited into State A,  $n_b$  is the number of electrons directly excited into State B,  $\tau_d$  is decay constant of electrons from State A to the lower stable state,  $\tau_r$  is the decay constant of electrons from State B to State A, and  $t_0$  is the trigger delay of the oscilloscope.

As the number of electrons undergoing the transitions is directly proportional to the number of photons released, the above equation can be used to represent the fluorescent signal.

Figure 5-7 shows the rise constant characteristics of YAGaG:Tb. For a dopancy level of 1a/o, the rise characteristic remains constant upto a quenching temperature of 450°C, from which point it decreases exponentially with a quenching rate of  $13.6\text{mC}^{-1}$ . Also, dopancy dependence is shown with the rise constant decreasing with an increasing dopancy level upto 10a/o, where no rise characteristics exist.

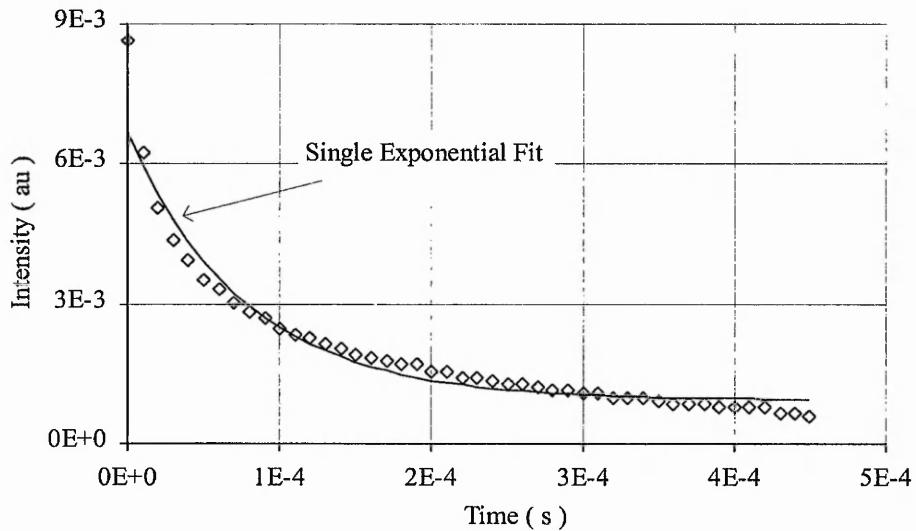


**Figure 5-7 Rise Constant Characteristics of YAGaG:Tb at 266nm Excitation**

### 5.3.2 Double Exponential Characteristics

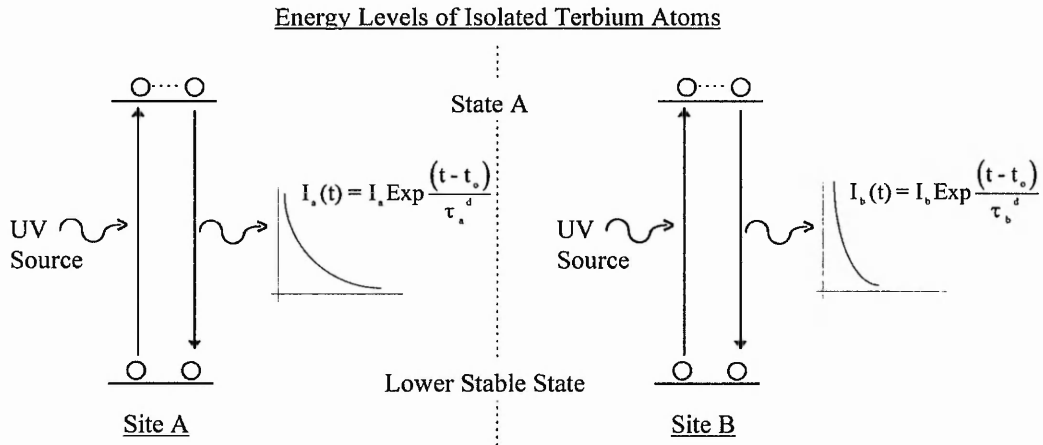
#### Decay Constant Characterisation

For YAGaG:Tb, the single exponential curve fits were not as accurate as those obtained for the calculation of  $\text{Y}_2\text{O}_3:\text{Eu}$  characteristics, especially at high temperatures. Figure 5-8 is the photoluminescent emission of YAGaG:Tb 5a/o at a temperature of 855°C. This clearly illustrates a single exponential fit is not suitable for the characteristics of YAGaG:Tb. As the temperature was increased, it became more apparent that the photoluminescent decay was of a double exponential nature. Therefore, the captured data required re-assessing, but with a double exponential curve fitting routine.



**Figure 5-8 Illustration of a Single Exponential Fit of the Photoluminescent from YAGaG:Tb at a Temperature of 855°C**

The reason for the double exponential characteristic is due to the addition of gallium to the compound. As discussed in the Crystal Structure section of this chapter, the gallium atom replaces the aluminium atom in YAGaG systems. As an example, with the terbium atom replacing the yttrium atom, its neighbouring cation will be either an aluminium or a gallium atom. As a result, the energy levels and probability of permissible transitions within the terbium atom are externally effected by these neighbouring atoms. This produces two possibilities of the resultant 544nm emission, whose probabilities of occurrence are independent of each other.

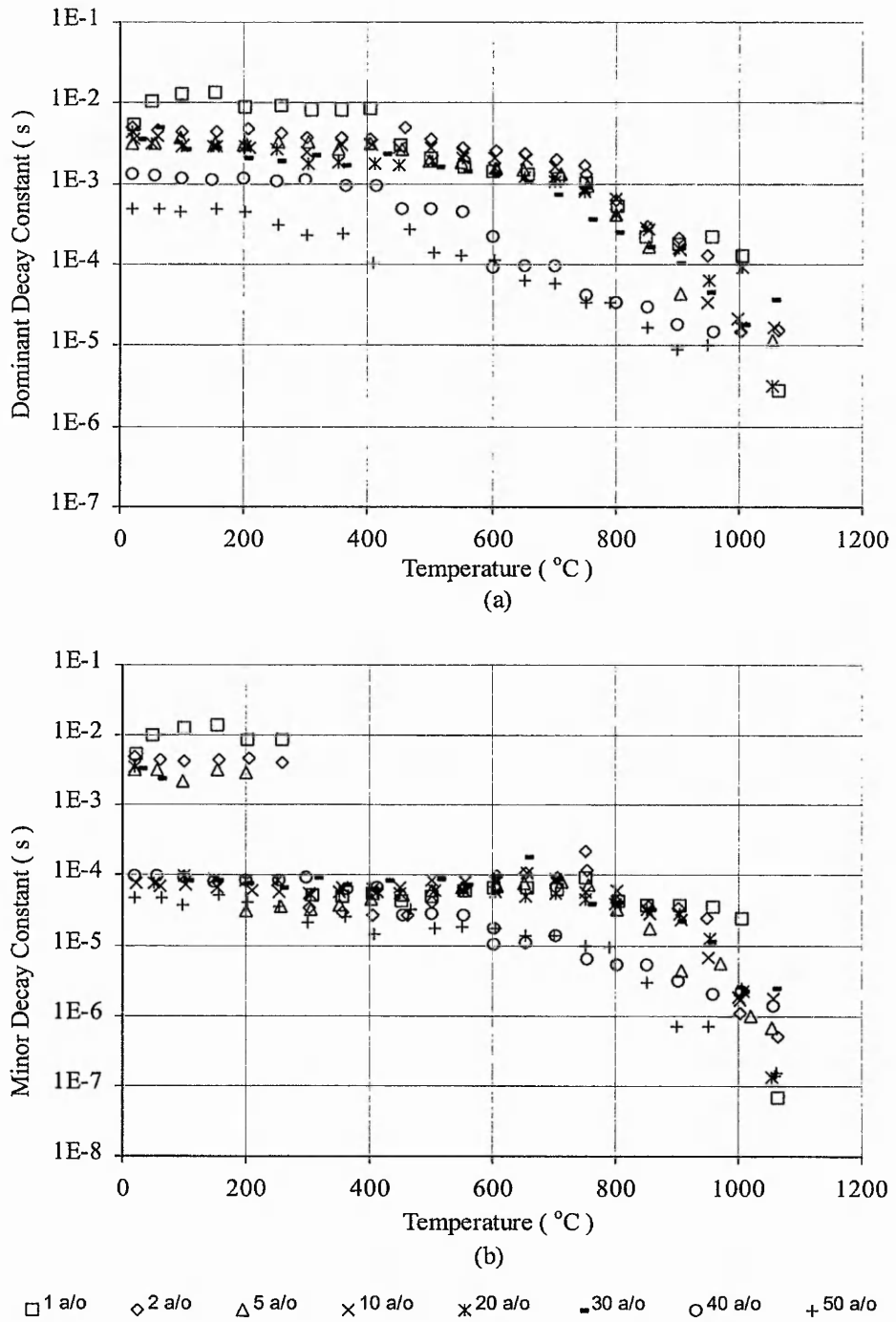


**Figure 5-9 An Illustration of the 544nm Transitions of Isolated Terbium Atoms**

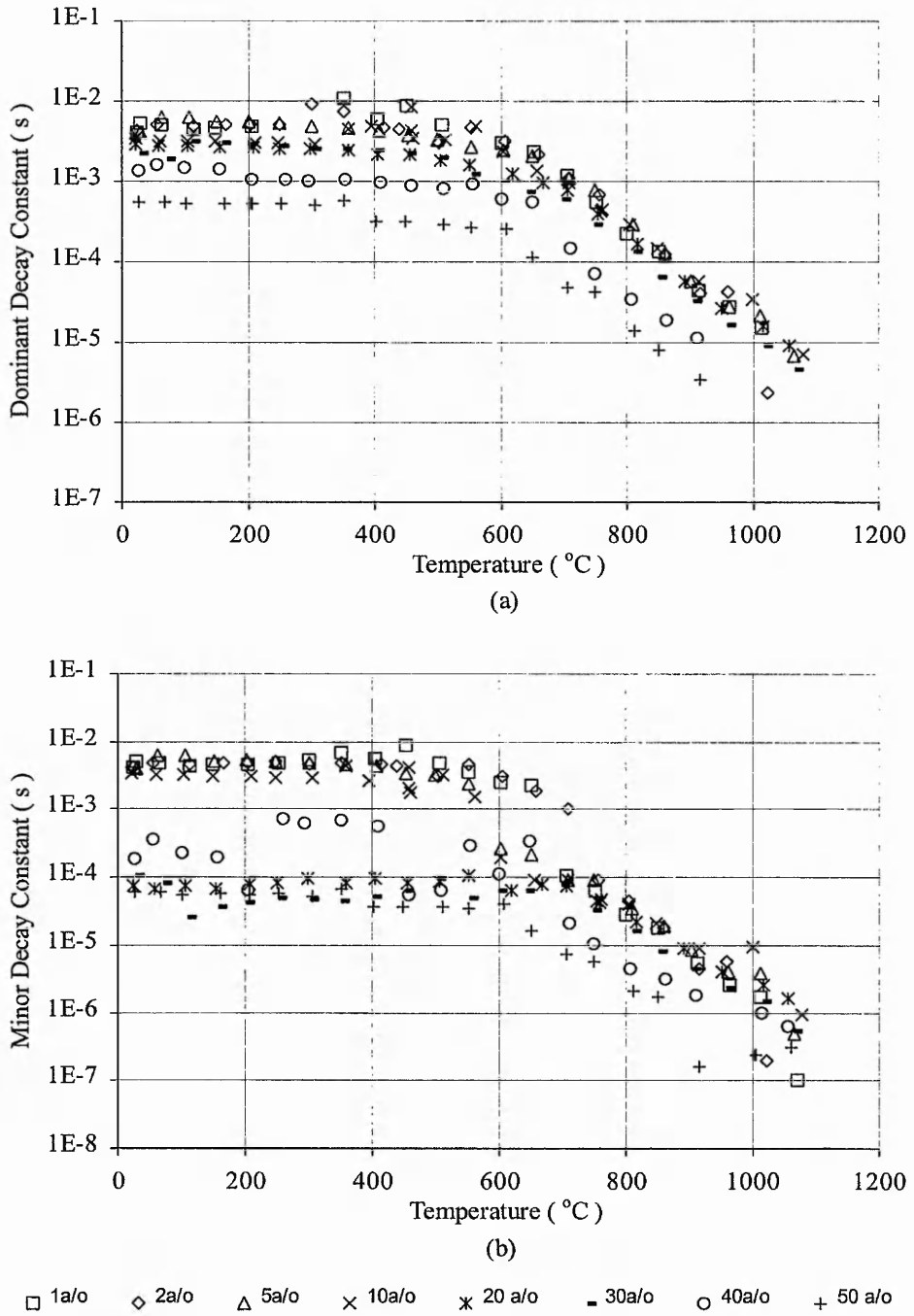
Figure 5-9 is a representation of the two possibilities of the 544nm emission from the terbium atoms. As the detector will collect both emissions, the resultant double exponential characterisation is a simple addition of both transitions. The equation utilised for the calculation of both decay constants is:

$$I_{\text{tot}}(t) = I_a \text{Exp} \frac{(t-t_0)}{\tau_a^d} + I_b \text{Exp} \frac{(t-t_0)}{\tau_b^d} + N \quad \text{Equation[17]}$$

where  $I_{\text{tot}}(t)$  is the total emission as a function of time,  $I_a$  is the intensity due to the transition within site A,  $\tau_a^d$  is the decay constant of site A,  $I_b$  is the intensity due to the transition within site B,  $\tau_b^d$  is the decay constant of site B,  $t_0$  is the triggering delay of the oscilloscope, and  $N$  is background noise level. This results in two decay constants, which both show temperature dependence as presented in Figure 5-10 and Figure 5-11.



**Figure 5-10 Double Exponential Characterisation of YAGaG:Tb Using 355nm Excitation**



**Figure 5-11 Double Exponential Characteristics of YAGaG:Tb Using 266nm Excitation**

Unfortunately, the characteristics measured show the dominance of one decay constant over the other. At low temperatures, the dominant decay constant masks the characteristic of the minor constant. This results in the miscalculation of the minor decay constant, as illustrated in Figure 5-8 and 5-9, with both figures showing the minor constant to have a value equalling that of the dominant constant. As the temperature increases, the double exponential characteristic of the photoluminescence becomes more apparent. Eventually, sufficient data to represent the minor constant is detected, allowing for its calculation. This occurs at 250°C for 355nm excitation and 600°C for 266nm excitation.

In terms of their temperature characteristics, the dominant constant has a quenching temperature of 700°C with a quenching rate of  $11.9\text{mC}^{-1}$  for 355nm excitation. At 266nm, the quenching temperature has reduced to 600°C with a quenching rate of  $12.0\text{mC}^{-1}$ . For the weaker decay constant, although the quenching temperature is 750°C for both 355nm and 266nm excitation, the quenching rates are  $14.8\text{mC}^{-1}$  and  $13.9\text{mC}^{-1}$  respectively.

### **Rise Constant Characterisation**

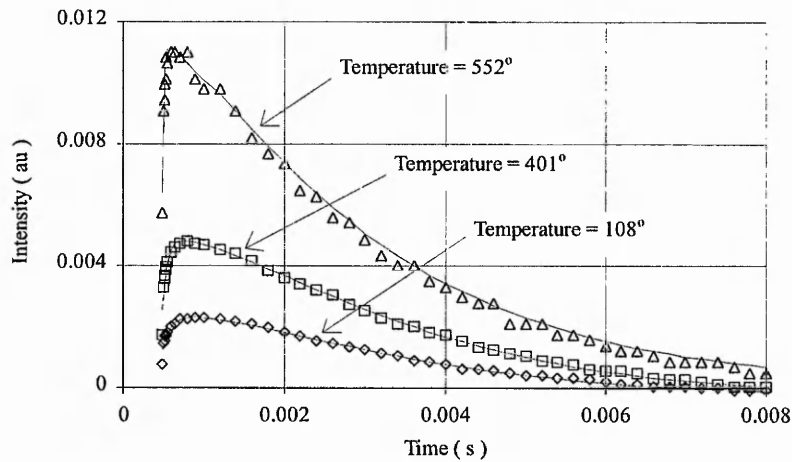
As presented with the decay constant, it appears a double exponential characteristic exists due to the influence of either a neighbouring aluminium or gallium atom on the terbium atom's energy levels and transition probabilities. Therefore, to calculate the rise constant characteristics of YAGaG:Tb using 266nm excitation, it is necessary to reformulate the rise constant equation to account for this double exponential characteristic. Continuing with the assumption that each site is independent from the other, a double exponential rise constant equation is derived from the addition of two individual single exponential rise equations. Referring back to Figure 5-6, the electrons which are excited directly into State B were described as undergoing a two stage relaxation process and were those which contributed to the rise in the photoluminescent signal. By reference to equation 16 - the single exponential rise constant equation - and by noting that intensity is proportional to the number of



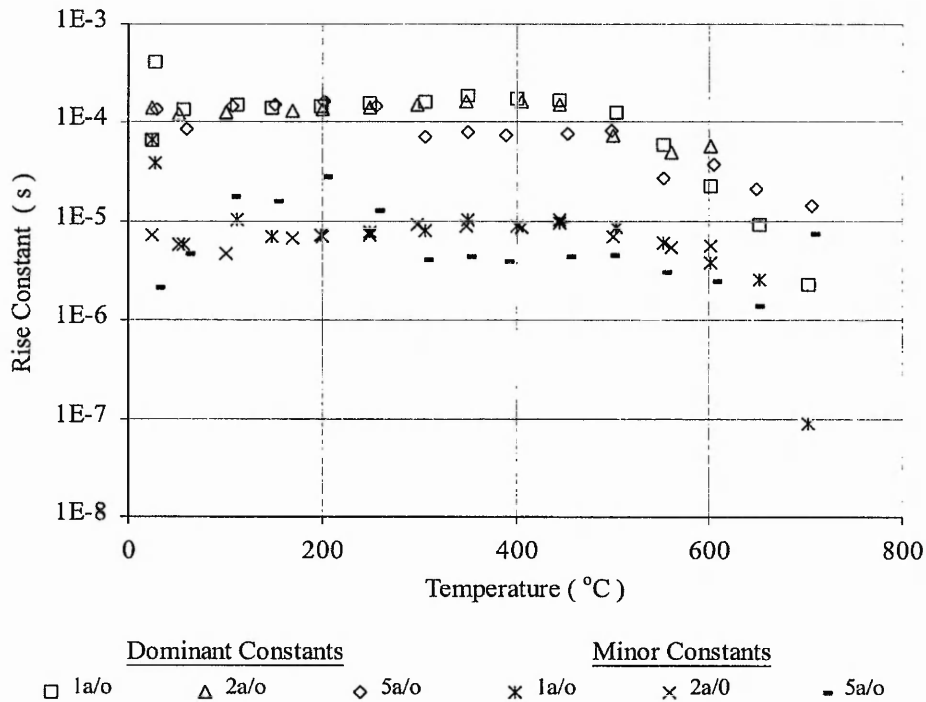
electrons undergoing the transitions; the resultant formula due to the combination of the relaxation processes within two isolated terbium atoms ( previously referred to as Site A and Site B) is:-

$$I(t) = \left[ I_{a1} \text{Exp} \frac{(t - t_0)}{\tau_a^d} + I_{a2} \left\{ \left[ 1 - \text{Exp} \frac{(t - t_0)}{\tau_a^r} \right] \text{Exp} \frac{(t - t_0)}{\tau_a^d} \right\} \right] \\ + \left[ I_{b1} \text{Exp} \frac{(t - t_0)}{\tau_b^d} + I_{b2} \left\{ \left[ 1 - \text{Exp} \frac{(t - t_0)}{\tau_b^r} \right] \text{Exp} \frac{(t - t_0)}{\tau_b^d} \right\} \right] \quad \text{Equation[18]}$$

where  $I(t)$  is fluorescent signal as a function of time,  $I_{a1}$  is the intensity due to electrons at Site A undergoing only the 544nm transition,  $I_{a2}$  is the intensity due to electrons at Site A which undergo the two stage relaxation process,  $\tau_a^d$  is the decay constant of Site A,  $\tau_a^r$  is the rise constant of Site A,  $I_{b1}$  is the intensity due to electrons at Site B undergoing only the 544nm transition,  $I_{b2}$  is the intensity due to electrons at Site B which undergo the two stage relaxation process,  $\tau_b^d$  is the decay constant of Site B,  $\tau_b^r$  is the rise constant of Site B, and  $t_0$  is the trigger delay of the oscilloscope. Figure 5-12 illustrates the resultant curve fits.



**Figure 5-12 Illustration of The Double Exponential Rise Characteristic of YAGaG:Tb 1a/o and The Resultant Curve Fits**

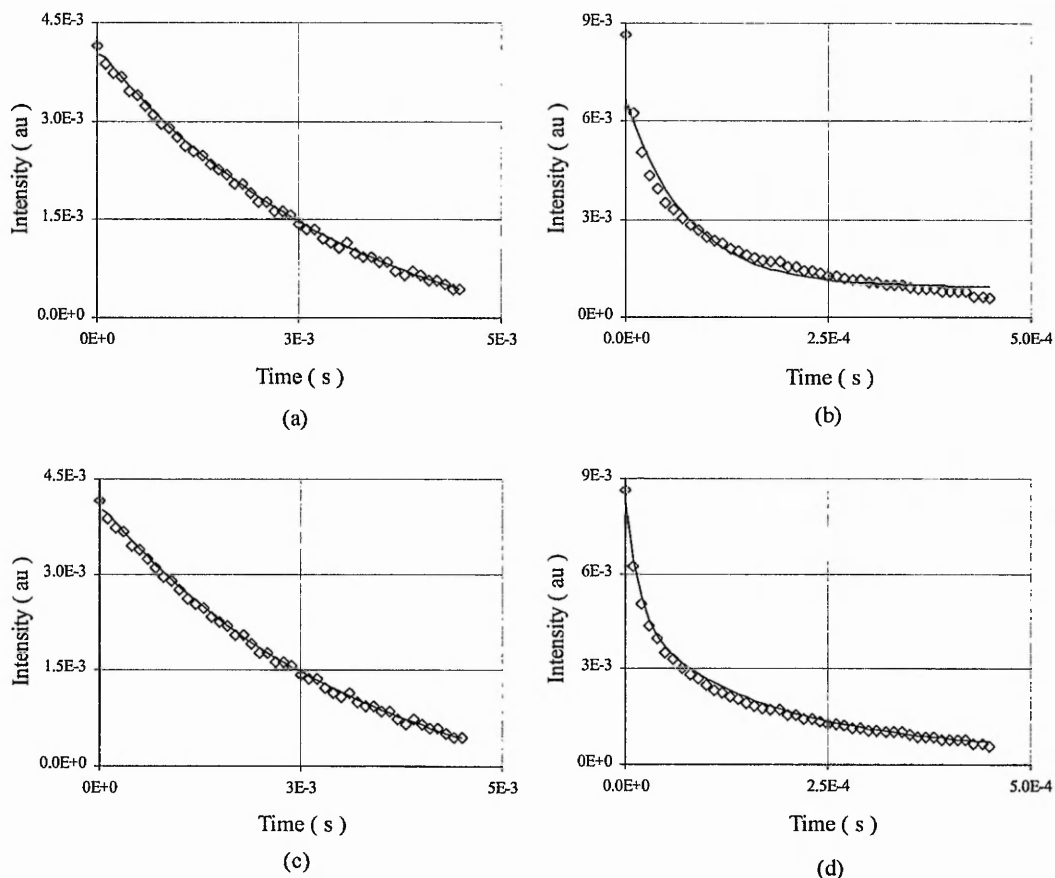


**Figure 5-13 Double Exponential Rise Constant Characterisation of YAGaG:Tb at 266nm Excitation**

The above figure shows the resultant double exponential rise constant characterisation. As with the decay characterisation, one constant is an order of magnitude faster than the other, and has a higher quenching temperature. The dominant constant has a magnitude of 0.15ms and a quenching temperature of 400°C, compared with the minor constant with a value of 9μs and a quenching temperature of 500°C. Upto a temperature of 700°C the rise constant is measurable, from which point the rise characteristic is saturated by the intensity of photon emission straight from the State A levels of both sites. These characteristics only exist for the lower dopancy levels upto and including 5a/o. At the higher dopant concentrations, intensity saturation of the rise characteristic occurs due to the increase in the amount of excited states.

### 5.4 Comparison of Single and Double Exponential Characterisation

From a temperature sensing point of view, a comparison between the use of a double exponential fit or a single exponential fit requires assessment. Figure 5-14 illustrates the advantages and disadvantages of both methods.



**Figure 5-14 Comparison of Exponential Fits for YAGaG:Tb 5a/o**  
 where (a) is a single exponential at 55°C, (b) is a single exponential at 855°C, (c) is a double exponential at 55°C, and (d) is a double exponential at 855°C.

At low temperatures, the domination of one constant over the other is clearly visible, with graph (b) showing that a single exponential fit is as accurate as a double exponential fit. Therefore, the double exponential fit derives two constants of equal value. At the higher temperatures the second constant becomes detectable, and so a double exponential equation

is a more accurate fit than the single exponential. Values derived by the single exponential fit are those relating to the dominant constant as shown in Table 5-1. The resultant temperature dependent characteristics derived maintain their accuracy to enable its use as a temperature sensing method.

Temperature °C	Single Exponential	Double Exponential Dominant Constant	Double Exponential Minor Constant
20	3.17e-3	3.18e-3	3.16e-3
154	3.15e-3	3.15e-3	3.15e-3
305	2.33e-3	3.37e-3	3.28e-5
746	5.72e-4	8.55e-4	8.42e-5
1020	1.16e-5	1.54e-5	9.94e-7

**Table 5-1 Comparison Table of Calculated Decay Constants For YAGaG:Tb 5a/o**

When excitation is at 266nm, further masking of the minor constant occurs due to the existence of the rise characteristic. This leads to derivation difficulties with obscure values being calculated. This is shown in Figure 5-10 to Figure 5-13 which indicates unstable characteristics, which can lead to inaccuracies in temperature measurement.

Single Exponential Characteristics					
		$T_Q$	$\tau_Q$	Q	Range
Decay at 355nm		700 °C	1.33 ms	13.2 mC <sup>-1</sup>	700 to +1100 °C
Decay at 266nm		650 °C	1.65 ms	12.1 mC <sup>-1</sup>	650 to +1100 °C
Rise at 266nm		450 °C	86.0 μs	13.6 mC <sup>-1</sup>	450 to 715 °C
Double Exponential Characteristics					
Decay at 355nm	Dominant	700 °C	1.29 ms	11.9 mC <sup>-1</sup>	700 to +1100 °C
	Minor	750 °C	73.0 μs	14.8 mC <sup>-1</sup>	750 to +1100 °C
Decay at 266nm	Dominant	600 °C	2.31 ms	12.0 mC <sup>-1</sup>	600 to +1100 °C
	Minor	750 °C	92.7 μs	13.9 mC <sup>-1</sup>	750 to +1100 °C
Rise at 266nm	Dominant	450 °C	149.0 μs	9.4 mC <sup>-1</sup>	450 to 700 °C
	Minor	500 °C	8.47 μs	8.8 mC <sup>-1</sup>	500 to 650 °C

**Table 5-2 Comparison Between The Single and Double Exponential Temperature Dependent Characteristics of YAGaG:Tb**

Table 5-2 shows the calculated constants of YAGaG:Tb for the single and double exponential characterisation at both excitation wavelengths. The values shown indicate that the single exponential fits provide characteristics which are temperature dependent over the same range and with a similar quenching rate as those obtained for the double exponential. Results presented have shown that a single exponential provides better stability in the characteristics than the double exponential, even though the curve fits are not as accurate.

### **5.5 Summary**

As with  $Y_2O_3:Eu$ , the complete characterisation of YAGaG:Tb has been examined. Results presented show YAGaG:Tb has a suitable major emission line which is independent of both temperature and dopancy; and has temperature dependent characteristics which have the ability to be utilised within phosphor thermography.

The emission spectra of YAGaG:Tb has a major emission line of 544nm. This 544nm emission line has shown consistency with respect to both dopancy concentration and temperature. With no shift in wavelength occurring, the phosphor shows the ideal characteristic for use within phosphor thermography and allows the spectrometer to be removed from the detection system. As with  $Y_2O_3:Eu$ , the detector can be positioned closer to the collection optics and so provided a stronger signal to enable the temperature dependent characteristics of the phosphor to be investigated.

Previous investigations into the temperature dependence of the 544nm emission of YAGaG:Tb had utilised a single exponential decay to characterise the phosphor. Results presented here, clearly show the existence of a double exponential especially at the high temperatures. This has been shown to be related to the addition of gallium, which previous work had shown to improve the intensity emission of the 544nm spectral line. The use of a double exponential curve fitting routine produces two decay constants which both show temperature dependence. The dominant decay constant masks the characteristics of the

minor constant at the lower temperatures, but both show dependency at higher temperatures. Also, utilisation of 266nm excitation results in a rise characteristic for low dopant levels of terbium, and has a temperature dependent range of 450°C to 715°C.

Concluding, YAGaG:Tb shows characteristics which can be utilised within temperature sensing of turbine blades. The 544nm emission is within the green region of the visible spectrum and so is less effected by blackbody radiation at high temperature levels. These characteristics show dependency over the temperature range of 450°C to 1050°C, but do show instability due the existence of a double exponential decay of photoluminescence. This instability is removed when characterised with a single exponential curve fitting routine, but the error in the calculation of the constant is increased which would lead to discrepancy within the sensing of temperature.

## 6. Comparison of Phosphors

### 6.1 Introduction

The choice of phosphor to be used for a particular application clearly depends upon the temperature measurement range to be encountered. Past experimental test-runs on turbine engines using sensors such as embedded thermocouples, pyrometers and thermographic paints, have shown temperatures to reach as high as  $1200^{\circ}\text{C}$ <sup>[1,6,82,83]</sup>. As shown in Chapters 4 and 5, both the phosphors under investigation meet the temperature range specification, but the question of 'which is the best' still remains unanswered. Several factors which need considering are:

- **Intensity Levels.** Within a harsh turbine environment, the temperatures reached leads to high levels of blackbody radiation. This decreases the signal-to-noise ratio of the collected luminescence - a reduction in the sensing capability of the system.
- **Rotational Speed.** Phosphor thermography is being developed for the measurement of turbine blades, which have rotating speeds of 30-45,000 rpm. The probe is to be positioned at an angle to the rotating blades with a limited field of view. Sufficient data must be collected within the period of time the blade is within the specified field of view, otherwise inaccurate measurement of the decay constant will lead to discrepancies of the temperature reading.
- **Bonding Ability.** The phosphor must have good adhesion to the components under test to withstand the hostile conditions. Currently utilised methods employ the use of a bonding agent, referred to in this chapter as the binder. Firstly, the phosphor must have no chemical reaction with the binder which induces changes in its thermal properties. And secondly, the correct binder must be developed for a

specific phosphor. Results shown here indicate that a correct binder for one phosphor may not necessarily be the best for another.

- **Lifetime.** Survivability within the turbine engine is of great importance in order to maintain sensing capability. Turbine engines are continuously being taken through thermal cycles leading to wide changes in temperatures. Also, the existence of hot gases and particles leads to high erosion of the phosphor film - an additional factor to its reduction in lifetime.

The following chapter makes a comparison between the two phosphors investigated with respect to the above mentioned points.

## **6.2 Intensity Comparison**

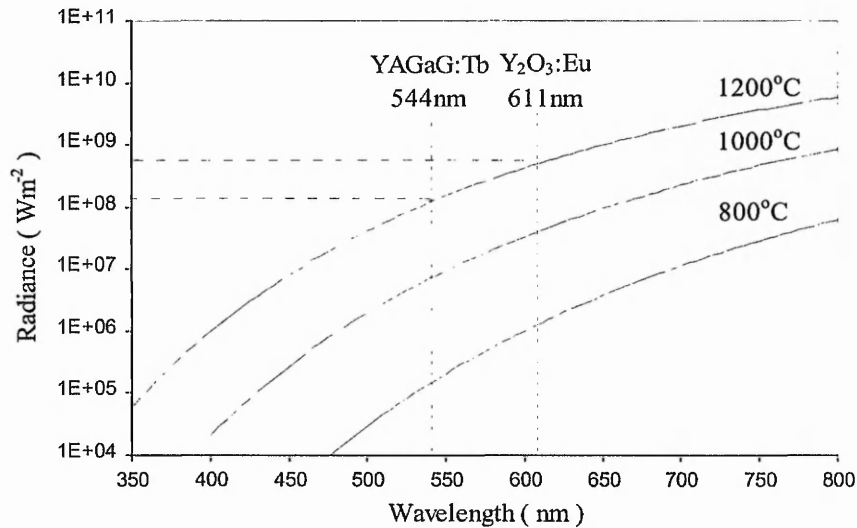
For optical detection, noise level in a high temperature environment is problematic due to the emission of blackbody radiation. All materials absorb and radiate electromagnetic energy and a blackbody source is one which radiates at all wavelengths. The radiated power of a specific wavelength is directly related to the temperature of the material, and is defined by Planck's Radiation Law<sup>[84,85]</sup> as :

$$W_{\lambda} = \frac{2 \pi h c^2}{\lambda^5} \left[ \frac{1}{\exp(hc / \lambda k T) - 1} \right] \quad \text{Equation [19]}$$

where  $W_{\lambda}$  is the spectral radiant emittance ( $\text{W m}^{-2}$ ),  $\lambda$  is the wavelength (m),  $h$  is Planck's Constant (J s),  $k$  is Boltzmann's Constant ( $\text{J K}^{-1}$ ),  $c$  is the speed of light ( $\text{m s}^{-1}$ ), and  $T$  is the temperature (K).

By calculating the spectral distribution of blackbody radiation at the temperature range of interest, the relative noise level of a specific wavelength can be deduced. Figure 6-1 shows blackbody radiation spectra at several temperatures and its relation to the wavelengths of the phosphors.



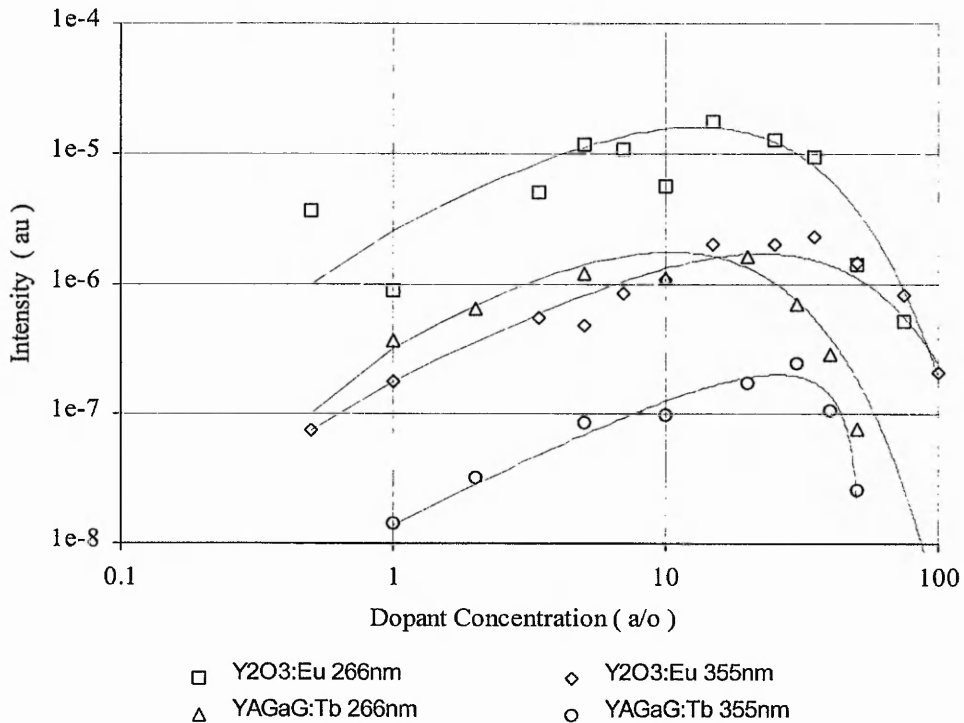


**Figure 6-1 Blackbody Radiance Of The Visible Spectrum At Various Temperatures**

At a temperature of 1200°C, the level of blackbody radiation at a wavelength of 544nm is a factor of 3.8 less than that at 611nm. Clearly, this indicates that YAGaG:Tb emission would be easier to detect due to the lower noise level. By the data presented in this thesis, the efficiency of YAGaG:Tb is much less than Y<sub>2</sub>O<sub>3</sub>:Eu which leads to lower emission levels. The strong intensity emission from Y<sub>2</sub>O<sub>3</sub>:Eu provides a clear signal above the high levels of blackbody radiation, and therefore remains the preferred phosphor for utilisation within phosphor thermography.

This point is clearly shown in Figure 6-2, an intensity comparison between both phosphors at all dopancies levels and between both excitation wavelengths. The intensity value has been obtained by integrating the phosphorescent pulse after excitation has ceased. Three important points are illustrated. Firstly, excitation at 266nm induces an order of magnitude greater phosphorescence for both phosphors compared with 355nm excitation. Secondly, again for both phosphors, the change from 355nm to 266nm excitation induces an optimum dopancy shift to lower concentrations. At 355nm excitation, Y<sub>2</sub>O<sub>3</sub>:Eu and YAGaG:Tb have optimum dopancy levels of 25a/o and 30a/o respectively. Compared with 266nm excitation,

the optimum dopancy levels are lower at 10-15a/o for  $Y_2O_3:Eu$ , and 10-20a/o for YAGaG:Tb.

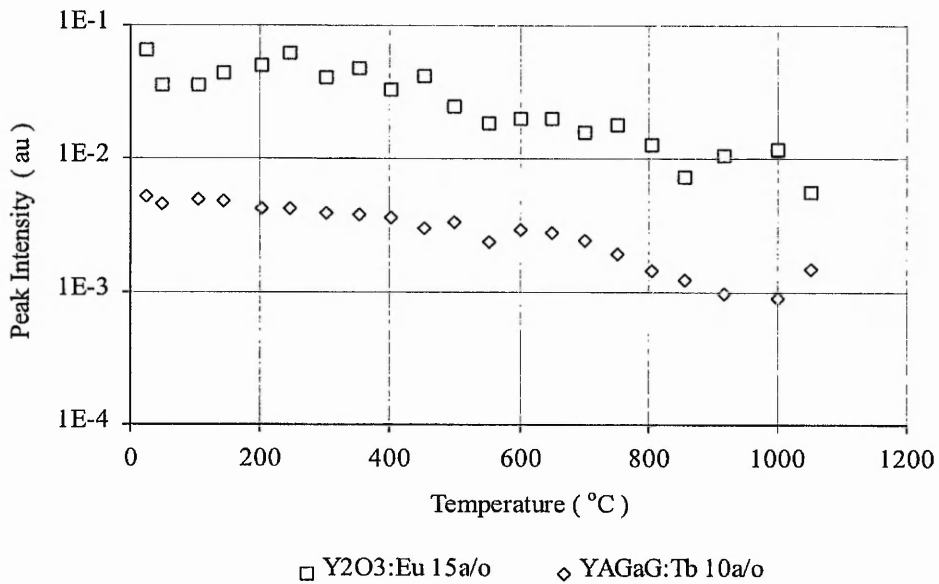


**Figure 6-2 Intensity Comparison of  $Y_2O_3:Eu$  and YAGaG:Tb at Room Temperature**

And thirdly,  $Y_2O_3:Eu$  is shown to be stronger than YAGaG:Tb at both excitation wavelengths by over an order of magnitude. This order of magnitude out-weighs the advantage YAGaG:Tb had in terms of blackbody noise level. But a question still remains; is this the case at the high temperatures ?

To overcome the blackbody noise level, it is not the overall intensity that is important, but the peak intensity. The stronger the peak intensity value, the greater the difference over blackbody, and so the easier it will be to detect. Figure 6-3 shows how the peak intensity of the phosphors vary with temperature. For the full temperature range,  $Y_2O_3:Eu$  maintains a much higher peak intensity level over YAGaG:Tb. This is an order of magnitude greater

and is maintained upto around 800°C, from which point the intensity ratio of the phosphors drops slightly. It is at 800°C, that blackbody radiation starts to effect the noise level of the system. It should be noted though, that these measurement have been made at the high temperatures where the noise level is increasing and so degrading the signal-to-noise ratio. Even though this is occurring, the peak intensity signal of the Y<sub>2</sub>O<sub>3</sub>:Eu is still strong enough to be detected, thus proving that a higher signal-to-noise ratio is achieved with Y<sub>2</sub>O<sub>3</sub>:Eu rather than YAGaG:Tb at high temperatures.



**Figure 6-3 Peak Intensity Comparison of Y<sub>2</sub>O<sub>3</sub>:Eu and YAGaG:Tb Over Full Temperature Range at 266nm Excitation**

### Phosphor Efficiency

A measurement of the quantum efficiency, Q.E.%, of the phosphors would provide a clear indication of their potential at high temperatures. For photoluminescence, quantum efficiency is defined as :-

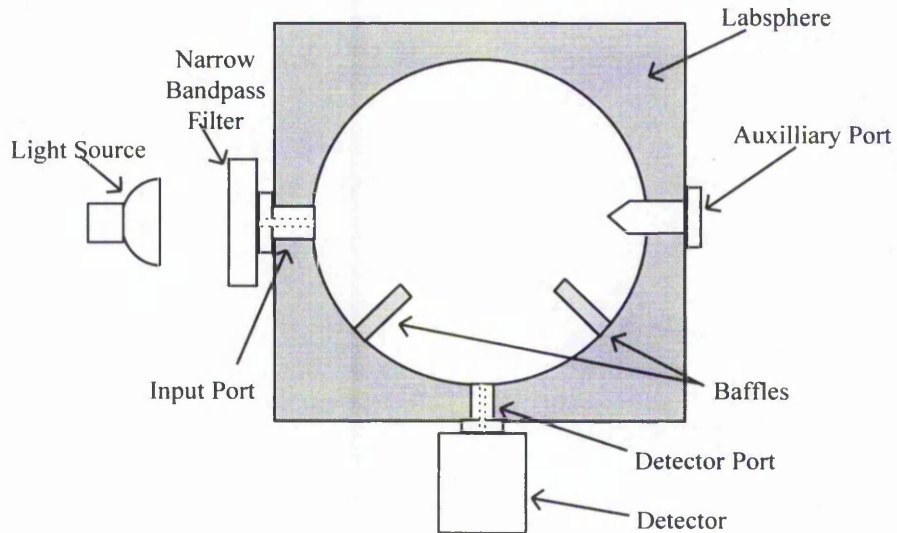
$$\text{Q.E.\%} = \frac{\text{No. of Emission Photons}}{\text{No. of Absorbed Photons}} \quad \text{Equation [20]}$$

To calculate the number of absorbed photons, three measurements are required; the number of incident photons, the number of reflected photons and the number of transmitted photons. The number of incident photons can be calculated from the energy of the laser pulse. Unfortunately, use of the Spectralon integrating sphere led to experimental difficulties with the measurement of the reflected and transmitted photons. Firstly, the reflected photons would be scattered off the rough surface of the phosphor under test in all directions. Therefore, it would be difficult to collect and measure all of these reflected photons. Secondly, to measure the number of transmitted photons, a detector would have to be positioned directly behind the phosphor to capture those incident photons which directly pass through. At the same time, the emission photons require capture and measurement.

Another method of determining a phosphor's efficiency is the measurement of the ratio of incident photons to emission photons. This is known as coupling efficiency and accounts for the loss of incident photons and the internal absorption efficiency within the phosphor. The experimentation involved the use of an integrating sphere purchased from Labsphere. The 4 inch diameter sphere is machined from a cube of Spectralon - a material with high reflective properties over the wavelength range of 250 to 2500nm. There are two 1 inch ports (an input port and an auxiliary port) and a 1/2 inch detector port. Light enters the sphere and is reflected many times off the Spectralon surface, therefore producing an even distribution of light within the sphere. The detector port collects a small percentage of light from within the sphere. The silicon detector provided is a SDA-050-U, whose response covers the range 200 to 1100nm. The Labsphere control system has been calibrated to both the detector and the Spectralon, therefore converting the detected signal into an overall value of light within the sphere. This value can be given in terms of luminous flux (lumens), luminance (foot lamberts), radiance (watts per m<sup>2</sup>), or power (watts).

Unfortunately, the SDA-050-U silicon detector was not suitable to measure the power levels of the laser pulse, nor was it able to integrate or capture the emitted pulse with

respect to time. As a result, a photomultiplier tube was used to capture the phosphorescent pulse and was calibrated against a Newport silicon power detector, specifically purchased for the power measurement of the Nd:YAG laser. Figure 6-4 shows the arrangement for the calibration between the two detectors.



**Figure 6-4 Labsphere Arrangement for the Measurement of Quantum Efficiency**

For calibration purposes, an OSRAM decostar 12V, 50W lamp was used as the light source. The photomultiplier tube required calibration of power at the phosphor emission wavelengths, 611nm and 544nm. The narrow bandpass filters, which were utilised for the collection of the phosphorescence for the decay constant measurement system, were positioned at the input port and so only allowed the wavelength of interest to enter the sphere. The baffles stop direct light being detected from either of the two ports. By varying the voltage of the lamp, a variety of intensity levels were achieved. The calibrated power meter was tuned to the wavelength of interest and the power reading was compared with the voltage produced when replaced with the photomultiplier tube. From the resultant calibration data, presented in Table 6-1, the voltage-to-power conversion factors were derived. Thus, by integrating the phosphorescent emission pulse obtained by the

photomultiplier tube, the resultant area can be converted into the power emitted by the phosphor. By measuring the power of the laser source prior to excitation, the coupling efficiency could be calculated.

611 nm						544 nm					
Power $\mu\text{W}$	Output Voltage (mV) at various PMT supply voltages (V)					Power $\mu\text{W}$	Output Voltage (mV) at various PMT supply voltages (V)				
	400	450	500	550	600		400	450	500	550	600
3.59	2.10	5.60	16.1	43.4	73.5	3.14	2.45	6.65	18.9	50.4	75.6
2.32	1.40	3.85	10.2	25.0	60.0	2.23	1.61	4.50	12.6	32.9	69.3
1.77	1.23	3.15	8.00	18.6	45.5	1.77	1.33	3.71	9.87	24.9	60.2
1.21	0.87	1.75	4.40	10.2	23.0	1.18	0.84	2.31	6.40	15.1	36.4
0.85	0.35	1.19	3.00	6.80	14.5	0.81	0.56	1.64	4.40	10.3	23.3

**Table 6-1 Calibration Data of the Photomultiplier Tube 9954B**

To capture the phosphorescent emission pulse, pellet samples of  $\text{Y}_2\text{O}_3:\text{Eu}$  were positioned on the tip of the auxiliary port. The excitation laser was then fired through the entrance port and directly onto the pellet. The photomultiplier tube was positioned at the detector port with two filters, a highpass filter with cut-on at 580nm and a narrow bandpass centred at 610nm. The 611nm phosphorescent emission was then collected at various supply voltage settings for each phosphor sample.

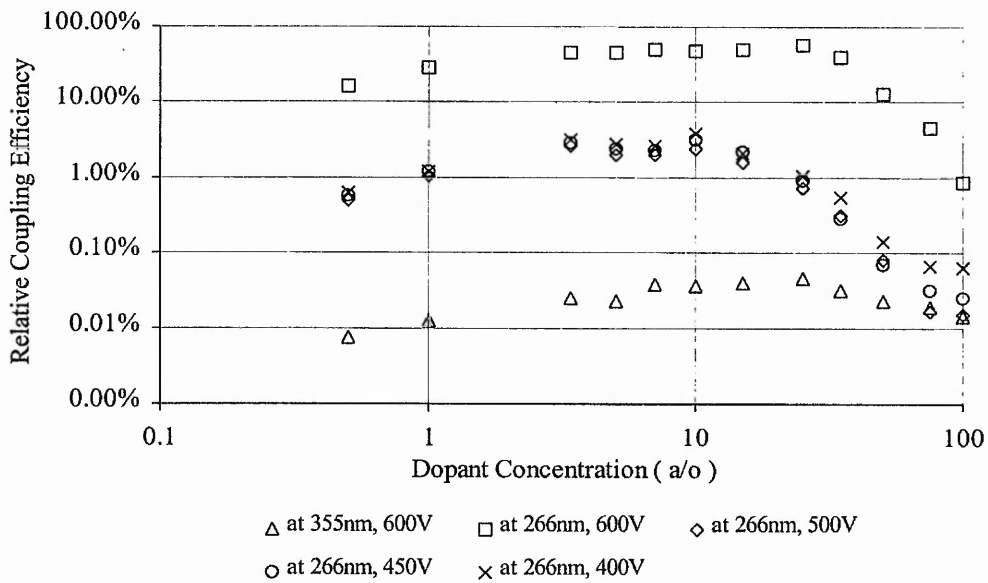
Before integrating the pulse and calculating the coupling efficiency, several factors required consideration. Firstly, there is the transmission percentage of each filter at the phosphorescent wavelength. These were 53% for the narrow bandpass filter and 82.5% for the highpass filter. Secondly, the integrating sphere evenly distributes the light throughout the sphere and the detector will only collect a small percentage of that light. This percentage is defined as the throughput,  $T\%$ , and is as follows :

$$T_{\%} = \frac{\rho f_e}{1 - \rho (1 - f_j)} \quad \text{Equation [21]}$$

where  $\rho$  is the reflectance of the sphere wall at the wavelength of interest,  $f_e$  is the fraction of the sphere wall being detected,  $f_j$  is the fraction of the sphere where no reflectance occurs. Hence,

$$f_e = \frac{\text{area of detector port}}{\text{area of sphere}} \quad \text{and} \quad f_j = \frac{\text{area of all ports}}{\text{area of sphere}}$$

Accounting for these factors, the power of the phosphorescent emission is measured. After converting the power into energy, the number of photons at the wavelength can be derived, and subsequently the coupling efficiency of the phosphor can be calculated. Tests were carried out on all the  $Y_2O_3:Eu$  samples at both 355nm and 266nm excitation. Figure 6-5 shows the measured coupling efficiency obtained.



**Figure 6-5 Relative Coupling Efficiency Measurement of  $Y_2O_3:Eu$**

Initially, measurements were made at both wavelengths with the photomultiplier tube at a supply voltage of 600V. Results indicated that the coupling efficiency at 266nm was three

orders of magnitude greater than that at 355nm, which was vastly different to the intensity comparison. Also, a flat response occurred around the optimum concentration. Both characteristics were due to saturation of the photomultiplier tube. Subsequently, measurements were repeated at 266nm excitation for a variety of photomultiplier supply voltages. The results presented in Figure 6-5, show consistency and indicate that 266nm excitation is over an order of magnitude more efficient than excitation at 355nm, agreeing with results obtained for the intensity comparison. References to the excitation spectra of  $Y_2O_3:Eu$  presented in Figure 4-1 confirms these relative efficiency measurements. Unfortunately, the experimentation could not be repeated for the YAGaG:Tb samples due to a coating of the  $Y_2O_3:Eu$  being deposited on the wall of the sphere, by laser ablation of the samples.

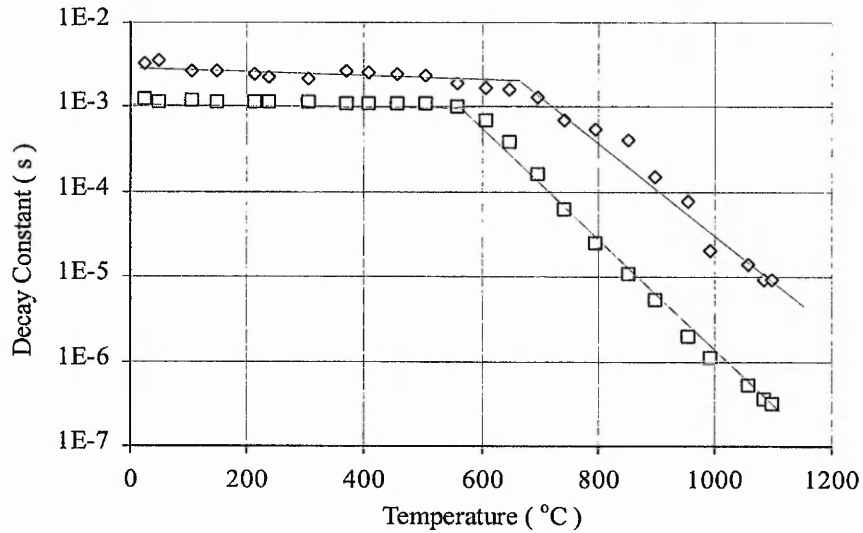
### **6.3 Temperature Dependency Comparison**

Presented in Chapters 4 and 5, the temperature dependent characteristics of both phosphors showed suitability for use as a thermographic sensor. The sensing range of particular interest for the temperature measurement of gas turbine blades is from 700°C to +1100°C. Both phosphors are temperature dependent within this range, but results demonstrate that  $Y_2O_3:Eu$  has several advantages over YAGaG:Tb.

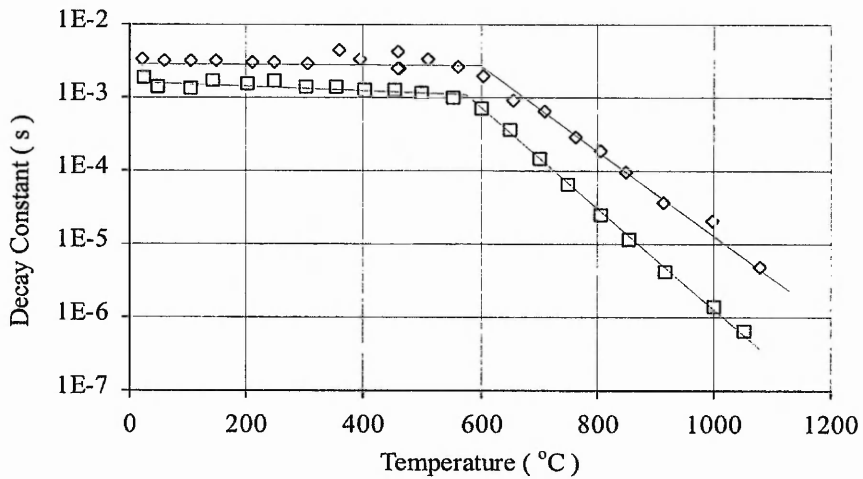
Firstly, there is the difference of the curve fitting routines. Considering decay characterisation only, YAGaG:Tb required a double exponential routine compared with  $Y_2O_3:Eu$  needing only a single exponential fit. As shown in Figure 5-10, the resultant calibration graph showed instability due to the dominance of one constant over the other. When fitted with a single exponential, stability of the dominant constant was achieved, but with the consequence of poor fits at high temperatures. Either way, instability and poor fits leads to loss of accuracy as a temperature sensor. Compared with  $Y_2O_3:Eu$ , a single exponential fit maintains accuracy and stability over the full temperature range, and



consequently provides a stable temperature calibration graph. Shown in Figure 6-6 is a comparison between the single exponential characterisation of  $Y_2O_3:Eu$  and  $YAGaG:Tb$  at both excitation wavelengths.



(a)



(b)

□  $Y_2O_3:Eu$  15a/o      ◇  $YAGaG:Tb$  10a/o

**Figure 6-6 Comparison of Decay Constant Characterisation (a) at 355nm and (b) 266nm excitation**

As previously stated, both the position of the probe and the speed of the engine will limit the capture time window a specific blade is viewed by the sensor. This capture time

window limitation has been calculated by Rolls-Royce. Through the use of thermographic paints during previous turbine engine test runs, the temperature at known engine speeds has been determined. Assuming a capture period of twice the lifetime would provide sufficient data to accurately complete the curve fitting routine. The specification of the required decay constant at these temperatures are :-

Speed of engine at 70% max rpm = 900°C = decay constant of 10 $\mu$ s

Speed of engine at 100% rpm = 1200°C = decay constant of 1 $\mu$ s

Reference to Figure 6-6 shows YAGaG:Tb to be outside and Y<sub>2</sub>O<sub>3</sub>:Eu to be within this specification.

As well as a more stable characteristic, Y<sub>2</sub>O<sub>3</sub>:Eu has a higher quenching rate and a wider sensing range. The higher quenching rate indicates that Y<sub>2</sub>O<sub>3</sub>:Eu is more sensitive to temperature variation than YAGaG:Tb. These characteristics are summarised in Table 6-2, a comparison of the calibration curves shown in Figure 6-6.

	266nm Excitation				355nm Excitation			
	Temperature	Decay			Temperature	Decay		
	Range °C	Constant $\mu$ s	T <sub>Q</sub> °C	Q mC <sup>-1</sup>	Range °C	Constant $\mu$ s	T <sub>Q</sub> °C	Q mC <sup>-1</sup>
Y <sub>2</sub> O <sub>3</sub> :Eu	550- <sup>+</sup> 1100	1010-0.6	550	15.4	550- <sup>+</sup> 1100	1000-0.3	550	15.7
YAGaG:Tb	650- <sup>+</sup> 1100	1650-4.8	650	12.1	700- <sup>+</sup> 1100	1330-9.5	700	13.2

**Table 6-2 Comparison of Single Exponential Calibration Details**

The accuracy of the phosphors can be determined from the above calibration data. For Y<sub>2</sub>O<sub>3</sub>:Eu, all captured data was fitted to a confidence limit of 99%. This confidence limit was extended to 95% for YAGaG:Tb due to the reduction in the accuracy of the single

exponential fits. Referring back to equation 5 in Chapter 2, a relationship is defined between the temperature and the decay constant. By inducing the confidence limits on the data, the error of the temperature determination can be calculated. For  $Y_2O_3:Eu$ , as a 99% confidence limit was maintained throughout the captured data, it has a temperature accuracy of  $\pm 0.65^\circ C$ . The accuracy of  $YAGaG:Tb$  is  $\pm 4.2^\circ C$ , due to the reduction of the confidence limits and the lower quenching rate.  $Y_2O_3:Eu$  is clearly shown to have a superior accuracy for use in the determination of temperature.

Another advantage for  $Y_2O_3:Eu$  is the existence of the rise characteristic at both excitation wavelengths. This extends the sensing capability of the phosphor, with the rise constant varying from  $100\mu s$  to  $10\mu s$  over the temperature range of  $25-800^\circ C$ . Although the rise constant exists at  $266nm$  for  $YAGaG:Tb$ , it is insensitive to variation in temperature until  $400^\circ C$  from which point the constant decreases from  $200\mu s$  to  $10\mu s$  at  $700^\circ C$ . For  $YAGaG:Tb$  the rise characteristic exists upto a dopancy level of  $5a/o$ , compared with  $Y_2O_3:Eu$  which exists upto  $10a/o$ . Further comparison of the intensity levels at these dopant concentrations shows the  $Y_2O_3:Eu$  to be 98% of its optimum, compared with  $YAGaG:Tb$  which is 79% the strength of its optimum concentration. Thus, enabling the use of rise constant characterisation of  $Y_2O_3:Eu$  with very little loss in signal-to-noise ratio at the high temperatures.

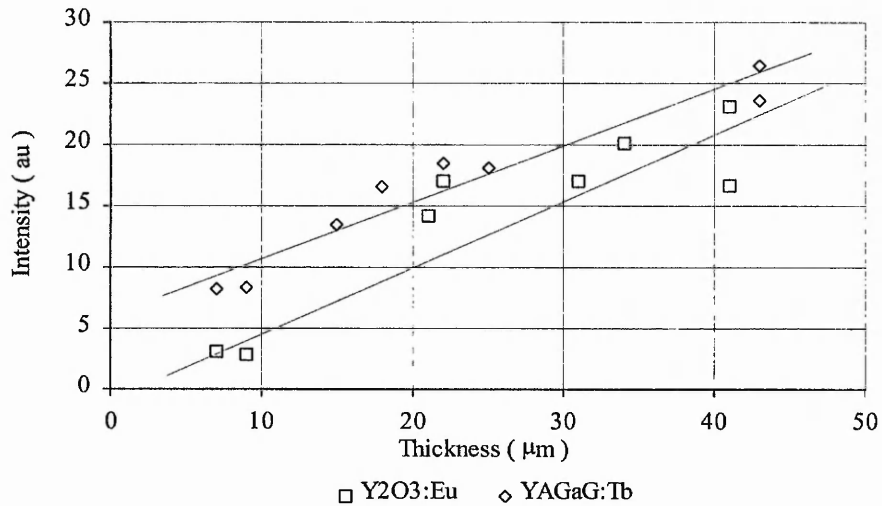
#### **6.4 Lifetime Comparison (Thick Film Only)**

For phosphor thermography to be utilised, the phosphor must adhere to the components-under-test. Due to the high temperature and hostile environment that exists, survivability of the phosphor is one of the most technically demanding aspects involved in the development of phosphor thermography. As discussed in Chapter 2, several methods have previously been investigated with varying success. Initially, experimentation involved the characterisation of thick film coatings produced using a chemical bonding method. They

were produced in-house at Rolls-Royce plc, who had perfected the method through the production of thermographic paints.

Thermographic paints of  $Y_2O_3:Eu$  and  $YAGaG:Tb$  were produced and administered onto test coupons - a one inch square of turbine blade material. The thickness of the paint applied is important for several reasons. Firstly, the intensity emitted improves with thickness due to the increase in the volume of phosphor. The optimum thickness would occur where the intensity no longer increased with thickness. Against this though is the bonding ability of the paint, which decreases with thickness and so shortens the life expectancy of the films. Also, thermal gradients exist between the top (excited with the laser) and the bottom (in contact with the blade) surfaces of the paint. The thermal gradient has to be accounted for in order to correctly determine the temperature of the blade. A thicker film will result in a greater thermal gradient and so a higher probability of error in the measurement of the temperature.

Coupons simulating turbine blades with various thicknesses (7 to  $43\mu m$ ) of phosphor paints were produced to investigate the above. The thinnest film produced was  $7\mu m$  in thickness but resulted in a very weak emission level due to the lack of phosphor. Although the thick films showed an intensity increase with thickness, the strength of the fluorescent signal varied across each film due to two reasons. Firstly, poor mixing of the phosphor with the epoxy resin leads to an uneven distribution of the phosphor. This creates what is termed as "hot-spots", densely phosphor populated areas of film, therefore producing a higher fluorescent signal. And secondly, difficulty exists in controlling the thickness of applied paint through use of a spray air-gun. This causes an uneven coating of the thermographic paint across the coupon.



**Figure 6-7 Intensity of Thermographic Paints**

Unfortunately, at the time of this experimentation, the use of the 266nm Nd:YAG was unavailable. Figure 6-7 shows the intensity measurement of the films using the 325nm CW HeCd laser. Results show YAGaG:Tb coatings to have a higher intensity than those of Y<sub>2</sub>O<sub>3</sub>:Eu. Referring back to excitation spectra of the phosphors, Figure 4-1 and Figure 5-1, it can be seen that this is because the efficiency of YAGaG:Tb is higher than Y<sub>2</sub>O<sub>3</sub>:Eu at this excitation wavelength. Also, upto thicknesses of 43μm the intensity of both phosphors is still increasing, so optimum thickness had yet to be achieved. Unfortunately, attempts to produce thicker samples failed with the thermographic paints failing to adhere to the coupons.

To investigate the thick films survivability, lifetime tests were carried out on five samples of various thicknesses of each phosphor. The furnace was set to a temperature of 1200°C and the samples were held for periods of 1, 2, 5, and 10 Hrs at this temperature. After each

period, the samples were removed and allowed to rapidly cool to room temperature. This accounted for the samples undergoing the harshest possible temperature variation and was aimed at imitating the cyclic behaviour of a turbine engine due to changes in the speed of rotation. Due to the temperatures reached, chemical reactions between the phosphor and the binder may have occurred and altered the thermal properties of the film. As a result, if the films survived they were then tested for decay constant calibration between 500°C to 1000°C.

All the samples tested showed poor survivability. As expected, samples of 43µm thickness immediately failed when held at 1200°C due to the poor binding properties of the thicker samples. All other samples began to lose their coating at various stages of the experiment. For both phosphors, none survived even these static tests for a period of more than five hours. As well as the loss of material, a darkening of the film occurs. Both these factors reduce the intensity emission of the phosphor, therefore reducing the signal-to-noise ratio.

Although the lifetime experimentation has shown a poor survivability of the thick films, a positive point is the decay constant measurements obtained. Figure 6-8 shows the decay constant characterisation of the samples. Both phosphors at all thickness show consistent characteristic upto to the five hour period for which they survived. This clearly indicates that the thermographic properties of the phosphors are unaffected by neither the binder nor due to any reaction occurring at the high temperatures for long periods of time.

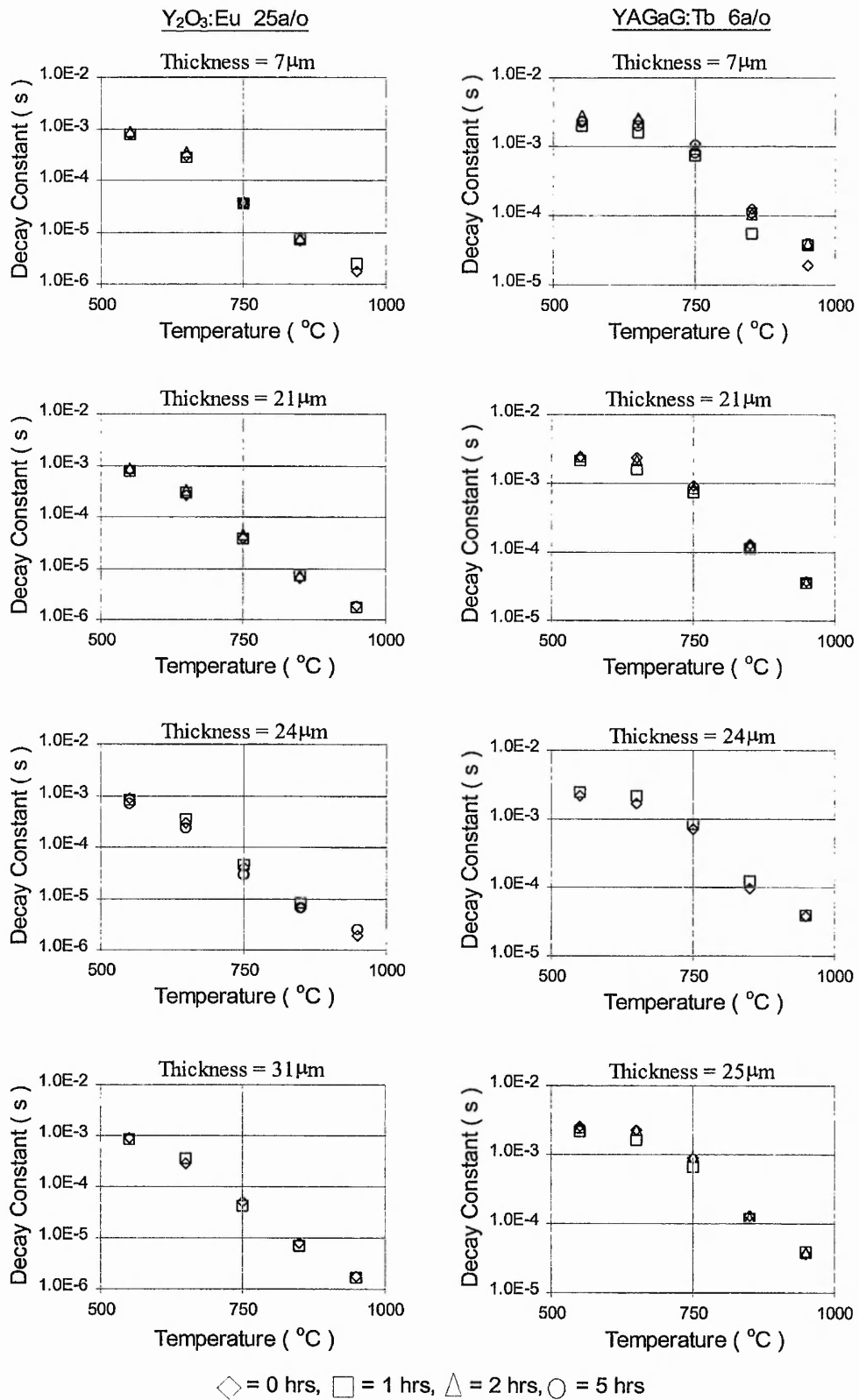


Figure 6-8 Lifetime Measurement of Thick Film Samples

### **6.5 Recommended Phosphor For Future Development**

Measurements obtained from both pellet and thick film samples of the phosphors, conclude that  $Y_2O_3:Eu$  is the recommended phosphor for future development within the field of thermographic sensing of turbine blades. As shown, even though the blackbody noise level is higher for 611nm than for 544nm at high temperatures, it was still easier to distinguish the  $Y_2O_3:Eu$  phosphorescent pulse than that of the YAGaG:Tb. This was also shown in the intensity measurements, with  $Y_2O_3:Eu$  maintaining a greater intensity level over the YAGaG:Tb, even with the existence of the blackbody radiation at the high temperatures.

Phosphor efficiency experimentation produced results for  $Y_2O_3:Eu$  to have an efficiency of 5% at optimum dopancy and with excitation at 266nm. Previous measurement made of the quantum efficiency of phosphors, have claimed  $Y_2O_3:Eu$  to be one of the most efficient phosphors with values of over 70%<sup>[86,87]</sup>. Direct comparison between the values cannot be made due to several differences. Firstly, these quoted values are given as quantum efficiency, whereas the efficiency measurement presented here are as coupling efficiency. Secondly, measurements were carried out at 266nm and 355nm excitation, which are shown within the phosphor's absorption spectrum not to be optimum.

Indirect comparison can be made between the intensity levels of the two phosphors. Consistent results have shown  $Y_2O_3:Eu$  to be over an order of magnitude greater than YAGaG:Tb at both excitation wavelengths. Also, 266nm produces intensity levels which are an order of magnitude greater than those achieved utilising 355nm excitation for both phosphors. This observation also existed for the efficiency measurements of  $Y_2O_3:Eu$  at 355nm and 266nm excitation wavelengths. As intensity is directly proportional to the efficiency of the phosphor, the coupling efficiency measurements clarify that  $Y_2O_3:Eu$  should be used over YAGaG:Tb.



Stability of the temperature characteristics provides  $\text{Y}_2\text{O}_3:\text{Eu}$  with another advantage over  $\text{YAGaG:Tb}$ . Due to a single exponential characteristics rather than the double exponential of  $\text{YAGaG:Tb}$ , the characteristics are stable and a higher level of accuracy is maintained throughout the curve fits at all temperatures. Also the existence of the rise characteristic varying from  $25^\circ\text{C}$  to  $800^\circ\text{C}$  extends its temperature sensing capabilities. With this characteristic existing upto a dopancy of 10a/o, a lower dopancy can be utilised within the sensor without the result of a dramatic reduction in its intensity emission level. Also, a higher accuracy is achieved with  $\text{Y}_2\text{O}_3:\text{Eu}$ ,  $\pm 0.65^\circ\text{C}$ , compared with  $\text{YAGaG:Tb}$ ,  $\pm 4.2^\circ\text{C}$ .

Unfortunately, lifetime tests carried out on thick films samples have proved unsuccessful. Neither phosphors survived for a period of more than five hours, and all showed reduction in intensity levels due to loss of material and the darkening of the coating. Positively though, both showed consistent decay constant characteristic. The solution is to produce a longer lasting and more robust form of the phosphor which can survive the hostile environment without a reduction in intensity. The method utilised was RF Magnetron sputtering to produce a thin film of  $\text{Y}_2\text{O}_3:\text{Eu}$  and is discussed in the following chapter.

## 7. Thin Film Phosphor Thermography

### 7.1 Introduction

As discussed in Chapter 1, the phosphor adhesion to the turbine blades plays an important role in the lifetime of the sensor. Although thick films of thermographic paint have proved the capabilities of phosphor thermography, results presented in the previous chapter show poor lifetimes for thick films. The solution needs the production of a more robust coating while maintaining the thermal characteristics. During the feasibility study carried out at the University of Bradford in 1992<sup>[30]</sup>, thin films of  $Y_2O_2S:Eu$  were produced for turbine engine test runs on the compressor blades. These experience hostile conditions with the temperature reaching in excess of 750°C. Although measurement of the thermographic properties of the films were unattainable due to weak emission levels, results did show a higher percentage of coating remained for thin films whereas the thermographic paints disappeared. Furthermore, post engine run tests showed the thin films had retained their room temperature photoluminescent characteristics.

Having established  $Y_2O_3:Eu$  to be the preferential phosphor for use on the turbine blades, thin films of the phosphor required characterisation and lifetime tests. Samples were grown by the author via the RF magnetron sputtering process with argon as the carrier gas. The films were examined using the following criteria :

- Thickness Dependency. The thickness of the phosphor coating has been shown to be important for two reasons. Firstly, results for thick films have shown emission intensity to increase with thickness. Due to high intensity levels being of great importance for distinction from blackbody noise levels, and with thin films previously<sup>[30]</sup> showing low emission levels, the intensity variation due to thickness requires calibration. Consideration must also be given for the existence of a thermal gradient across the thermographic phosphor. The thicker

the film, the larger the thermal gradient will be between the top surface of the phosphor coating and the surface of the blade. As a result, the requirement is for a phosphor coating of minimal thickness and maximum emission intensity.

- **Thermal Annealing.** Once a thin film has been grown, the post-growth process of annealing is required to activate the phosphor. The sputtering process involves the breaking down of the phosphor into its individual atoms and molecules while depositing them on the substrate to reform the crystal structure. Unfortunately, due to the deposition mechanism, mis-alignment of neighbouring atoms results in an inefficient energy transfer mechanism within the film and leads to weak emission levels. Post-growth thermal treatment assists in ensuring luminescent centres to occupy the appropriate sites, therefore increasing the efficiency of the phosphor. Thin films of  $\text{Y}_2\text{O}_3:\text{Eu}$  have not been grown previously at the university and so characterisation of the thermal annealing process is required.
- **Angular Measurement.** Within the final diagnostic equipment, the probe will be positioned at an angle with respect to the turbine blades. Therefore, both the excitation and collection angle will not be perpendicular to the surface of the blade. An investigation into the angular distribution of intensity will determine the maximum permissible angle for which the probe can be positioned in order to obtain the optimum intensity. Results shown later demonstrate that comparison between thick and thin films have proved advantageous for thin films of  $\text{Y}_2\text{O}_3:\text{Eu}$ .
- **Roughness Measurement.** Measurement of surface roughness will provide an indication of the detrimental effects a coating will have on the aerodynamics of the turbine engine. Of the thick films provided, although they started as very

smooth in appearance, after long periods at high temperatures, the roughness increased. This would lead to a higher loss of material within a running engine due to the centripetal/centrifugal effects and air-flow forces. A thin film should provide a smoother surface finish and so be less detrimental.

- Lifetime Measurement. The experimentation for the lifetime of the phosphor coatings was repeated for thin films with some thick film samples being re-tested for comparison. Again, results proved advantageous for thin films over thick films. As well as surviving for upto ten hours at 1200°C, the thin films showed very little loss in terms of material and intensity compared with the thick film samples.

## **7.2 Growth of Y<sub>2</sub>O<sub>3</sub>:Eu Thin Films**

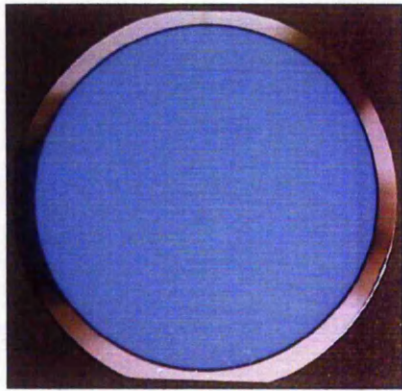
As described in Chapter 3, the system utilised for the growth of the thin films was an RF Magnetron Sputtering vacuum deposition system<sup>[88,89]</sup>. Unfortunately, due to limited availability of the sputtering system, thin films of only one dopant concentration could be grown at various thicknesses. As a result, the decision was taken to grow thin films which would provide maximum intensity levels and without the interference of the rise characteristic. Of the samples available, there was only a sufficient quantity of Y<sub>2</sub>O<sub>3</sub> doped with 35a/o of europium to produce a sputtering target. The films were grown onto 4" silicon wafers which were held a distance of 15cm away from the target on a rotating arm in a cluster magnetron system. The rotating arm assists in the production of an even thickness across the full wafer.

The system was initially pumped down to a base pressure of 10<sup>-7</sup> mTorr. The inert gas of Argon was fed into the system and RF power of 100W at 13.56MHz is supplied to form the plasma. Once formed the plasma pressure is reduced to 3mTorr. A low pressure is preferable to minimise the collision between sputtered atoms and those of the plasma. The

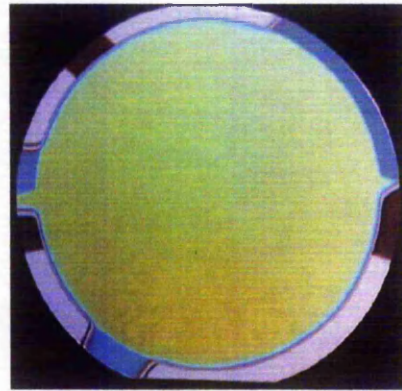
reduction in the number of collision results in a higher deposition rate. All samples were grown at room temperature. For the samples grown, the equivalent thickness for one complete cycle of the interferometer averaged  $1560\text{\AA}$  at a deposition rate of  $580\pm 10\text{\AA}/\text{Hr}$ . Photographs of the grown samples are presented in Figure 7-1 and show a very even growth across the wafer. This is indicated by the consistent colour. It works on the same principle as the interferometer, where the phase difference between reflected light from the top surface of the grown film and that from the surface of the silicon wafer produces the colours seen. A thickness colour chart can be produced via the calibration of a multitude of samples and then be used to estimate the thickness of a grown film. The thickness colour chart for  $\text{Y}_2\text{O}_3:\text{Eu}$  is given in Table 7-1. The refractive index for  $\text{Y}_2\text{O}_3:\text{Eu}$  has been calculated as 2.15, referencing equation 9 from Chapter 3.

Colour	$\text{Y}_2\text{O}_3:\text{Eu}$ Thickness ( $\text{\AA}$ )
Silicon	0-190
Brown	190-370
Golden Brown	370-510
Red	510-680
Deep Blue	680-700
1st Blue	700-840
Pale Blue	840-910
Very Pale Blue	910-1050
Silicon	1050-1120
Light Yellow	1120-1190
Yellow	1190-1400
Orange-Red	1400-1675
1st Red	1675-1745
Dark Red	1745-1955
2nd Blue	1955-2165
Blue-Green	2165-2300
Light Green	2300-2585
Orange-Yellow	2585-2790
2nd Red	2790-3070

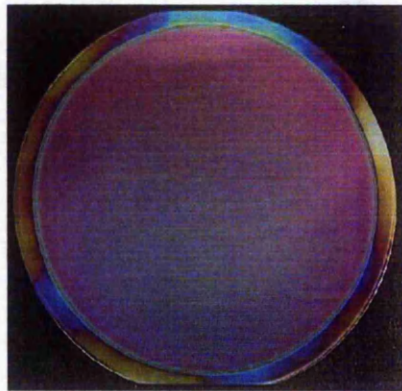
**Table 7-1 Thickness Colour Chart for  $\text{Y}_2\text{O}_3:\text{Eu}$  Thin Film Grown onto Silicon Substrate**



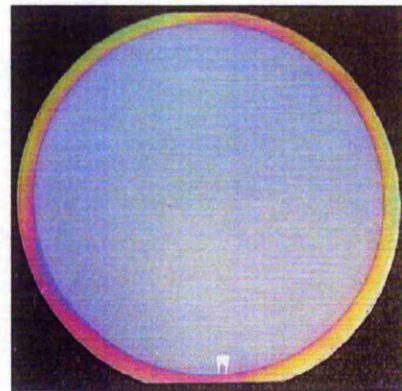
1000 Å



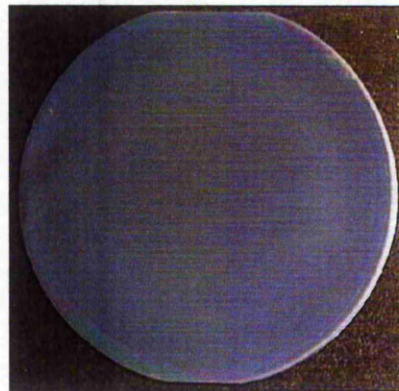
3000 Å



7000 Å



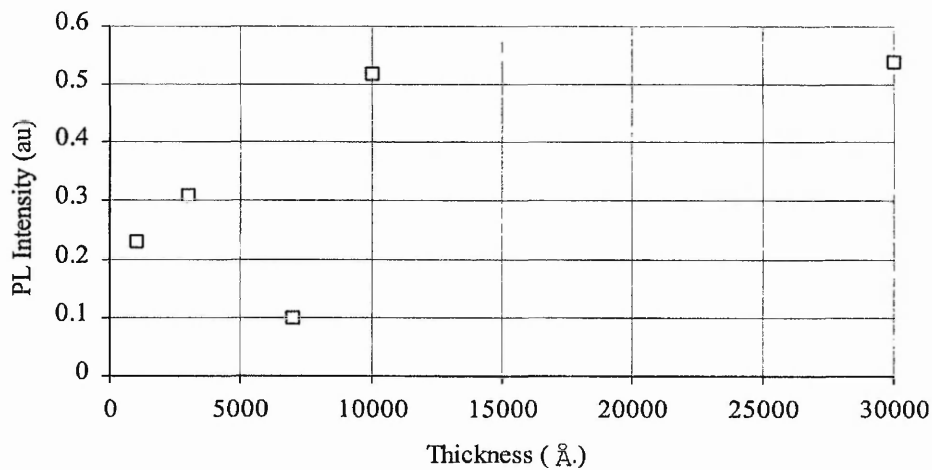
10 000 Å



30 000 Å

**Figure 7-1 Photographs of the  $Y_2O_3:Eu$  samples of various thickness grown by RF Magnetron Sputtering**

Due to the numerous experiments to be carried out on the samples for the optimisation of annealing criteria the wafers were cut into 1cm squares. Intensity measurements of the samples were then obtained using the continuous 325nm HeNe laser, as shown in Figure 7-2. The intensity of non-annealed samples was very weak but did show thickness dependency. Unfortunately, discrepancy exists with the 7000Å sample. Later tests carried out after annealing indicated it was due to the mis-alignment of the europium atoms within the crystal structure of  $Y_2O_3$ .



**Figure 7-2 Intensity Comparison of Non-Annealed  $Y_2O_3:Eu$  35a/o Thin Films**

To confirm the thickness of the films, a dry etching process was performed to define a step between the film and the silicon wafer. The height of the step is then measured using a Sloan Dektak IIA profilometer. Results matched those obtained through the in-situ interferometer by  $\pm 100\text{\AA}$ .

### **7.3 Post Growth Annealing Process**

After deposition, the dopant atoms are situated in a variety of positions and rotations within the crystal structure of the host material. As a result, these atoms experience a variety of crystal field effects, leading to a phosphor with low efficiency. The post-growth process of

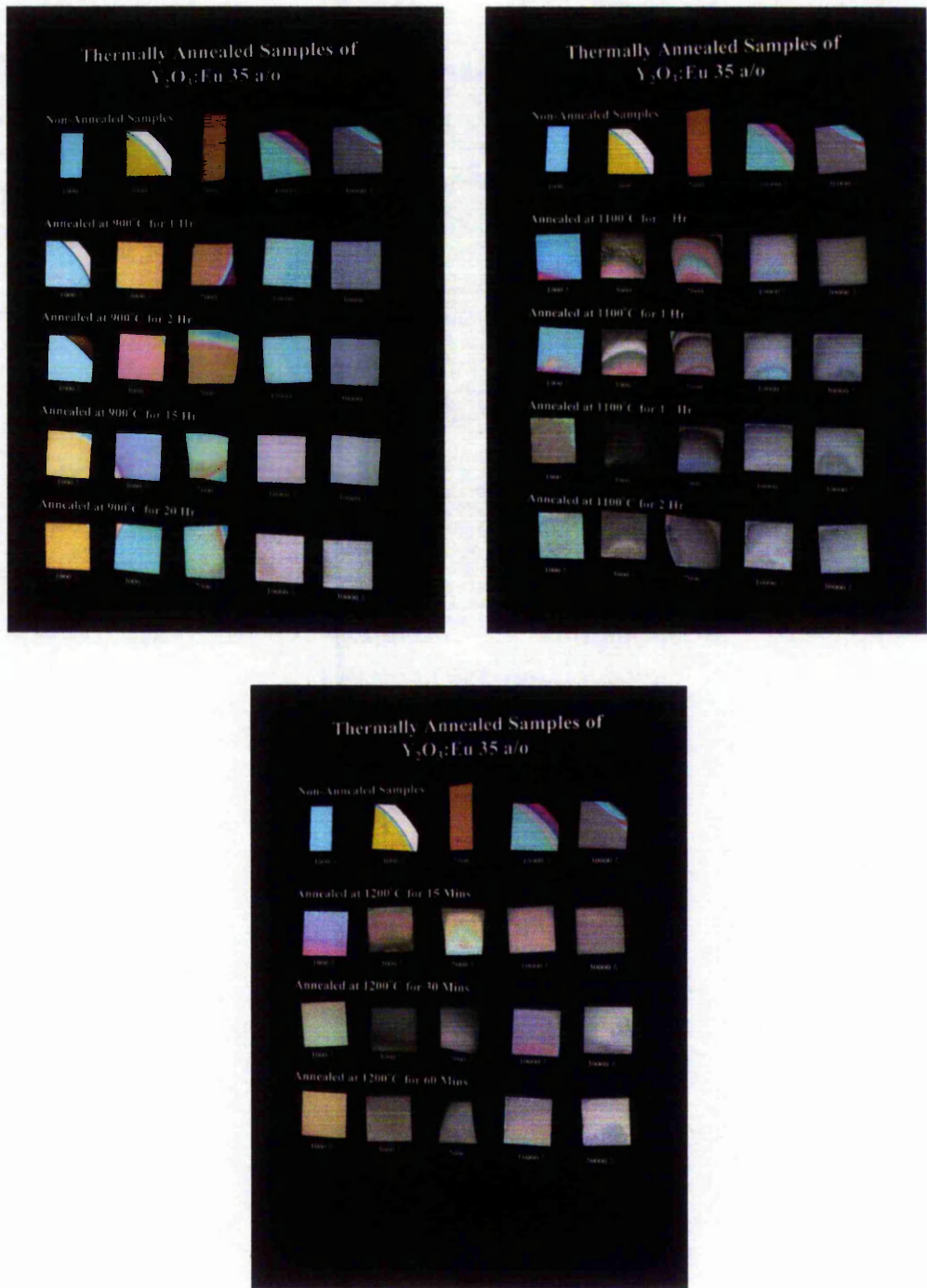
annealing enables the dopant ions to re-position within the host structure and therefore restore the crystalline quality. In turn, this results in the improvement of coupling of excitation energy to the electrons, and therefore enhances the intensity of the phosphor emission levels.

The process of annealing performed was the commonly utilised method of thermal annealing. Other techniques exist including laser annealing<sup>[90]</sup> and rapid thermal annealing<sup>[91]</sup>. For thermal annealing, the sample is heated to a sufficient temperature for thermal energy to be absorbed into the host material and is held at this temperature for a period of time. As long as the temperature is non-detrimental to the component functions and properties, thermal annealing remains the more common method due to lower costs.

### **7.3.1 Thermal Annealing Experimentation**

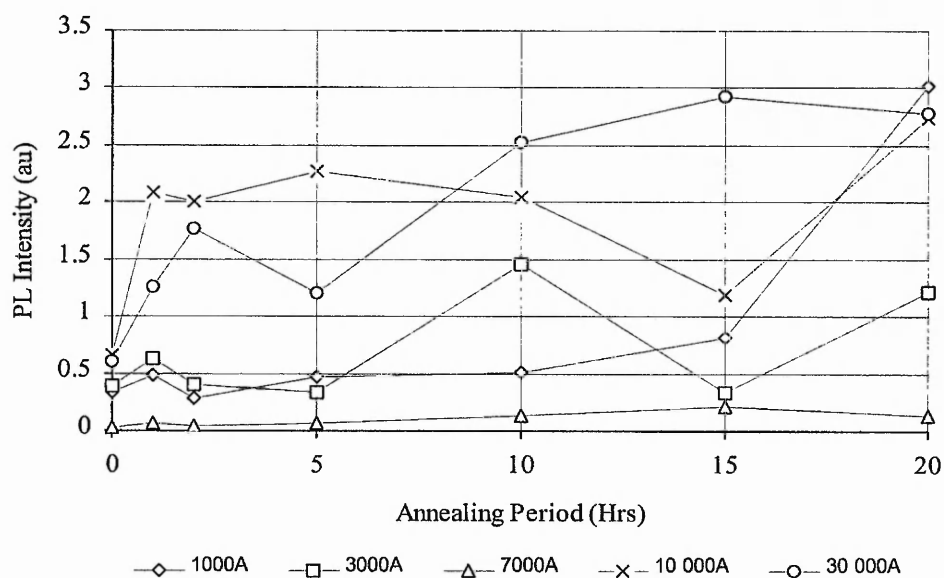
As discussed in section 7.2, the thin film samples were grown onto 4" silicon wafers at five thicknesses. These wafers were then cut into 20mm square samples. This provided 15 samples of each thickness to undergo a series of annealing and lifetime experimentation. Four samples were assigned for lifetime measurement. This allowed eleven to be utilised in a series of annealing experiments to determine optimum annealing temperature and period.





**Figure 7-3 Annealed Samples of  $Y_2O_3:Eu\ 35a/o$  for Various Temperatures and Periods of Time**

Figure 7-3 are photos of the samples after annealing. After each annealing test, the samples were excited with the HeCd 325nm laser and a comparison was made of the emission intensity. Initially, samples were annealed at 900°C for periods of 1, 2, 5 and 10 Hrs. Although the intensity improved, results indicated an even longer period of time was required to achieve maximum emission. Therefore, the samples which had been annealed for periods of 5 and 10 Hrs were returned to the furnace and annealed for a further 10 hours. The intensity improvement achieved is illustrated in Figure 7-4.

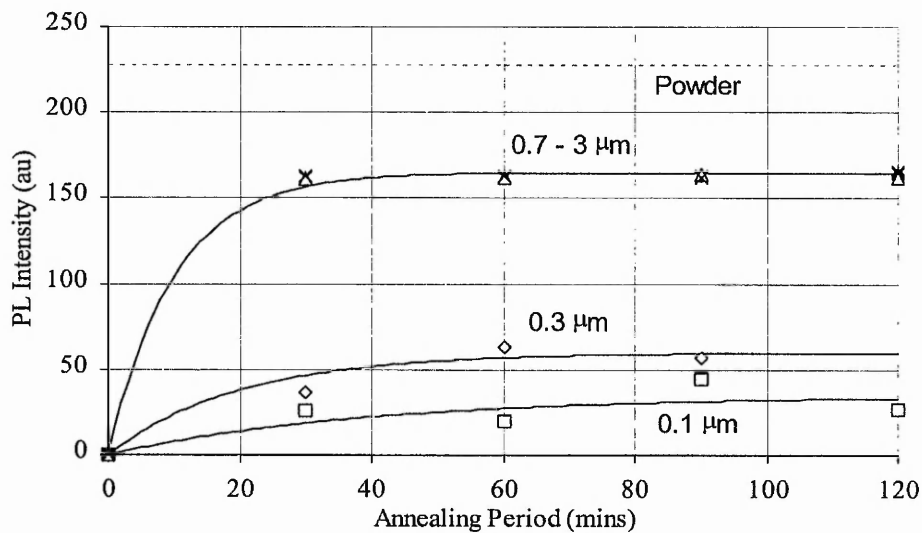


**Figure 7-4 Intensity Measurement of Annealed Thin Film Samples at 900°C**

The results obtained from the 900°C annealed samples are inconclusive. Although the intensity improvement is achieved, the values varied depending on the excited region of the sample. This effect is due to not arriving at the optimum annealing conditions with some areas of the film are annealed, to some extent, and other regions not.

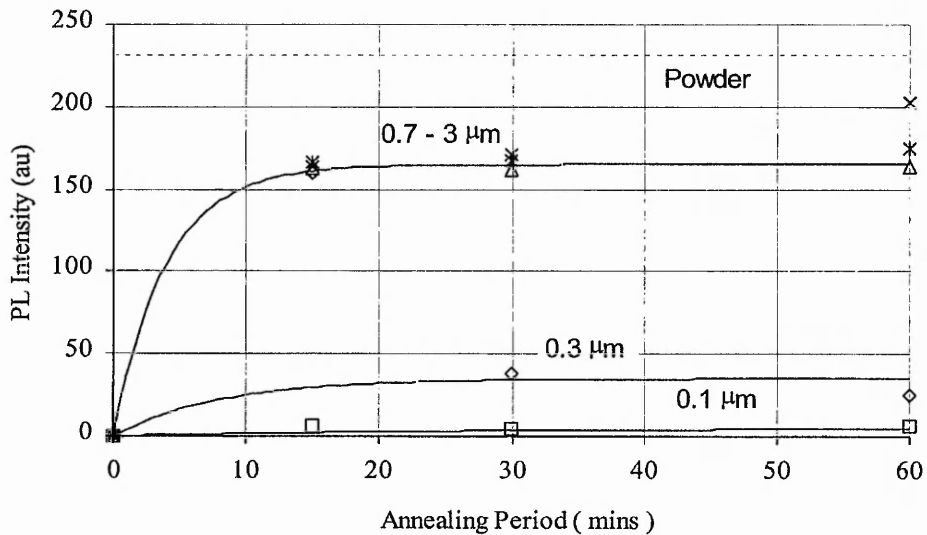
As a result, the annealing temperature was increased to 1100°C and samples were annealed for periods of 0.5, 1, 1.5 and 2 Hrs. From the photo in Figure 7-3, the thin films appear to have an evenly annealed area with less colour variation across each sample. This

consistency is backed up by the intensity measurement as shown in Figure 7-5. Measurement was consistent for 0.7 to 3 $\mu\text{m}$  thickness, indicating an optimum thickness of 0.7 $\mu\text{m}$ . The samples of 0.3 and 0.1 $\mu\text{m}$  have also shown intensity improvement due to the increase in annealing temperature, but are still weaker than the thicker samples. The results also indicated a shorter annealing period is required at a higher temperature. Comparison with the intensity of a powder sample shows the maximum permitted intensity of  $\text{Y}_2\text{O}_3:\text{Eu}$  35a/o has yet to be met and further annealing experimentation was required.



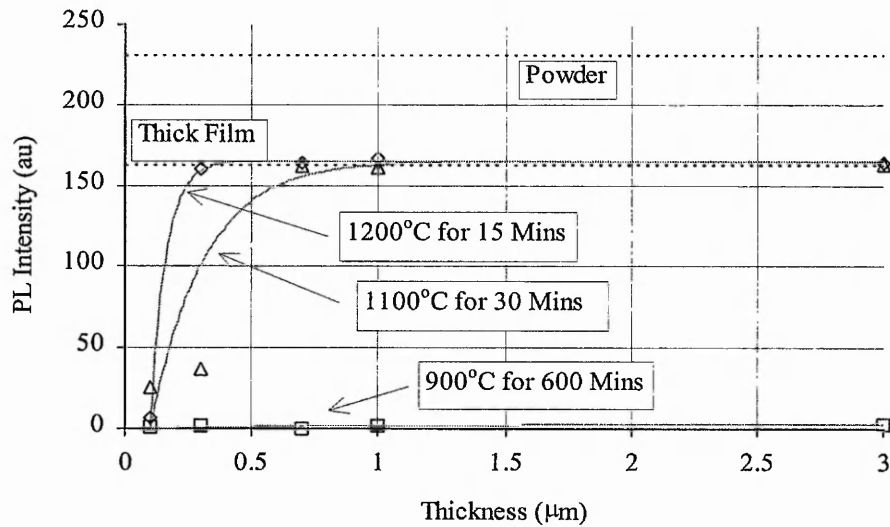
**Figure 7-5 Intensity Measurement After Annealing at 1100°C**

The final set of samples were annealed at a temperature of 1200°C, shown in Figure 7-6. Again, results have shown consistency in the annealing of the 0.7 to 3 $\mu\text{m}$  samples with very little difference in intensity value. There is slight discrepancy with the 0.3 $\mu\text{m}$  sample annealed for a period of 15mins. This showed constant intensity across the complete sample and had an intensity equivalent to that of the thicker samples. Although, the samples annealed for longer periods of time present weaker intensity values, the high intensity of the 15 mins annealed sample should not be dismissed.



**Figure 7-6 Intensity Measurement After Annealing at 1200°C**

In Figure 7-7, a comparison is shown between the annealed thin film samples, thick film samples and powder samples of  $Y_2O_3:Eu$  35a/o. Firstly, it can be concluded that the optimum annealing conditions investigated are 15 mins at 1200°C. It is shown that as annealing temperature increases, the necessary annealing period decreases. Unfortunately, the capabilities of the furnace did not allow for the investigation at higher annealing temperatures. Secondly, comparison with thick film samples indicates an intensity of equal magnitude has been achieved with the annealed thin film samples. Prior to this investigation, the intensity magnitude emitted by a thin film had been its downfall for long term use within phosphor thermography; being lower than that of thick films. Thirdly, optimum thickness for a thin film is between 0.3 to 0.7μm. This is significantly less than the thickness required for a thick film to achieve the equivalent intensity levels. For a thin film, the excitation source will only penetrate to a particular depth which is dependent upon the wavelength and the material. As the thick film contains both the phosphor and the binder, the excitation source penetrates to a greater depth before optimum emission is achieved. As a result, the thermal gradient for a thin film will be less than that of a thick film and so will be a much closer representation of the temperature of the turbine blade.



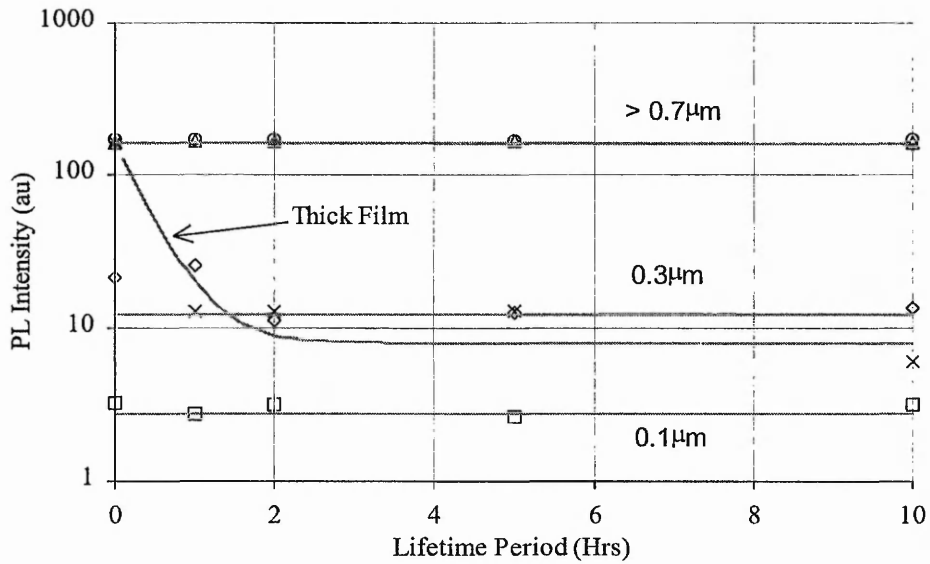
**Figure 7-7 Comparison of the Annealing Conditions Investigated**

With equivalent intensity levels being achieved for the thin films compared with the thick film samples, the next stage was to investigate the lifetime capabilities of the thin films.

#### **7.4 Lifetime Experimentation**

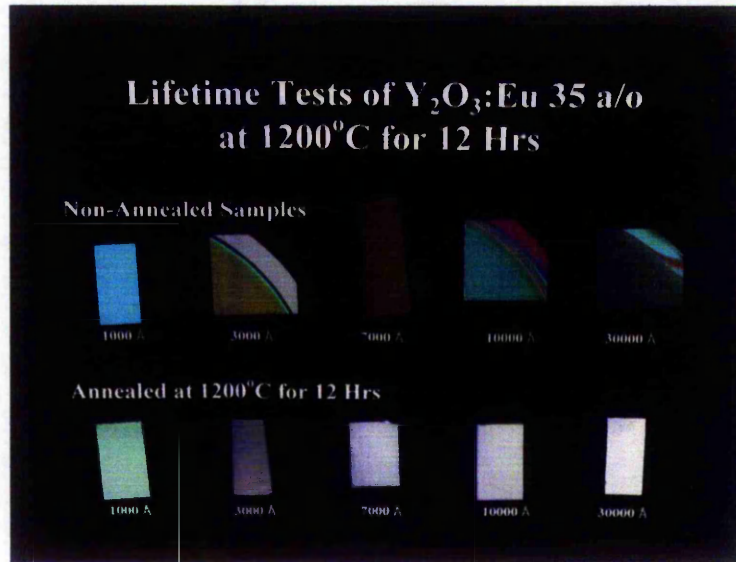
During this experimentation, thick films were also be tested for comparison purposes and therefore subjected to the exact same hostile environment and conditions. The thin film samples were annealed for a period of one hour at 1200°C prior to lifetime measurements. All samples were then left for periods of 1, 2, 5 and 10 Hrs at a temperature of 1200°C. As with the tests carried out previously on the thick films, after the set period of time the samples were removed directly from within the furnace and allowed to rapidly cool to room temperature - simulating the thermal cycles of a turbine engine.

Before and after each lifetime period, the intensity of the films were measured as an indication of degradation due to the hostile environment. Figure 7-8 shows that the intensity levels of the thin film samples remained unaffected compared with the thick films, whose intensity levels degraded after only one hour.

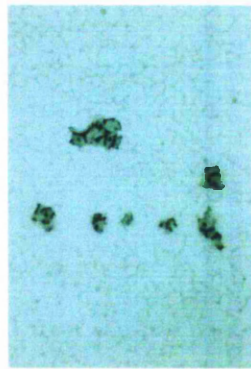


**Figure 7-8 Intensity Measurement of Thin and Thick Film Samples During Lifetime Experimentation**

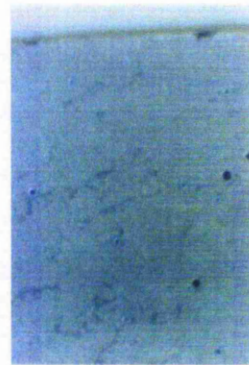
A further lifetime test was carried out on the remaining samples available. These were left for a period of 12 hours at 1200°C. The photograph (a) shown in Figure 7-9 indicates that loss of material occurs for the thicker samples, but it is noted a thin film still strongly adheres beneath. This still shows strong emission and represents no loss of intensity levels. PL intensity measurement showed no difference to the levels experienced during the annealing experimentation at 1200°C. Also shown in Figure 7-9 are close photographs of both thick, (b), and thin, (c), films that have been subjected to 1200°C for a long period of time. Clearly shown is the breakdown of the thick film with cracks occurring throughout. This had been visually noted during the lifetime experimentation of the thick films and eventually led to the loss of material and reduction in intensity emission levels. The thin film, after 12 hours at 1200°C, does not show any defects occurring within the film, proving its long term survivability.



(a)



(b)



(c)

**Figure 7-9 Photographs of Lifetime Experimentation.**

(a) represents the thin films subjected to  $1200^\circ C$  for a period of 12 hours, (b) is a magnified shot of the physical defects of a thick film, and (c) magnified shot of a thin film  $1\mu m$ .

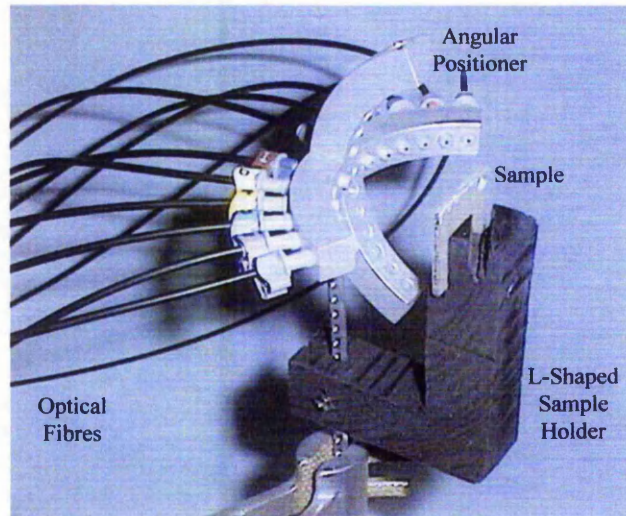
Lifetime measurements have clearly indicated a thin film's survivability advantage over the thick films. With very little degradation in both physical appearance and intensity emission levels, thin films are advantageous over thick films.

### **7.5 Angular Measurement**

An aspect of the photoluminescent emission which requires consideration is the angular distribution. For the diagnostic equipment at Rolls-Royce, a probe has been designed to transmit the pulsed excitation wavelength and collect the resultant emission. Due to the lack of available space within a turbine engine, technical consideration has been given to the size and positioning of the probe to maximise the collection time, area and angle of the probe in relation to the rotating turbine blades. Full technical details cannot be provide due to confidentiality, but it is known the probe will be at an angle of between 30 to 60 degrees to the blade and will be positioned at a distance of approximately 120mm.

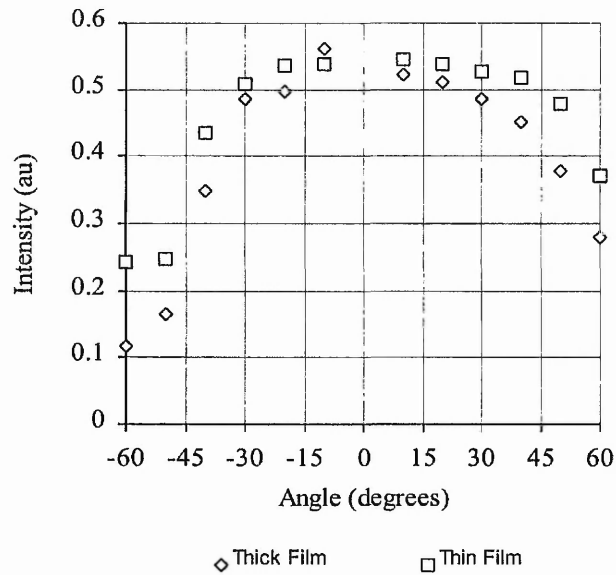
Therefore, the excitation and collection will occur at this angle. Up until this point in the investigation, the pulse laser has been fired at an angle of approximately 20 degrees and the photoluminescent emission collected perpendicular to the surface of the excited source. An angular system was designed to investigate the distribution of emitted light from both thick and thin films. The photograph in Figure 7-10 shows the system. It consisted of two aluminium arcs at 90 degrees to each other which stopped at an angle of 65 degrees to the centre. This allowed holes to be drilled at 10 degree separation within which optical fibres were sited. A simple 'L' shaped holder was produced to hold the samples at the focal point of the angular system. For measurement of the photoluminescent intensity, the CW HeCd 325nm laser was utilised and could be fired through any of the holes of the system. Therefore, the laser could be fired at an angle of 0 to 60 degrees to the surface of the sample and the subsequent emission detected via the optical fibres at other angles. To extend the angular capability of the system, a further slot was set at 30 degrees to the central hole, i.e. the sample could be positioned perpendicular to the 30 degree hole. This enabled collection upto an angle of 90 degrees to the surface of the sample.





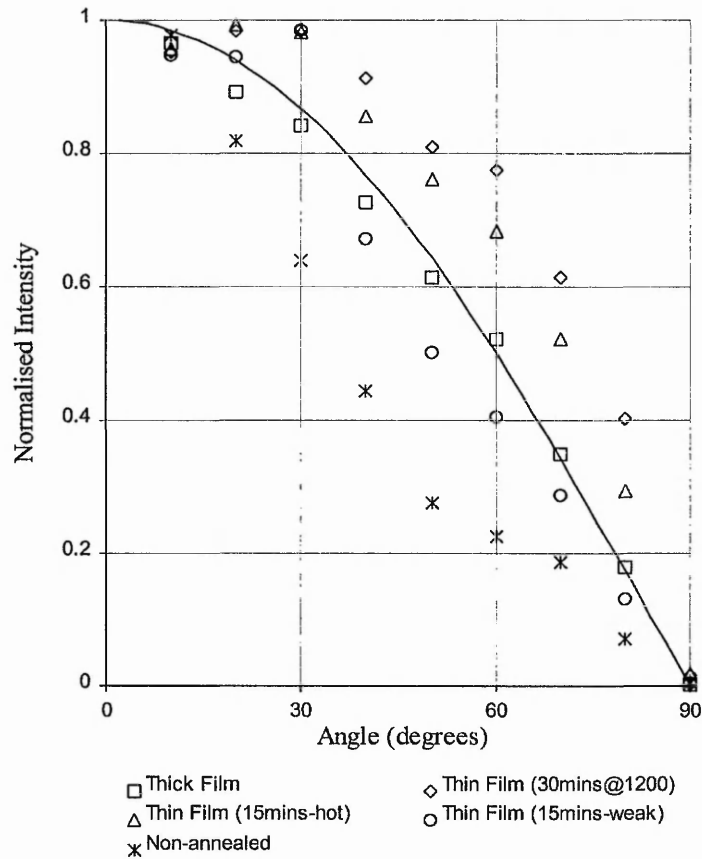
**Figure 7-10 Photograph Of The Angular Distribution Measurement System**

To measure the intensity emitted, the optical fibres were positioned directly in front of the detector and two filters, specific to the wavelength being capture, were attached. Initial tests involved firing the laser perpendicular to the sample and measuring the angular intensity upto 60 degrees to the surface of the sample. The graph shown in Figure 7-11, shows that thin films have a more directional outcoupling of light than the thick film samples. In terms of phosphor thermography, this indicates that a stronger intensity level can be detected from a thin film compared to the signal strength of a thick film at a specific angle.



**Figure 7-11 Comparison of Angular Distribution between Thick and Thin Films**

Although the results do show that thin films distribute better than thick films, they do not indicate even “side-lobes” . This was due to multiple fibres being utilised and each one having a slightly different transmission efficiency. Therefore, a second series of measurements were made with the samples positioned within the 30 degree slot. The laser was fired through the 30 degree hole, allowing for full angular distribution to be measured from 0 to 90 degrees. Also, a single optical fibre was utilised so that the same efficiency would be achieved for all measurements.

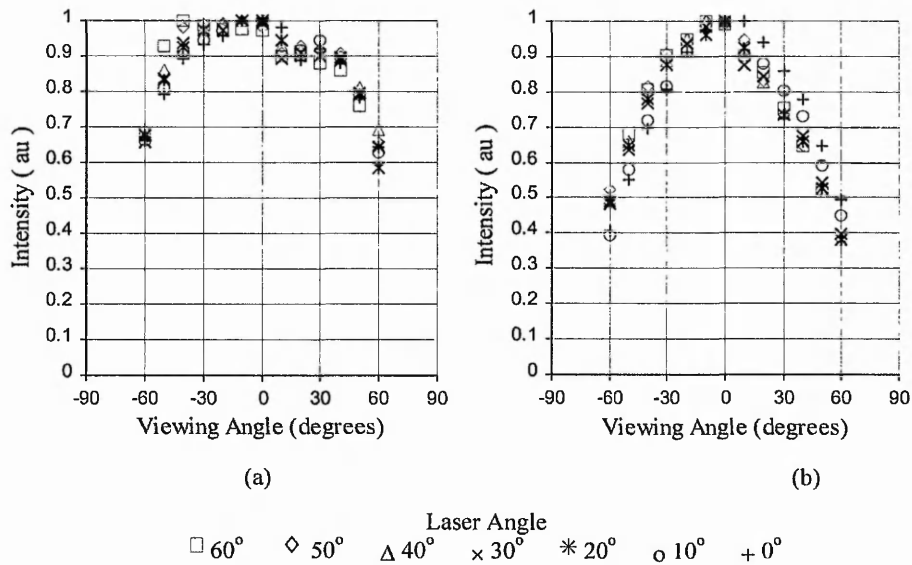


**Figure 7-12 Comparison of the Emission Angular Distribution of Thin and Thick Films**

The above figure shows the variance in angular distribution as a thin film goes through its annealing process. The samples tested were the  $7000\text{\AA}$  films annealed at  $1200^{\circ}\text{C}$ . The thin film sample annealed for 15 minutes was examined twice as only partial annealing had occurred, indicated by 'hot' and 'weak' spots of intensity across the film. Results show that as a thin film is annealed, the intensity dramatically increases and the angular distribution of the light emitted becomes less directional. In other words, the surface of the thin film is tending towards a perfect scattering source - equal emission intensity in all directions - and would be shown within Figure 7-12 as a straight line. Compared with the thick film, its

angular distribution follows a Lambertian distribution - shown as the solid line - and is defined as equal intensity per unit of projected area<sup>[92,93]</sup>.

A second series of experiments involved firing the laser at various angles to investigate whether or not the angle of excitation varied the angular distribution of the light emitted. With the samples sited perpendicular to the centre of the angular measurement system, the laser was fired at angles of 0 to 60 degrees and the intensity at the remaining angles were measured. Unfortunately at the time of the experimentation, the stability of the laser output was questionable with absolute values for the measured intensity varying from test to test. Although this was the case, when the measurements were normalised, consistency was shown in the profiles of the angular distribution and so are presented in this fashion. Figure 7-13 shows the angular distribution of the light emitted is independent of the angle of the excitation source for both thick and thin films.



**Figure 7-13 Angular Distribution of Emitted light with Laser fired at Various Angles**

The above results show consistent angular distributions of emitted light for both thick and thin films. Relating this to the diagnostic equipment for phosphor thermography, if the

probe is to be positioned at an angle of  $45^\circ$  to the surface of the turbine blade, the signal strength from a thin film is 80% compared to 65% of a thick film from perpendicular to the surface. More specifically, the probe was specified as being positioned between an angle of 30 to 60 degrees, indicating the signal strength of a thin film will be between 12.5 to 45 % stronger than a thick film.

By referencing back to intensity comparison measurements made when the laser power output was stable, further conclusions can be drawn. During the annealing experimentation, it was shown that the thin films were emitting a signal strength equal to that emitted by a thick film. These measurements were made using the quartz rod collection system which is positioned perpendicular to the emitting surface. Therefore, it can be concluded that the signal detected by the probe will be stronger for a thin film.

From these measurements, it can be concluded that a thin film is much more efficient than a thick film. It is known that the quartz collection rod has a diameter of 12.5mm and is positioned at a distance of 30mm from the surface of the film. Assuming the surface of the film under test is acting as a point source, it can be calculated that the rod was collecting the light emitted at angles  $\pm 10$  degrees. Through integrating the angular distribution graphs, we can see that this represents 19.6% of the total light emitted by a thick film compared to 15.5% of a thin film. Given that previous measurements showed a thin film to have equal intensity to that of a thick film when collecting at normal to the surface, we can now deduced that from the angular measurements it represented only a small percentage of total light emitted and that a thin film is 25% more efficient in the photoluminescent process than a thick film.

## **7.6 Roughness Measurement**

The surface roughness of the thermographic coating utilised for phosphor thermography must be non-detrimental to the aerodynamics of the engine. Prior to all tests carried out, the surface roughness of the thick film is smooth in appearance. Unfortunately, due to the harsh environmental conditions the film has to survive within, high loss of material leads to an increase in surface roughness. As well as the detrimental effects on the engine's efficiency due to the disruption of air-flow around the turbine blades, both the forces of the air-flow and the centrifugal forces of the rotating blades leads to an increase in the loss of material. This is a further contribution to the reduction of lifetime for the thermographic coating. Also, a measurement of the surface roughness of the coatings provides an indication of the even thickness of coating achievable for both methods of application, thick film or thin film.

To investigate the surface roughness of the films, a Sloan Ila DEKTAK profilometer was used to measure the variance of the roughness across a thermographic coating. Each sample was measured over a profile of 1mm in length and was averaged over five areas of the coating. The film sample is placed on the base plate of the equipment which is controlled by X-Y motion. With the needle of the Dektak making contact with the film sample at a set pressure, a scan of the film is undertaken, and the subsequent movement in the needle is plotted as the films profile.

The profilometer provides two pieces of information concerning the surface texture<sup>[94]</sup>. Firstly, the maximum peak-to-valley height within the sampling length ( $R_{max}$ ) and is a measure of how even is the profile. In the case of the thermographic coatings, it is representative of the variation of thickness across the films. And secondly, the roughness average (R.A.) of the film. This is calculated as the averaged amplitude difference from the mean, where n is the number of sampling points:-

$$R.A. = \frac{\sum |y - \bar{y}|}{n} \quad \text{Equation [22]}$$

	7000 Å Thin Film Samples			Thick Film
	Non-Annealed	15mins@1200°C	30mins@1200°C	
R <sub>max</sub>	500 Å	1200 Å	2000 Å	45,000 Å
R.A.	78 Å	163 Å	354 Å	8,895 Å

**Table 7-2 Roughness measurements of both thin and thick films of Y<sub>2</sub>O<sub>3</sub>:Eu**

The results presented in Table 7-2 shows that a thick film is over 100 times rougher than the annealed thin films. These values provide clear information of how much smoother a thin film is compared to a thick film, and therefore gives an indication of how much less a thin film would be detrimental compared to a thick film for the aero-dynamics and performance of the engine. Clearly, this requires verification through actual test-engine runs.

Also, the roughness measurements may provide information on the angular distribution of emitted light. It is assumed that a luminescent centre acts as an isotropic light emitter, i.e. it emits equally in all directions. Following the laws of reflection and refraction only a percentage of total light created within the luminescent centre will be outcoupled. This percentage can be increased via roughening the surface of the film to act as a scattering source. Comparison between the roughness measurements given in Table 7-2 and the angular distribution comparison graph in Figure 7-12, indicate the annealing process improves the outcoupling of light due to the roughening of the surface. It is known from the Rayleigh scattering principle, that the optimum scattering source would have a radius equal to a quarter of the wavelength. The wavelength emitted by Y<sub>2</sub>O<sub>3</sub>:Eu is 611nm and therefore the optimum radius of a scattering source would be 1527.5Å. Each individual peak-to-valley in the films surface can be viewed as an individual scattering source and therefore its R<sub>max</sub> value is representative of the Rayleigh Scattering Principle. Relating this to the roughness measurements, it is noted that optimum scattering is achieved between R<sub>max</sub> values of 1200Å for 15 minutes annealed sample and 2000Å for the 30 minutes annealed sample. For the

thick film,  $R_{\max}$  is 5 times the optimum radius of a scattering source, therefore losing its scattering properties.

The roughness measurements have once again proved advantageous for thin films. As well as the smoother surface finish, and so less detrimental to aero-dynamics of the engine; the increase in roughness through the annealing process has improved the films scattering properties, hence leads to a stronger signal being detected by the probe at an angle of 40 to 60 degrees.

### **7.7 Summary**

This section of the investigation has proved that thin film phosphor thermography is the probable method of the future for the temperature sensing of remote components within a turbine engine. It has been shown that thin films are advantageous over thick films for several reasons.

Firstly, it has been shown that thin films of  $Y_2O_3:Eu$  can be grown via RF magnetron sputtering, producing films of even thickness and emission intensity across the complete sample surface. This differs from thick films, whose intensity varies from sample to sample and can lead to an increased error in the measurement of temperature when high levels of blackbody radiation is detected at the extreme temperatures. Secondly, intensity comparison of thermally annealed thin films initially showed the emission intensity to be equal to the levels achieved of the thick films. Post annealing experimentation has indicated the required thickness of a thin film to achieve maximum emission permissible is a tenth less than the minimum thickness achievable for thick films. Thick films required a thickness of 25-35 $\mu\text{m}$  to achieve equal intensity obtained by a thin film of 0.7 $\mu\text{m}$ . The reduction in the necessary thickness of coating required for maximum emission assists in the minimisation of the thermal gradient between the top surface of the coating and the surface of the turbine



blade; therefore a reduction in the error between measured temperature and actual temperature of the turbine blades.

Further investigation into the angular distribution of the fluorescent emission has provided thin films with another advantage over thick films. Due to the positioning of the probe being both problematic and limited within an enclosed spacing of the turbine engine, the angular excitation and collection limits the probe's field of view. The information provided by Rolls-Royce Plc, indicated the probe's angular position in relation to the surface of the turbine blade to be within the range 30 to 60 degrees. Angular measurements have shown the intensity to be between 12.5 and 45 % stronger for thin films than for thick films.

Finally, and most importantly, lifetime experiments have shown thin films survive for upto ten hours at 1200°C compared with thick films whose intensity degraded immediately. The degradation of intensity is due to the loss of material from the coating. Although, the surface of the thin film coatings roughens, the strong adhesion properties maintains the coating's survivability.

It can be concluded from this investigation that the phosphor required for the successful temperature measurement of turbine blades through use of phosphor thermography is a thin film coating of  $Y_2O_3:Eu$ . The next stage of the investigation is to apply the thin film coating to the turbine blades and during a turbine engine test-run, monitor the temperature of the turbine blades. This work will be carried out during the next stage of the development of phosphor thermography with a continuation of the collaboration of Rolls-Royce Plc.

## 8. Conclusions and Future Work

### 8.1 Introduction

The aim of this research was to investigate the temperature dependent characteristics of phosphors, specifically for the measurement of the surface temperature of turbine blades within a gas turbine engine. Accurate temperature sensing of vital components within an engine will lead to an increase in engine efficiency and design. The use of a sensor must be non-detrimental to the aerodynamics and hence the efficiency of the engine. With a phosphor thermography based measurement system, this effect is minimised by coating the turbine blades with a thin layer of a thermographic phosphor. The collection and analysis of the photoluminescent emission after pulsed excitation leads to the determination of the surface temperature of the blade.

The measurement systems for the characterisation of thermographic phosphors have been calibrated and optimised to allow for maximum signal-to-noise ratio. These systems are automated through use of LabVIEW software creating virtual instruments; providing a user friendly graphical system. Work has concentrated on the thermographic characterisation of  $\text{Y}_2\text{O}_3:\text{Eu}$  and  $\text{YAGaG}:\text{Tb}$  phosphors for a full range of dopancy levels. This includes the emission spectra of the phosphors at various temperatures; decay constant characterisation with respect to temperature and excitation wavelength; and the optimisation of emission intensity levels for the maximisation of the detected signal.

Two new concepts have been demonstrated during the course of this study, for which patent applications have been completed (see List of Publications section). Firstly, the discovery of the novel rise constant characteristic has extended the temperature sensing range of  $\text{Y}_2\text{O}_3:\text{Eu}$ . This enables a single phosphor to be utilised for the temperature range of  $25^\circ\text{C}$  to  $+1100^\circ\text{C}$ . Previously a combination of phosphors would have been required, each with a specific temperature sensing range. And secondly, the fabrication of thin films of  $\text{Y}_2\text{O}_3:\text{Eu}$

by RF Magnetron Sputtering have produced robust thermographic coatings which have the capability of surviving hostile environments. These thin films have shown emission intensity levels equal to those obtained with thermographic paints, but have the advantage of surviving in an environment at 1200°C for a period of ten hours. A thermographic paint survived less than one hour in identical conditions.

To conclude this thesis, there follows a discussion of the achievements of this study, and the possible future of phosphor thermography within the field of temperature sensing of turbine blades.

## **8.2 Achievements**

The achievements of this research programme can be summarised as below:-

- 1) Development of an automated analysis system for the characterisation of thermographic phosphors.
- 2) Thermographic characterisation of  $Y_2O_3:Eu$ .
- 3) Identification of a novel low temperature dependent characteristic.
- 4) Thermographic characterisation of  $YAGaG:Tb$ .
- 5) Comparison of  $Y_2O_3:Eu$  and  $YAGaG:Tb$  thermographic phosphors.
- 6) Evaluation of the lifetime of  $Y_2O_3:Eu$  and  $YAGaG:Tb$  thermographic paints.
- 7) Thin film phosphor thermography.

### **1) Development of an analysis system for the characterisation of thermographic phosphors.**

This can be split into the emission spectrum analysis equipment and the decay constant characterisation system. For both systems, an increase in the capability to detect weak

emission levels has been achieved through the use of a quartz rod. This optimisation has provided a signal of sufficient strength to allow characterisation of the temperature dependent properties up to  $+1100^{\circ}\text{C}$ . The limiting factor within this system has been the maximum temperature attainable within the furnace. The strength of the detected signal was further increased by the removal of the spectrometer from the decay constant characterisation system. The spectrometer was replaced with two filters which were specific to the wavelength being detected, thus positioning the detector closer to the quartz rod and so reducing the loss of signal. An investigation into the sensing capabilities of the detector concluded that a gating system was inappropriate due to its slow response time, and hence, interference with the photoluminescent characteristics. Finally, the development of virtual instruments using LabVIEW software has enabled both systems to become fully automated.

## 2) Thermographic characterisation of $\text{Y}_2\text{O}_3:\text{Eu}$ .

$\text{Y}_2\text{O}_3:\text{Eu}$  has been characterised for a range of dopancy levels - 0.5a/o to 75a/o. This involved the optimisation of the main emission peak (611nm) intensity level through the variation of the dopancy levels and the excitation wavelengths available with a Nd:YAG pulse laser (355nm and 266nm). The decay constant temperature dependency has been characterised by using a single exponential curve fitting routine. Results show 355nm excitation provides a quenching temperature of  $550^{\circ}\text{C}$  with a quenching rate of  $15.4\text{mC}^{-1}$ . These characteristics remained consistent up to a dopancy of 25a/o. Improvement was gained through utilisation of the excitation wavelength 266nm. This resulted in an intensity increase of the 611nm spectral line by an order of magnitude and induced an optimum dopancy shift to a lower concentration of 10a/o, without effecting the decay constant characteristics.

### 3) Identification of a novel low temperature dependent characteristic.

A delayed rise in photoluminescent emission led to the discovery of new temperature dependent characteristic within  $\text{Y}_2\text{O}_3:\text{Eu}$ . This has been modelled by consideration of the possible internal transitions occurring between the neighbouring sites of symmetry -  $C_{3i}$  and  $C_2$  within the host lattice. The rise constant characteristic of  $\text{Y}_2\text{O}_3:\text{Eu}$  has a temperature dependency range of  $25^\circ\text{C}$  to  $700^\circ\text{C}$  with a quenching rate which is dependent on the dopancy. Identification of this new characteristic has been demonstrated to successfully extend the temperature sensing capabilities of  $\text{Y}_2\text{O}_3:\text{Eu}$ . Hence, by utilising both the decay and rise characteristics of  $\text{Y}_2\text{O}_3:\text{Eu}$ , a full temperature range from  $25^\circ\text{C}$  to  $+1100^\circ\text{C}$  can be monitored.

### 4) Thermographic characterisation of YAGaG:Tb.

The thermographic characteristics of YAGaG:Tb have been measured, with dopancy dependency being investigated over the range of 1a/o to 50a/o. Intensity is maximised at 10a/o for 266nm excitation, which has been shown to produce higher intensity levels of the 544nm spectral line compared with the excitation wavelength of 355nm. Results presented indicate the photoluminescence decay of YAGaG:Tb has a double exponential characteristic. This has been modelled by considering the effect of the two possible neighbouring cations to the terbium atom - aluminium or gallium. This results in the determination of two decay constants. The dominant constant has a quenching temperature of  $600^\circ\text{C}$  with a quenching rate of  $12.0\text{mC}^{-1}$  at the optimum excitation wavelength of 266nm. At the same excitation wavelength, the minor constant has a quenching temperature of  $750^\circ\text{C}$  with a quenching rate of  $13.9\text{mC}^{-1}$ . This provides YAGaG:Tb with the same decay constant temperature sensing range of  $\text{Y}_2\text{O}_3:\text{Eu}$ , but with a lower quenching rate. Hence, is less sensitive to temperature fluctuations. YAGaG:Tb also exhibits a rise characteristic

which occurs only at an excitation wavelength of 266nm. It has a temperature sensing range of 400°C to 700°C.

5) Comparison of Y<sub>2</sub>O<sub>3</sub>:Eu and YAGaG:Tb thermographic phosphors.

Results presented have shown Y<sub>2</sub>O<sub>3</sub>:Eu to be a more efficient phosphor than YAGaG:Tb, thus producing higher intensity emission levels at both excitation wavelengths. The stronger emission intensity of Y<sub>2</sub>O<sub>3</sub>:Eu is therefore easier to detect, even with the existence of high levels of blackbody radiation emitted within a high temperature environment. Also, decay constant characterisation has shown instability for YAGaG:Tb due to the double exponential characteristic; compared to Y<sub>2</sub>O<sub>3</sub>:Eu, whose characteristics are consistent and cover a wider temperature sensing range. Finally, the accuracy achievable with Y<sub>2</sub>O<sub>3</sub>:Eu is ±0.65°C, compared with ±4.2°C of YAGaG:Tb.

6) Evaluation of the lifetime of Y<sub>2</sub>O<sub>3</sub>:Eu and YAGaG:Tb thermographic paints.

Thermographic paints of both phosphors were produced and coated onto test coupons. Intensity variation due to thickness showed optimum thickness was unachievable due to the paint failing to adhere to the coupons at thicknesses of 35µm. Prior to high temperature tests, the maximum intensity achievable was with a coating thickness of approximately 25-30µm. Lifetime experimentation carried out at temperatures of 1200°C for periods of up to ten hours, immediately showed a decrease in peak intensity emission due to the loss of film. These poor lifetime measurements, resulted in the investigation into the growth of thin films.

7) Thin film phosphor thermography.

Thin films of Y<sub>2</sub>O<sub>3</sub>:Eu 35a/o have been grown via RF Magnetron Sputtering at various thicknesses. Thermal annealing experimentation shows optimum conditions to be 1200°C for a period of 15 minutes. Maximum intensity is achieved with a thickness of 0.7µm and is

equal to the intensity levels obtained with a thermographic paint of 25 $\mu\text{m}$  thickness. Thin film thermographic phosphors have thus demonstrated for the first time to be advantageous over thermographic paints due to a longer survivability rate within hostile environments, a better angular distribution of the photoluminescent emission, and the minimisation of the error induced by the existence of a thermal gradient.

### **8.3 Recommendations**

To meet the requirements for turbine engine diagnostic equipment and with reference to the phosphor specification as given in Chapter 3, the recommendation is :

To use a thin film coating with a thickness of 0.7 $\mu\text{m}$ , of  $\text{Y}_2\text{O}_3:\text{Eu}$  at a dopancy level of 7a/o and to utilise the excitation wavelength of 266nm available from the Nd:YAG pulse laser.

This allows use of both the rise and decay constant characteristics in the determination of the temperature of components. By using a dopancy level which is slightly below the optimum for 266nm excitation, a wider temperature range can be detected for a minimal loss of intensity. Also, this enables the use of a single phosphor throughout the turbine engine, allowing for the diagnostic equipment to detect within the lower temperature regions as well as the high. These characteristics meet the rotational speed limitations of the turbine blades. Finally, it has been proved that thin films can survive the high temperatures reached for periods of up to ten hours and produce better angular distributions of the photoluminescent emissions, which is very important the positioning of the probe within a confined space.

### **8.4 Future Work.**

The research undertaken during this doctoral study is part of the ongoing process into the development of phosphor thermography at The Nottingham Trent University, with the specific aim of utilisation within turbine engine diagnostic equipment. As stated in the

previous section, this stage of the process has recommend the use of thin films of  $Y_2O_3:Eu$ .

The future work required for such a research programme is :-

- a) the development of the growth process of  $Y_2O_3:Eu$  thin films to optimise the europium concentration and the probable  $Y_2O_3$  composition of the matrix.
- b) the investigation of the post-growth process of annealing / laser annealing of the above films.
- c) the conduction of field tests of thin film coated turbine blades during an engine test-run.

Firstly, the films grown via RF magnetron sputtering process have currently involved the use of  $Y_2O_3:Eu$  35 a/o. Work presented has shown that the recommended dopancy is 7a/o. It is further recommended that samples of thin films are grown via RF cluster magnetron sputtering. This involves the use of two sputtering targets - an undoped  $Y_2O_3$  target and a heavily doped  $Y_2O_3:Eu$  target. By applying different power to each target, the dopant concentration of the grown thin film can be controlled<sup>[88]</sup>. This will allow a variety of concentrations to be grown to establish the optimum dopancy. Also, past investigation on the growth of  $ZnS:Mn$  films for display technology, have shown the existence of sulphur deficiency which reduces the photoluminescent efficiency of the films. Subsequently, films were grown in an  $Ar:H_2S$  environment, reduced the density of sulphur vacancies and hence improved the photoluminescent efficiency of the films<sup>[95]</sup>. Hence, growth of  $Y_2O_3:Eu$  within an  $Ar:O_2$  environment could reduce the number of oxygen vacancies, possibly leading to a higher efficiency in photoluminescent intensity.

Secondly, the development of the post-growth annealing process requires investigating. Current results have shown thermal annealing requires a temperature of  $1200^\circ C$  for a period of 15 minutes. Phosphor suppliers and the literature state that during the manufacturing process of powder phosphors, temperatures of above  $1400^\circ C$  are utilised during the firing



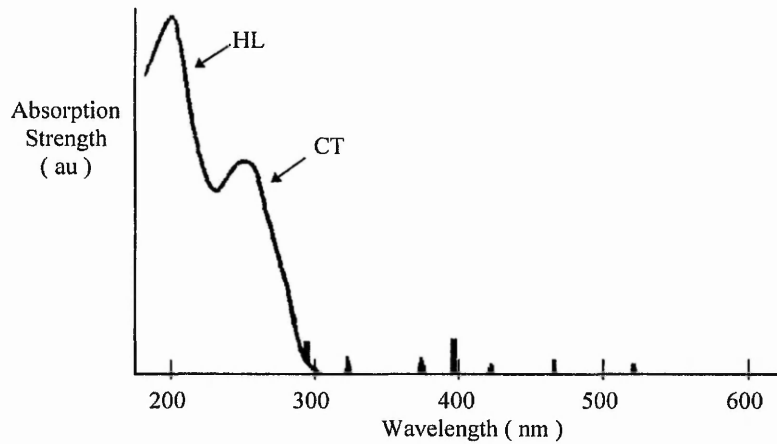
stage of the process. Eventually, thin film coatings will be fabricated onto the turbine blades which cannot survive this high thermal annealing temperature. Therefore, the alternative method of laser annealing requires investigating.

The process of laser annealing is currently under investigation for the improvement of emission intensity of ZnS:Mn for thin film electroluminescent displays<sup>[96,97]</sup>. It involves irradiating the thin film with photons of energy which are greater than the band gap of the host lattice. The absorption of the energy induces a rise in temperature within the host lattice, and is sufficient enough to allow for the re-formation of the crystalline structure. Recent tests carried out on thin films of Y<sub>2</sub>O<sub>3</sub>:Tb have induced an improvement in photoluminescent emission levels when laser annealed using a KrF laser at 249nm (~4.98eV). Tropf<sup>[98]</sup> states that information obtained from a variety of sources give the band gap of Y<sub>2</sub>O<sub>3</sub> at values between 5.5 to 6.0 eV. The energy provided by the KrF laser is insufficient to be absorbed into the host lattice, so an alternative mechanism for the transfer of the energy must be occurring to result in the improvement of emission levels.

The origin of this mechanism is currently unknown. It is possible, the laser energy is absorbed by the lattice defects. Within a poly-crystalline structure, lattice defects result in states existing sub-band gap, and are not limited to the valence and conduction bands of the host. It is proposed these states which exist sub-band gap are those which absorb the energy of the KrF laser, resulting in the annealing process of the thin films.

A second explanation involves the absorption by the oxygen. Figure 8-1, shows the absorption spectrum of Y<sub>2</sub>O<sub>3</sub>:Eu<sup>[99]</sup>. It shows two broad band absorption regions which are associated with the host lattice, HL, and the charge-transfer transition, CT, and are present for most phosphor absorption spectra. The host lattice absorption region peaks at 197nm (~6.0eV), the energy gap of Y<sub>2</sub>O<sub>3</sub>. The charge-transfer region exists due to absorption by the oxygen, whose excited state is then transferred to the europium. This region is centred

at 250nm, and therefore, it is suggested that the laser energy of the KrF is absorbed by the oxygen, and hence allows the annealing of the localised area.



**Figure 8-1 Absorption Spectrum Of  $Y_2O_3:Eu$**

In terms of laser annealing of thin thermographic phosphors, the advantage lies in the effect of only raising the temperature of the surface-under-examination. This is because the laser pulse will penetrate to a depth which is dependent upon the wavelength utilised. As a result, the annealing process remains localised and damage to the turbine blades would be minimised. An investigation into the process of laser annealing of thermographic thin film phosphors is therefore required.

Finally, field test studies on turbine blades coated with the optimum thermographic thin film would be undertaken to test the complete temperature sensing diagnostic equipment. Experimentation would involve the capturing of photoluminescent characteristics and subsequent determination of the temperature of rotating blades during a turbine engine test-run. The results obtained would provide vital information to assist in the design and improvement in efficiency of the turbine engines.

## References

- 1 SW Allison, GT Gillies; "*Remote Thermometry with Thermographic Phosphors : Instrumentation and Applications*" Rev. Sci. Instrum ,Vol.68, No.7, pp2615-2650, July 97.
- 2 KTV Gratten, AW Palmer; "*Infrared Fluorescence 'Decay-Time' Temperature Sensor*", Rev. Sci. Instrum., Vol.56, No.9, pp1784-1787, Sept 85.
- 3 LJ Dowell; "*Fluorescence Thermometry*" Appl. Mech. Rev., Vol.45, No.7, pp253-260, July 92.
- 4 Noltingk, BE; "*Instrumentation Reference Book*", Butterworth-Heinemann Ltd, 2nd Ed, (1995, )Part 2 Chapter 1 *temperature sensing* pp 1-67.
- 5 C Loughlin; "*Sensors for Industrial Applications*", Kluwer Academia Publishers, 1993.
- 6 K Ding; "*Tests of Jet Engine Turbine Blades by Thermography*", Jn Optical Eng., Vol.24, No.6, pp1055-1059, Dec 85.
- 7 H Cohen, GFC Rogers, HIH Saravanamuttoo; "*Gas Turbine Theory*", Addison Wesley Longman Ltd, 4th Ed, 1996.
- 8 C Bird, JE Mutton, R Shepherd et al; "*Surface Temperature Measurement In Turbines*", AGARD PEP Symposium on Advanced Non-Intrinsic Instrumentation for Propulsion Engines, Paper no.21, Brussels, Belgium, 20-24 Oct'97.
- 9 MR Cates et al; "*Remote Thermometry of Moving Surfaces by Laser-Induced Fluorescence of Surface-Bonded Phosphor*", ICALEO'83 Proceedings: Inspection, Measurement and Control, Vol.39, pp50-53, 1983.
- 10 KH Butler; "*Fluorescent Lamp Phosphors - Technology and Theory*", Pennsylvania University Press, May 1980.
- 11 Neubert; US Patent No. 2,071,471 , 1937.
- 12 S Shionoya, WM Yen; "*Phosphor Handbook*", CRC Press, 1999.
- 13 G Blasse, BC Grabmaier; "*Luminescent Materials*" Springer-Verlag, 1994.
- 14 MR Cates et al; "*Applications of Pulse Laser Techniques and Thermographic Phosphors to Dynamic Thermometry of Rotating Surfaces*" ICALEO'84 Proceedings: Inspection, Measurement and Control, Vol.45, pp4-10, 1984.
- 15 L Mannik, SK Brown, SR Campbell; "*Phosphor Based Thermometry of the Rotor in a High Power Electric Generator*" Applied Optics Vol.30, No.19, pp2670-2677, 1987.

- 16 SW Allison et al; "*Monitoring Permanent Magnet Motor Heating with Phosphor Thermography*", IEEE Trans Instrumentation and Measurement, Vol.37, pp637-641, 1988.
- 17 SS Lutz et al; "*Remote Temperature Measurement Instrumentation for a Heated Rotating Turbine Disk*" 34th Int Instr Symp Alb, ISA Paper 88-0725, 1988.
- 18 BW Noel et al; "*Evaluating Thermographic Phosphors in an Operating Turbine Engine*", Gas Turbine and Aerospace Congress and Exposition Brussels, ASME Paper 90-gt-266, 11-14 June 1990.
- 19 LE Tannas Jr; "*Flat-panel Displays and CRTs*" Van Nostrand Reinhold, New York, 1985.
- 20 L Owaza; "*Cathodoluminescence*", VCH, Weinheim, 1990.
- 21 N Apriarian; "*The Centenary of the Discovery of Luminescent Zinc Sulphide*", Proc. Int. Conference of Luminescence, pp903-906, 1966.
- 22 As Ref.12; page 217-230.
- 23 HG Jenkins, JN Bowtell; "*High Voltage Fluorescent Tubes*", Trans Illum Eng Soc (London) Vol.13, pp61-87, 1945.
- 24 Humbolt Leverenz; "*An Introduction to Luminescence Solids*", Dover Publications, 1968.
- 25 D Curie; "*Luminescence in Crystals*", John Wiley & Sons, 1963.
- 26 As Ref. 20; page 165.
- 27 LP Goss, AA Smith, ME Post; "*Surface Thermometry by Laser Induced Fluorescence*", Rev Sci Instr. Vol.60, No.12, pp3702-3706, Dec'89.
- 28 MK Chyu, DJ Bizzak; "*Two Dimensional Laser Induced Fluorescence Temperature Measurement on a Rotating Surface*", ASME - Visualisation of Heat Transfer Process, HTD-Vol. 252, pp 47-53, 1993.
- 29 As Ref.13; page 38.
- 30 AJ Simons, CB Thomas; "*Phosphor Thermography - A Feasibility Study*", University of Bradford, SERC/MOD Research Report Ref GR/F29509, 1992.
- 31 As Ref. 25; page 37-40.
- 32 As Ref. 12; page 86-87.
- 33 RC Ropp; "*Luminescence and the Solid State*", Elsevier, 1991.

- 34 S Erdei, R Roy, G Harshe *et al*; "*The Effect of Powder Preparation Processes on the Luminescent Properties of Yttrium Oxide Based Phosphor Materials*", Materials Research Bulletin, Vol.30, No. 6, pp745-753, 1995.
- 35 SW Allison, DL Beshears, MR Cates *et al*; "*Phosphor Thermometry of Gas Turbine Surfaces*", Int. Gas Turbine and Aeroengine Congress, Houston, Texas, 5-8 June, 1995.
- 36 BW Noel, SW Allison, DL Beshears *et al*; "*Evaluating and Testing Thermographic Phosphors for Turbine-Engine Temperature Measurements*", AIAA/SAE/ASME/ASEE 23rd Joint Propulsion Conference, San Diego, California, 29 June - 2 July, 1987.
- 37 AR Bugos, SW Allison, LJ Dowell and GT Gillies; "*Remote High Temperature Electro-Optical Sensing Using  $YVO_4:Dy^{3+}$  Thermographic Phosphors*", Proceedings of IEEE Southeast Conference, 1990.
- 38 AR Bugos, SW Allison and MR Cates; "*Computer-Assisted Method For Determining The Onset Quenching Temperature Of Luminescent Thermographic Phosphors*", Proceedings of IEEE Southeast Conference, 1990.
- 39 W Lewis, WD Turley, HM Borella and BW Noel; "*Noncontact Thermometry in Excess of 2500°F Using Thermographic Phosphors*" ISA 1990, Paper #90-103, pp23-27.
- 40 AR Bugos, SW Allison and MR Cates; "*Laser-Induced Fluorescent Properties of Europium-doped Scandium Orthophosphate Phosphors For High Temperature Sensing Applications*", IEEE Proceedings of The Southeastcon 91, Vols 1 and 2, Ch 280, pp 1143-1147, 1991.
- 41 SW Allison, MR Cates *et al*; "*Remote Thermometry in a Combustion Environment Using Phosphor Technique*", Flow Visualisation and Aero-Optics in Simulated Environments, Ch 13, pp90-99, 1987.
- 42 KW Tobin, SW Allison, MR Cates *et al*; "*High-Temperature Phosphor Thermometry of Rotating Turbine Blades*", AIAA Journal, Vol 28, No.8, pp1485-1490, 1990.
- 43 L Mannik, SK Brown and SR Campbell; "*Phosphor-Based Thermometry of Rotating Surfaces*", Jn of Applied Optics, Vol.26, No.18, pp 4014-4017, 1987.
- 44 BW Noel, HM Borella, LA Franks *et al*; "*Proposed Laser-Induced Fluorescence Method For Remote Thermometry in Turbine Engines*", Jn of Propulsion and Power, Vol.2, No.6, pp 565-568, 1986.
- 45 Z Zhang, KTV Grattan and AW Palmer; "*Thermal Characteristics of Alexandrite Fluorescence Decay at High Temperatures, Induced by a Visible Laser Diode Emission*", Jn of Applied Physics, Vol 73, pp3493-3498, 1993.

- 46 SD Alaruri, AJ Brewington, MA Thomas and JA Miller; "*High-Temperature Remote Thermometry Using Laser-Induced Fluorescence Decay Lifetime Measurements of  $Y_2O_3:Eu$  and YAG:Tb Thermographic Phosphors*" IEEE Transactions on Instrumentation and Measurement, Vol.42, No.3, pp735- 739, 1993.
- 47 MR Cates, SW Allison, LA Franks *et al*; "*Laser-Induced Fluorescence of Europium-Doped Yttrium Oxide for Remote High- Temperature Thermometry*" Proceedings of the Medicine and Biology; Optical Techniques for Measurement and Control; Spectroscopy, Photochemistry and Scientific Measurement Symposia of ICALEO '85, Ch 27, pp 142-147.
- 48 Z Zhang, KTV Grattan and AW Palmer; "*Fiber Optic Temperature Sensor Based On The Cross Referencing Between Blackbody Radiation and Fluorescence Lifetime*" Review Of Scientific Instruments, Vol.63, No.5, pp 3177-3181, 1992.
- 49 Z Zhang, KTV Grattan and AW Palmer; "*Fiberoptic High-Temperature Sensor Based on the Fluorescence Lifetime of Alexandrite*", Review of Scientific Instruments, Vol.63, No.8, pp 3869-3873, 1992.
- 50 K Sowa, M Tanabe *et al*; "*Growth of  $Y_2O_3:Eu$  Thin Films by Reactive Magnetron Sputtering and Electroluminescent Characteristics*", J Appl. Phys. Vol.32, No.12a, pp5601-5602, Dec 1993.
- 51 WD Turley, HM Borella, DL Beshears; EG&G Energy Measurements, Inc Technical Report No. EGG-10617-2133, March 1992.
- 52 RP Roa; "*Preparation and Characterisation of Fine-Grain Yttrium-Based Phosphors by Sol-Gel Process*", Jn. Electrochem. Soc., Vol.143, No.1, pp189-197, Jan 1996.
- 53 RP Roa; "*Growth and Characterisation of  $Y_2O_3:Eu^{3+}$  Phosphor Films by Sol-Gel Process*", Solid State Comms. Vol.99, No.6, pp439-443, 1996.
- 54 SL Jones, D Kumar, RK Singh *et al*; "*Luminescence of Pulsed Laser Deposited Eu doped Yttrium Oxide Films*", Appl. Phys. Lett., Vol.71, No.3, pp404-406, July 1997.
- 55 KG Cho, D Kumar, DG Lee *et al*; "*Improved Luminescence Properties of Pulsed Laser Deposited  $Eu:Y_2O_3$  Thin Films on Diamond Coated Silicon Substrates*" Appl. Phys. Lett., Vol.71, No.23, pp3335-3337, Dec 1997.
- 56 WM Cranton, DM Spink, R Stevens *et al*, "*Growth and Dielectric Characterisation of Yttrium Oxide Thin Films Deposited on Si by RF Magnetron Sputtering*", Thin Film Solids, Vol.226, pp156-160, 1993.

- 57 MR Craven, WM Cranton, S Toal *et al*, "*Characterisation of BaTiO<sub>3</sub> Thin Films Deposited by Rf Magnetron Sputtering for use in a.c. TFEL Devices*", *Semicond. Sci. Technol.*, Vol.13, pp404-409, 1998
- 58 WM Cranton, CB Thomas, R Stevens *et al*, "*Laterally Emitting Thin Film Electroluminescent Devices for Head Mounted Displays*", *Proc. Electronic Information Displays Conference*, invited paper, 1997
- 59 *CRC handbook of Chemistry and Physics*, Ed. by DR Lide, CRC Press 1990, Ch 12, page125.
- 60 *SPEX Operation and Maintenance Instructions*, Cat. No.1702, Spex Industries, 1985.
- 61 *Guide to Spectroscopy*, Jobin Yvon/Spex Division, Instruments SA, Inc. 1994.
- 62 *Photomultipliers and Accessories*, Electron Tube Ltd, 1996.
- 63 RH Bube; "*Photoelectronic Properties of Semiconductors*", Cambridge University Press, 1992.
- 64 As Ref.12; page 840.
- 65 LG Van Uitert, RC Linares, RR Soden *et al*; "*Role of f-Orbital Electron Wave Function Mixing in the Concentration Quenching of Eu<sup>3+</sup>*", *Jn Chem. Phys.*, Vol.36, No.3, pp702-705, Feb 1962.
- 66 As Ref.13; page 10-19.
- 67 MJ Weber; "*Radiative and Multiphonon Relaxation of Rare-Earth Ions in Y<sub>2</sub>O<sub>3</sub>*", *American Physical Soc. : The Physical Review*, 2nd Series, Vol.171, No.2, pp283-294, July 1968.
- 68 H Forest, G Ban "*Evidence of Eu<sup>3+</sup> emission from two symmetry Sites in Y<sub>2</sub>O<sub>3</sub>:Eu*" *Jn Electrochem Soc: Solid State Sci*, Vol.116, No.4, pp474-478, April 1969
- 69 SZ Toma, DT Palumbo; "*Broad Emission and Excitation Bands in Y<sub>2</sub>O<sub>3</sub> and YVO<sub>4</sub>*", *Jn Electrochem. Soc:Solid State Sci.*, Vol.117, No.2, pp236-241, Feb 1970.
- 70 JHeber, KHHellwege, VKobler, HMurmann, "*Energy level and Interaction between Eu<sup>3+</sup> Ions at Lattice Sites of Symmetry C<sub>2</sub> and C<sub>3i</sub> in Y<sub>2</sub>O<sub>3</sub>*" *Z Phys* Vol 114, pp237, 1970.
- 71 J Dexpert-Ghys, M Faucher; "*Laser-induced Polarized Fluorescence in Cubic Sesquioxide Doped with Trivalent Europium*", *Physical Review B*, Vol.20, No.1, pp10-20, July 1979
- 72 RB Hunt Jr, RG Pappalardo "*Fast Excited State Relaxation of Eu-Eu pairs in Commercial Y<sub>2</sub>O<sub>3</sub> Phosphors*", *Jn Luminescence*, Vol.34, pp133-146, April 1985.

- 73 RG Pappalardo, RB Hunt Jr, "Dye Laser Spectroscopy of Commerce  $Y_2O_3:Eu$  Phosphor", Jn. Electrochem. Soc.: Solid State Sci and Technol., Vol.132, No.3, pp721-730, March 1985.
- 74 M Buijs, A Meyerink, G Blasse; "Energy Transfer between  $Eu^{3+}$  Ions in a Lattice with Two Different Crystallographic Sites:  $Y_2O_3:Eu^{3+}$ ,  $Gd_2O_3:Eu^{3+}$  and  $Eu_2O_3$ ", Jn Luminescence, Vol.37, pp9-20, 1987.
- 75 As Ref.20; page 75.
- 76 As Ref. 12; page 838-839.
- 77 K Ohno, T Abe; "Bright Green Phosphor,  $Y_3Al_{5-x}Ga_xO_{12}:Tb$ , for Projection CRT", Jn. Electrochem Soc.:Solid State Sci. and Technol., Vol.134, No.8, pp2072-2076, Aug 1987.
- 78 MF Yan, TCD Huo, HC Ling; "Preparation of  $Y_2Al_5O_{12}$  Based Phosphor Powders", Jn.Electrochem Soc.:Solid State Sci. and Technol., Vol.134, No.2, pp493-498, Feb 1987.
- 79 JE Bamforth; "A Study of the Thermally-Induced Reactions of Yttrium and Aluminium Nitrates to form Yttrium Aluminium Garnet(YAG)", Bsc. Thesis Applied Chemistry, The Nottingham Trent University, 1996.
- 80 Internal Technical Report, Rolls-Royce Plc.
- 81 AJ Simons, CB Thomas; Report 6 SERC Grant Ref:Gr/F29509, 1992.
- 82 S Alaruri, L Bianchini, A Brewington; "Effective Spectral Emissivity Measurements of Superalloys and YSZ Thermal Barrier Coating at High Temperatures Using a 1.6mm Single Wavelength Pyrometer", AGARD PEP Symposium on Advanced Non-Intrinsic Instrumentation for Propulsion Engines Paper no.22, Brussels, Belgium, 20-24 Oct'97.
- 83 OJ Gregory, JD Cooke, JM Beinkiewicz; "High Temperature - Thin Film Strain Gages Based on Alloys of Indium Tin Oxide", AGARD PEP Symposium on Advanced Non-Intrinsic Instrumentation for Propulsion Engines Paper no.42, Brussels, Belgium, 20-24 Oct'97.
- 84 As Ref. 61, Page 4.
- 85 J Wilson, JFB Hawkes, "Optoelectronics - An Introduction", Prentice-Hall, 1989.
- 86 As Ref.10, Page 447.
- 87 SS Trond, JS Martin, JP Stanavage *et al*;"Properties of Some Selected Europium-Activated Red Phosphors", Jn Electrochem Soc., Vol.116, No.7, pp1047-1050, 1969.
- 88 WM Cranton; PhD Thesis, University of Bradford, 1995.



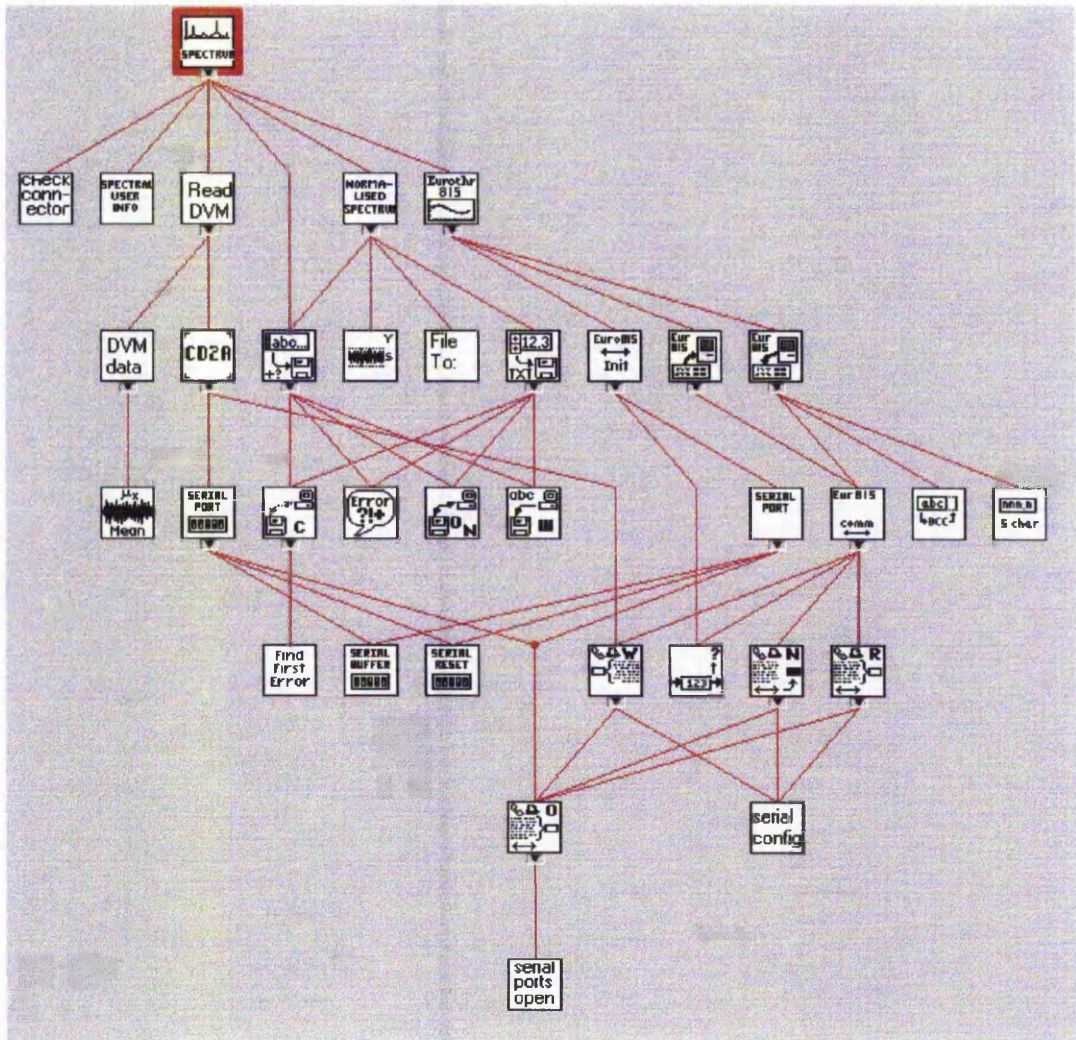
- 89 JL Vossen, W Kern; *"Thin Film Processes"*, Academia Press, 1978.
- 90 J McKittrick et al; *"Enhanced Photoluminescent Emission of Thin Phosphor Films via Pulsed Excimer Laser Melting"*, Jn. Materials Research, Vol.13, No.11, pp3019-3021, Nov 1998.
- 91 PJ Timans; *"Rapid Thermal Processing Technology for the 21st Century"*, Material Science and Semiconductor Processing, Vol.1, No.3/4, pp169-179, 1998
- 92 M Born, E Wolf; *"Principles of Optics - Electromagnetic Theory of Propagation, Interference and Diffraction of Light"*, Pergamon Press, 1987.
- 93 FW Sears; *"Principles of Physics Series - Optics"*, 3rd Edition, 1948
- 94 H Dagnall; *"Exploring Surface Texture"*, Rank Taylor Hobson Ltd, 1986
- 95 C Tsakonas, CB Thomas; *"Role of Sulphur Vacancies on the Electrical Characteristics of Sputtered Films of ZnS"*, Jn. Appl. Phys., Vol.78, No.9, pp1-6, Nov 1995.
- 96 WM Cranton, E Mastio, CB Thomas et al; *"Laser Annealing for High Intensity Flat Screen Displays"*, CLF Annual Report, pp147-147-148, 1996/97.
- 97 E Mastio, WM Cranton, CB Thomas et al; *"Pulsed KrF Laser Annealing of RF Sputtered ZnS:Mn Thin Films"*, Jn. Appl. Surface Sci., Vol.9, pp35-39, Feb 1998.
- 98 WJ Tropf, DC Harris; *"Mechanical, Thermal, and Optical Properties of Yttria and Lanthana-doped Yttria"*, SPIE- Window and Dome Technologies and Materials, Vol.1112, pp9-19, 1989.
- 99 As Ref.13; Chapter 2, pp8-32.

## **Appendix A**

### **LabVIEW Control Programmes**

**LabVIEW Emission Spectrum Programme**

**Hierarchy Window**



**Emission Spectrum Main VI**

**Connector Icon**

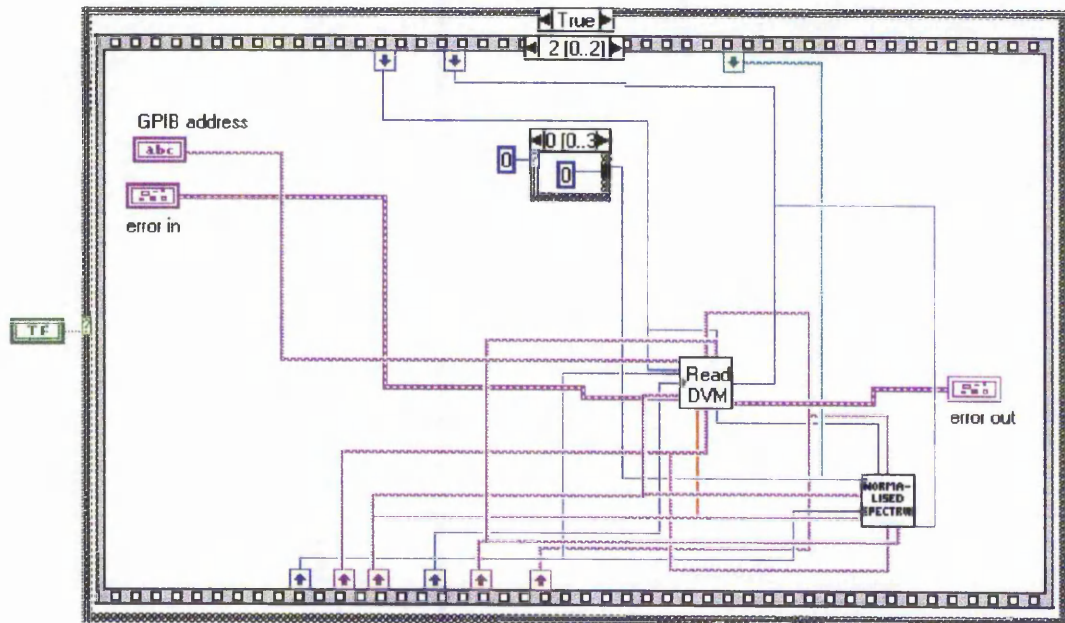
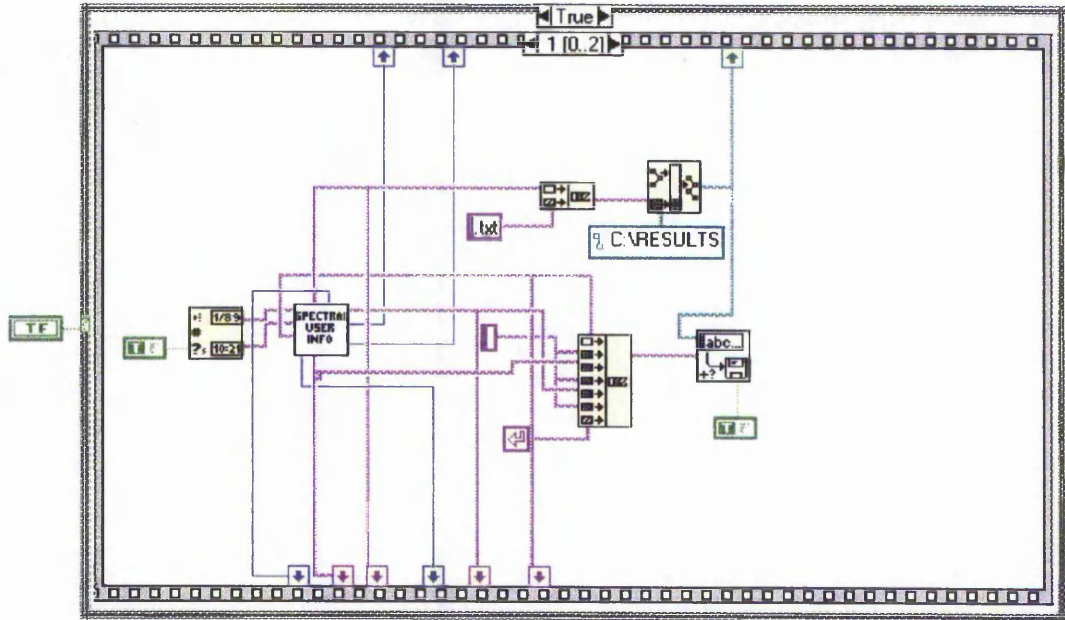
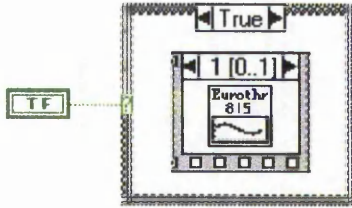


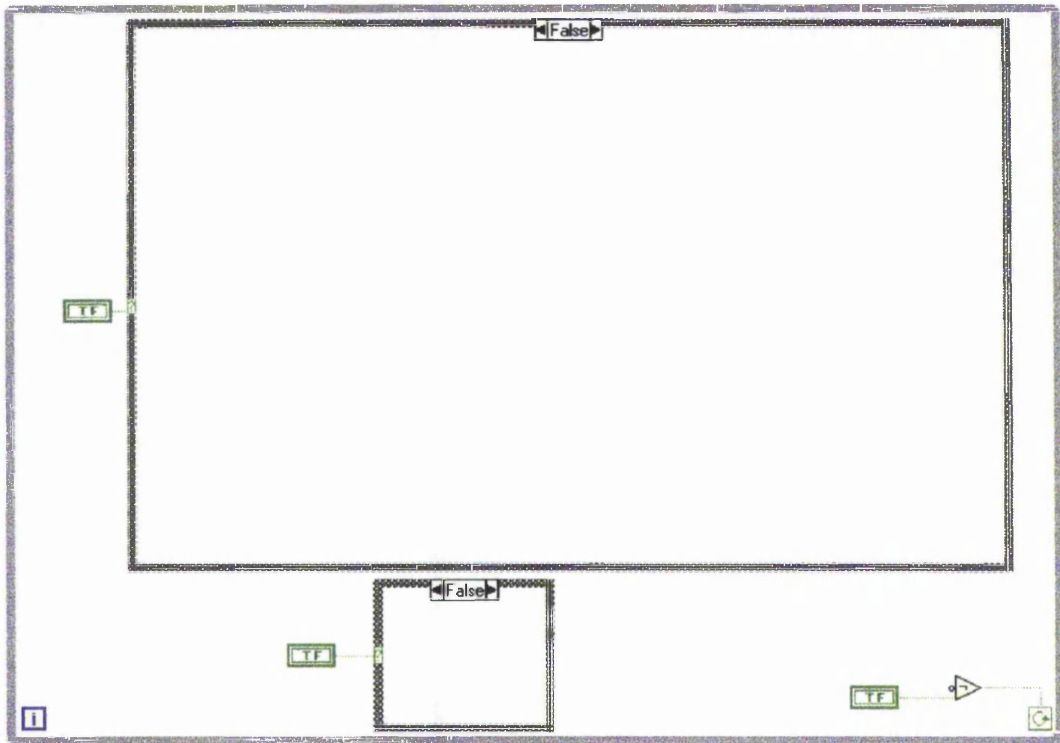
**CW Spectrum using DVM.vi**

This programme has been written to measure the emission spectra of phosphors. The main VI controls the temperature setting of the eurotherm, the wavelength setting of the compudrive, and measures a value of intensity from a Keithley digital voltmeter. The operator enters the spectrum's variables and filenames via a user interface panel. A check procedure is in-built to ensure the serial port is connected to the correct equipment.

The front panel allows the user to either set the temperature or collect the spectrum by clicking on the appropriate button. The stop button will terminate the programme.







**List of SubVIs Used**

- Check Connectors .vi
  - Set Temperature of Eurotherm 815.vi
  - Get Spectral Parameters.vi
  - Write Characters To File .vi
  - CW Spectrum Collected via DVM.vi
  - Normalise Spectrum.vi
-

**Check Connector SubVI**

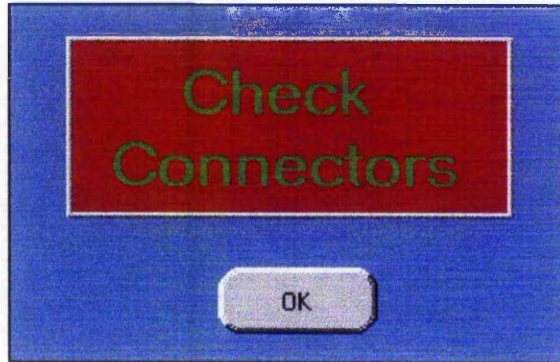
**Connector Icon**



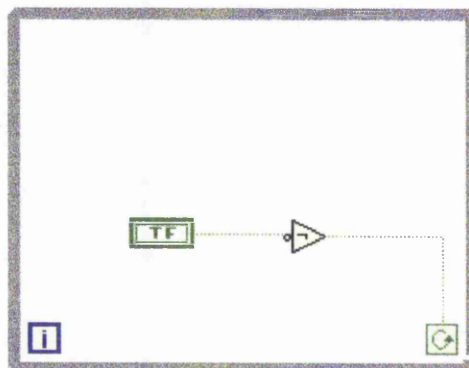
**Check Connectors.vi**

This subVI is a simple True-False Statement allowing the operator to check the serial port connector before proceeding.

**Front Panel**



**Block Diagram**



**Eurotherm SubVI**

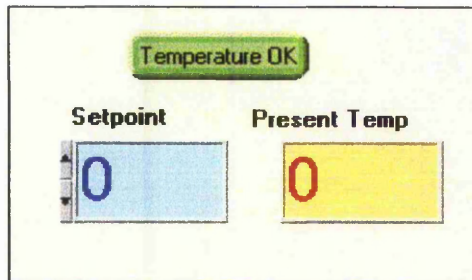
**Connector Panel**



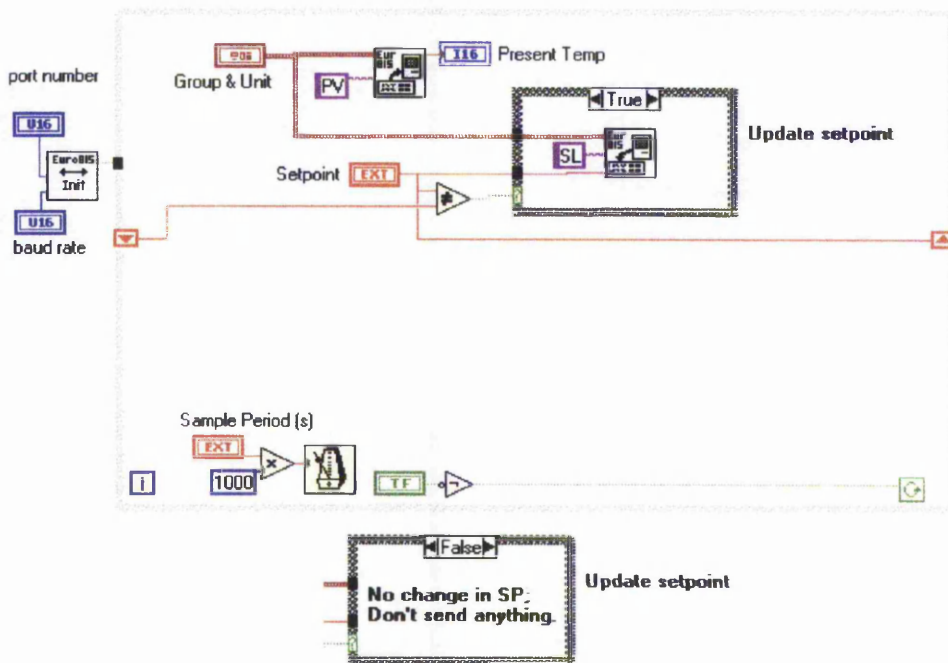
**Set Temperature of Eurotherm 815.vi**

This VI is creates a user interface to control the temperature set by the Eurotherm. The driver VIs used include : Init, Read, Write and Status. The process variables are read from the Eurotherm controller and are updated over the sampling period. If the Setpoint temperature is changed at any time, the new value is sent to the controller during the next sampling period.

**Front Panel**



**Block Diagram**



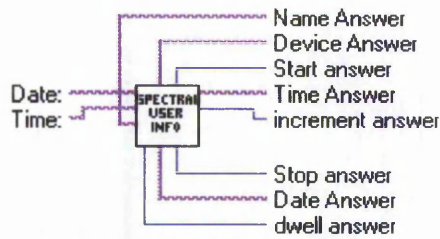
**List of SubVIs Used**

- Eurotherm 815 Init.vi
- Eurotherm 815 Read.vi
- Eurotherm 815 Write.vi



**Get Spectral Parameters SubVI**

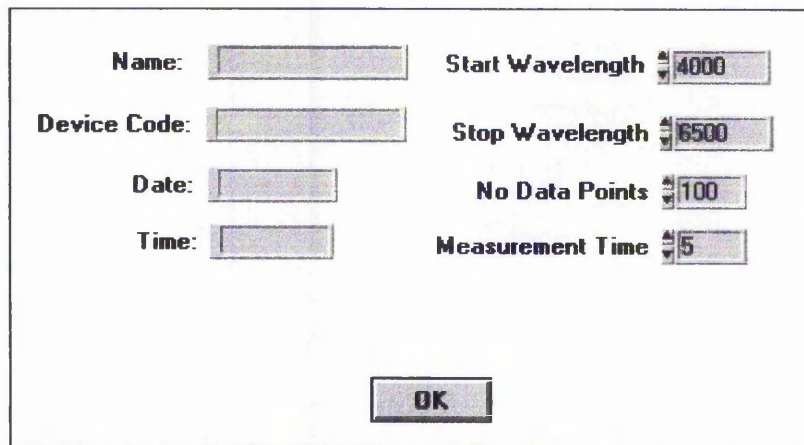
**Connector Panel**



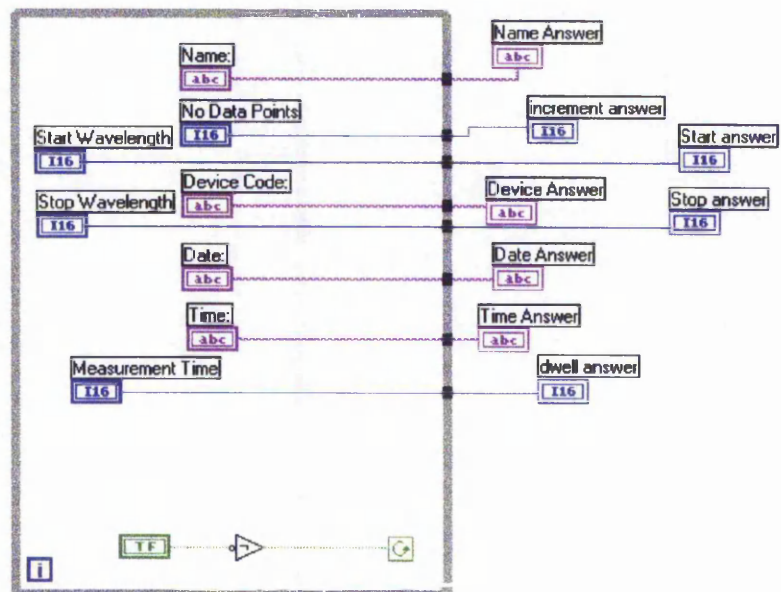
**Get Spectral Parameters.vi**

A simple user interface panel to obtain parameters required for the measurement and saving of spectral data.

**Front Panel**

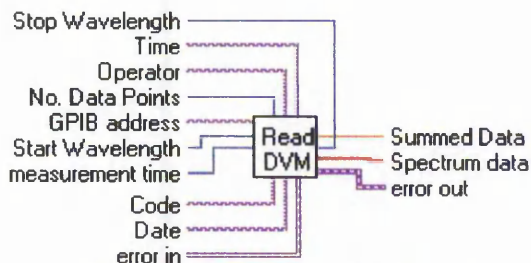


**Block Diagram**



**Read DVM SubVI**

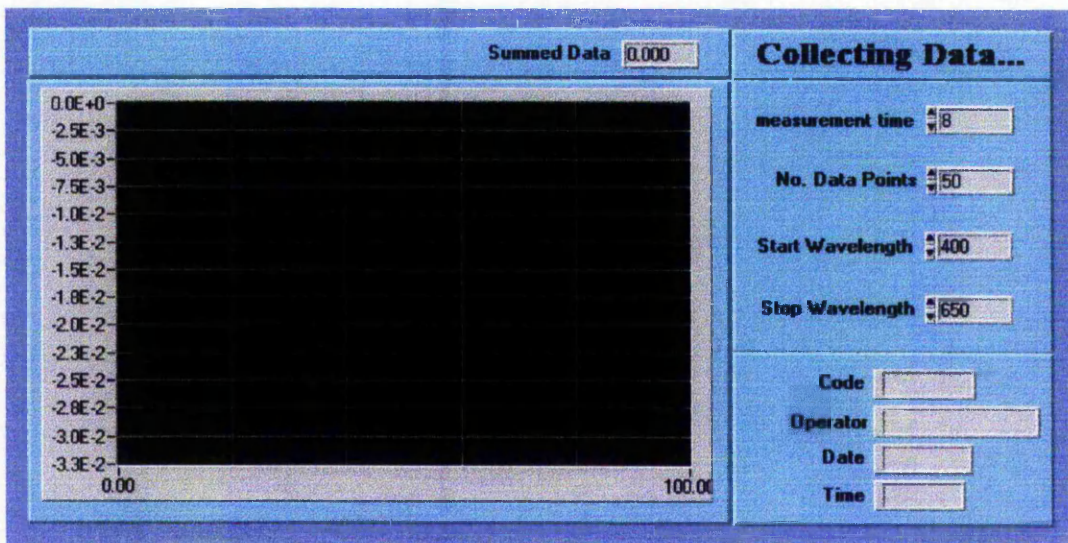
**Connector Panel**



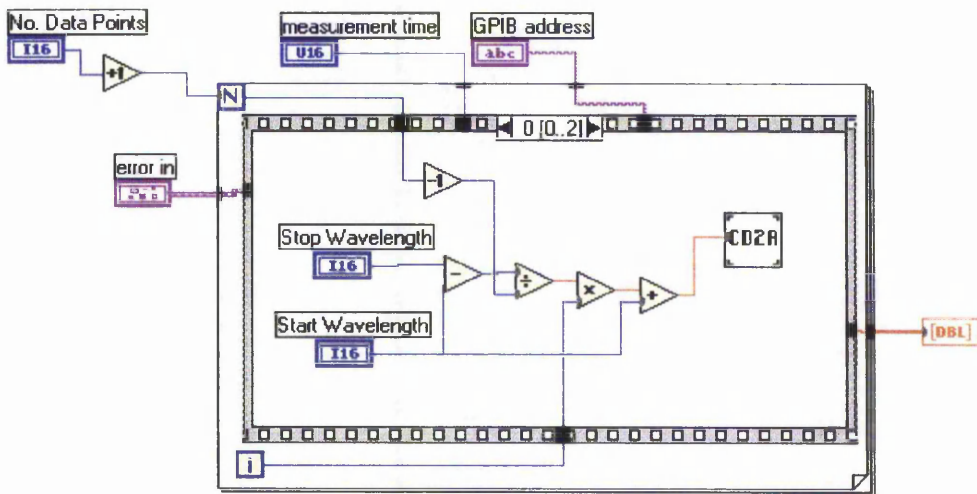
**CW Spectrum Collected via DVM.vi**

From the spectral parameters provided by the operator, this vi calculates the required wavelength for the next intensity reading. The calculated value is sent to the SPEX driver vi, which in turn, sends the setting to the compudrive. Over the measurement time set, the value of intensity is obtained through the Keithley driver vi.

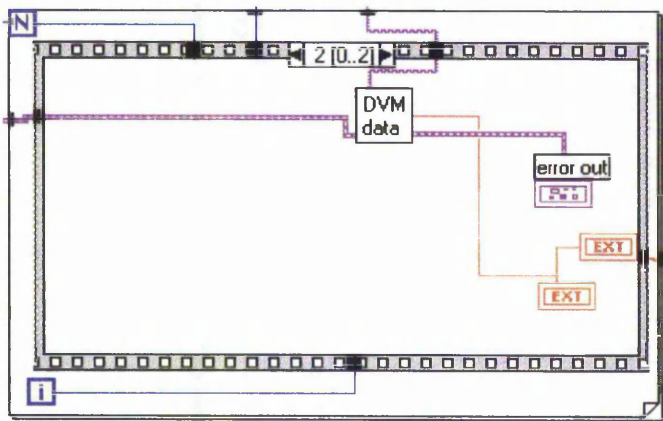
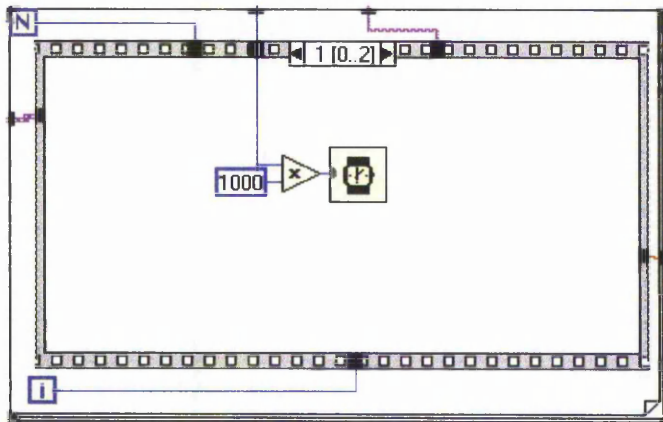
**Front Panel**



**Block Diagram**



Date	Code	Time	Operator
abc	abc	abc	abc

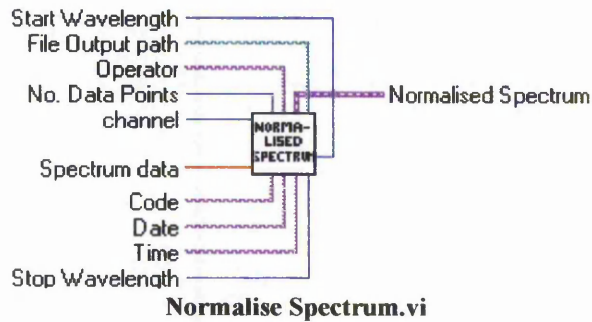


**List of SubVIs**

- Spex Positioning CD2A.vi
- Keithley 175 Get Reading.vi

**Normalise Spectrum SubVI**

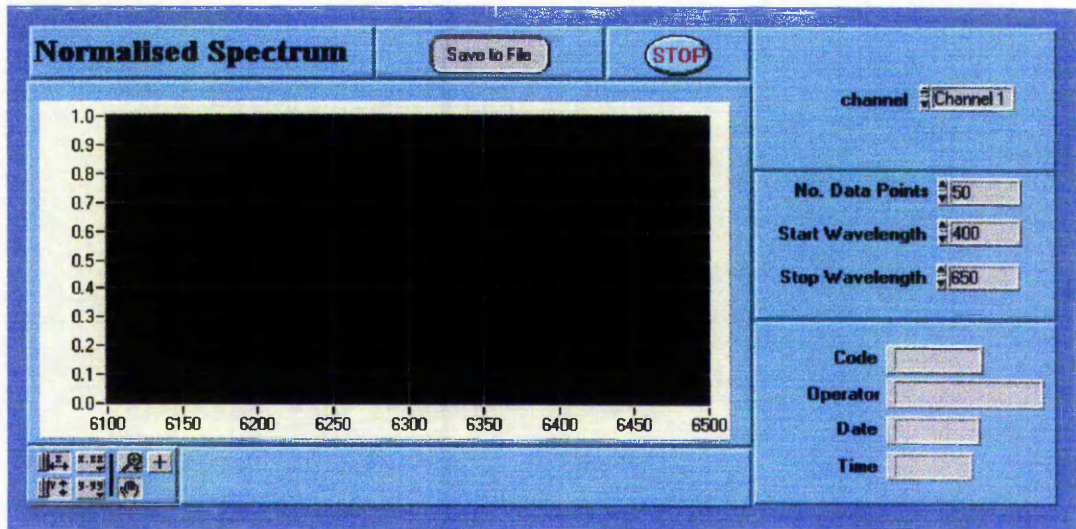
**Connector Panel**



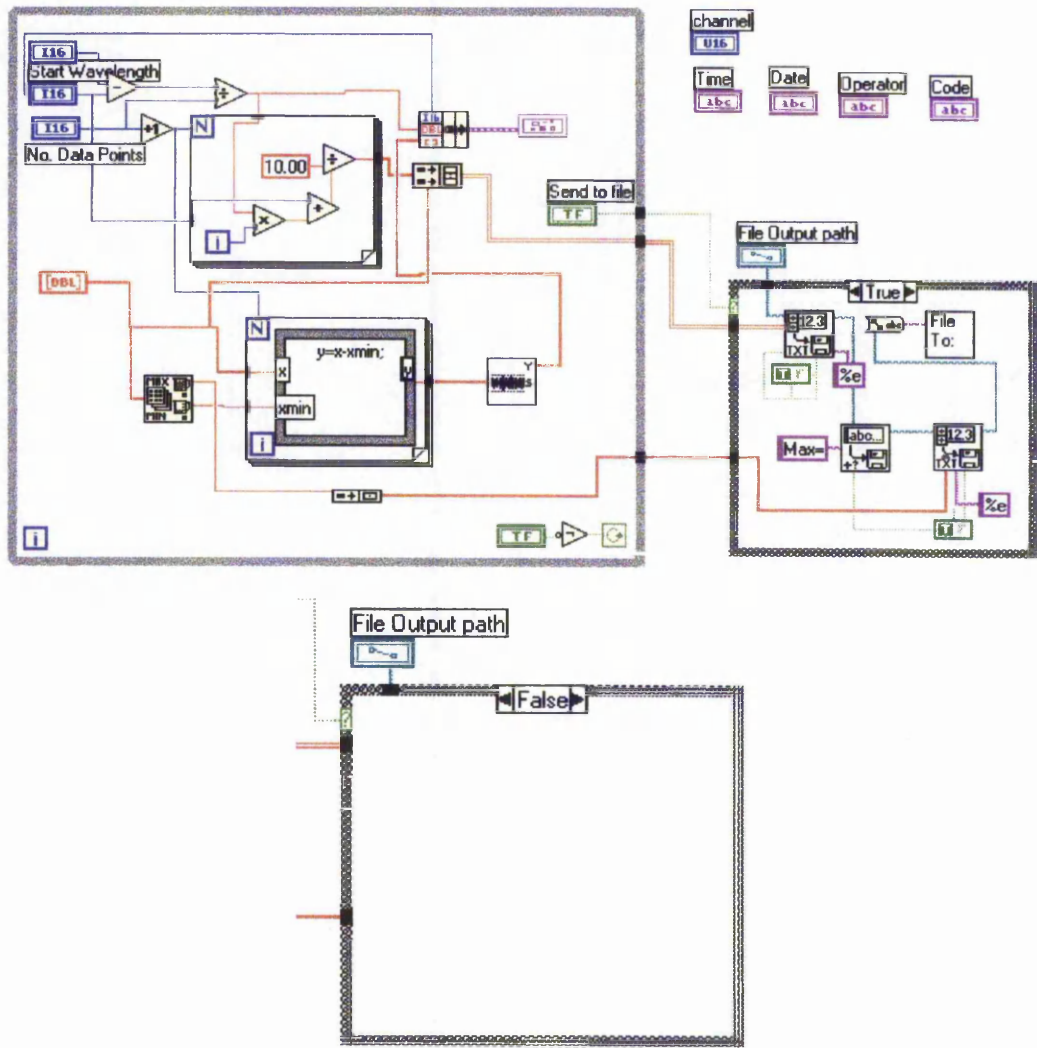
The spectrum data collected by the Read DVM subVI is analysed as a data array. The maximum and minimum values of X are determined, and all data is then scaled using the quick scale 1D vi programme. The wavelength values are converted into nanometers. The subsequent data is then written to the user interface panel and shown as a normalised spectrum. All data is then written to the file as a spreadsheet. This allows the operator to analyse the data at a later time using Microsoft Excel

The user has the option of either saving or discarding the data. On terminating the procedure the file is saved or discarded and the operator is returned to the main menu.

**Front Panel**



**Block Diagram**



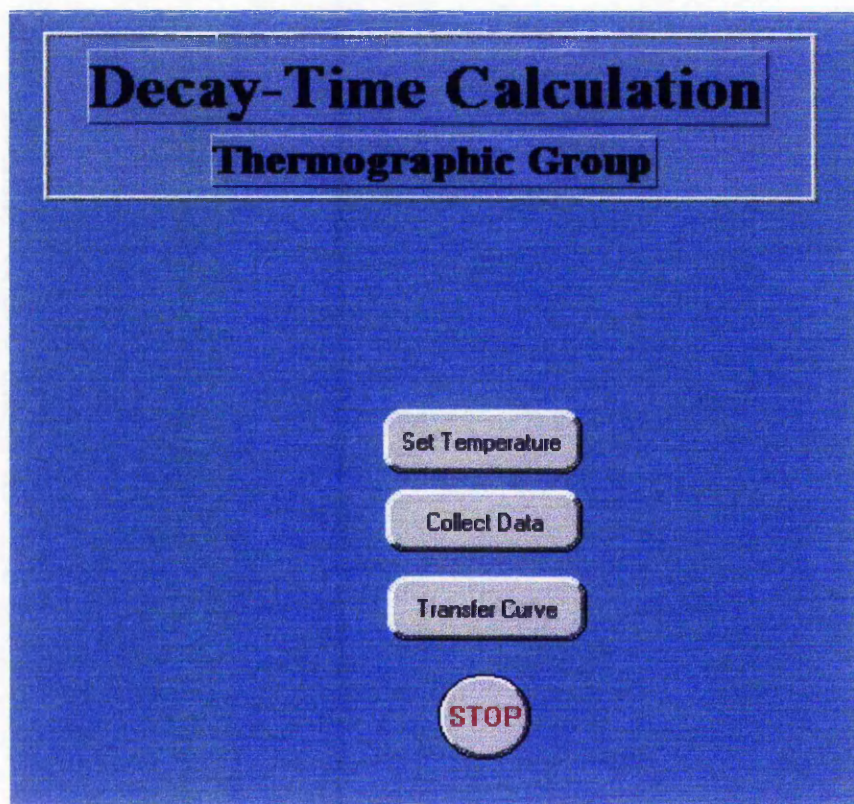
**List of SubVIs**

- Quick Scale 1D.vi
- Write Characters to File.vi
- Write to Spreadsheet File.vi
- Saved File Name.vi

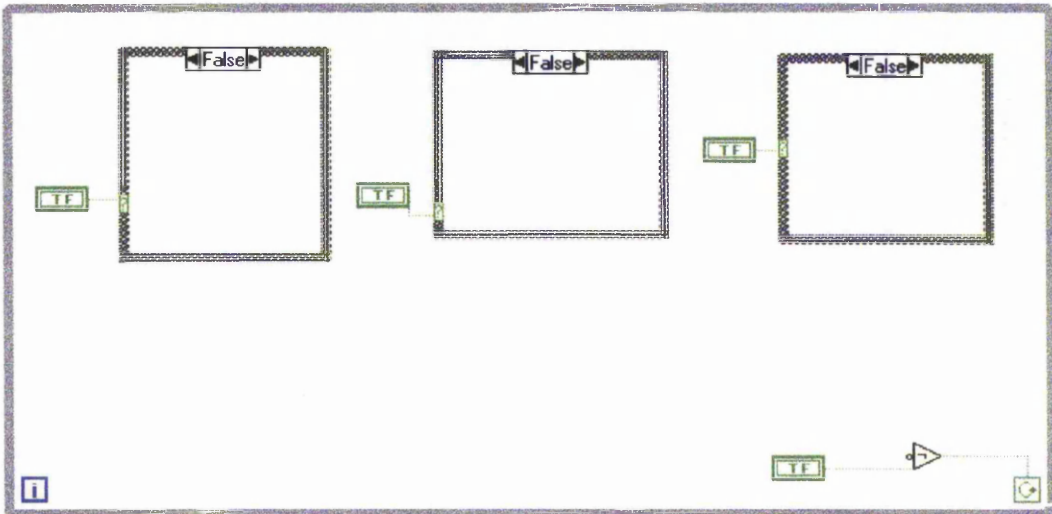
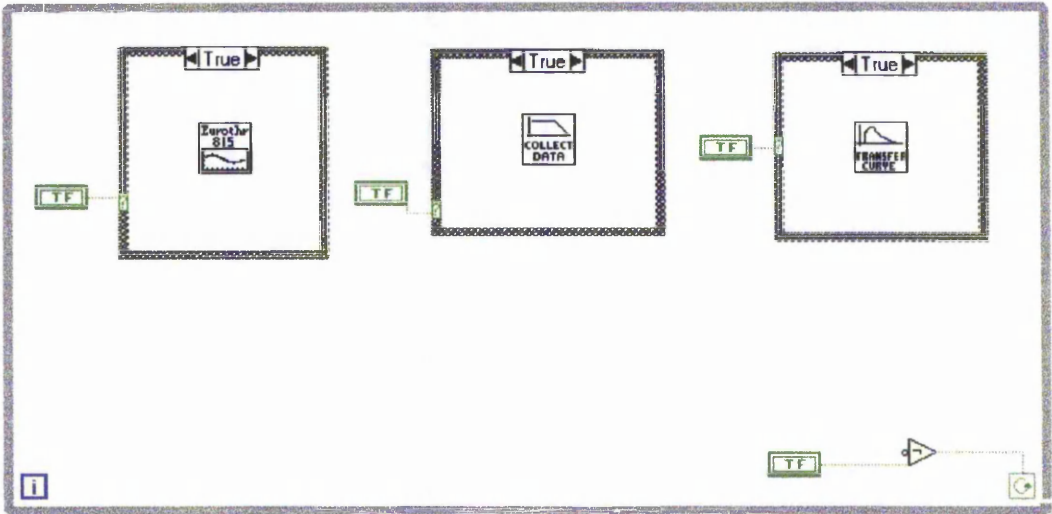


**Decay Time Main VI****Connector Panel****Decay-Time.vi**

This programme has been written to allow automated capture and measurement the phosphorescent signal. The programme controls the temperature of the sample under test and is able to capture data from a Gould digital storage oscilloscope. The operator has the option of setting and monitoring the temperature, capturing a decay curve and measuring its decay constant, or transferring the detected signal to a file.

**Front Panel**

**Block Diagram**



**List of SubVIs Used**

- Set Temperature of Eurotherm 815.vi
- Collect Data 4072.vi
- Transfer Data 4072.vi



**Eurotherm SubVI**

This SubVI is the same as used within the Spectrum VI Programme

**Collect Data SubVI**

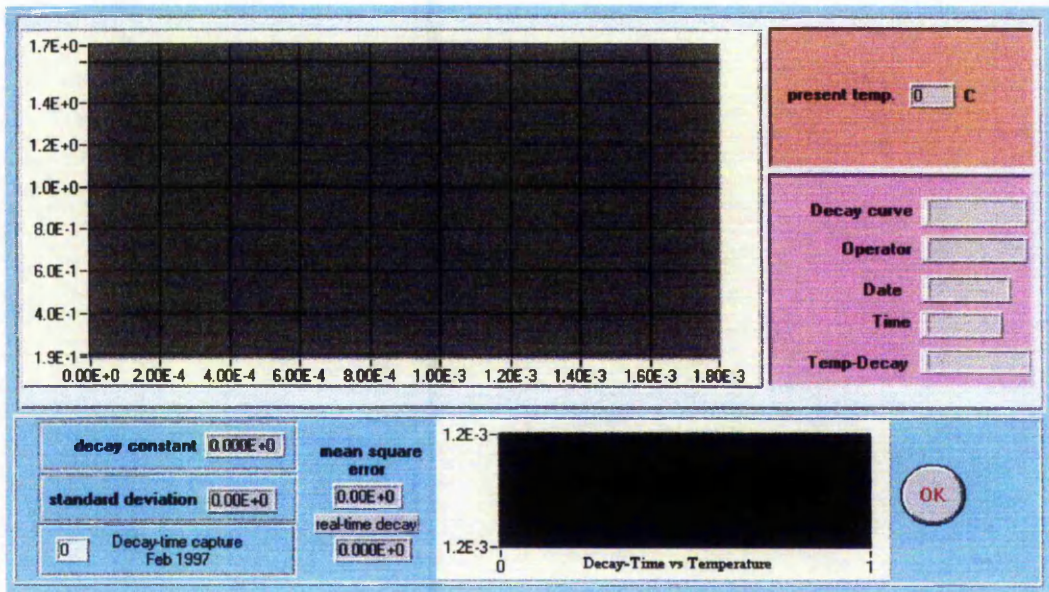
**Connector Panel**



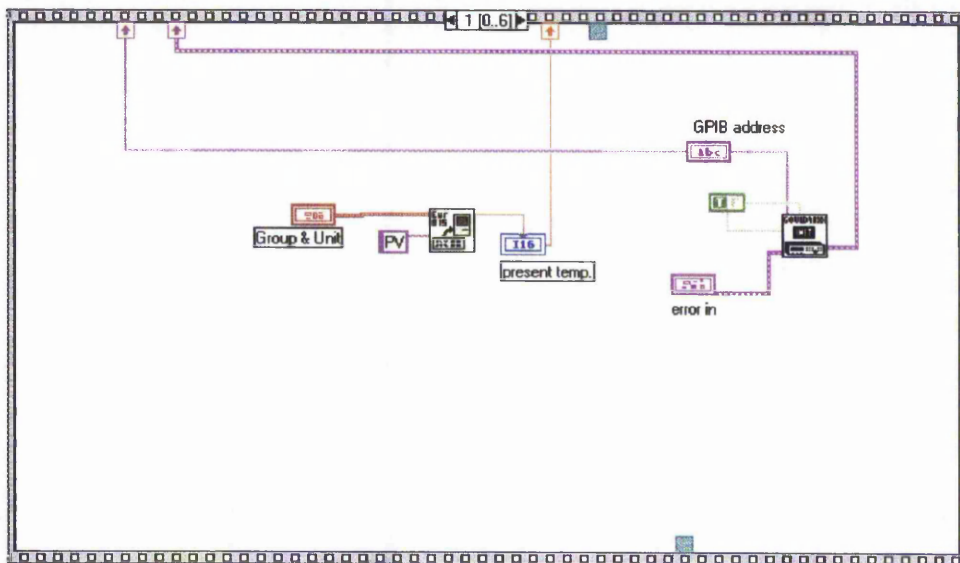
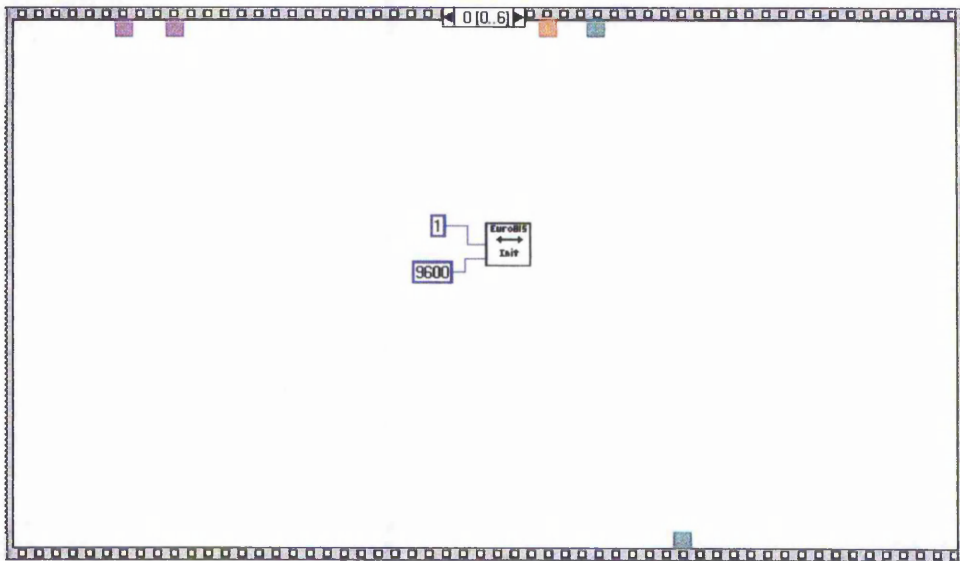
**Collect Data 4072.vi**

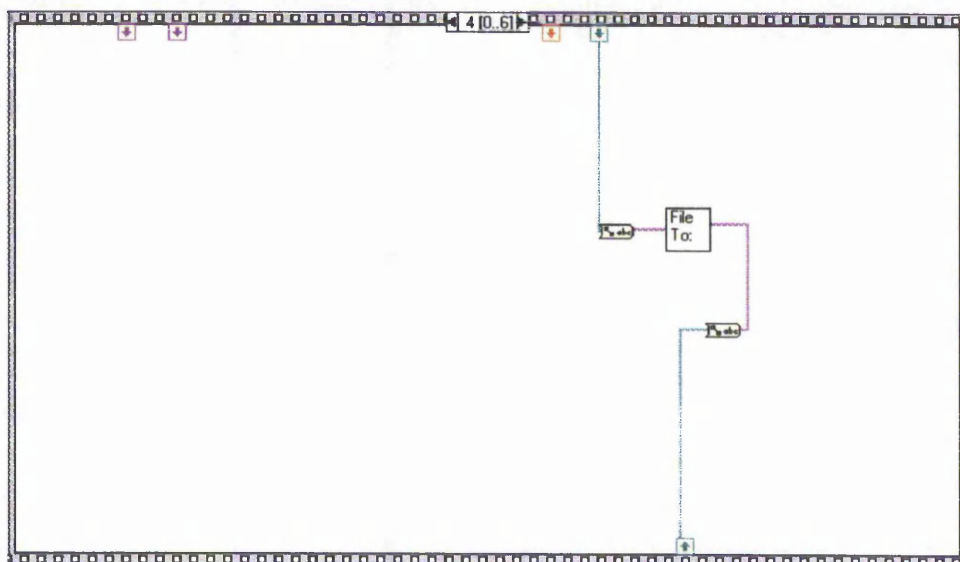
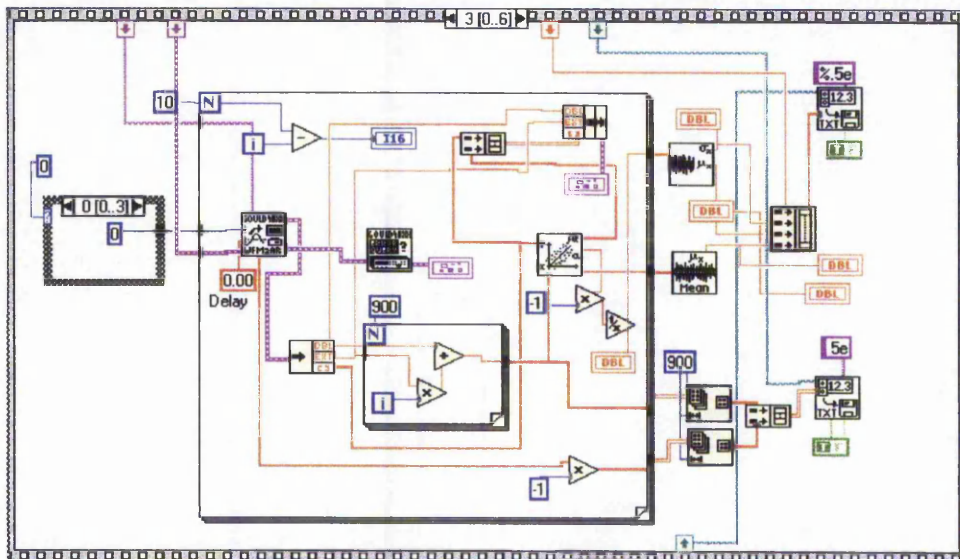
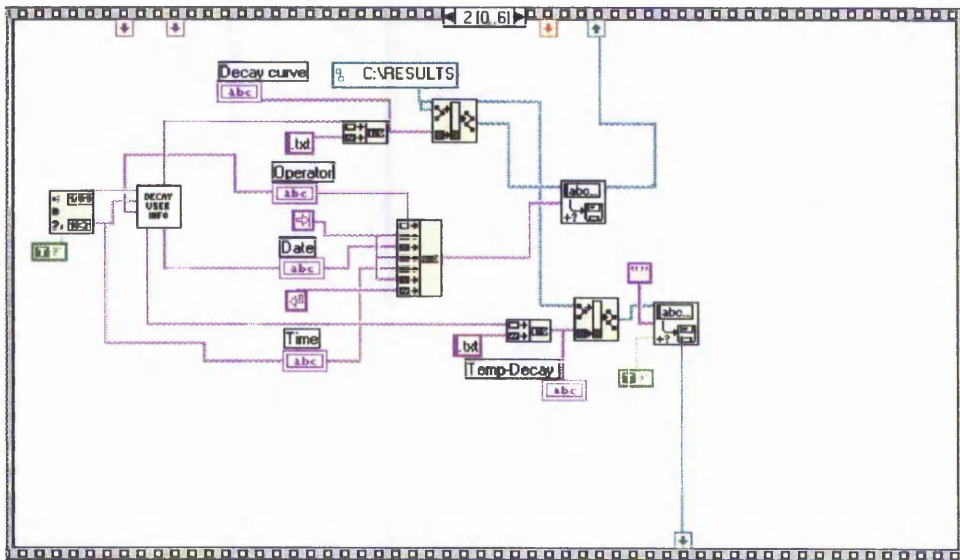
This VI is based on the instrument driver for the Gould 4072 digital storage oscilloscope (DSO). The eurotherm 815 is initialised to allow the present temperature to be read during measurement. The Gould DSO is initialised and is set to store mode. An operator interface panel then allows the filenames to be entered and the files are created. The waveform is then read from the Gould 4072. A curve fitting routine is carried out to calculate the decay constant of the curve. This is averaged ten times and the mean decay constant is stored. The data is then written to appropriate files and saved. The Gould 4072 is then changed back to local mode and the procedure returns to the main menu.

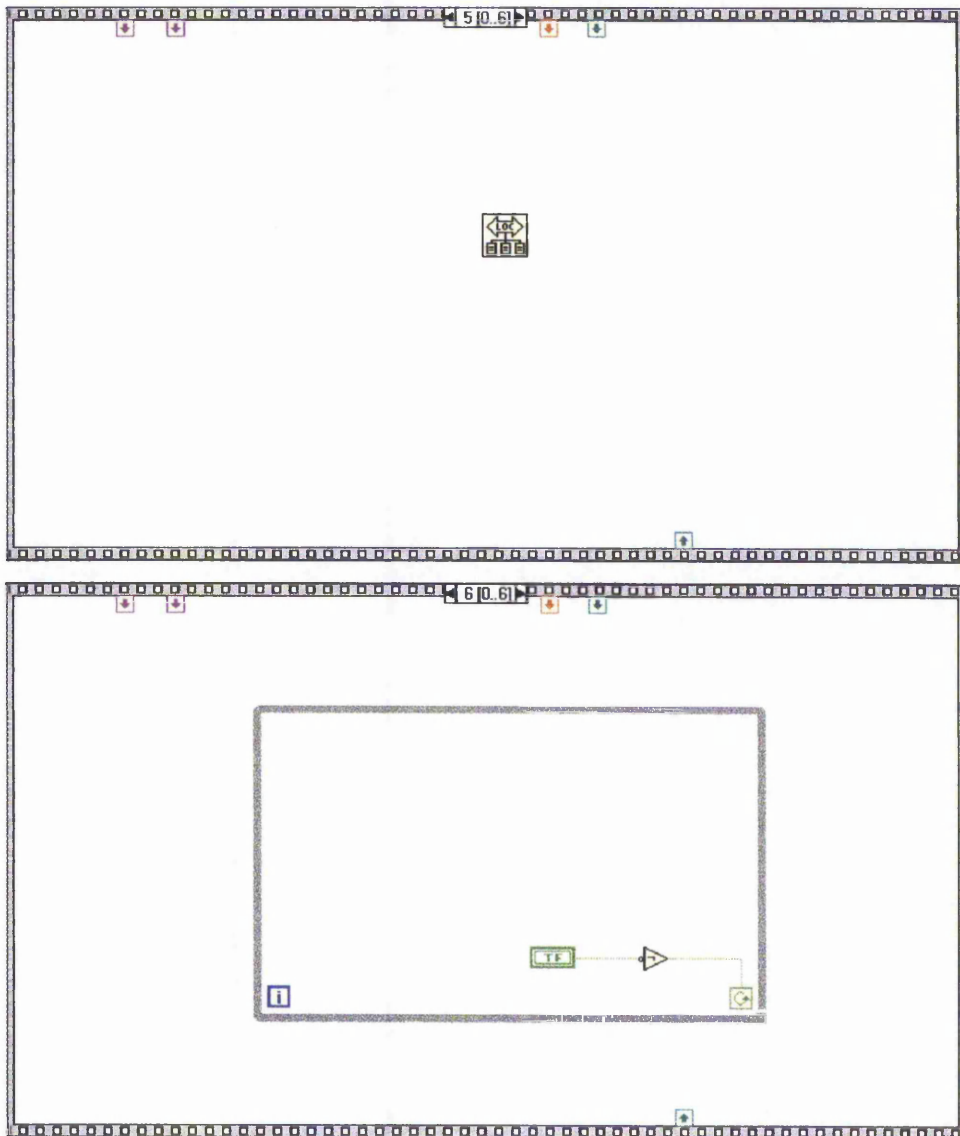
**Front Panel**



**Block Diagram**





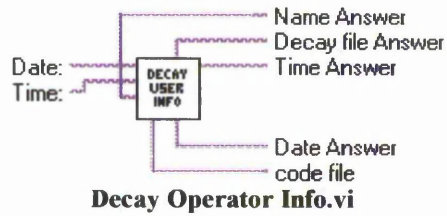


**List of SubVIs Used**

- Eurotherm 815 Init.vi
- Eurotherm 815 Read.vi
- Initialise Gould 4072.vi
- Decay Operator Info.vi
- Gould 4072 Read a Waveform.vi
- Gould 4072 Error Query.vi
- Linear Fit.vi
- Mean.vi
- Standard Deviation.vi
- Write to Spreadsheet File.vi
- Write Characters to File.vi
- Saved File Name.vi

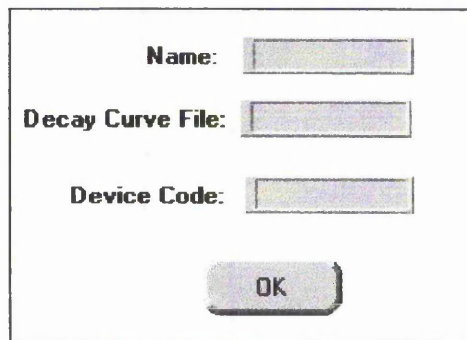
**Decay Operator Information SubVI**

**Connector Panel**

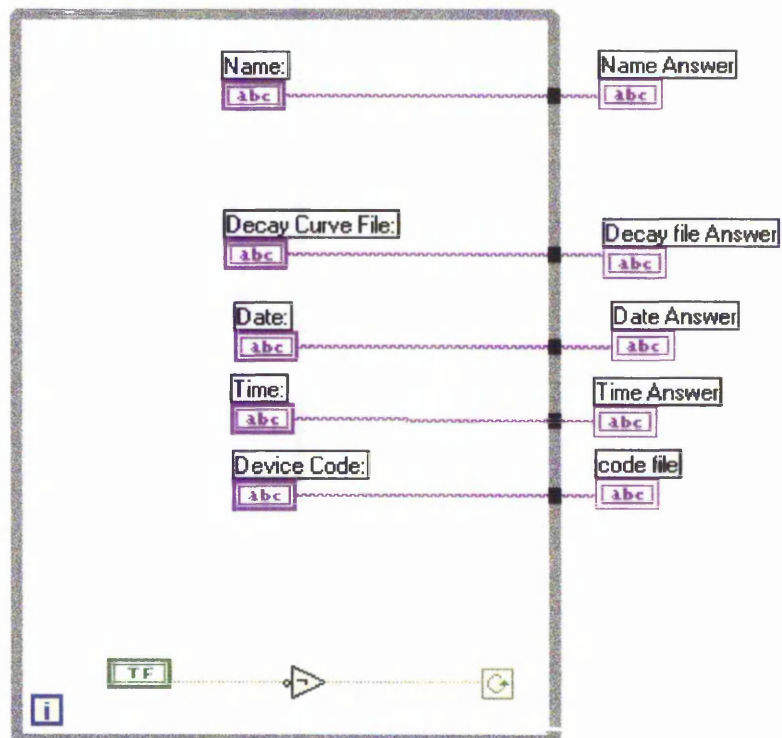


This interface panel reads the date and time from the computer, and has the filenames entered by the operator.

**Front Panel**



**Block Diagram**



**Transfer Curve SubVI**

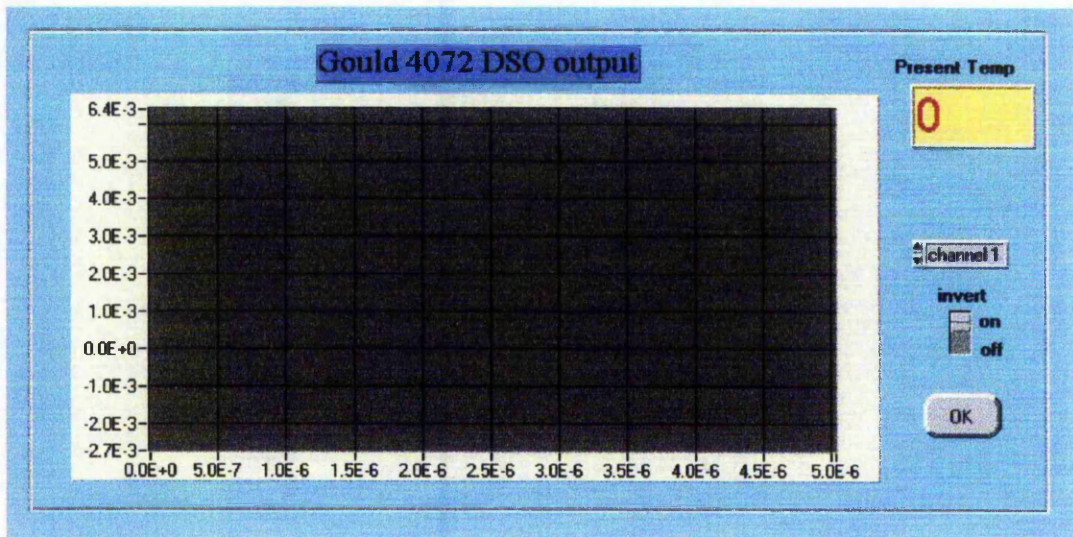
**Connector Panel**



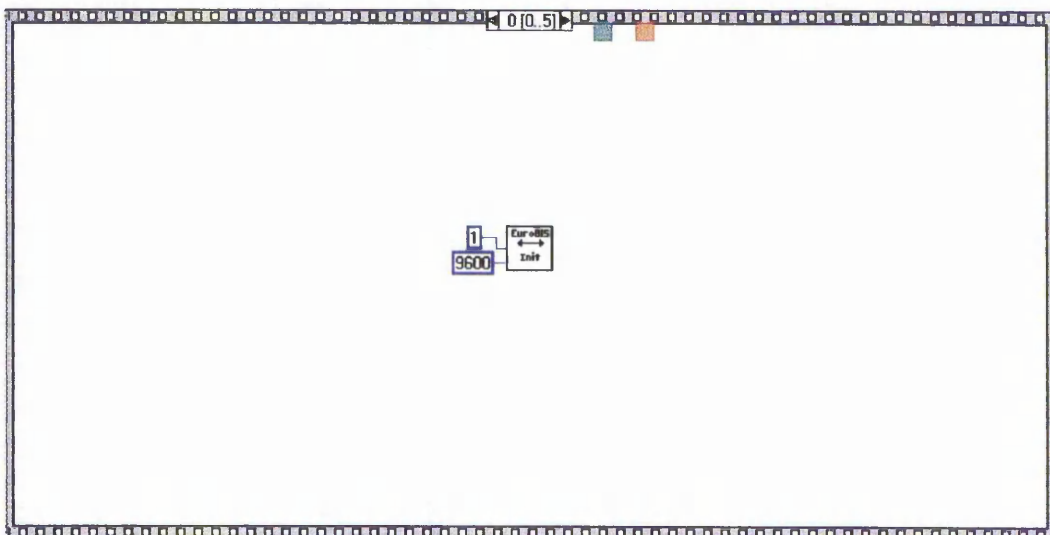
**Transfer Curve 4072.vi**

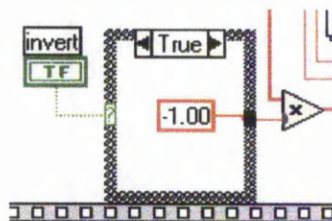
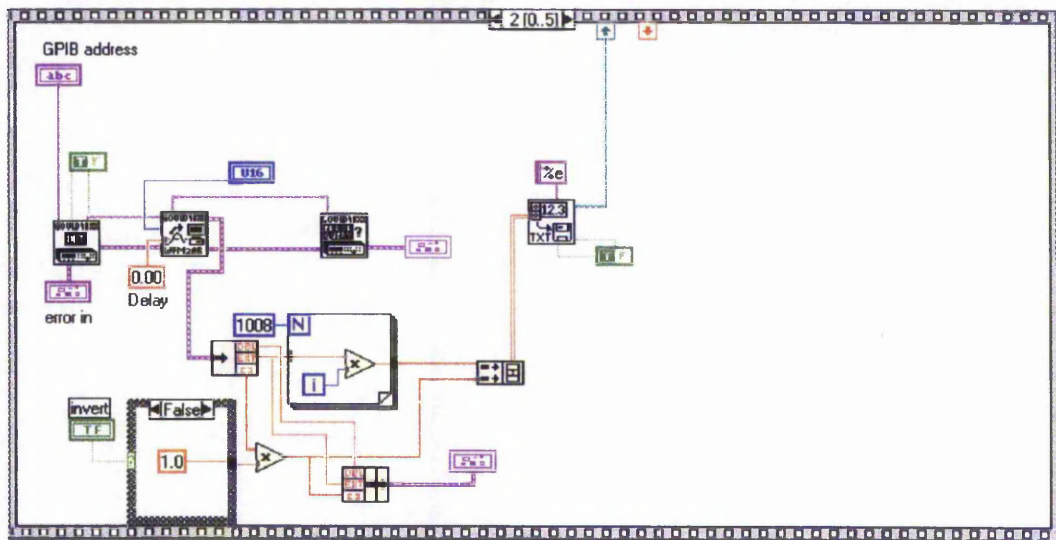
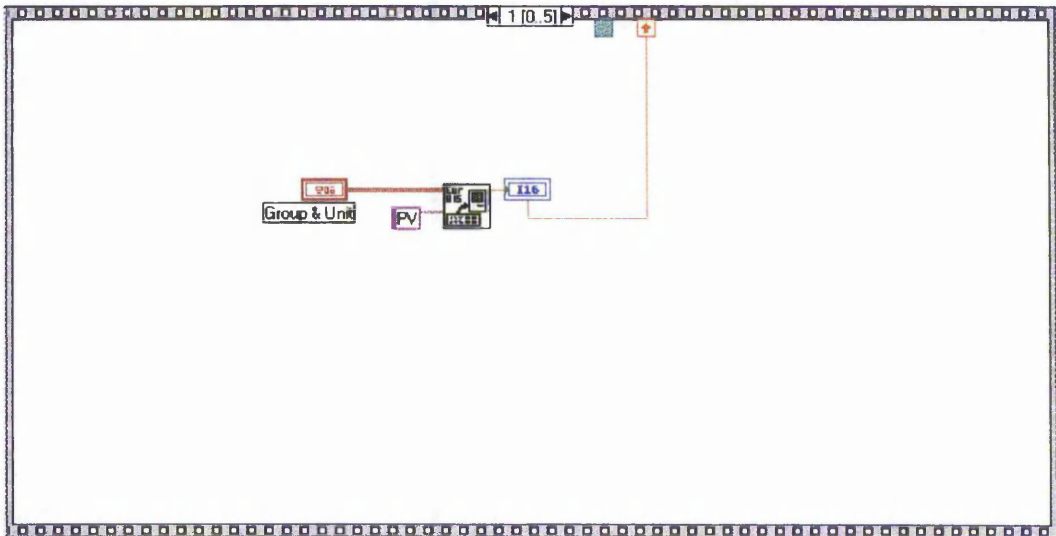
This VI is based on the Collect Data VI. Again, the Eurotherm 815 is initialised and its present temperature is read. The Gould 4072 is then initialised and the waveform is captured from the screen. Along with the present temperature reading, the data is written to a spreadsheet file. The operator is then prompted for a filename and the file is saved. This file can be analysed at a later time. Exiting the procedure returns the operator to the main menu.

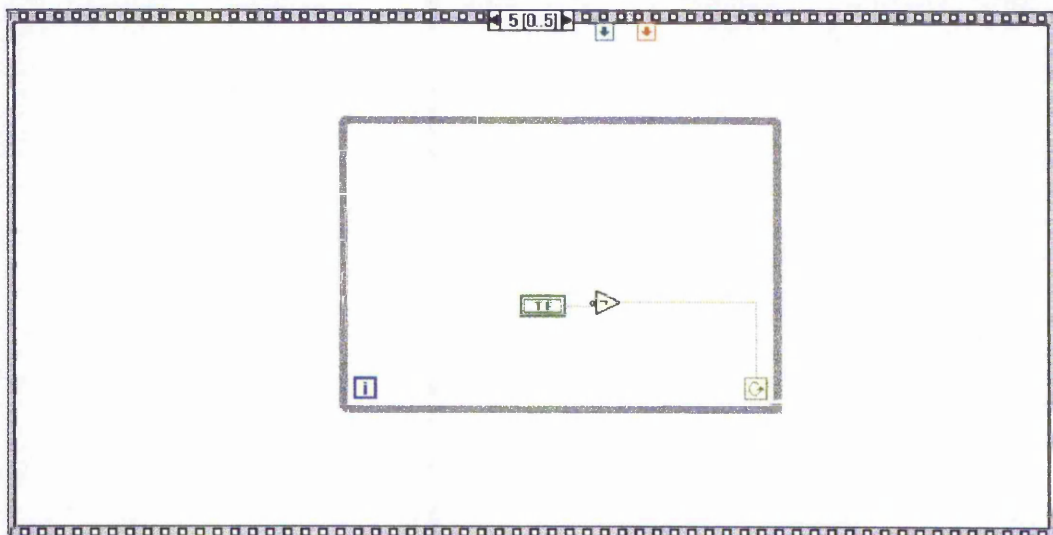
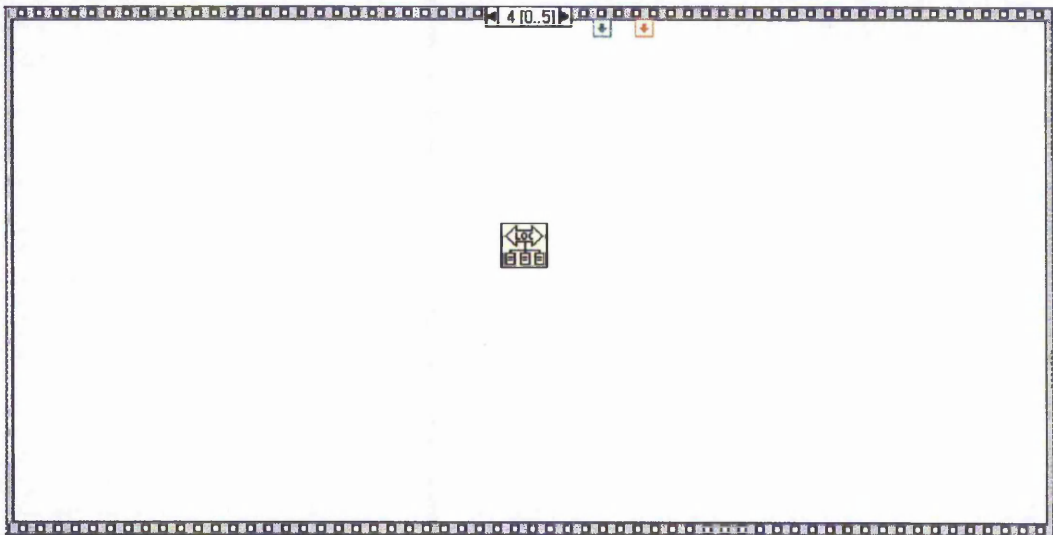
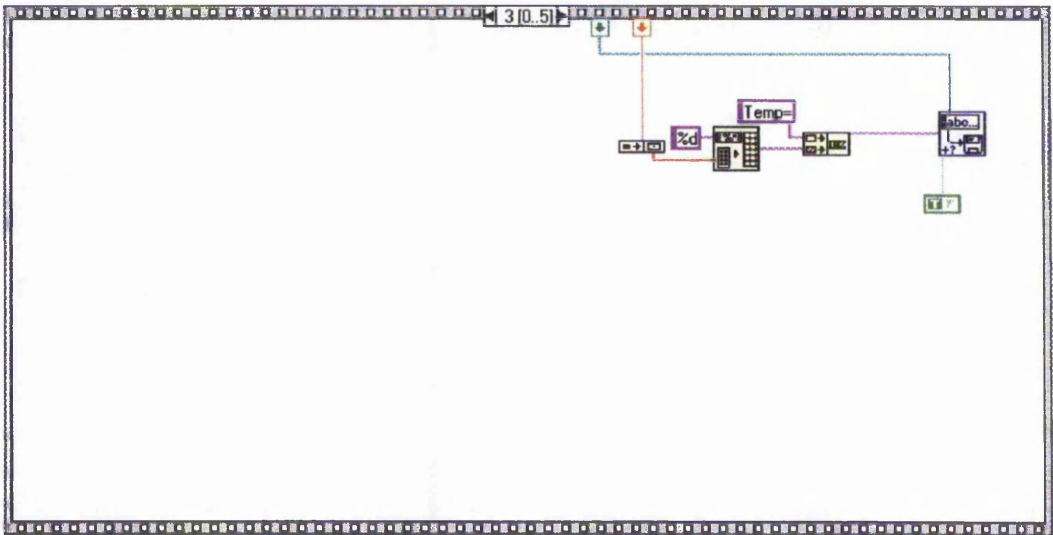
**Front Panel**



**Block Diagram**









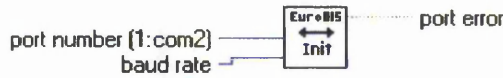
**List of SubVIs**

Eurotherm 815 Init.vi  
Eurotherm 815 Read.vi  
Initialise Gould 4072.vi  
Gould 4072 Read a Waveform.vi  
Write Characters to File.vi  
Write to Spreadsheet File.vi

---

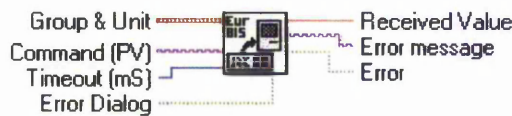
**Information on all SubVIs Used**

**Eurotherm 815 Init.vi**



Initialises the serial port and saves the port number in the Port Number Global, used by the communications VIs. Must be used before any other Eurotherm VIs.

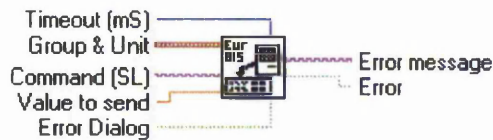
**Eurotherm 815 Read.vi**



Basic data read VI for Eurotherm 815 temperature controllers. This driver decodes incoming messages and returns a numeric value. Uses a serial port for communication. Must be preceded by the Eurotherm 'Init' VI.

Speed benchmark: At 9600 baud on an fx, 34mS per execution (=30Hz).

**Eurotherm 815 Write.vi**



Basic data write VI for Eurotherm 815 temperature controller. This driver sends the specified command and Value to Send to the instrument. Uses serial port for communication and must be preceded by the Eurotherm 'Init' VI.

Value to Send will be rounded to the nearest 1.0 because the Eurotherm does not like fractional settings.

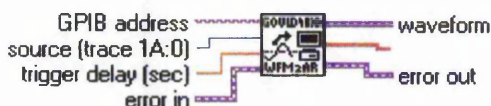
Speed benchmark: At 9600 baud on an fx, 50mS per execution (=50Hz)

**Initialise Gould 4072.vi**



The Initialise VI sets up the Gould Instrument. This VI must be used before using any other of the instrument driver VIs for this instrument. The Gould 40XX driver is an instrument driver which will support the Gould 4070 and 4090 series scopes (4074, 4072, 4094, 4092, 4090).

Gould 4072 Read.vi



This subVI reads the horizontal and vertical settings of the scope, then reads the waveform data. The waveform is sent to the computer in binary format and is then scaled accordingly and placed in an array. Due to the scope limits in passing back waveform information, this parameter is needed in order to properly scale the horizontal axis and identity t(0).

Gould 4072 Error Query.vi



This subVI produces a dialogue box containing the error message.

Spex Positioning CD2A.vi



SPEX CD2A SPECTROMETER COMPUDRIVE

This VI is used for RS-232 control of the CD2A. This programme initialises the compudrive and sends the basic commands and parameters to the CD2A. These commands include start, stop increment, set position and dwell parameters for the various scanning options available. Specifically for the emission spectrum software, the simple set position parameter is used.

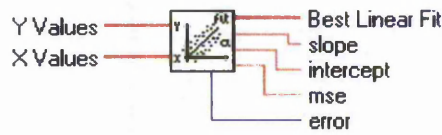
The RS-232 parameters are set in the diagram of the CD2A. This VI is set for a baud rate of 1200, 8 data bits, 1 stop bit, parity off. In addition to the serial port, the following CD2A configurations should be setup. RS-232 parameters are set in the CD2A in configuration elements 15,16 and 17. Element 21 should be set for 2-way RS-232 communication and datalogger output format ( element 21 = 1010). The Remote button on the CD2A must be pressed for RS-232 communication. For more information on the CD2A configuration elements consult the Spex Operation and Maintenance Manual.

Keithley 175 Get Reading.vi



This VI communicates with the Keithley DVM by GPIB. The range of the DVM is set to Auto-range. The DVM is set to remote mode and the current voltage is read at a sampling period of 1 second. Over the full measurement period set, the voltage is averaged

Linear Fit.vi



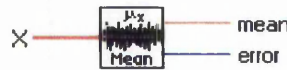
Finds the line values and the set of linear fit coefficients, slope and intercept, which best represent the input data set. The general form of the output is

$$F = mX + b$$

where F is the output sequence Best Linear Fit, X is the input sequence X values, m is the slope and b is the intercept. The MSE between the output Best Linear Fit and the input sequence Y Values is computed using the MSE VI and returned in the output mse.

$$MSE = 1/n * \sum[f(i)-y(i)]^2$$

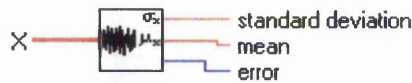
Mean.vi



Computes the mean (average) of the values in the input sequence X. The mean is computed using the following formula :

$$\text{mean} = \sum[X(i)] / n$$

Standard Deviation.vi



Computes the mean value and the standard deviation (STD) of the values in the input sequence X. The mean and standard deviation are computed using the following formula :

$$\text{mean} = \sum[X(i)] / n \quad \text{STD} = \sqrt{\sum[(X(i)-\text{mean})^2] / n}$$

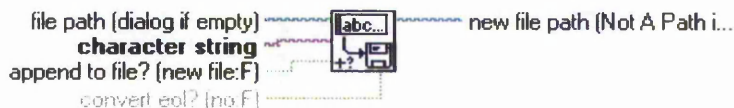
Quick Scale 1D.vi



Determines the maximum absolute value of the input array, X, and then scales X using this value. The elements of the output array, Y, are given by

$$Y[i] = X[i]/\max|X|$$

Write Characters to File.vi



Writes a character string to a new byte stream file or appends the string to an existing file. The VI opens or creates the file beforehand and closes it afterwards.

file path is the path name of the file. If file path is empty (default value) or is Not A Path, the VI displays a File dialogue box from which you can select a file. Error 43 occurs if the user cancels the dialogue.

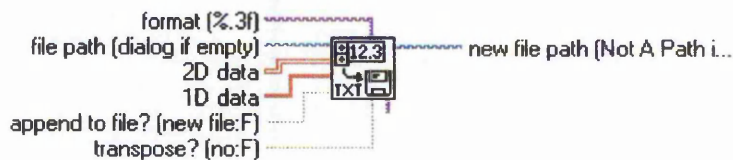
character string is the data the VI writes to the file,

append to file? Set to TRUE if you want to append the data to an existing file; you can also set it TRUE to write to a new file. Set to FALSE (default value) if you want to write the data to a new file or replace an existing file.

new file path is the path of the file to which the VI wrote data. You can use this output to determine the path of the file that you open using dialogue. new file path returns Not A Path if the use selects Cancel from the dialogue box.

---

### Write to Spreadsheet File.vi



Converts a 2D or 1D array of single-precision numbers to a text string and writes the string to a new byte stream file or appends the string to an existing file. You can optionally transpose the data. This VI opens or creates the file beforehand and closes it afterwards. You can use this VI to create a text file readable by most spreadsheet applications.

file path is the path name of the file. If file path is empty (default value) or is Not A Path, the VI displays a File dialogue box from which you can select a file. Error 43 occurs if the user cancels the dialogue.

2D data contains the single-precision numbers the VI writes to the file if 1D data is not wired or is empty.

1D data contains the single-precision numbers the VI writes to the file if this input is not empty. The VI converts the 1D array into a 2D array before transposing it and converting it to string and writing it to a file. If transpose ? is FALSE, each call to this VI creates a new line or row in the file.

append to file? Set to TRUE if you want to append the data to an existing file; you can also set it TRUE to write to a new file. Set to FALSE (default value) if you want to write the data to a new file or replace an existing file.

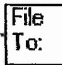
transpose ? Set TRUE to transpose the data before converting it to string. The default value is FALSE.

format specifies how to convert the numbers to characters. If the format string is %3f (default), the VI creates a string long enough to contain the number, with three digits to the right of the decimal point. If the format is %d, the VI converts the data to integer form using as many characters as necessary to contain the entire number. Refer to the discussion of format strings and the Array To Spreadsheet String function in Chapter 6, String Functions, of LabVIEW Function Reference Manual.

new file path is the path of the file to which the VI wrote data. You can use this output to determine the path of the file that you open using dialogue. new file path returns Not A Path if the use selects Cancel from the dialogue box.

---

Saved File Name.vi

File Sent To: 

A dialogue box is displayed showing the path of the file which has just been saved.

---